Applications of Raman Spectroscopy in Radiation Oncology: Clinical Instrumentation and Radiation Response Signatures in Tissue.

by

Samantha J. Van Nest
B.Sc., University of Manitoba, 2011
M.Sc., University of Victoria, 2013

A Dissertation Submitted in Partial Fulfillment of the
Requirements for the Degree of

DOCTOR OF PHILOSOPHY

in the Department of Physics and Astronomy

© Samantha J Van Nest, 2018
University of Victoria

All rights reserved. This dissertation may not be reproduced in whole or in part, by photocopying or other means, without the permission of the author.

Applications of Raman Spectroscopy in Radiation Oncology: Clinical Instrumentation and Radiation Response Signatures in Tissue.

by

Samantha J. Van Nest
B.Sc., University of Manitoba, 2011
M.Sc., University of Victoria, 2013

Supervisory Committee

Dr. A. Jirasek, Supervisor
(Department of Physics and Astronmy)

Dr. W. Ansbacher, Departmental Member
(Department of Physics and Astronomy)

Dr. M. Lefebvre, Departmental Member
(Department of Physics and Astronomy)

Dr. A.G. Brolo, Outside Member
(Department of Chemistry)

Supervisory Committee

Dr. A. Jirasek, Supervisor
(Department of Physics and Astronmy)

Dr. W. Ansbacher, Departmental Member
(Department of Physics and Astronomy)

Dr. M. Lefebvre, Departmental Member
(Department of Physics and Astronomy)

Dr. A.G. Brolo, Outside Member
(Department of Chemistry)

ABSTRACT

Radiation therapy (RT) plays a crucial role in the management of cancer, however, current standards of care have yet to account for patient specific radiation sensitivity. Raman spectroscopy (RS) is a promising technique for radiobiological studies as a way to measure radiation responses in biological samples and could provide a method for monitoring and predicting radiation response in patients. The work in this dissertation gives way to significant advances in the implementation of RS for applications in radiation oncology. Specifically, instrumentation improvements for clinical implementation of RS were achieved through the investigation and development of Raman microfluidic systems. Unique magnesium fluoride based microfluidic systems were engineered and evaluated for applications in radiobiological studies. These systems were found to yield superior spectral quality over traditional microfluidic designs.

Furthermore, in order to assert RS as a key technique for clinical monitoring and prediction of radiation responses, human non-small cell lung cancer (NSCLC) and breast

adenocarcinoma tumour xenograft models were investigated for Raman signatures of radiation response. These studies found that RS can identify unique and distinct signatures of radiation response in tumours, that can be tracked over time. In particular, NSCLC tumours were found to have key radiation induced modulations in cell cycle and metabolic linked spectral features- including glycogen. Breast adenocarcinoma tumours were found to exhibit distinct fluctuations in spectral features linked to cell cycle as well as protein content. In the case of NSCLC, radiation response signatures were found to be linked to tumour regression and hypoxic status of the tumour- a key factor that dictates radiation resistance in the disease.

This work provides the first application of RS to measure radiation response signatures of tumours irradiated *in vivo*. These results show that RS is a versatile technique that can offer insight into radiation induced molecular changes that are unique to the type of cancer and can be monitored over several days following radiation exposure. Together with improved instrumentation for radiobiological studies using microfluidics, the work presented in this dissertation further emphasizes the key role RS can have in radiation oncology and personalization of RT.

Contents

Supervisory Committee ii

Abstract iii

Table of Contents v

List of Tables xi

List of Figures xii

List of Abbreviations xv

Acknowledgements xxi

Dedication xxiii

Epigraph xxiv

1 Personalized Radiation Therapy 1

1.1 The problem of cancer 1

1.2 Modernizing radiation therapy 2

1.3 Biologically informed radiation therapy 3

1.4 Personalizing radiation therapy 5

1.4.1 Intrinsic assays 5

1.4.2 Extrinsic assays 6

1.4.3 Genome-wide indicators 6

1.4.4 Radiomic and functional imaging 7

1.4.5 New innovations in radiation response assays 8

1.5 Raman spectroscopy for applications in radiation oncology 8

1.6 Raman spectroscopic applications in cancer care: Diagnostics 9

1.7 Raman spectroscopic applications in cancer care: Radiobiology 10
1.8 Dissertation scope 11

2 Clinical Radiation Biology **13**
2.1 The biology of tumours 13
2.1.1 The building blocks of tissue: Biomolecules 14
2.1.2 Basic cellular functions: Cell cycle 17
2.1.3 Basic cellular functions: Metabolism and the role of glycogen . 18
2.1.4 Tumour environment 22
2.2 Radiation biology 25
2.2.1 Mechanisms of radiation damage 25
2.2.2 Radiation induced damage 27
2.2.3 Factors associated with radiation response 30
2.3 Summary 32

3 Raman Spectroscopy: Theory, Instrumentation and Data Processing 33
3.1 The physics of Raman spectroscopy 33
3.1.1 Classical description of light scattering 34
3.1.2 Raman peak intensity 36
3.1.3 Selection rules for Raman activity 37
3.1.4 Raman shift 39
3.2 Instrumentation considerations for Raman spectroscopy 40
3.2.1 Raman microscopy 40
3.2.2 Spectroscopic principles in Raman microscopy 43
3.2.3 Detecting and displaying Raman spectra 45
3.3 Spectral analysis 45
3.4 Considerations for Raman spectroscopy in biological applications . . . 49
3.5 Summary 51

4 Materials & Methods **52**
4.1 Murine tumour models 52
4.1.1 Cell lines 53
4.1.2 Tumour xenografts 54
4.2 Tumour irradiations and harvesting 55
4.2.1 LINAC based irradiations 56
4.2.2 SARRP based irradiations 56

4.2.3 Tumour harvesting . . . 57
4.3 Raman microscopy . . . 57
4.3.1 Instrumentation . . . 57
4.3.2 Spectral acquisition . . . 59
4.3.3 Data processing . . . 61

5 Raman Microfluidics 67
5.1 Introduction . . . 67
5.1.1 Limitations for clinical implementation of single cell Raman spectroscopy . . . 68
5.1.2 Instrumentation considerations . . . 69
5.1.3 Microfluidic chip considerations . . . 72
5.1.4 Current designs for single cell Raman microfluidics . . . 76
5.1.5 Objective . . . 78
5.2 Materials & Methods . . . 78
5.2.1 PDMS system . . . 78
5.2.2 Au-PDMS system . . . 79
5.2.3 MgF_2 system . . . 79
5.2.4 Parafilm-MgF_2 system . . . 80
5.2.5 Raman system . . . 80
5.2.6 Cell samples . . . 80
5.3 Results . . . 80
5.3.1 PDMS system . . . 80
5.3.2 Au-PDMS system . . . 82
5.3.3 MgF_2 system . . . 83
5.3.4 Parafilm-MgF_2 system . . . 87
5.4 Discussion . . . 89
5.5 Concluding statement . . . 91

6 Raman Spectroscopic Study of Irradiated Tumours: Non-Small Cell Lung Cancer 92
6.1 Preface . . . 92
6.2 Introduction . . . 93
6.3 Materials & methods . . . 95
6.3.1 Cell lines and tumour xenografts . . . 95

6.3.2 Tumour irradiation and harvesting 96
6.3.3 Raman microscopy measurements of tumour tissue 97
6.3.4 Spectral processing and statistical analysis 97
6.3.5 Periodic acid-Schiff staining 99
6.3.6 Code availability 99
6.4 Results 100
6.4.1 Principal components and score trends with radiation exposure. 100
6.4.2 Radiation-induced Raman differences in tissues correlate with *in vitro* signatures 104
6.4.3 Radiation-induced Raman signatures are expressed heterogeneously throughout tissue 105
6.4.4 Expression of radiation-induced Raman signatures varies among tumours 106
6.4.5 Glycogen accumulation confirmed using periodic acid-Schiff staining 106
6.5 Discussion 108
6.6 Concluding statement 110

7 Radiation Effects on Tumour Metabolism in Non-small Cell Lung Cancer 111
7.1 Preface 111
7.2 Introduction 112
7.3 Materials & methods 114
7.3.1 Cell lines and tumour implantation 114
7.3.2 Tumour irradiation and harvesting 114
7.3.3 *Ex vivo* Raman microscopy 115
7.3.4 Spectral processing and analysis 115
7.3.5 Immunofluorescence imaging 116
7.3.6 Co-registration of Raman and immunofluorescence data 117
7.3.7 Statistical procedures 118
7.4 Results 118
7.4.1 Raman spectroscopy identifies radiation induced glycogen perturbations as early as 2 hours and up to 10 days post irradiation 118
7.4.2 Glycogen expression is correlated to tumour regression in NSCLC 120
7.4.3 DNA damage and hypoxia are associated with RT exposure . 122

7.4.4 Irradiated tumours exhibit higher CAIX expression 124
7.4.5 Intra-tumour glycogen expression is correlated to CAIX expression 125
7.5 Discussion 125
7.6 Concluding statement 129

8 Raman Spectroscopic Study of Irradiated Tumours: Triple Negative Breast Cancer 130
8.1 Preface 130
8.2 Introduction 131
8.3 Materials & methods 133
8.3.1 Cell line and tumour xenografts 133
8.3.2 Tumour irradiation and harvesting 133
8.3.3 *Ex vivo* Raman microscopy 134
8.3.4 Spectral processing and analysis 134
8.3.5 Statistical analysis 135
8.4 Results 136
8.4.1 Principal component analysis identifies common spectral features between days 1 and 3 136
8.4.2 Principal component analysis identifies spectral composition changes in human breast adenocarcinoma xenografts that are radiation dose dependent 140
8.4.3 Raman spectroscopy identifies spectral changes at days 1 and 3 that are related to radiation exposure 141
8.4.4 Correlation of spectral features between *in vitro* and *ex vivo* Raman studies 141
8.5 Discussion 142
8.6 Concluding statement 145

9 Conclusion 146

Bibliography 149

Appendices 185

Appendix A Principal Component Band Assignments in Non-Small Cell Lung Cancer Study 186

Appendix B Principal Component Band Assignments in Non-Small Cell Lung Cancer Metabolism Study **190**

Appendix C Principal Component Band Assignments in Breast Cancer Study **193**

List of Tables

Table 4.1 Cell culturing media and its contents. 54
Table 4.2 Dose and harvesting groups for the mouse cohorts. 58

Table A.1 Raman peak assignment for radiation induced component (PC1) in H460 tumour xenografts of Cohort A. 187
Table A.2 Raman peak assignment for cell cycle component (PC2) in H460 tumour xenografts of Cohort A. 189

Table B.1 Raman peak assignment for radiation induced component (PC1) in H460 tumour xenografts of Cohort C. 191
Table B.2 Raman peak assignment for cell cycle component (PC2) in H460 tumour xenografts of Cohort C. 192

Table C.1 Raman peak assignment for cell cycle component (PC1) of MDA-MB-231 tumour xenografts of Cohort B. 194
Table C.2 Raman peak assignment for radiation induced component (PC2) of breast tumour xenografts of Cohort B. 196

List of Figures

Figure 1.1 Factors considered for treatment design in radiation therapy. . . 4

Figure 2.1 Monomer units of RNA and DNA. 15
Figure 2.2 The cell cycle. 18
Figure 2.3 The fate of glucose in the cell. 19
Figure 2.4 Glycogen synthesis and metabolism. 21
Figure 2.5 Tumour survival mechanisms regulated by HIF-1 under hypoxia. 24
Figure 2.6 Schematic of a clinical linear accelerator. 26

Figure 3.1 Scattering interactions involving visible light. 34
Figure 3.2 Schematic of a Raman microscope. 40
Figure 3.3 Microscope objective with definition of θ. 41
Figure 3.4 Filtering and collimation in the Raman microscope. 43
Figure 3.5 Light dispersion in a single grating spectrometer. 44
Figure 3.6 Light dispersion and the CCD detector. 46

Figure 4.1 Raman spectrometer with incident and scattered light paths. . 59
Figure 4.2 Mapping regions of a tissue section. 60
Figure 4.3 Raw and background subtracted Raman spectrum from tissue. . 63
Figure 4.4 Raman spectral shifting using the phenylalanine peak. 64

Figure 5.1 Raman microscope coupled with a microfluidic chip 69
Figure 5.2 Objectives for observing particles under a coverslip. 70
Figure 5.3 Objective working distance. 71
Figure 5.4 Materials suitable for microfluidic chip fabrication. 74
Figure 5.5 PDMS system. 81
Figure 5.6 PDMS background spectra. 82
Figure 5.7 PDMS cell spectrum. 83
Figure 5.8 Au-PDMS system. 84
Figure 5.9 Au-PDMS background spectrum. 84

Figure 5.10Au-PDMS cell spectra. 85
Figure 5.11MgF_2 system. 86
Figure 5.12MgF_2 background spectra. 86
Figure 5.13MgF_2 cell spectra. 87
Figure 5.14Parafilm-MgF_2 system. 88
Figure 5.15Parafilm-MgF_2 background spectra. 88
Figure 5.16Parafilm-MgF_2 cell spectra. 89

Figure 6.1 Radiation related Raman spectral changes identified using principal component analysis. 101
Figure 6.2 Comparison of principal components derived from Raman spectra of non-small cell lung cancer irradiated *in vitro* and *in vivo*. 104
Figure 6.3 Spatial maps of principal component (PC) 1 score at three unique regions within a single tumour irradiated to 15 Gy. 105
Figure 6.4 Periodic acid-Schiff staining images from irradiated and unirradiated tumour tissue and liver tissue control. 107

Figure 7.1 Raman spectral changes linked to glycogen (PC1) and cell cycle (PC2) in NSCLC xenograft tissue following irradiation. 119
Figure 7.2 Raman spectroscopy identifies increased glycogen, which is correlated with radiation induced tumour regression. 121
Figure 7.3 Concurrent immunofluorescence staining of γ-H2AX associated DNA damage, and hypoxia indicated through pimonidazole. . . 122
Figure 7.4 Quantification of immunofluorescence staining of γ-H2AX and pimonidazole. 123
Figure 7.5 Trends in CAIX expression between irradiated and unirradiated tumours harvested at 3 days post-treatment. 124
Figure 7.6 Local correlations between cellular glycogen using RS and CAIX immunofluorescence. 126

Figure 8.1 Mean Raman spectrum of MDA-MB-231 xenograft tissue. . . . 136
Figure 8.2 Raman spectral changes linked to cell cycle (PC1) in MDA-MB-231 xenograft tissue following radiation. 138
Figure 8.3 Biochemical response (PC2) in MDA-MB-231 xenograft tissue following radiation. 139

Figure 8.4 Comparison of principal components derived from Raman spectra of *in vivo* irradiated MDA-MB-231 tumour xenografts and cells irradiated *in vitro*. 142

List of Abbreviations

γ-H2AX phospho-histone H2AX.

3D-CRT three dimensional conformal RT.

A adenine.

AKT protein kinase B.

AMP adenosine monophosphate.

AMPK 5' adenosine monophosphate-activated protein kinase.

ATCC American Type Culture Collection.

ATM ataxia telangiectasia mutated.

ATP adenosine triphosphate.

ATR ataxia telangiectasia and Rad3 related.

BCCRC British Columbia Cancer Research Centre.

BL baseline.

BNIP3 Bcl2/E1B 19 kDa-interacting protein 3.

BSA bovine serum albumin.

BSC biological safety cabinet.

BSL2 Biological Safety Level 2.

C cytosine.

CAIX carbonic anhydrase IX.

CAXII carbonic anhydrase XII.

CBCT cone beam computed tomography.

CCD charge coupled device.

CK2 casein kinase 2.

CT computed tomography.

DBE glycogen debranching enzyme.

DDR DNA damage response.

DI deionized.

DMEM Dulbecco's Modified Eagle's Medium.

DMSO dimethyl sulfoxide.

DNA deoxyribonucleic acid.

DRC The Deeley Research Centre.

DSB double strand breaks.

ECM extra-cellular matrix.

ER estrogen receptor.

FACS fluorescence activated cell sorting.

FBS fetal bovine serum.

FT Fourier transform.

G guanine.

G0 gap 0.

G1 gap 1.

G1P glucose-1-phosphate.

G2 gap 2.

G6P glucose-6-phosphate.

GAA alpha-acid glycosidase.

GBE glycogen branching enzyme.

GMCSF granulocyte-macrophage colony-stimulating factor.

GSK3β glycogen synthase kinase 3 beta.

GYG glycogenin.

GYS1 glycogen synthase.

HCA hierarchical cluster analysis.

HER2 human epidermal growth factor 2.

HIF-1 hypoxia-inducible factor one.

HK2 hexokinase 2.

HNSCC head and neck squamous cell carcinoma.

HPV human papilloma virus.

HR homologous resection.

IF Immunofluorescence.

IGRT Image guided radiation therapy.

IMRT intensity modulated radiation therapy.

IP intraperitoneal.

IRIF ionizing radiation-induced foci.

KHD Kramer Heisenberg Dirac.

LDA linear discriminate analysis.

LINAC clinical linear accelerator.

MCT4 H+/monocarboxylate transporter 4.

MLC multi-leaf collimator.

MRI magnetic resonance imaging.

mRNA messenger RNA.

NA numerical aperture.

NADH nicotinamide adenine dinucleotide.

NADPH nicotinamide adenine dinucleotide phosphate.

NHEJ non-homologous end joining.

NSCLC non-small cell lung cancer.

OBI On-Board Imager.

PAS periodic acid-Schiff.

PBS phosphate buffer saline.

PC principal component.

PCA principal component analysis.

PDK1 pyruvate dehydrogenase kinase 1.

PDMS polydimethylsiloxane.

PET positron emission tomography.

PGM1 phosphoglucomutase.

PIMO pimonidazole.

PKA protein kinase A.

PP1 protein phosphatase 1.

PPARγ peroxisome proliferator-activated receptor γ.

PR progesterone receptor.

PYGL glycogen phosphorylase.

RACS Raman activated cell-sorting.

RBE relative biological effectiveness.

RNA ribonucleic acid.

RPMI Roswell Park Memorial Institute.

RS Raman spectroscopy.

RSI radiation sensitivity index.

RT radiation therapy.

S DNA synthesis.

SAD source-axis-distance.

SARRP small animal radiation research platform.

SBRT Stereotactic body radiation therapy.

SERS surface enhance Raman spectroscopy.

SF2 surviving fraction at 2 Gy.

SNPs single nucleotide polymorphisms.

SSB single strand breaks.

STAT1 signal transducer and activator of transcription-1.

T thymine.

U uracil.

UGP2 G1P uridyltransferase.

VEGF vascular endothelial growth factor.

VMAT volumetric modulated arc therapy.

ACKNOWLEDGEMENTS

I am truly grateful for all of the amazing friends and colleagues I crossed paths with in Victoria. To name you all is nearly impossible, but without you this project would not be what it is.

To the talented staff at UVIC including the electronics shop guys, Koh Yiin Hong, Alex Wlasenko and the talented folks at The Deeley Research Centre, in particular Lindsay DeVorkin, Nils Pavey, Katy Milne and Angela Lum thank you for your guidance. Further, thank you to all of the Medical Physicists as well as Stephen Gray, Sandra Clawson and Mark Goldie at BC Cancer. Your support, encouragement and many interesting conversations have been invaluable to me. To the Medical Physics grad students, thank you for the much needed laughs and fun as we all continued down the path of grad studies together.

To my mentors Wayne Beckham, Magdalena Bazalova-Carter and Devika Chithrani I am so grateful for the time you spent helping me shape my career even though I was not your student. Your wisdom and advice will last a lifetime for me.

Thank you to my co-researchers Phiranuphon Meksiarun and Martin Isabelle for taking the time to have engaging conversations with me and bringing such a high level of skill and creativity to our group.

To my (unofficial) co-supervisors Andrew Jirasek, Julian Lum and Alexandre Brolo, thank you for teaching me to ask questions and challenge what I know. Your mentorship has shaped me into the researcher I am today and I am thankful for that. It has been a pleasure working on your team!

I would also like to thank my committee members Will Ansbacher and Michel Lefebvre for their support and guidance throughout my degree and for having the patience to read this dissertation!

To my Girl Guiding family here in Victoria, in particular Leslie Simpson and Lesley Ruzicka, thank you for being great role models for me and supporting me through all of life's ups and downs.

To my parents and brother, thank you for always supporting me and encouraging me to chase my dreams. You have been by my side for all 25 years of my schooling and I honestly could not have done it without you!

Finally, I am indebted to my two dear friends and colleagues, Leah Nicholson and Chris Johnstone. Their bright smiles and support throughout my degree have really kept me motivated. Leah, your assistance on all of the projects and "operations" helped make this research possible. You are a brilliant lady and I am honoured I was able to work with you in one of your first experiences as a nurse. Chris, your support and encouragement has helped me through some of the most difficult moments of my career. Thank you for believing in me and always being there to adventure with me.

To Judy, Patsy, Elsie and all the other strong women I have had the privilege of knowing that have battled cancer; your determination, perseverance and grace are something I admire and will continue to strive towards each and every day. Your story keeps me motivated to continue researching.

For Judy

No matter what you do, have fun!

-JVN



Chapter 1

Personalized Radiation Therapy

1.1 The problem of cancer

Cancer is a disease characterized by cells that have lost the ability to control normal growth and death processes and have the potential to invade distant tissues. This disease can originate from many different cell types throughout the body including epithelial, mesenchymal, blood, immune, central and peripheral nervous system cells [1]. Both inter- and intra-disease heterogeneity exists in terms of genotypic and phenotypic characteristics, disease progression and response to treatment. This means that while there are key differences between various types of cancer, there are even differences in characteristics among a population of individuals with the same type of cancer, making this a complex disease to both characterize and treat.

Cancer therapy is often a multifaceted approach, making use of a combination of treatment strategies including surgery, radiation therapy (RT), chemotherapy and immunotherapy. RT plays a key role both as a strategy for definitive treatment and palliative care. Radiation can be administered either adjuvant or on its own, for a variety of disease sites including: breast, colon, non-hodgkins lymphoma, lung, melanoma, and prostate [2]. As such, nearly 50% of all cancer patients undergo RT at some point during their treatment. Further, 29% of cancer patients in the USA received RT during their initial treatment course in the years 2003-2005, and by 2020 it is expected this number will increase by 22% [3]. RT is a highly implemented and relatively cost efficient approach to cancer care, and demand for this treatment only

continues to increase.

1.2 Modernizing radiation therapy

Radiation therapy uses ionizing radiation to induce damage in deoxyribonucleic acid (DNA) within cancerous cells while minimizing damage to surrounding healthy tissues. Typically, high energy photons (MV energy) are either supplied from a radioactive source (e.g. ^{60}Co, brachytherapy) or produced using a clinical linear accelerator (LINAC). These photons are delivered to the disease site with the aim of achieving relatively uniform dose coverage in the tumour and doses below specified tolerances in the surrounding normal tissues.

To date, efforts to individualize RT have come in the form of using anatomical imaging and clinical parameters to deliver a conformal radiation dose to the disease site [4, 5]. These efforts have been made possible through key technological advancements in the field of RT physics. Prior to the 1950s, radiation field delivery to lesions was primitive, with little conformality to the site of the lesion. The introduction of an isocentrically rotating ^{60}Co treatment machine by Johns and Cunningham in 1959 initiated the push towards conformal radiation field delivery [6]. By the mid 1960s concepts in three dimensional conformal RT (3D-CRT) on the LINAC were developed [7], delivering multiple statically shaped beams in a three dimensional dose distribution [8]. The next major advancement came in the late 1990s, when intensity modulated radiation therapy (IMRT) became commercially available [9]. IMRT uses a multi-leaf collimator (MLC) to produce field intensity modulations that are optimized to achieve superior conformal dose escalation of the tumour and improved healthy tissue sparing [10]. IMRT has proven particularly valuable in sites such as: lung [11], head and neck [12, 13] and prostate [14, 15]. Contemporary clinical RT techniques primarily use volumetric modulated arc therapy (VMAT) which combines the field shaping achieved in IMRT with simultaneous changes in dose rate, gantry arching and couch motion. intends to maximize conformal dose delivery capabilities as obtained with IMRT, while improving treatment times [16].

Modern MLCs have lead to dose-shaping capabilities that approach the physical limit in IMRT and VMAT [17]. The primary challenge in radiation dose delivery currently lies in target selection and delineation as well as daily patient set-up accuracy and

tumour localization [17]. Image guided radiation therapy (IGRT) makes use of in-treatment image guidance using either cone beam computed tomography (CBCT) [18] or magnetic resonance imaging (MRI) [19, 20] to account for tumour location and patient-set up changes day-to-day. Stereotactic body radiation therapy (SBRT) combines improved dose conformality and targeting accuracy through image guidance to deliver large, ablative doses of radiation. This technique makes use of improved biological effectiveness with hypofractionation, with the intention of improved treatment outcomes. SBRT has shown favourable results as an alternative to surgery in non-small cell lung cancer (NSCLC) [21], liver [22–24] and spine [25–28].

Recent advances in particle therapy (e.g. proton, carbon ion) have the potential to further improve dose conformity as a result of the short range dose deposition characteristics associated with charged particles [29], leading to sparing of normal tissue [30] compared to photon-based treatments. Particle therapy also has the potential for improved biological cell kill through higher relative biological effectiveness (RBE) compared to photons [30]. As a result, particle therapy has shown potential advantage over conventional photon therapy for some cases including pediatric cancers [31, 32] and eye tumours [31].

Particle therapy and SBRT showcase two key clinical technologies that attempt to exploit biological factors in order to make improvements to treatment outcome. However, the majority of advances in RT have focused on improving conformality and accuracy of radiation dose delivery. Key opportunities for improvement of RT exist, including consideration of biological factors for radiation response such as microenvironment effects and targeting radioresistance [17]. Although current RT approaches lead to uncomplicated local or locoregional control for many disease sites [33], this is not always the case (e.g. glioblastoma, NSCLC [34–36]). Furthermore, dose escalation or de-escalation could further reduce normal tissue toxicity [37]. Therefore, substantial room for RT improvement exists in considering biological factors of radiation response.

1.3 Biologically informed radiation therapy

The decision to include RT in a patient's treatment regimen is based on evidence that it would improve local tumour control, relieve symptoms or improve quality of life [38].

Once RT is indicated several key decisions are to be made regarding specifics of the treatment, including whether RT will be used alone or adjuvant and the radiation dose to be delivered. Treatment approach is often decided based on a combination of empirical understanding, research based knowledge and personal experience [38]. In particular, factors predictive of therapy outcome such as tumour and patient related clinical indicators, treatment technicalities and the dose response relationship between tumour control and normal tissue injury are typically considered [38–40]. Figure 1.1 gives a detailed list of some commonly considered factors that allow the physician to estimate the probability of tumour control for a patient [40], based on previous understanding of how a similar population of patients responded to treatment. This is generally a one-size fits all approach to treatment and does not account for any inter-individual and intra-individual heterogeneities in radiosensitivity.

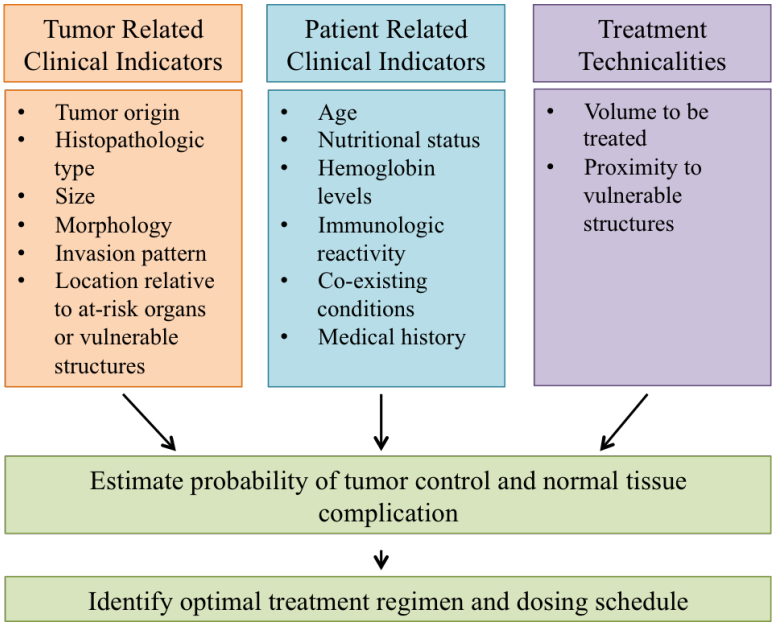


Figure 1.1: Factors considered for treatment design in radiation therapy. These include: characteristics related to the patient, disease and technicalities for treatment delivery. Compiled from sources [39, 40]

Variation in response of both normal tissue [41–43] and tumour [39, 40, 44] has been observed among patients presenting with similar clinical indicators. Several factors have been proposed that lead to variations in response among patients including: the random nature of radiation induced cell damage [45], genetic variations [46], tumour microenvironment differences [40, 47]. Beyond patient-to-patient variations, intra-tumour phenotypic heterogeneities within the tumour, have the potential to

affect treatment outcome [48]. Therefore, efforts to characterize these heterogeneities, and develop a RT treatment strategy based on personalized indications of radiation resistance and sensitivity have the potential to revolutionize the field of radiation oncology.

1.4 Personalizing radiation therapy

Various biomarkers of radiation response have been investigated, although clinical implementation is limited at this time. For example, retrospective and prospective trials within the Radio-oncology group of the German Cancer Consortium identified human papilloma virus (HPV) positive status in head and neck squamous cell carcinoma (HNSCC) as indicative of low risk for locoregional recurrence [49]. Further, HPV negative patients were found to stratify with favourable treatment outcomes if they were associated with low levels of stem cell markers and hypoxia [50]. While this is one example of biomarkers that may inform treatment outcome, a variety of other markers have been investigated. These markers are defined at various levels, including both intrinsic cellular characteristics (e.g. intrinsic radiation sensitivity, DNA response pathways), extrinsic characteristics (e.g. hypoxia, repopulation rates), genome-wide, radiomic and functional imaging indicators.

1.4.1 Intrinsic assays

Intrinsic assays include measuring cell radiosensitivity as characterized by counting the surviving fraction at 2 Gy (SF2). This is a direct measure of cell response to radiation through observing colony formation of a cell population following irradiation. SF2 has been shown to be a significant prognostic factor in head and neck [51] and cervix [52] cancers. Unfortunately, such assays are time consuming (four weeks incubation), labour intensive (cell culturing, colony counting) [53] and suffer from poor reproducibility (due to technical complexity of methodology). This assay is a direct measure of colony formation and therefore gives little insight into the underlying mechanisms driving radiation response. Alternatively, surrogates for cell radiosensitivity such as DNA break and repair [54], chromosome aberrations [55] or apoptosis [56] could be used. Such measures of inherent radiosensitivity are less

time consuming than colony assays however the surrogate technique is an imperfect measure of radiosensitivity [39].

1.4.2 Extrinsic assays

Oxygen levels in the tumour play an important role in radiation sensitivity (see chapter 2, section 2.1.4), making the measure of hypoxia (both directly and indirectly) a key target for radiosensitivity assays. As an example, hypoxia has been shown to indicate poor RT response in head and neck patients [57]. Hypoxic status can be measured directly through polarographic electrodes [58], or indirectly through endogenous hypoxic markers [59, 60]. Indirect measures of hypoxia include tumour vasculature density, perfusion and tumour metabolic activity using functional imaging. Unfortunately, direct measures of hypoxia are invasive to the patient while indirect measures may require injection of a chemical tracer.

Tumour repopulation, as indicated through cell proliferation rates can also be an indicator of radiosensitivity. This can be measured by counting the mitotic index (fraction of cells in mitosis), measuring tumour potential doubling time through thymidine analogue uptake [61] or staining for proteins associated with proliferation (e.g. Ki67) [62, 63]. Unfortunately, clinical implementation of techniques associated with determining cell proliferation rates are limited because thymidine uptake studies require injection of a drug/tracer making it invasive for the patient, and common protein labelling assays give little information on the involved radiation response mechanisms.

1.4.3 Genome-wide indicators

Recent shifts in technology leading to accessible genomic profiling techniques has led to rapid development of genetic signatures of radiation resistance. One approach has been targeting gene expression associated with a radiation response mechanism (e.g. hypoxia or proliferation) to identify signatures of response. For example, Khodarev et al. showed a link between signal transducer and activator of transcription-1 (STAT1) expression and increased tumour survival following radiation exposure [64]. However, the predictive power of this pathway has not been tested clinically. p53 has also been extensively studied as a biomarker for radiation response in a variety of tumour sites

(e.g. central nervous system, bladder, ovarian, colon, prostate) [65–69]. Carcinomas originating in brain, bladder and ovary with wild-type p53 gene status were associated with cell sensitivity to radiation, however the presence of this gene does not necessarily predict radiation sensitivity because other radiation response mechanisms can annul its function [65]. Loss of p53 function in colorectal carcinoma was found to have no effect on cell radiosensitivity [66]. Conversely, functional p53 was related to significantly increased clonogen survival in prostate carcinoma [67]. Although extensively studied, p53 gene status has yet to be verified through clinical trial as a predictive indicator.

Status of a single gene (e.g. p53 only) may be insufficient as a predictor of radiation sensitivity because its implications seem to vary with tissue of origin. Genome-wide assays eliminate the narrow scope associated with single gene assays, because many biological processes can be monitored in an unbiased manner. One such genetic signature was developed for indicating decreased recurrence rates in breast cancer [70]. Another approach has been development of the radiation sensitivity index (RSI), a gene expression model that can be used to predict intrinsic tumour radiation sensitivity and treatment response [71–74], The RSI has shown promise for a variety of tumour sites including rectal, esophageal, breast or head and neck cancer [71, 75] and more recently RSI has been combined with the linear quadratic model to genetically guide adjustments to RT dose [76]. More recently, single nucleotide polymorphisms (SNPs) have been found to correlate to histopathologic tumour responses to radiation [77–79]. Circulating cell free DNA also shows promise to assess response to chemotherapy, but has the potential to inform about response in radiation oncology as well [80].

1.4.4 Radiomic and functional imaging

Radiomics and functional imaging are also two highly promising areas of development for radiosensitivity assays. Radiomics uses image features extracted from radiographic (computed tomography (CT)) images to inform about functional characteristics of the patient that could not be identified with the naked eye. Mattonen et al. report radiomics is capable of detecting early changes linked to local recurrence in early-stage lung cancer [81]. Currently applications of radiomics in radiation oncology are very limited, but surely this area is promising.

Functional imaging methods include positron emission tomography (PET), MRI and optical imaging techniques like fluorescence imaging. These techniques image the entire tumour, eliminating selection bias associated with biopsy-based techniques [82]. Imaging based techniques provide spatial information about distributions in the disease and in some cases allow for dynamic imaging options. Tumour characteristics linked to radiation response including hypoxia [83] (measures of oxygen uptake or surrogates for hypoxia like perfusion [84] and angiogenesis [85]), cell proliferation [86], apoptosis [87], receptors or gene expression [88] have been investigated. Unfortunately, these techniques can involve injection of toxic or radioactive agents, making them invasive to the patient. Clinical studies investigating molecular imaging as a radiation response assay have shown some promise [84, 85, 89, 90], however, further clinical validation in large controlled studies is required.

1.4.5 New innovations in radiation response assays

While genome-wide assays and some radiomic assays show clinical promise, additional assays to augment these techniques and alleviate the draw backs associated with them are needed. Ideally, a clinically implemented assay would be based *in vivo* or *ex vivo* and: can be performed rapidly relative to the time line of a patients treatment, is cost effective, is reproducible, is insensitive to tumour sampling, is non-invasive, has high specificity and sensitivity to identifying changes in radiosensitivity and correlates directly to local tumour control [39, 40]. Finally, an assay which can directly measure radiation induced biochemical changes would improve understanding of radiation response mechanisms that could be targeted to enhance treatment and determine the optimal treatment for a patient.

1.5 Raman spectroscopy for applications in radiation oncology

Raman spectroscopy (RS) is a non-destructive, potentially non-invasive and label-free technique to quantitatively measure the biochemical fingerprint of systems including live cells and fresh tissue. RS has been extensively applied to study biological systems, as reviewed extensively by Fabian et al. [91]. Briefly, RS has been used to determine

secondary structure and side chain chemical environment in proteins [92], determine chromatin structure [93], distinguish DNA structure types, study characteristics of DNA/ribonucleic acid (RNA) [91] or DNA/protein hybrid structures [94] as well as nucleic acids and membranes (protein/lipid assemblies).

RS has also been extensively applied to study live and fixed human cells. Puppels et al. applied RS to study the biomolecular content of cytoplasmic and nuclear regions that make up human cells [95], emphasizing the sensitivity of RS to biomolecular content differences between these two regions. Further work showed biochemical content stratification among neutrophilic, eosinophilic and basophilic cells using RS [96]. Cell functions like cell cycle [97], proliferation [98] and cell death [97, 99] have also been monitored using RS. Further tissue composition changes arising from factors like disease (e.g. cancer [100] or Alzheimers [101, 102]) and tissue structure changes (e.g. muscle contraction [103, 104]) have also been studied.

Developments in Raman instrumentation have allowed for vast applications of RS to biological systems. With appropriate laser selection, biochemical content can be probed in a non-destructive manner allowing cells to remain viable following RS analysis. Furthermore, depending on instrumentation selection RS can be applied *in vitro*, *in vivo* or *ex vivo* without the use of labelling agents. Raman spectra can be obtained from sample regions on the order of the size of a cell (10 μm) or sub-cellular [95, 105], allowing for selective analysis of nuclear or cytoplasmic events. Taken together RS is an excellent candidate technique for clinical implementation. Despite these advantages, one key drawback for clinical implementation is the lengthy times for data acquisition and its labour intensive nature. However possibility for circumventing these drawbacks exist.

1.6 Raman spectroscopic applications in cancer care: Diagnostics

It is expected that cancer leads to changes in the molecular composition of diseased tissue, which should be reflected in Raman spectral differences [106]. Accordingly, research using RS on *ex vivo* biopsies has demonstrated differentiation between healthy and cancerous tissue in a variety of sites including brain [107], breast [108, 109],

cervix/gynecological [110,111], colon [112–114], bladder [113], head and neck [115,116] and prostate [115]. Technological advancements in fiber optic probes has lead to *in vivo* Raman spectral acquisition leading to effective differentiation between healthy and basal cell/squamous cell carcinomas [117] as well as breast [108], colon [114] and cervix [118] carcinoma.

Tumour margin demarcation and tumour grading has also been achieved using RS. In particular, tumour border demarcation has been demonstrated in basal cell carcinoma [119] and glioma tumours during surgery [120]. Furthermore, differentiation between metaplasia, inflammation, normal tissue, and low and high grade cervical pre-cancers [118] as well as between different grades of prostate carcinoma [121] have been achieved using RS.

1.7 Raman spectroscopic applications in cancer care: Radiobiology

The sensitivity of RS to structural and chemical changes has made this technique appealing for studying the effects of ionizing radiation on biological materials. Irradiated and unirradiated DNA solutions were found to have significant Raman spectral differences [122–124] attributed to structural changes in the DNA as a result of radiation damage. Dose dependent structural changes in bovine and human serum albumin [125], as well as other proteins [126] and lipid chains of artificial lipid membranes [127] have been identified using RS. Furthermore, RS has been used to study the effect of lipid phase state on lipid membrane radiation sensitivity [128], the effect of radiation on liposomes in the presence of proteins [129] and to identify radiation induced changes in plasma membranes isolated from hamster cells [130]. Gamma and proton radiation induced destruction of primary structure, functional group loss and cross-linking in sodium hyaluronate has also been examined [131].

RS has also been applied beyond basic biomolecules, to study the effects of radiation on cells. Single cell studies are valuable to radiobiology because they have the potential to reveal cell-specific radiation response mechanisms. By studying cells, a clear picture of the radiation response can be obtained and has the potential to lead to classifications and targeting of radiation responses. Radiation induced perturbations

in single cells have been studied in a variety of human lung, prostate and breast cancer cell lines, *in vitro* following irradiation to doses ranging from 2-50 Gy [105, 132–136]. Low dose radiation effects (<0.5 Gy) and bystander effects in human keratinocytes have also been studied using RS [137]. Interestingly, in some cell lines Raman signatures of radiation response have been found to segregate with p53 gene status and intrinsic radiosensitivity [135]. These results illustrate both the potential of RS to investigate driving mechanisms behind radiation response and act as a radiosensitivity predictive assay to monitor patient response during treatment.

While RS has proven successful in identifying radiation responses in cells, clinical implementation of this technique will involve applications in tissue. Tissue is a more complex system than elementary single cell systems because it is made up of a composition of cells and varying levels of extracellular matrix or basement membrane (in epithelial tissue) constituents [138]. Therefore Raman studies in such complex systems are key for establishing clinical implementation. RS has shown potential for distinguishing between radioresistant and radiosensitive oral [139] and cervical [140] cancer subtypes as well as identifying biochemical signatures of radiation response in human lymphocytes exposed to low radiation doses (<0.5 Gy) [141]. Furthermore, RS can identify radiation-induced spectral changes in skin (mouse, swine, human) and human pancreatic adenocarcinoma xenografts exposed to proton radiation *ex vivo* [142].

Tumour heterogeneity plays a key role in radiobiology, as it has the potential to lead to complex and varied radiation responses within the tumour. Therefore, *in vivo* irradiation investigations are necessary. In the case of mouse brain, distinct Raman spectral features could be identified following *in vivo* irradiation [143]. This result demonstrates the potential of RS for clinical applications in monitoring radiation response, however the key features of tumour microenvironment and dynamics are not addressed. Currently no applications of RS exists that investigate the radiation response of tumours *in vivo*.

1.8 Dissertation scope

The purpose of this dissertation is to address key components in asserting RS for clinical implementation in radiation oncology. First, design considerations for a Ra-

man microfluidic system are presented which would promote high throughput and automated analysis of biological samples. The aim of this system is to provide an alternative to traditional data acquisition techniques in order to reduce labour intensiveness and time for spectral acquisition. Next, the first application of RS to study radiation induced biochemical changes in human tumours irradiated *in vivo*, using murine models, is presented. The breadth of RS for studying irradiated tumours is investigated through NSCLC and triple negative breast tumour models, at various doses and time points post irradiation. Key molecular signatures of radiation response are identified and compared with results previously found in *in vitro*. In order to better understand the nature of Raman signatures of radiation response in NSCLC, links to hypoxia and hypoxic recovery within the tumour microenvironment are investigated.

This dissertation commences by reviewing key concepts in radiobiology, including particular focus on tumour microenvironment and hypoxia in chapter 2. Chapter 3 presents theoretical and instrumentation considerations for RS with particular emphasis on applications to biological systems. Chapter 4 describes the materials and key methodologies associated with experiments presented in this work.

The results of this dissertation are presented in a series of four chapters. First, chapter 5 presents instrumentation and design details for Raman microfluidic systems. Chapter 6 presents the initial RS analysis of *in vivo* irradiated NSCLC tumour xenografts, and discusses the key biomolecular changes in response to radiation exposure. Chapter 7 expands on the work in Chapter 6 by providing detailed analysis of the radiation induced Raman signatures identified in NSCLC tumours, linking these responses to tumour microenvironment and hypoxic fluctuations. Furthermore, temporal evolution of these response signatures are investigated. Chapter 8 presents Raman signatures of radiation response discovered in triple negative human breast xenografts.

This work is completed by highlighting the main conclusions drawn from the presented Raman studies and the implications of these results for integration of RS in radiation oncology. Appendices A, B and C offer supporting Raman spectral assignment for the corresponding studies.

Chapter 2

Clinical Radiation Biology

This chapter summarizes key concepts in radiation biology with particular emphasis on tumour microenvironment and metabolism. Section 2.1 presents the basic building blocks of tumours by discussing the common biomolecules and cell functions that drive cellular processes, tumour microenvironment and metabolism. Section 2.2 discusses the mechanisms of energy deposition by radiation in tissue, and the subsequent cellular processes that occur as a result of radiation damage. Factors affecting radiation damage are also discussed.

2.1 The biology of tumours

Tumours are a collection of neoplastic and stromal cells, supported by the tumour vasculature and embedded in an extracellular matrix [38]. The tumour system is therefore controlled by the collective functionality of cells and the biomolecules that drive cellular processes. Further, the tumour microenvironment itself plays an important role in progressive genetic evolution and clonal selection, which can influence development and characterization of the disease [38]. This section examines the fundamentals of biomolecules, cells and tumours in the context of normal functions and dynamics in the complex tumour environment.

2.1.1 The building blocks of tissue: Biomolecules

Human cells are made up of an outer cellular membrane which encloses the nucleus and organelle containing cytoplasm. The majority of the cell is composed of water (75% of cell content) [144], however further constituents include inorganic materials (1%) and a collection of organic materials including several key biomolecules: protein (15%), nucleic acid (1%), lipids (2%) and carbohydrates (1%) [145]. These biomolecules drive cellular function and form the basis of the cell's structure. The cell membrane defines the outer wall of the cell, isolating it from its surroundings. This membrane controls what enters and exits the cell and is made up of 40-50% lipid and 50-60% protein [144]. Cytoplasm is encased in the cellular membrane, which is an aqueous solution of proteins, RNA, glucose, cellular waste products, enzymes and electrolytes. Organelles are suspended within the cytoplasm and consists of the mitochondria (cellular metabolism), endoplasmic reticulum (synthesis of steroids, phospholipids and complex polysaccharides), ribosomes (protein synthesis), golgi apparatus (protein storage) and lysosomes (contain enzymes for autolysis of cell contents). Furthermore, the nucleus is central to cellular function and is made up of a double-layered membrane separating cellular DNA from the cytoplasm. This membrane is porous allowing for the exchange of proteins between the nucleus and rest of the cell. The nucleus holds nucleoprotein, RNA, enzymes, free amino acids, lipids, calcium, magnesium and potassium as well as chromatin [144]. Also located in the nucleus is the nucleolus, a small dense structure which contains 10-20% of the RNA for the entire cell [144]. The unified action of these cellular units yields cell function, which is ultimately driven by chemical processes dictated by the reactivity of key biomolecules.

Nucleic acids

Nucleic acids are nucleotide-based polymers, found in the form of DNA and RNA in the cell. Figure 2.1 shows the basic structure of nucleic acids, made up of nitrogenous base-pentose sugar-phosphate group monomers, linked through a 3,5-phosphodiester bond. RNA monomers are formed with a ribose sugar backbone (Figure 2.1a) and DNA is formed with a deoxyribose sugar backbone (Figure 2.1b). Nitrogenous bases available in DNA include adenine (A), guanine (G), cytosine (C) and thymine (T), with uracil (U) replacing thymine in RNA. Ordering of the bases within the nucleic

acid dictates primary structure, ultimately influencing function and physical properties. DNA is stored in compact entities called chromosomes, which are composed of a series of genes each containing a finite segment of DNA characterized by a specific sequence of bases. The structure of DNA is two polynucleotide chains, wound together in a double helix formation such that complimentary bases maintain stable contact through double (A-T) or triple (G-C) hydrogen bonds. Unlike DNA, RNA mainly exists in single strand form.

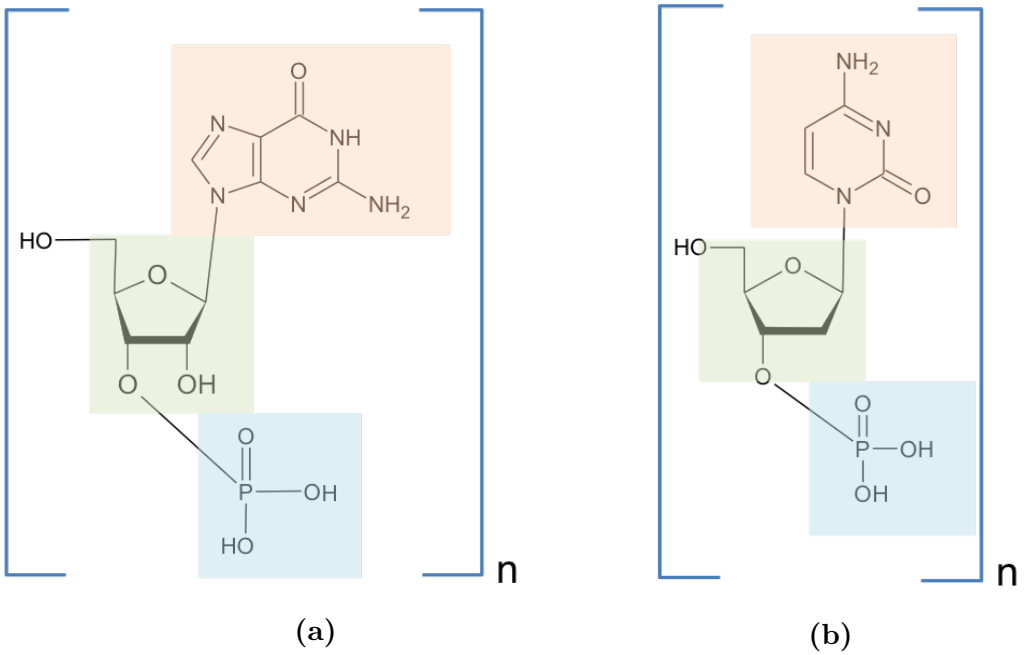


Figure 2.1: Monomer units of RNA (a) containing a guanine base and DNA (b) containing a cytosine base. The base is highlighted in orange, phosphate in blue and sugar (deoxyribose for DNA and ribose for RNA) shown in green.

DNA is primarily responsible for directing cell activity and passing on genetic information from one cell to the next. The ordering of base pairs on the DNA molecule stores and regulates all of these processes, and is activated by transcription of the DNA base ordering to yield messenger RNA (mRNA). mRNA leaves the nucleus and travels to the ribosomes where its base sequence forms the template to generate proteins. Therefore, the base ordering in the mRNA dictates the ordering of amino acids for polymerization into a specific protein. Proteins subsequently go on to carry out a variety of different biological functions within the cell. Nucleic acids form the basis of protein synthesis, yielding proteins that drive biological function of the cell and

tissue.

Proteins

Proteins drive essential cellular functions including maintaining fluid balance (serum albumin), regulating metabolism (hormones or enzymes), cellular transport and defence mechanisms. Proteins are high molecular weight polymers composed of α-amino acid subunits connected through peptide bonds, forming a polypeptide chain. The physical, chemical and biological properties of the protein are dictated by the amino acids that form it, as this determines the structure of the protein. The linear sequence of amino acids making up the polypeptide chain is referred to as the primary structure. Arrangement of the polypeptide chain in either helical, pleated sheet or random coils is described as the secondary structure. Tertiary structure is the final three-dimensional interaction of the helices, sheets and coils. Lastly, the quaternary structure is the aggregation of various proteins to make up a functioning unit.

Lipids

Lipids provide a key source of energy for the cell, as well as form an important component in cellular and organelle membranes. Lipids are classified based on possessing three key characteristics: 1) insolubility in water but soluble in organic solvents, 2) actual or potential to be an ester of fatty acids and 3) potential to be used by a living organism. Lipids can be classified as simple, compound or derived. Simple lipids are esters of fatty acids with alcohols (e.g. triglycerides, cholesterol esters), where as compound lipids which are esters of fatty acids with alcohols and other groups. Derived lipids yield from hydrolysis of either a simple or compound lipid and still possesses the characteristics of a lipid (e.g. saturated and unsaturated fatty acids, mono and di-glycerides, sterols, carotenoids and vitamins E and K).

Carbohydrates

Carbohydrates are a key energy source for cells composed of carbon, oxygen and hydrogen in a polyhydroxyl alcohol with aldehyde or ketone groups. They can be classified as basic monosaccharides (simple sugars), oligiosaccharides (composed of a

few monosaccharides) or polysaccharides which are formed by polymerization of one (homo-) or several (hetero-) types of monosaccharides. Glucose is a key carbohydrate that drives cellular function, as its metabolism yields the necessary precursors for synthesis of biological substances including purines, pyrimidines, amino acids, cholesterol, mucopolysaccharides (e.g. hyaluronic acid), fatty acids, glycoproteins and glycolipids.

The biochemical content of a cell varies depending on the type and function of that cell as well as progression through common cellular functions. Several key functions drive the life cycle of a cell, including cellular metabolism which provides energy sources for regular functioning of the cell and cycle progression which leads to cell propagation.

2.1.2 Basic cellular functions: Cell cycle

The cell cycle describes the process of cell division which yields two exact copies (daughter) of a parent cell. The cell cycle is bi-phased, consisting of interphase and mitosis, as depicted in Figure 2.2. Interphase takes up approximately 90% of the cell cycle [146], and is divided into three parts: gap 1 (G1), DNA synthesis (S) and gap 2 (G2). G1 is a phase of cell growth through increased RNA and protein content in preparation for DNA replication [147, 148]. Following from G1, cells enter S phase where DNA synthesis forms two new DNA strands identical to the parent strand. Cellular levels of RNA, protein and DNA increase during S phase [148] beyond G1 levels. Cells then enter G2 where RNA and protein levels further increase in preparation for replication [148]. At the end of G2, cells enter into mitosis in which the parent cell cleaves into two separate daughter cells. Each daughter cell contains a full compliment of the parent DNA, and approximately half of the biological content of the parent cell [145].

It is also possible for a cell to suspend progression through the cell cycle, entering into gap 0 (G0) phase. In this phase, the cell stays in a quiescent state with relatively low levels of RNA and protein [147, 149]. However, a cell still maintains its capabilities to divide in G0. Most cells will enter G0 during G1 and re-enter at S phase [150].

A human cell progress through the cell cycle in approximately 24 hours [150], although this can vary depending on the type of cell. This cycle is divided into approximately 1

hour for mitosis, 15 hours for S phase and 1-5 hours for G2 [145]. All remaining time is spent in G1 (approximately 8 hours), although the greatest variation in temporal progression amongst cells is during this phase [145].

2.1.3 Basic cellular functions: Metabolism and the role of glycogen

Glucose is a key carbohydrate used to fuel activity within the cell through controlled stepwise enzymatic action which degrades glucose and releases energy. Glycolysis splits a glucose molecule to form two pyruvate molecules, two adenosine triphosphate (ATP) molecules and two nicotinamide adenine dinucleotide (NADH) molecules. The latter two molecules are significant sources of energy to be used within the cell. Under conditions where glucose reserves get used up faster than they can be replenished from outside sources, glyconeogenesis can be regulated to synthesize glucose from pyruvate. However glyconeogenesis is energetically expensive and therefore under conditions of fasting or stress, cells can not afford this process. Rather, glucose is retrieved through the break down of glycogen [151].

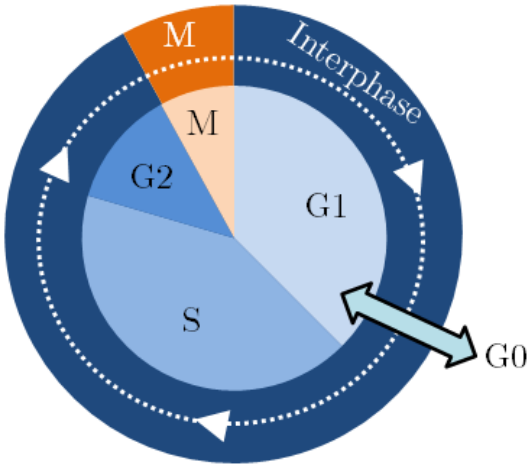


Figure 2.2: The cell cycle. Phases of the cell cycle are depicted, with the relative time spent in each phase reflected in the size distribution for gap 1 (G1), DNA synthesis (S) and gap 2 (G2) in interphase, as well as mitosis (M). Cells can also enter a state of cellular quiescence (G0).

The fate of glucose in the cell

Glucose is taken up in the cell through glucose transporter protein (GLUT1/2/3/4) and is subsequently phosphorylated by hexokinase 2 (HK2) to form glucose-6-phosphate (G6P), which remains bound in the cell. G6P has three primary metabolic fates as illustrated in Figure 2.3: 1) entering the pentose phosphate pathway for nicotinamide adenine dinucleotide phosphate (NADPH) and nucleotide precursors, 2) entering glycolysis to produce pyruvate, ATP and NADH, 3) entering into the glycogen synthesis pathway to produce glycogen [152].

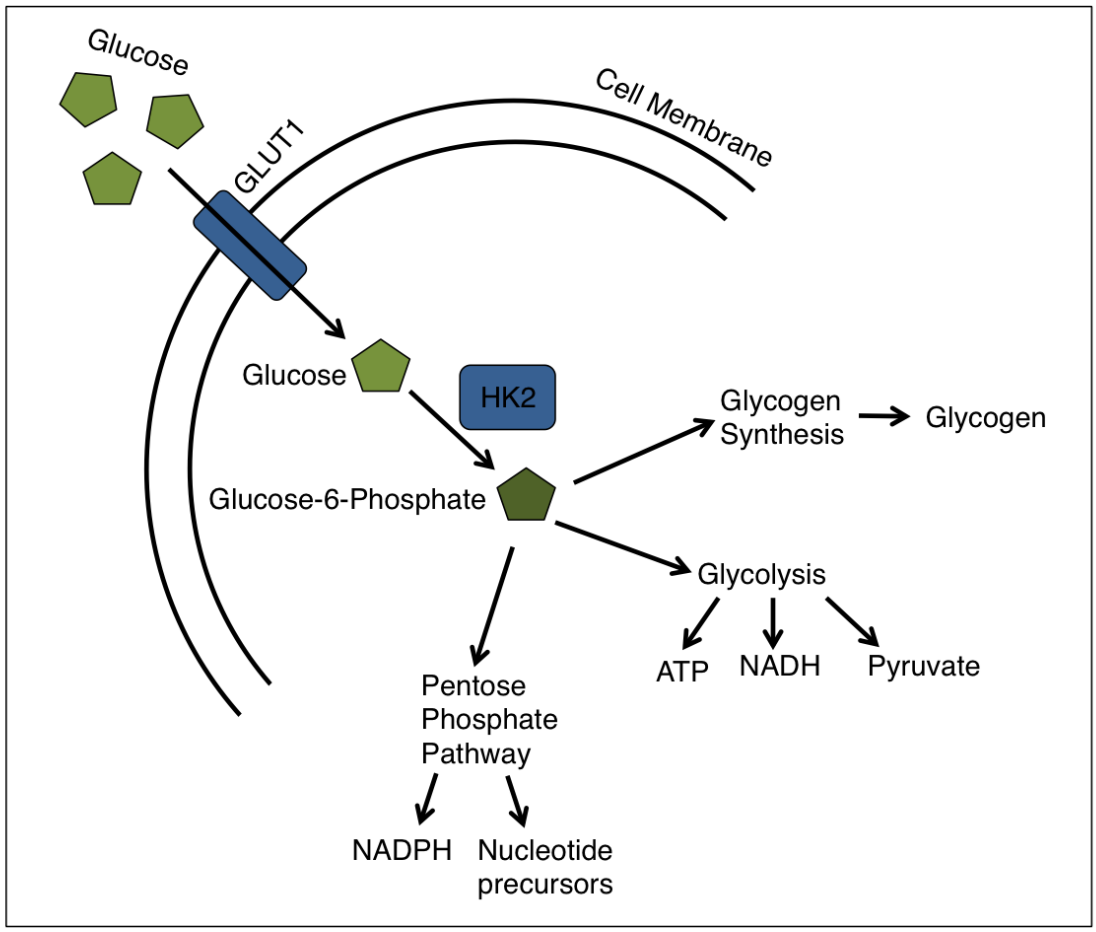


Figure 2.3: The fate of glucose in the cell. Glucose is imported into the cell via GLUT1, and is phosphorylated through HK2 to yield glucose-6-phosphate. Glucose-6-phosphate can be metabolised through the pentose phosphate pathway or glycolysis, or stored as glycogen through glycogen synthesis.

Glycogen synthesis

While processes 1 and 2 described in Figure 2.3 lead to the breakdown of glucose for energy supply within the cell, process 3 is an energy storage process in which glucose can be stored for later use in the form of glycogen. Glycogen is a branched polymer made up of several α1,4-linked glucose molecules with branching of α1,6-glucose polymers. This polymer is stored as small granules (20-50 nm, up to 200 nm) in the cytoplasm [152], typically in liver and muscle cells. However, glycogen storage has also been found to be particularly high in breast, ovary, skin and brain cancer cell lines, to name a few [152]. Glycogen synthesis and degradation is regulated by several enzymes and proteins, typically occurring in the cells of liver and muscle tissues. However, glycogen synthesis could occur in other cells (e.g. cancer) implying a survival mechanism which ensures a source of energy during stress [152].

Glycogen is formed from G6P through glycogen synthesis as illustrated in Figure 2.4. This process is initiated by conversion of G6P to glucose-1-phosphate (G1P) via phosphoglucomutase (PGM1). G1P uridyltransferase (UGP2) adds uridine to G1P to form the nucleotide sugar substrate UDP-glucose.

The core protein glycogenin (GYG) is auto-glucosylated, providing an oligiosaccharide primer for glycogen synthase (GYS1). GYS1 elongates the glucose chain by forming α1,4-glycosidic linkages of glycogen, using UDP-glucose as the glucosyl donor. GYS1 activity is regulated by several different kinases including: glycogen synthase kinase 3 beta (GSK3β) (further regulated by protein kinase B (AKT)), 5' adenosine monophosphate-activated protein kinase (AMPK), protein kinase A (PKA), casein kinase 2 (CK2) and protein phosphatase 1 (PP1).

Additional α1,6-glycosidic linkages form through the action of glycogen branching enzyme (GBE), creating a highly branched structure that can contain up to 55 000 glucose units [152,153]. The highly branched nature of glycogen increases its solubility in the cytosol and provides several docking sites for glycogen binding proteins [152].

Glycogen metabolism

The metabolism of glycogen takes place in the cytosol or lysosomal compartment of autophagosomes. Figure 2.4 depicts glycogen metabolism within the cytosol. This

process is characterized by cleaving of the α1,4- or α1,6-glycosidic linkages by glycogen phosphorylase (PYGL) or glycogen debranching enzyme (DBE), respectively. This results in conversion of glycogen back to the G1P substrate, which can subsequently be converted back to G6P by PGM1. Glycogen may also be delivered to the lysosomal compartments of an autophagosome where it can undergo glycophagy via

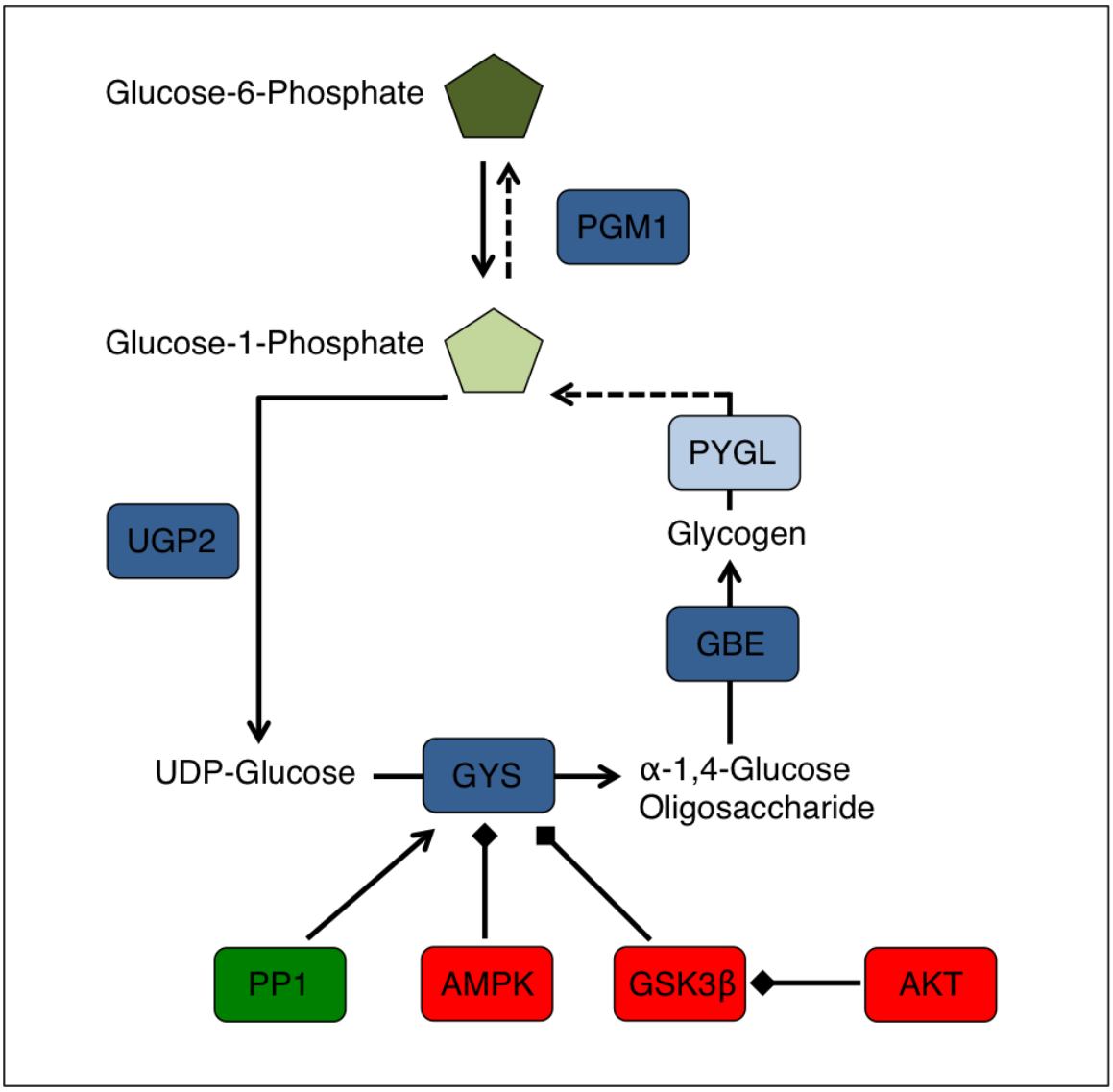


Figure 2.4: Glycogen synthesis and metabolism. Glucose-6-phosphate is converted to glucose-1-phosphate via PGM1, which then gains uridine to form UDP-glucose via UGP2. Glycogen synthase (GYS) elongates glucose chains forming α-1,4-Glucose Oligiosaccharides which leads to a branched glycogen entity through GBE. Glycogen returns back to glucose-1-phosphate through the action of PYGL. GYS is regulated by PP1, AMPK and GSK3β- which is further regulated by AKT.

hydrolysation by alpha-acid glycosidase (GAA) [154].

Reprogramming glycogen metabolism in cancer

Neoplastic disease is characterised not only by deregulated control of cell proliferation but also adjustments to energy metabolism. Under aerobic conditions, normal cells first preferentially direct glucose through glycolysis in the cytosol and the resulting pyruvate is processed in the mitochondria via oxidative phosphorylation. In the case of neoplastic cells, glucose metabolism can be reprogrammed to limit their energy metabolism primarily to aerobic glycolysis [155–157]. Glycolysis is of substantially poorer efficiency for ATP production (approximately 18-fold lower) in comparison to mitochondrial oxidative phosphorylation [158]. In an effort to compensate, the cell upregulates GLUT1, substantially increasing glucose import into the cytoplasm [159–161].

2.1.4 Tumour environment

Tumours are a complex community of cells including lymphocytes, erythrocytes, stromal cells and fibroblasts supported by signalling molecules and tissue framework such as vasculature and extra-cellular matrix. Tumours are initially of monoclonal origin [1], however they acquire heterogeneity with time due to a stepwise evolutionary acquisition of multiple genetic and epigenetic aberrations [1, 38, 162] and microenvironmental influences [38]. The microenvironment of tumours is characteristically different from normal tissues. In particular, abnormal vasculature and heterogeneity in circulation throughout the tumour lead to regions that are nutrient rich and poor [163]. This prompts anisotropic distributions of hypoxia, extracellular acidosis, glucose deprival, energy deprivation, high levels of lactate, interstitual fluid flow and hypertension throughout the tumour [163]. Of these microenvironmental factors, hypoxia is of particular clinical interest because it can lead to altered cellular metabolism, treatment response [164] and increased invasiveness [165].

Tumour hypoxia

Hypoxia is described as regions of low oxygen that can occur chronically or acutely within the tumour [166]. Chronic hypoxia is a permanent form of hypoxia resulting from limitations in diffusion of blood to regions of the tissue [167] as a result of poor vasculature development. Acute hypoxia on the other hand refers to spatial and temporal cycling of hypoxia which can occur on the order of seconds, minutes, hours and days [166,168,169]. Proposed factors involved in acute hypoxia include temporal fluctuations in red blood cell flux [166, 170] as well as metabolic fluctuations via the glycolytic oscillator [171].

Hypoxic conditions lead to the activation of hypoxia-inducible factor one (HIF-1), a transcription factor that binds to DNA and upregulates over 30 genes that facilitate oxygen delivery, angiogenesis via vascular endothelial growth factor (VEGF), and energy preservation (glucose transporters and glycolytic enzymes) [172–174]. Figure 2.5 shows the HIF-1 related cellular outcomes that can be promoted during hypoxia. Importantly, HIF-1 has been found to induce GLUT1/3 activation leading to increased glucose uptake in anaerobic conditions [175,176] and influence the metabolic activity of cells, favouring glycolysis and downregulating mitochondrial function [158, 177], possibly through pyruvate dehydrogenase kinase 1 (PDK1) activation [178]. The increased flux of glycolysis provides a rapid supply of ATP for the cell under hypoxic conditions at the expense of rapid acidosis in the cell through glucose breakdown to lactic acid. Therefore HIF-1 also regulates cellular pH by inducing expression of H+/monocarboxylate transporter 4 (MCT4) as well as carbonic anhydrase IX (CAIX) and carbonic anhydrase XII (CAXII) [179].

Cell survival is promoted through activation of autophagy via Bcl2/E1B 19 kDa-interacting protein 3 (BNIP3) [179], lipid synthesis via peroxisome proliferator-activated receptor γ (PPARγ) and glycogen synthesis [179] via HIF-1 activation [180]. However hypoxia has also been associated with AMPK activation, a promoter of cellular energy preservation through activation of catabolic pathways and inhibition of glycogen synthesis [181] (an anabolic activity). AMPK is upregulated through an increase in the ratio of adenosine monophosphate (AMP) to ATP, therefore ATP availability within the cell may drive switches between glycogen synthesis and glycogenolysis [182].

Beyond metabolic alterations, hypoxia can also affect cell cycle progression or promote

cell death. Specifically, activation of p21 and p27 promotes cell cycle arrest at G1/S [183] under anoxic conditions. Also, the activation of apoptosis through increased p53 levels [184] has also been suggested. Taken together, the cellular response to hypoxia is one which promotes the preservation of resources during a state of emergency.

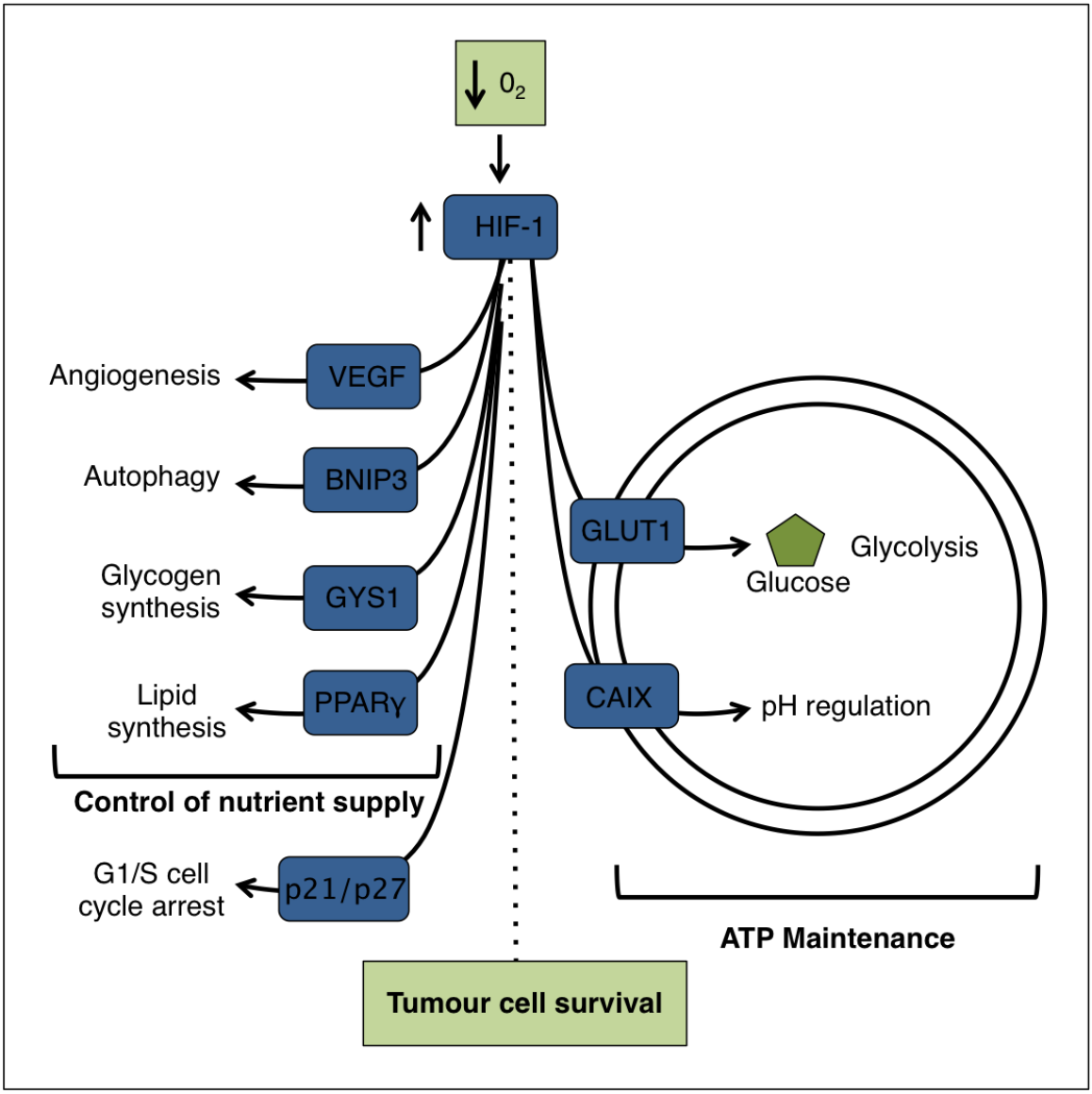


Figure 2.5: Tumour survival mechanisms regulated by HIF-1 under hypoxia. Hypoxia (low oxygen levels) activates HIF-1 which promotes nutrient supply (left) through angiogenesis, autophagy, glycogen and lipid synthesis. HIF-1 also promotes energy maintenance (right) by favouring glycolysis and consequently pH regulation via CAIX. Together with possible cell cycle checkpoint activation, tumour cell survival is promoted.

2.2 Radiation biology

Radiation damages tissue, leading to a cascade of signalling events. Ultimately this cell signalling dictates the fate of the cell; to repair and survive or die following radiation exposure. This section describes how radiation deposits energy in tissue and the tissue response as we currently understand it.

2.2.1 Mechanisms of radiation damage

Once RT is indicated as part of the patient's treatment regimen imaging (e.g. CT, PET, MRI) is used to locate the site of macroscopic disease within the patient. The radiation dose is prescribed to this region, plus an additional margin surrounding the region to account for patient motion, set-up errors and microscopic spread of the disease forming the treatment volume. Factors as discussed in chapter 1, section 1.3 are used to determine the specific dose of radiation to be delivered and subsequently a conformal and accurate dose delivery is facilitated using a LINAC, brachytherapy techniques or possibly particle beams (e.g. protons).

The linear accelerator

The clinical LINAC can produce both electron and photon beams to treat patients, however only photon mode will be discussed here. Figure 2.6 depicts the key components of a LINAC, where power is supplied to a modulator which simultaneously emits high voltage pulses to an electron gun and magnetron or klystron. The magnetron or klystron produces a magnetic field, while at the same time the modulator pulse heats a wire filament in the electron gun to release electrons at an initial energy of approximately 50 keV [185]. These electrons are injected into the linear accelerating structure using thermionic emission and the electromagnetic field causes acceleration to energies of 4-25 MeV. Bending magnets direct these electrons to a high atomic mass target (e.g. tungsten) where inelastic collisions cause the electrons to decelerate and emit bremsstrahlung photons. These photons produce the treatment beam which is subsequently collimated and shaped to produced a custom radiation field directed towards and aligned to the treatment volume. The LINAC is designed to have an axis of rotation centred around isocentre as indicated in Figure 2.6, and typically the

patient is aligned and immobilized relative to isocentre for treatment. The distance from target to isocentre is referred to as the source-axis-distance (SAD).

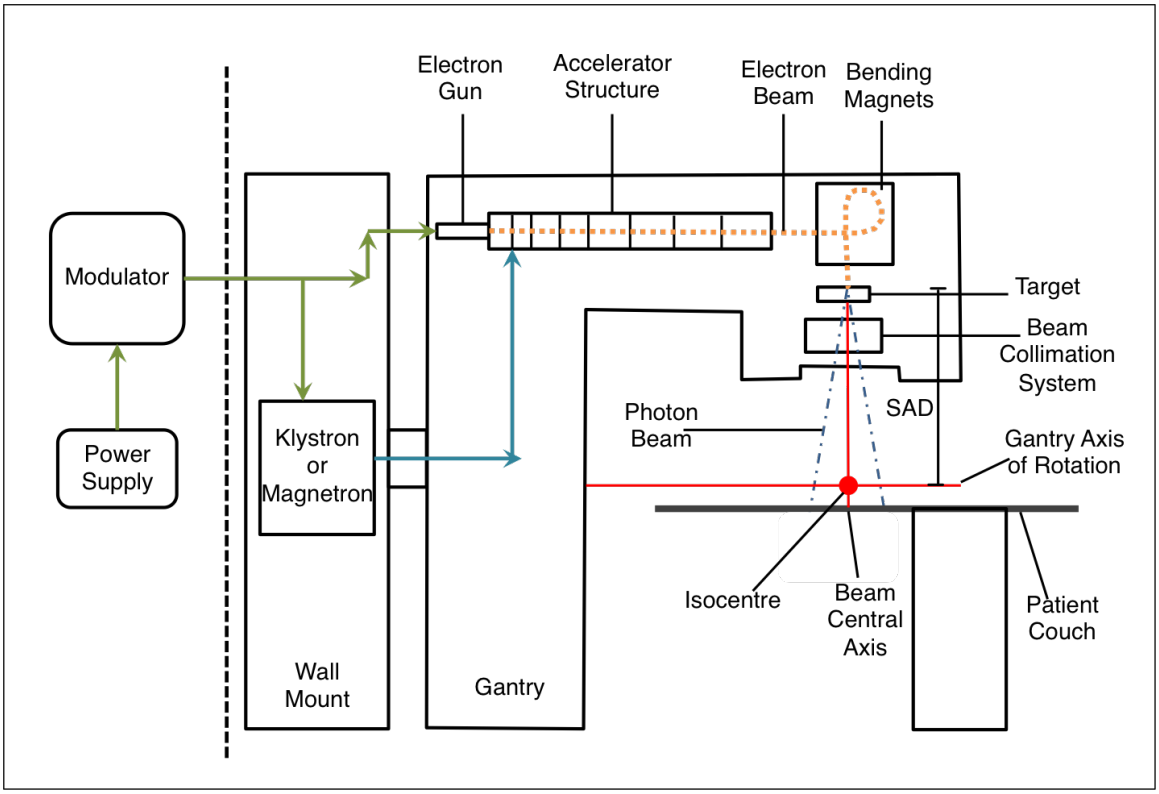


Figure 2.6: Schematic of a clinical linear accelerator. The treatment volume is aligned at isocentre and source-to-axis distance (SAD) is used to measure the distance from the target to isocentre. SAD is typically set to 100 cm.

Interactions of radiation with tissue

Photons emerging from the LINAC will interact primarily with the tissue of a patient. The radiation interaction properties of tissue (composed of 73% oxygen and 10% hydrogen) are highly similar to those of water (composed of 89% oxygen, 11% hydrogen) [186]. The LINAC produces photons that range in energy from 100 keV to the maximum accelerated energy of the electrons (typically 6 MeV) and therefore primarily interact through photoelectric, coherent scattering, incoherent scattering and pair production. Lower energy photons (below 20 keV in water [187]) tend to interact via photoelectric effect, incoherent scattering dominates for photon energies between 20 keV and 20 MeV [187] and pair production dominates for photon energies above

20 MeV [187]. The net meaningful (in terms of dose deposition in a patient) result of these processes (except for coherent scattering) is the release of at least one energetic electron which can go on to deposit energy in tissue. In addition to the release of an electron, these processes also release lower energy photons that can continue to interact in the tissue.

Dose deposition in tissue

Photons are considered indirectly ionizing radiation, meaning energy is deposited in the material by first interacting to release electrons which are then capable of depositing their energy into the medium. As electrons propagate through the tissue they can interact by: 1) inelastic collisions with atomic electrons (ionization or excitation), 2) inelastic collisions with nuclei (bremsstrahlung), 3) elastic collisions with atomic electrons and 4) elastic collisions with nuclei. Inelastic collisions result in energy loss by the electron, and resulting energy transfer to the medium (as is the case for type 1 interactions) or into photon energy which can then propagate accordingly (as is the case for type 2 interactions). Elastic collisions result in no loss of kinetic energy. Ionizing events with atomic electrons constitute the dominant energy loss mechanism of electrons in water [188]. Electrons continue to lose energy as they propagate through the medium, until thermal energy is reached and they are captured by surrounding atoms. The energy absorbed by the interacting medium through these charged particle interactions gives rise to dose deposition by the photon beam.

Dose is measured in units of Gray (Gy) and is described as the amount of energy transferred per kilogram of interacting material (1 Gy= 1 $\frac{\mathrm{J}}{\mathrm{Kg}}$). The energy deposited by radiation has the potential to cause molecular, and subsequently, biological damage.

2.2.2 Radiation induced damage

The process of radiation induced damage in cells can be divided into three parts: the physical, chemical and biological phase. The physical phase consists of charged particles (e.g. electrons) ionizing atoms in the cell including those within the nucleus, cytoplasm, and organelles. This phase occurs immediately following radiation expo-

sure, as it takes approximately 10^{-18} s for an electron to traverse a DNA molecule and on the order of 10^{-14} s to traverse a cell [189].

Radiation damage can result in functionality altering structural damage to carbohydrates, proteins and lipids. However, the consequences of damage in these abundant and continually regenerated biomolecules is minimal in comparison to the limited and biologically important DNA [190–192]. Ionizing radiation either directly damages molecular components of the DNA or indirectly affects DNA (e.g. via water) by the creation of highly reactive free radical species through electron interactions with biomolecules (e.g. carbon species in DNA, water). The chemical phase consists of radiation induced free radicals rapidly (within 1 ms of radiation exposure) reacting with surrounding molecules to form stable chemical changes in biologically important molecules [189]. In particular DNA single strand breaks (SSB) and double strand breaks (DSB) are key effects of radiation induced damage in the cell. These molecular changes drive the biological phase which spans from approximately 1 s after radiation exposure throughout the lifetime of living system; starting with an initial cascade of cell signalling to identify and address the chemical damage and later transitioning into acute and late effects of radiation exposure.

Initial DNA damage response

Upon radiation-induced DNA damage, the DNA damage response (DDR) pathways are initiated in order to determine cell outcome. Within 5-30 minutes of a DNA DSB or SSB [190] proteins which phosphorylate histone phospho-histone H2AX (γ-H2AX) are recruited to the site of damage. These include ataxia telangiectasia mutated (ATM) and the ataxia telangiectasia and Rad3 related (ATR) protein. Phosphorylation of γ-H2AX accompanies the activation of over 700 other proteins [193], which collectively are referred to as the ionizing radiation-induced foci (IRIF). Through activation of the DDR and formation of IRIF, the cell focuses its attention on damage response and halts normal cell processes in order to appropriately respond to the damage and determine the fate of the cell. This response includes three main mechanisms: cell cycle checkpoints, DNA damage repair and cell death.

Cell cycle checkpoints

Cell cycle checkpoints are initiated following formation of IRIF and act to delay cells with detectable DNA damage from progressing into mitosis. In doing so, the cell is afforded more time to repair DNA damage and prevent development of mutations or other complications due to mis-repair in the cell's progeny. Four different cell cycle checkpoints exists, and the phase of cell cycle occupied during time of irradiation dictates which of these four is initiated.

Irradiation during G1 causes cells to undergo G1 arrest, which is the transient or permanent delay of progression from G1 to S [194]. Cells irradiated during S phase undergo a reversible delay in this phase through inhibition of any new DNA replication initiation signalling [195]. Cells in G2 during irradiation can undergo the G2-early checkpoint which rapidly blocks progression from G2 to mitosis, requiring doses as low as 0.5 Gy to be activated [196]. This checkpoint leads to a rapid decrease in the number of cells in mitosis following irradiation [197]. The G2 late checkpoint is characterized by a long, dose-dependent G2 delay [197] and becomes activated in cells that are irradiated in G1 or S but still made it to G2 with DNA damage. This checkpoint is often initiated several hours after irradiation, leading to an accumulation of cells in G2 [197].

DNA repair

DNA damage is repaired within several hours (up to 6 hours) of radiation exposure [190] through homologous resection (HR) or non-homologous end joining (NHEJ) for DSBs. In the case of SSBs base damage repair can also occur, in addition to HR and NHEJ. Details on these repair processes can be found elsewhere [190].

Cell death

Irradiated cells may undergo interphase or post-mitotic cell death in an attempt to avoid dangerous mutations rather than attempting damage repair. Interphase death takes place within a few hours of irradiation [198], while post-mitotic death can occur after a cell attempts DNA repair [199] and pass through the cell cycle several times [200]. Since cell death can occur early, or several divisions post irradiation, defining a

dead cell is challenging. Traditionally cell death is described as the loss of clonogenic capabilities of a cell. Cell death can be accomplished through a variety of mechanisms including: apoptosis, autophagy, necrosis, senescence and mitotic catastrophe.

Interphase or post-mitotic death can be accomplished through apoptosis, a programmed cell death, often referred to as type I cell death. Apoptosis can be initiated if enough IRIFs are present in a single cell, causing the amount of apoptosis-promoting proteins to initiate cell death before other effector pathways can be activated (e.g. for repair). Type II cell death typically refers to autophagy, which is also commonly initiated in response to radiation induced damage. Further, cell death can occur through necrosis which is typically initiated by changes in the cell environment. Cells may enter senescence, retaining some metabolic function but entering a state of cell cycle arrest [201]. Finally a cell entering mitosis with DNA aberrations can trigger initiation of a cell death pathway, this process being referred to as mitotic catastrophe.

2.2.3 Factors associated with radiation response

Several characteristics at the cellular and tumour level dictate tissue response to radiation. These include cell cycle and tumour microenvironment, including hypoxia. Importantly, irradiation also influences the post-irradiation kinetics of the tumour. These factors include reoxygenation, changes to tumour metabolism and cell cycle synchronization and can hold significant importance for post-irradiation evaluation of the tumour.

Cell cycle and synchronization

Cellular radiation sensitivity is dependent on the phase of cell cycle occupied during irradiation. Experiments have found that cells with a short G1 phase are most sensitive to radiation in mitosis and G1 with sensitivity decreasing in G2 and is lowest in S phase. Cells with a long G1 phase were found to be most sensitive during the end of G1, late G2 and mitosis and less sensitive in early G1 and S [202]. Following irradiation, cells are more likely to be in the more radioresistant S phase suggesting a degree of cell cycle synchronization as a result of radiation exposure.

Microenvironment

The tumour microenvironment is characterized by heterogeneous distributions of oxygen and metabolism, which plays a key role in the sensitivity of the tissue to radiation. In particular, the presence of O_2 in a cell increases sensitivity to radiation, decreasing the dose necessary to obtain the same level of cell kill [203]. Direct DNA damage creates free radicals on the DNA ($\dot{\mathrm{R}}$) which readily reacts in the presence of oxygen (O_2)

$$\dot{\mathrm{R}} + \mathrm{O}_2 \rightarrow \mathrm{R}\dot{\mathrm{O}}_2 \rightarrow \mathrm{ROOH} \ .$$

This leads to stabilization of the DNA radical by oxygen fixation, and is subsequently recognized as DNA damage by the DDR. However, under anoxic conditions it is more likely that the DNA radical will recombine with H^+ returning it back to its original state [204]. Ultimately, the presence of oxygen increases the likelihood of DNA damage, increasing intrinsic radiation sensitivity. Therefore tumours that are inherently more hypoxic are also found to be more radioresistant [205].

Reoxygenation

Following irradiation, the majority of radiosensitive aerobic cells in a tumour will be killed [204] and the surviving cells will predominantly be hypoxic. Therefore immediately after irradiation the hypoxic fraction of the tumour will be nearly 100%, but within minutes recirculation through temporarily closed vessels can lead to reoxygenation of the once hypoxic tumours that remained following irradiation. Within minutes or hours, reduced nutrient uptake from radiation damaged cells and ischaemic cell death further promote reoxygenation. Within days, mitotic death of irradiated cells leads to tumour shrinkage and improved blood distribution supporting reoxygenation [204]. The rate of reoxygenation has been found to vary among tumours from hours to several days [204].

2.3 Summary

In this chapter the fundamental cell biology associated with tumours and their radiation response are addressed together with mechanisms of radiation induced damage and its biological effect in tumours. Tumours are complex cell systems where common processes like metabolic activity and cell cycle drive biomolecular content within the tumour. Further, radiation exposure can lead to activation of a myriad of signalling pathways that ultimately decide the fate of cells within this population; either leading to cell death or survival and repair. The many biomolecular changes that result from radiation exposure have the potential to be monitored using Raman spectroscopy. In the next chapter, a discussion on Raman spectroscopy with specific focus on applications to biological samples will be presented.

Chapter 3

Raman Spectroscopy: Theory, Instrumentation and Data Processing

Raman spectroscopy exploits photon scattering interactions between molecules and highly focused laser light to probe the underlying molecular composition of a sample. The phenomenon of RS was first observed experimentally by Raman and Krishnan in 1928 [206] and has since contributed to applications in biology, materials science, medicine, inorganic and organic chemistry. This chapter presents fundamental concepts in RS with particular emphasis on applications to biological systems. In section 3.1 an overview of the theoretical basis of RS will be presented. Section 3.2 will discuss instrumentation considerations for a Raman experiment while section 3.3 will address data handling procedures to facilitate analysis of Raman spectral data sets. Finally, section 3.4 will discuss special experimental considerations for carrying out Raman studies of biological systems.

3.1 The physics of Raman spectroscopy

Raman scattering arises when a photon of light is inelastically scattered, inducing transitions to a vibrationally excited normal mode in a molecule. Alternatively, a photon could undergo Rayleigh scattering resulting in no net frequency shift in the

scattered photon. Rayleigh scattering does not lead to any valuable information about the interacting medium, however Raman scattering has the potential to inform about the molecular bonds present in the sample.

Inelastic Raman scattering can exist as either Stokes or anti-Stokes scattering. Stokes Raman scattering originates from photon interactions with a molecule found in its ground vibrational energy state (Φ_0) as shown in Figure 3.1. A photon with frequency ν_0 interacts with this molecule by distorting its electron cloud, causing it to enter a short-lived virtual state. The molecule then returns to an excited vibrational state (Φ_k), and concurrently re-radiates the photon with a lower frequency compared to the incident photon.

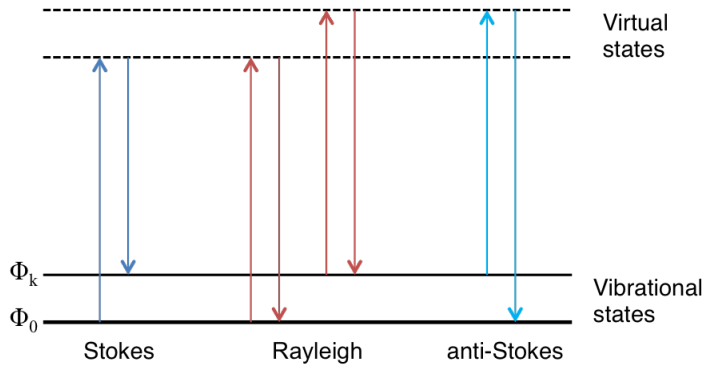


Figure 3.1: Scattering interactions involving visible light. Energy level transitions between a molecule's ground (Φ_0) and excited vibrational energy state (Φ_k) including Rayleigh (red), Stokes Raman (dark blue) and anti-Stokes Raman (light blue) scattering.

Anti-Stokes Raman scattering originates from photon interactions with a molecule originally in an excited vibrational energy state (Φ_k) as shown in Figure 3.1. The photon interacts by distorting the molecule's electron cloud, causing it to enter a virtual state. Subsequently relaxation of the molecule back to the ground vibrational energy (Φ_0) occurs. The scattered photon emitted through this relaxation has gained energy and therefore is shifted to a higher frequency.

3.1.1 Classical description of light scattering

A non-polarized classical electromagnetic field (**E**) with amplitude E_0 and frequency ν_0, which evolves in time (t) according to

$$\mathbf{E} = \mathrm{E}_0 \cos(2\pi\nu_0 t). \tag{3.1}$$

Consider a molecule (approximated as a polarizable electron cloud), in proximity to the electric field. Under these conditions, the electromagnetic field will induce a distortion in the electron cloud by displacing charges and creating a dipole moment **M**. This dipole moment is dependent on the polarizability of the molecule, α, according to

$$\mathbf{M} = \alpha\mathbf{E}. \tag{3.2}$$

Atomic nuclei in the molecule vibrate at specific frequencies characterized by the bond strength between two atoms. This vibration is referred to as a normal mode (Q). The k^{th} normal mode vibrates at a characteristic frequency (ν_k) with amplitude (Q_k^0), evolving in time according to

$$Q_{\mathrm{k}} = Q_{\mathrm{k}}^0 \cos(2\pi\nu_{\mathrm{k}} t). \tag{3.3}$$

Raman scattering results from the interaction between the polarizability and a normal mode of the molecule. Expanding the polarizability in terms of the k^{th} normal mode gives

$$\alpha \approx \alpha_0 + (\frac{\delta\alpha}{\delta Q_{\mathrm{k}}})Q_{\mathrm{k}} + ... \tag{3.4}$$

where $\frac{\delta\alpha}{\delta Q_{\mathrm{k}}}$ is the rate of change of the polarizability with respect to the k^{th} normal mode about the equilibrium position, and α_0 is the polarizability of the molecule at its equilibrium position. Substituting equations 3.3 and 3.4 (neglecting 2^{nd} order terms and higher) into 3.2 gives

$$\begin{aligned}\mathbf{M} &= \alpha_0 \mathrm{E}_0 \cos(2\pi\nu_0 t) + \frac{\delta\alpha}{\delta Q_\mathrm{k}} Q_\mathrm{k} \mathrm{E}_0 \cos(2\pi\nu_0 t) \\ &= \alpha_0 \mathrm{E}_0 \cos(2\pi\nu_0 t) + \frac{\delta\alpha}{\delta Q_\mathrm{k}} Q_\mathrm{k}^0 \cos(2\pi\nu_\mathrm{k} t) \mathrm{E}_0 \cos(2\pi\nu_0 t) \\ &= \alpha_0 \mathrm{E}_0 \cos(2\pi\nu_0 t) + \mathrm{E}_0 \frac{\delta\alpha}{\delta Q_\mathrm{k}} Q_\mathrm{k}^0 [\cos(2\pi(\nu_0 + \nu_\mathrm{k})t) + \cos(2\pi(\nu_0 - \nu_\mathrm{k})t)]. \end{aligned} \quad (3.5)$$

Equation 3.5 describes the dipole moment ($\mathbf{M}$) resulting from the interaction of the electron cloud of a molecule with an incident electric field ($\mathbf{E}$). The dipole moment is made up of two separate terms, first the Rayleigh light scattering term for which the frequency of the incident electromagnetic field is unshifted. Second, the Raman scattering term in which the incident electromagnetic field oscillates at a frequency shifted according to the vibrational frequency of the involved normal mode; $\nu_0 \pm \nu_k$. One in 10^6 to 10^8 scattered photons undergo Raman scattering, therefore Rayleigh scattering is the dominant interacting mechanism [207].

The Raman scattering term in equation 3.5 is made up of a portion corresponding to anti-Stokes scattering ($\nu_0+\nu_k$) as well as Stokes scattering ($\nu_0-\nu_k$). The proportion of Stokes vs. anti-Stokes scattering is dependent on the number of molecules in excited vibrational states during the interaction. This is dictated by Boltzmann statistics and is proportional to temperature. At room temperature, the fraction of molecules in excited vibrational states is low, therefore this work is focused exclusively on Stokes Raman scattering.

3.1.2 Raman peak intensity

The intensity of Raman peaks arising from Raman active vibrational modes is informative for determining which peaks are expected to be present in a spectrum. Typically a quantum mechanical approach to light scattering theory is used to describe peak intensity, and is described in detail elsewhere [208, 209]. Briefly, the intensity of a Raman scattering event between a ground vibrational state (Φ_0) and the k^{th} vibrational state (Φ_k), both in an electronic ground state but passing through an intermediate vibrational state in an excited electronic state (Φ_I) can be described as

$$I = \frac{\pi^2}{c\varepsilon_0^2}(\nu_0 \pm \nu_{0k})^4 \mathrm{E}_0^2 \sum_{\rho\sigma} |[\alpha_{\rho\sigma}]_{0k}|^2. \tag{3.6}$$

Where c is the speed of light, ε_0 is the permittivity of free space, ν_0 and ν_{0k} are the frequencies of the incident radiation and Raman transition between the ground and k^{th} vibrational states and E_0^2 is the intensity of the incident radiation. $|[\alpha_{\rho\sigma}]_{0k}|^2$ is the $\rho\sigma^{\mathrm{th}}$ element of the transition polarizability tensor which is defined by the Kramer Heisenberg Dirac (KHD) expression [207].

In terms of Raman peak intensity, equation 3.6 shows a dependence on molecular polarizability, which is a sample dependent parameter. However, equation 3.6 also indicates that the Raman peak intensity is dependent on incident photon frequency and intensity, both parameters that can be selected through considerations for experimental design as discussed in detail in section 3.4.

3.1.3 Selection rules for Raman activity

The primary selection rule governing Raman activity is found in the Raman scattering term of equation 3.5, which is prefixed by $\frac{\delta\alpha}{\delta Q_{\mathrm{k}}}$. The Raman scattering term is non-zero only if there is a change in the polarizability of the molecule during a vibration [210]. Interactions of an electromagnetic field with the electron cloud of a molecule produces a dipole moment that can be described in three dimensions according to

$$\begin{bmatrix} M_x \\ M_y \\ M_z \end{bmatrix} = \begin{bmatrix} \alpha_{x,x} & \alpha_{x,y} & \alpha_{x,z} \\ \alpha_{y,x} & \alpha_{y,y} & \alpha_{y,z} \\ \alpha_{z,x} & \alpha z, y & \alpha_{z,z} \end{bmatrix} \begin{bmatrix} E_x \\ E_y \\ E_z \end{bmatrix} \tag{3.7}$$

where α is the polarizability tensor of the molecule and a larger value of α means greater polarizability. Therefore, if one of the elements of the polarizability tensor changes during a vibration, it is said to be a Raman active vibrational mode.

Molecular structure and atomic content are the key factors that dictate the number of vibrational modes available to a molecule. The total number of vibrational degrees of freedom (D) in a molecule containing η atoms is found by subtracting the possible

translational and rotational degrees of freedom from the total possible degrees of freedom (3η). For a linear molecule the number of vibrational degrees of freedom is

$$D_l = 3\eta - 5, \tag{3.8}$$

and for a non-linear molecule

$$D_{nl} = 3\eta - 6. \tag{3.9}$$

Of the available vibrational modes, only those causing a change in the polarizability of the molecule are Raman active. In the case of complex molecules (more than 3 atoms), Raman activity can be described elegantly using group theory, as detailed elsewhere [210].

Further selection rules can be described through solutions to the KHD expression, of which elements are present in the last term of the Raman peak intensity equation (equation 3.6). A detailed discussion of the KHD expression can be found in the literature [207]. Briefly, the KHD expression is represented as

$$[\alpha_{\rho\sigma}]_{0k} = \frac{1}{h}\sum_I \left(\frac{\langle \Psi_k | \mu_\rho | \Psi_I \rangle \langle \Psi_I | \mu_\sigma | \Psi_0 \rangle}{\nu_{0I} - \nu_0 - i\Gamma_I} + \frac{\langle \Psi_I | \mu_\rho | \Psi_0 \rangle \langle \Psi_k | \mu_\sigma | \Psi_I \rangle}{\nu_{Ik} + \nu_0 - i\Gamma_I} \right). \tag{3.10}$$

Where ρ and σ are the incident and scattered polarization directions, h is Plank's constant, and the polarizability element is found by summing over all vibronic states of the molecule. Ψ_0, Ψ_k and Ψ_I are the total wavefunctions for the ground (0), k$^{\text{th}}$ excited state (k) and intermediate (I) state, operated on by the electronic transition moment μ associated with the transition from the ground to excited electronic state. $i\Gamma_I$ is the oscillation damping factor which relates to the lifetime of the excited state and affects the width of the Raman lines [207]. The size of $i\Gamma_I$ is small compared to that of the laser or transition frequencies, however it is a vital component to ensure that the polarizability does not become infinite if the laser and transition frequency are the same.

The numerator of the first term in equation 3.10 describes the mixing of the ground

and excited states (right hand term) then the excited and final states (left-hand term). The second term in equation 3.10 mixes the excited state with the final state (right-hand term) and then ground state with the excited state (left-hand term) and accounts for the fact that the entire scattering process need not start in the ground state. The second term in equation 3.10 has a denominator for which the laser and transition frequencies are added together and is therefore less important (and is often neglected [207]) in describing the polarization compared to the first term, in which the laser and transition frequencies are subtracted.

Solving the KHD expression gives two selection rules for Raman activity. First, solutions to the KHD expression yield a series of integrals which are non-zero only if there is a single quantum of energy difference between the initial and final vibrational states (e.g. $\Phi_k - \Phi_0 = \pm 1$), forming a selection rule for Raman activity.

Next, the solution integrals to the KHD equation have operators of ungerade (odd parity) nature such that multiplication of these operators give a gerade (even parity) result. Since the solution of the KHD expression is of even parity, only symmetric vibrations (which result in a change in polarizability) are allowed for Raman activity, forming another selection rule.

3.1.4 Raman shift

The energy associated with a detected Raman scattered photon is conventionally reported using units of wavenumbers (cm^{-1}). The Raman shift for a photon with incident frequency ν_0, wavenumber $\bar{\nu_0}$ and wavelength λ_0 and scattered frequency ν, wavenumber $\bar{\nu}$ and wavelength λ is

$$\Delta\bar{\nu} = \frac{1}{\lambda_0} - \frac{1}{\lambda} = \frac{\nu_0}{c} - \frac{\nu}{c} = \bar{\nu_0} - \bar{\nu}. \tag{3.11}$$

3.2 Instrumentation considerations for Raman spectroscopy

The Raman microscope is made up of several components that together allow for high spatial resolution molecular probing of a sample. An excitation laser, sample holder, microscope, spectrometer and detector work together and provide a wide range of instrumentation customization to optimize the device for a specific application. This section discusses the key components necessary for a Raman system and its operation, with particular emphasis on spectroscopic studies of biological samples.

3.2.1 Raman microscopy

Raman microscopes are a variation of a traditional Raman spectrometer, comprised of a microscope coupled to a spectroscopic system. A schematic of a Raman microscope is shown in Figure 3.2. The excitation laser is coupled to a microscope which acts as the sample holder and precisely focuses the laser onto the sample using a motorized stage. Excitation light passes through the microscope objective, is focused to a small section of the sample and interacts at that region. The microscope objective also collects the Raman scattered light which is then passed through a series of filters and on to the spectrometer and detector, producing the Raman spectrum.

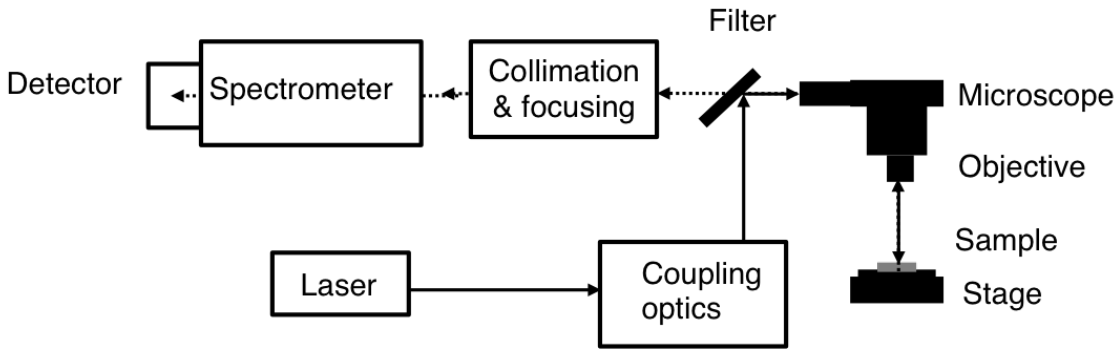


Figure 3.2: Schematic of a Raman microscope. Monochromatic light from a laser (solid line) is passed through coupling optics and into a microscope where it is focused on the sample. Raman scattered light (dashed line) is collected by the objective, filtered, collimated and passed on to the spectrometer and detector to produce Raman spectra.

Raman microscopy offers excellent spatial control of the excitation laser, facilitating single-cell studies and highly controlled probing of tissue sections. The advantage of using Raman microscopy to study biological systems is clear, however optimal operation of this system is dependent on some important technical considerations.

Microscope coupling and beam expansion

The excitation laser has a pre-defined beam size which must be expanded in order to fill the back aperture of the microscope objective. This allows the full power of the laser to be used efficiently and is achieved by focusing the laser through a pinhole and expanding the beam diameter, using lenses, to match the size of the objective's back aperture.

Microscope objective

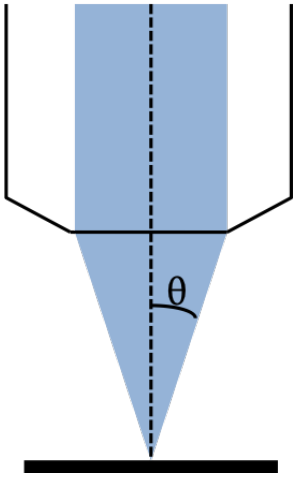


Figure 3.3: Microscope objective with definition of θ. The angle of θ is defined as the angle subtended by one half of the area of the light cone entering a microscope objective. Definition of numerical aperture is dependent on the angle θ. The dotted line illustrates the orientation of the principal optical axis.

Selection of the microscope objective is an important factor in the quality of spectra obtained from the system. Objective components must be of high optical quality in order to avoid disruptive fluorescence background in the Raman spectra. Furthermore, the numerical aperture (NA) will determine several key features that affect spectral quality. Numerical aperture is defined as

$$\mathrm{NA} = \mathrm{n} \sin \theta, \tag{3.12}$$

where n is the refractive index in the medium and θ is one half of the objective angular aperture which is defined as the maximum area of the light cone captured by the objective, as shown in Figure 3.3. The collection efficiency of the objective as well as image brightness is influenced by NA and is important because it determines the signal strength of the collected spectrum. The laser spot size at the sample is proportional to the square of the objective NA and inversely proportional to the square of its lateral magnification. In the plane perpendicular to direction of light propagation the minimum detectable resolution (r) of the objective is dependent on the NA [211]

$$r = \frac{\lambda}{2\mathrm{NA}}. \tag{3.13}$$

Along the principal optical axis, the size of the laser spot is described by the depth of field (DOF) [212], which is also dependent on the NA,

$$DOF = \frac{\lambda \mathrm{n}}{\mathrm{NA}^2}. \tag{3.14}$$

Therefore, considering two objectives with the same magnification, one with a higher NA will have improved light collecting ability and smaller collecting volume. The trade-off to this is that a smaller collection volume means there is less of the sample being probed, further reducing the already weak Raman signal. Therefore, the laser spot size is an important consideration for biological spectra where cellular or sub-cellular resolution may be desired but high spectral quality is needed.

Collection orientation

A 180° collection orientation is preferred in Raman microscopy because it can allow for high NA objectives to be brought close to the sample. This enables the precise focusing of the laser spot onto a small portion of the sample, and facilitates incorporating Raman systems with microfluidic designs.

Rayleigh and Raman scattered light are collected through the microscope objective. A filter set is used to remove the Rayleigh scatter and the Raman scattered light is subsequently focused and passed through a confocal aperture as shown in Figure 3.4. The confocal aperture leads to improved spatial resolution by removing strongly diverging light that originates from scattering events outside the sample volume being probed. Light emerging from the confocal aperture is then passed on to the spectrometer.

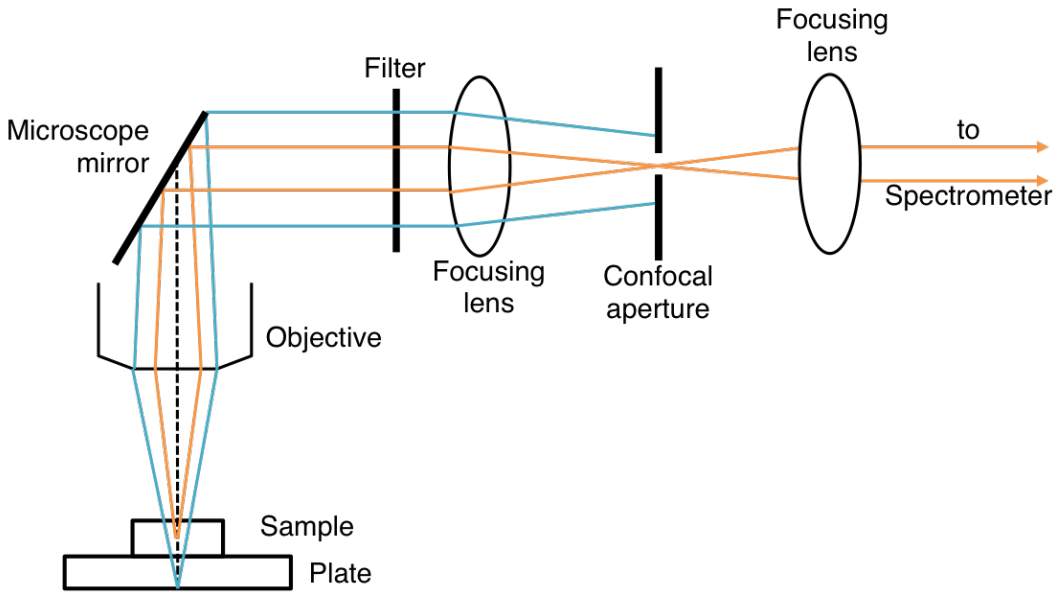


Figure 3.4: Filtering and collimation in the Raman microscope. Raman scattered light originating in the region of interest (orange) and outside the region of interest (blue) is collected by the microscope objective. This light is filtered and focused on a confocal aperture which eliminates light from outside the region of interest. Light is then then passed on to the spectrometer.

3.2.2 Spectroscopic principles in Raman microscopy

When Raman scattered light enters the spectrometer, the various wavelengths of light scattered off the sample are spatially separated before moving on to the detector. Common spectrometer systems are either Fourier transform (FT) or dispersive spectrometer systems [207]. Dispersive spectrometers are typically used with visible laser excitation wavelengths, and a common form is the single grating Czerny-Turner dispersive spectrometer. As shown in Figure 3.5, light incident on the entrance slit

of the spectrometer is passed through a diffraction grating where light of a specific wavelength emerges from the diffraction grating at a unique angle, according to

$$\sin\alpha + \sin\beta = k\mathrm{d}\lambda. \tag{3.15}$$

Where α and β are the angle of incidence and angle of diffraction of light with wavelength λ, k is the diffraction order and d is the density of slits in the diffraction grating. The spatially separated light is then reflected off a plane mirror and focused at the focal plane of the spectrometer. The spatial distribution for the light emerging from the spectrometer is dependent on the linear dispersion of the diffraction grating [213], commonly expressed in units of $\frac{\mathrm{nm}}{\mathrm{mm}}$ and defined as

$$\frac{d\lambda}{dx} = \frac{\cos\beta}{k\mathrm{d}L_B}, \tag{3.16}$$

where x is the unit interval and L_B is the effective exit focal length. Linear dispersion is associated with spectral resolution of the system where higher linear dispersion means the system can better resolve fine spectral detail. The spatial distribution of the light becomes very important as it is passed on to the detector.

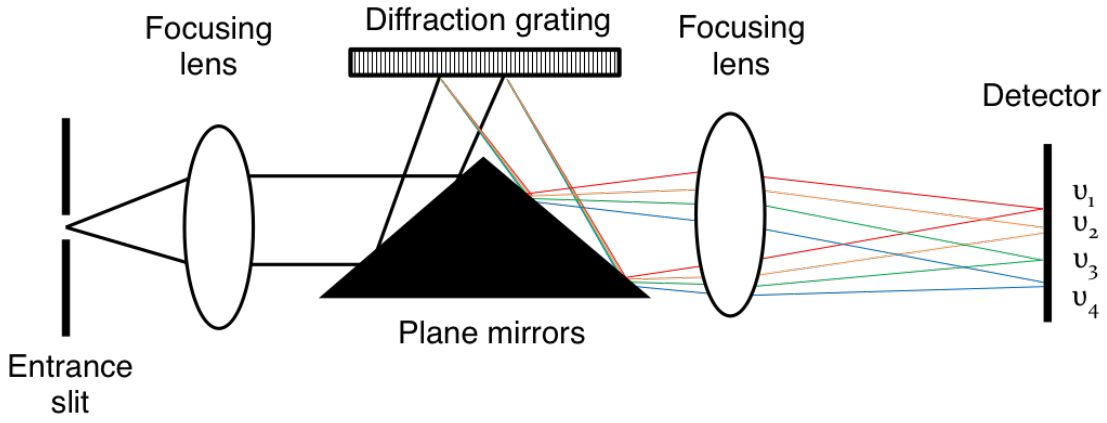


Figure 3.5: Light dispersion in a single grating spectrometer. Polychromatic Raman scattered light (ν_z) enters the entrance slit of a spectrometer and is passed through a diffraction grating. Light emerges from the diffraction grating at an angle unique to the wavelength and each wavelength reaches the detector at a discrete position.

3.2.3 Detecting and displaying Raman spectra

A charge coupled device (CCD) is commonly used for detecting Raman scattered light [210]. The CCD is placed at the focal plane of the spectrometer and since the various Raman shifts have been spatially dispersed, each wavelength falls at a unique position on the detector. A CCD is comprised of a two dimensional array of photosensitive diode detector elements, as shown in Figure 3.6, made of a silicon-metal-oxide semiconductor material [214]. An element ranges in size from 6-30 μm along each pixel dimension and is held at a positive charge. Photons incident on the photosensitive detector elements release electrons from the material, resulting in an accumulation of charge proportional to the photon intensity incident on the element and the length of time an element is exposed. Following CCD exposure, the charges collected on each element are read out sequentially down the columns of the array. The charge collected at the end of each column is then read out along the dispersion axis, converted into a voltage, amplified and converted into a digital signal. The read out signal at each column is proportional to the binned charge collected (and hence number of photons exposed) at each column position in the detector.

3.3 Spectral analysis

RS studies on biological systems commonly yield large data sets where multiple processes (e.g. metabolic, cell cycle, radiation response) occur simultaneously. Such systems benefit from sophisticated data analysis techniques like deconvolution,principal component analysis (PCA), hierarchical cluster analysis (HCA), linear discriminate analysis (LDA) and other multivariate analysis techniques in which correlations and trends in the data set can be isolated. This dissertation focuses on results derived from Raman data sets using PCA, and the theoretical basis is presented here. Specific details for applications in this dissertation are addressed in chapter 4, section 4.3.3.

PCA is valuable for analyzing data sets where the relationships between the variables are not easily visualized. The observations in a dataset undergo an orthogonal linear transformation of the data set to a new basis in which the dataset is described by linearly uncorrelated variables. The principal components make up this new basis, with the first principal component (PC) comprising the largest variance in the data

set, and subsequently lower variance contributes with higher order PCs. There is a requirement of orthogonality amongst all of the PCs in the basis set, leading to orthogonal groupings of observations that are organized based on how much variability they account for in the data set.

A rigorous description of PCA can be found in the literature [215], however key concepts in the theoretical basis of PCA will be discussed. First, consider an $n \times p$ matrix ($\mathbf{X}$) containing the observations ($x_{i,j}$) with n samples ($i = 1, ..., n$) and p measurements ($j = 1, ..., p$). The empirical mean of $\mathbf{X}$, is a row vector ($\bar{\mathbf{x}}$) and is defined as the mean of all measurements in the j^{th} column over all n samples

$$\bar{x}_j = \frac{\sum_{i=1}^{n} x_{i,j}}{n}. \tag{3.17}$$

The centred data set ($\tilde{\mathbf{X}}$) is found by subtracting the mean of each measurement ($\bar{x}_j$) from $\mathbf{X}$ [215]

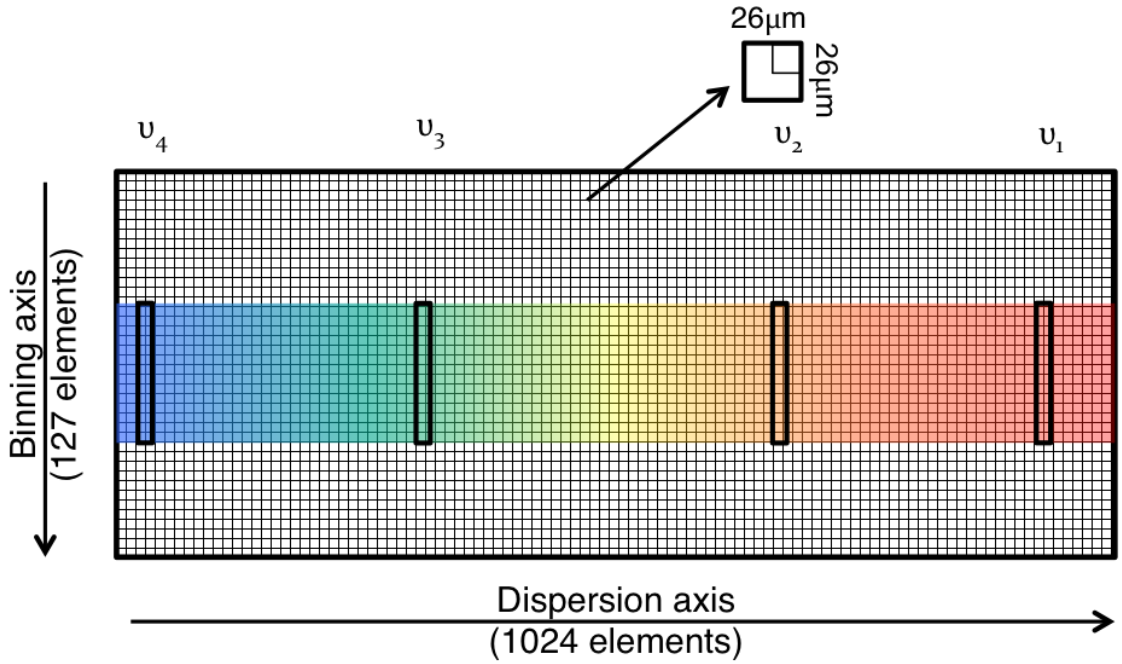


Figure 3.6: Light dispersion and the CCD detector. Light of varying wavelengths (ν_z) is spatially separated by the spectrometer and focused at the detector. Each wavelength lands at a unique position on the CCD and registers to a unique column of detector elements. Incident photon intensities are binned along the binning axis and read out along the dispersion axis.

$$\tilde{x}_{i,j} = x_{i,j} - \bar{x}_j. \tag{3.18}$$

The sample covariance matrix ($\mathbf{C}$) of $\tilde{\mathbf{X}}$ is then determined according to [1]

$$\mathbf{C} = \frac{\tilde{\mathbf{X}}^\dagger \tilde{\mathbf{X}}}{n-1}. \tag{3.19}$$

The following equation must be solved such that $\mathbf{C}$ is diagonalized

$$\mathbf{A}^\dagger \mathbf{C} \mathbf{A} = \mathbf{\Lambda}, \tag{3.20}$$

Where matrix $\mathbf{A}$ is the orthogonal matrix containing the eigenvectors of $\mathbf{C}$, each with length p. $\mathbf{\Lambda}$ is the diagonal matrix containing the eigenvalues (λ) of $\mathbf{C}$. The set of eigenvectors described in $\mathbf{A}$ forms a complete orthogonal basis set [215] of $\tilde{\mathbf{X}}$ and it follows that

$$\alpha_l^\dagger \alpha_m = \delta_{lm}. \tag{3.21}$$

Where $l, m = 1, ..., p$.

The k^{th} eigenvector of $\mathbf{C}$, corresponds to the k^{th} column of $\mathbf{A}$, α_k, and is the k^{th} principal component. The PCs described in $\mathbf{A}$ each correspond to a specific eigenvalue of $\mathbf{C}$. The eigenvalues in $\mathbf{\Lambda}$ correspond to the variance of a specific PC

$$\lambda_k = \text{variance}(\tilde{\mathbf{X}}\alpha_k). \tag{3.22}$$

By definition, all PCs are orthogonal to one another and each PC describes the relationships between a specific set of measurements. The first ($k = 1$) PC is selected to account for the largest portion of the total variance of $\tilde{\mathbf{X}}$. Similarly, the second PC contributes the second largest variance and the k^{th} PC has the k^{th} highest variance.

[1] A general formalism for PCA is presented in this section, with the dagger operation representing the complex conjugate transpose. However in the work of this dissertation all data sets are made up of real numbers and this just becomes the transpose.

Since the variance is larger in the first few PCs, they will contain information which represents the variability in the data set more than the later PCs which typically resemble noise. Therefore, PCA can be used to essentially reduce the size of a data set.

It is important to note that a single PC will contain both positive (counts > 0) and negative features (counts < 0). The selection of positive and negative is arbitrary, and the features can be reflected about zero without affecting the results. However, it is essential that the positive and negative features remain complimentary to one another, in order to maintain orthogonality of the basis set.

The PC score of the k^{th} PC, can be found for all ($\tilde{\mathbf{x}}_i$) samples in $\tilde{\mathbf{X}}$ (n samples total) using

$$z_{i,k} = \tilde{\mathbf{x}}_i \alpha_k, \tag{3.23}$$

where $i = 1...n$.

The degree of expression of a PC for a given sample is quantified using PC scores. Therefore, a single sample ($\mathbf{x}_i$) in the full data set ($\mathbf{X}$) can be reconstructed using the PC scores as weightings for the PCs,

$$\mathbf{x_i} = \bar{\mathbf{x}} + z_{i,1}\mathrm{PC}_1 + z_{i,2}\mathrm{PC}_2 + z_{i,3}\mathrm{PC}_3 + ...z_{i,n-1}\mathrm{PC}_{n-1}. \tag{3.24}$$

The PC score of a sample quantifies the extent to which that PC is represented in a given sample. Negative PC scores correspond to a greater expression of the negative features relative to positive features of the PC, and positive PC scores correspond to a greater expression of positive features relative to negative features. Using PC scores, trends between samples can be identified.

3.4 Considerations for Raman spectroscopy in biological applications

Raman spectroscopic applications to living biological systems require particular considerations for key experimental parameters including spectral range, laser wavelength and power, sample handling and spatial resolution. General experimental considerations are addressed here.

Spectral range

Biomolecules common in cells and tissue have Raman bands located in two key spectral ranges. Raman active normal modes attributed to protein, nucleic acid, lipid and carbohydrates have Raman shifts between 450-1800 cm^{-1}. Lipid and proteins also have Raman shifts from 2400-3600 cm^{-1}. Therefore, the work presented in this dissertation involves spectra collected in the 450-1800 cm^{-1} range. Since all four classes of biomolecules found in cells have Raman peaks in this range it is an ideal spectral window to analyze.

Laser wavelength and power

Raman studies on biological samples require careful consideration of laser wavelength, power and exposure time. All of these factors have an effect on tissue viability and biochemical integrity as well as Raman peak intensity and spectral quality (in terms of biological fluorescence).

Maintaining phenotypic integrity and viability in the biological sample during data acquisition is especially important when trying to assess damage induced from external stressors such as ionizing radiation. Laser wavelength, exposure time and power all contribute to the extent of photodamage. Longer wavelengths cause less photodamage in cells as demonstrated by Puppels et al. for laser powers from 0.5-20 mW at 457.9 nm, 488 nm, 514.5 nm, 632.8 nm and 660 nm [216]. Notingher et al. demonstrated that living human cells exposed to 785 nm light with 115 mW power for 40 minutes did not express noticeable changes to the Raman spectrum of the cells or affect cell viability [217]. Therefore the use of a higher laser wavelength (e.g. 785

nm) reduces photodamage and allows much higher laser powers and exposure times to be used.

Inherently low Raman scatter efficiency can be addressed by using a higher laser power and low wavelength of excitation (such as in the ultra violet range). However a trade-off between improved signal intensity and biological fluorescence exists. Biological fluorescence levels increase for low laser wavelengths [218], causing a disrupting background in the Raman spectrum. Fluorescence can be minimized by using lasers with wavelengths in the upper visible or near-infrared region ($\lambda \geq 600$ nm) [218, 219]. Reducing the incident laser power reduces biological fluorescence, however the Raman scattering intensity will also decrease. High powered lasers in the near-infrared region (e.g. 785 nm) significantly reduce biological fluorescence and operate in the spectral region for which CCD detectors have relatively high quantum efficiency [220], making the 785 nm laser a good compromise between biological fluorescence and improved Raman signal. Furthermore, since the 785 nm laser does not induce noticeable levels of photodamage in biological material for high laser powers and long exposure times (e.g. 115 mW, 40 minutes), Raman peak intensity can be improved by using a higher total integrated (over time) laser power exposure at this wavelength.

Sample holding environment

Appropriate selection of a substrate to plate the biological sample is important. Depending on the laser spot size, the plating substrate may be within the sampling volume of the laser. If this is the case, it could contribute background fluorescence and Raman peaks to the spectrum. Selection of a plating substrate which does not have Raman peaks in the spectral region of interest and has low background fluorescence is key. As long as the background fluorescence is minimal enough to allow good presentation of the Raman peaks in the biological sample and has a reproducible and consistent background, spectral processing techniques can be used to remove these effects [221]. A variety of substrate materials have been investigated for use in RS including sodium glass [219], quartz [219, 222], barium fluoride [223], magnesium fluoride [135] and calcium fluoride [218, 224]. However, fluoride-based materials ($X\text{-}F_2$) appear to work best for RS [218].

Spatial resolution

Tissue is comprised of a collection of cells, and a cell is on the order of tens of micrometers with the organelles within the cell ranging from 50 to 100 nm [150]. Therefore selection of the spatial and confocal resolution of the excitation laser is dependent on the application of interest. For tissue studies, laser spot sizes on the order of the size of a cell are sufficient. However, sub-cellular investigations would require laser spot sizes on the order of 1 μm^3 [95].

3.5 Summary

This chapter address the theoretical basis of RS and PCA, a common processing technique for large spectral datasets. Instrumentation considerations are also addressed with particular focus on applications to study biological materials. Raman spectroscopic considerations specific to the research presented in this dissertation are addressed in chapter 4.

Chapter 4

Materials & Methods

This chapter provides detailed explanations of the materials and experimental techniques consistently used throughout this dissertation. Details of techniques specific to experiments found only in a given chapter are presented in the methods section of that chapter. Section 4.1 presents the cell lines, culturing techniques and mouse model protocols. Section 4.2 describes the procedures for tumour irradiation using either a LINAC or small animal irradiation system. Methodology for Raman spectral mapping of tissue using a commercial Raman spectrometer, including instrumentation details and data processing techniques are discussed in section 4.3.

In total three separate mouse cohorts form the datasets for the work presented in this dissertation. Since there are slight variations in experimental protocol and instrumentation among these three cohorts, a naming convention has been assigned to each of the cohorts to allow easy identification and separation. Cohort A is a set of 12 mice implanted with H460 tumours. Cohort B is a set of 19 mice implanted with MDA-MB-231 tumours, and Cohort C is a set of 28 mice implanted with H460 tumours.

4.1 Murine tumour models

Human tumour xenografts were established in murine hosts to study radiation effects using RS. This tumour model provides an experimental environment which is similar

to human tumours including irregular vasculature, microenvironment heterogeneities and a host system to support the radiation response *in vivo*. First, a cell line is selected for the given experiment, cultured and batched up to produce a colony of sufficient size for tumour implantation. Mice are selected to host human-derived cell lines and therefore are immune-compromised. The cultured cells are implanted in mice and the cohort is monitored for tumour growth and health. Once tumours reach a predefined size the mice can progress on to radiation treatment and Raman studies.

4.1.1 Cell lines

The human-derived NSCLC cell line H460 and human-derived breast adenocarcinoma cell line MDA-MB-231 were selected for experiments. These cell lines were selected because they are human-derived diseases that have shown success for establishing tumours in mice. Further, these cell lines have proven to yield measurable and unique radiation response signatures using RS, *in vitro* [132]. Cell lines were purchased from American Type Culture Collection (ATCC) (Manassas, VA, USA), tested pathogen-free using Charles River Laboratories (Montreal, QC, Ca) and cultured according to standard sterile handling techniques for adherent cell lines. Cell culturing took place in a Biological Safety Level 2 (BSL2) lab at The Deeley Research Centre (DRC) located at BC Cancer Victoria. All cell handling took place in a laminar flow biological safety cabinet (BSC) to maintain sterility of the cell populations.

Stock cells were cryopreserved by suspending cells in fetal bovine serum (FBS) (Hyclone Labs Inc., Logan, UT, USA) supplemented with 10% dimethyl sulfoxide (DMSO) (Hyclone) by volume and frozen at a rate of 1 $\frac{^{\circ}\mathrm{C}}{\mathrm{min}}$ in a -80°C freezer. Once frozen, cells were transferred for long-term storage in a nitrogen vapour storage tank held at -182°C.

Cells were thawed by warming the cell pellet to 37°C and resuspending in appropriate medium. Roswell Park Memorial Institute (RPMI) medium was used for culturing in the case of H460 cells and Dulbecco's Modified Eagle's Medium (DMEM) media was used for the MDA-MB-231 cell line (both sourced from Hyclone), with contents as listed in Table 4.1. The sample was then centrifuged at 1500 rpm for 5 minutes at 4°C and supernatant was removed. The cells were resuspended in 1 mL of media and an aliquot of this suspension was plated in a T-75 culturing flask (75 cm^2 growth area,

polystyrene, vented cap, BD Falcon, Franklin Lakes, NJ, USA) containing 15 mL of media. A hemacytometer was used to determine the cell density and appropriate aliquot size to plate 1×10^5 cells per flask. The flask was then placed in an incubator at 37°C with 5% CO_2.

Cell Line	**Media Characteristics**
H460	RPMI-1640 Medium + L-Glutamine + 25 mM HEPES + 10% FBS
MDA-MB-231	DMEM High Glucose Medium 4500 mg/L Glucose + 4.00 mM L-Glutamine + Sodium Pyruvate + 10% FBS

Table 4.1: Cell culturing media and its contents.

The cell population was split every three to four days, depending on the cell line. The rate of splitting is selected in order to keep the number of cells in a flask below $50 - 60\%$ confluency, promoting exponential growth and avoiding using up all of the nutrients in the media. Splitting was carried out by pouring off the old media and rinsing fixed cells with 9 mL of phosphate buffer saline (PBS) (1×, 0.00067 M PO_4, Hyclone) to remove excess media and debris. Enzymatic dissociation of cells was achieved using 3 mL of 0.25% Porcine Trypsin-EDTA (1×) (Hyclone) added to the flask and incubated at 37°C for 5 to 10 minutes. Once cells were detached from the flask surface, 9 mL of media was added and the suspension was centrifuged at 1500 rpm for 5 minutes at 4°C. The supernatant was poured off and cells were resuspended in 1 mL of media. A portion of this suspension was used to assess viability and cell density using a hemacytometer and 1×10^5 cells were plated into a new T-75 flask and then placed back into the incubator. Colonies were batched up to achieve a large enough population for tumour cell implantation within 3-4 passages from thawing.

4.1.2 Tumour xenografts

Animal procedures were approved by the University of Victoria Animal Care Committee (Victoria, BC, Ca) and performed in accordance with the guidelines set forth by the Canadian Council on Animal Care.

Mice were obtained from British Columbia Cancer Research Centre (BCCRC) Animal Resource Centre (Vancouver, BC, Ca). 4-6 week old NOD.CB17-Prkdc^{scid}/J female mice were housed in HEPA filter microisolator cages within a bioexclusion containment room. Upon delivery, mice remained in isolation and were allowed to acclimatize for 1 week prior to study initiation. Animals were allowed access to food and water *ad libitum* and all animal handling took place in a BSC.

Mice were approximately 8 weeks of age upon tumour cell implantation. Isoflurane inhalation at 3% in oxygen using a precision vapourizer was used to anesthetize the animals and the right flank of the mouse was shaved. Tumour cells were injected subcutaneously at a concentration of 5×10^6 cells in 0.1 ml PBS. Following cell implantation, mice returned to their cages and tumour growth (area) was monitored three times a week using digital calipers. Animals were only included in the study if tumour area was greater than 80 mm^2 or less than 130 mm^2. In the case of H460 tumours, it took approximately 4 weeks to reach the predetermined size criteria whereas MDA-MB-231 tumours required 9 weeks. Tumours typically reached the inclusion size range within a span of 10 days of each other.

4.2 Tumour irradiations and harvesting

Animals were randomized into treatment groups once their tumour size reached the predetermined end point, and investigators were blinded to radiation dose received by a given mouse during radiotherapy treatment. All treatments were delivered within 10 days of each other. Due to changes in the infrastructure at our institution, two different irradiation methods were used throughout the work presented in this dissertation. Irradiations were carried out using a LINAC for Cohort A, but a small animal radiation research platform (SARRP) was used for Cohort B and C. Both methods will be described here. A control experiment between LINAC and SARRP based irradiations was carried out using H460 tumours harvested at 3 days post irradiation. Raman spectral signatures were found to be repeatable between tumours in Cohort A and Cohort C, suggesting changing the irradiation process does not affect experimental outcomes.

4.2.1 LINAC based irradiations

Tumour irradiations for Cohort A were carried out using a commercial LINAC system. Mice were housed at The University of Victoria Animal Care Unit and irradiated at BC Cancer Victoria. Since transportation was required and the animals were not isolated in a sterile environment during treatment, a broad spectrum antibiotic (Enrofloxacin) was added to the drinking water 10 days prior to treatment. Mice remained on this prophylactic treatment until the end of the study. A single intraperitoneal (IP) injection of Ketamine/Dexdomitor dosed at 50 $\frac{\text{mg}}{\text{kg}}$ Ketamine and 0.5 $\frac{\text{mg}}{\text{kg}}$ Dexdomitor was used to anesthetize the mice for treatment. Individual mice were placed into a custom designed restraint chamber made from acrylic, and a 10 mm non-toxic removable dental wax bolus was placed over the tumour. The On-Board Imager (OBI) feature of the Varian Truebeam STx LINAC (Varian Medical Systems Inc., Palo Alto, CA, USA) was used to align the posterior base of the tumour to isocentre. A treatment plan using parallel-opposed beam geometry was developed for tumour diameters of 10-15 mm using Eclipse treatment planning software (version 11, Varian Medical Systems Inc.) and was used for all treatment deliveries. Irradiations took place using a 6 MV photon beam with a dose rate of 6 $\frac{\text{Gy}}{\text{min}}$ at isocentre. Single dose fractions of either 0, 5 or 15 Gy were delivered depending on the treatment group assigned to the mouse. Following treatment, sedation reversal was achieved through an IP injection of $1\frac{\text{mg}}{\text{kg}}$ Atipamezole and recovery with thermal support.

4.2.2 SARRP based irradiations

Tumour irradiations for Cohort B and C were carried out on the SARRP (Gulmay Medical Inc., Suwanee, GA, USA). Mice remained isolated in a sterile environment throughout treatment and were not transported, therefore no broad spectrum antibiotics were given to the animals. Mice were first anesthetized using isoflurane inhalation (3% in oxygen) and placed on the treatment bed of the SARRP. Body temperature was maintained throughout treatment using a BioVet stand-alone heating unit (m2m Imaging, Cleveland, OH, USA). First, mice were imaged using a single CBCT scan at 60 kVp, 0.8 mA for 1 minute. A treatment plan was devised for the animal based on this image, using Muriplan treatment planning software (Gulmay Medical Inc.) and the tumour was automatically aligned with isocentre of the treat-

ment unit based on this plan. Two 220 kVp parallel-opposed beams collimated to 1×1 cm^2 were delivered to isocentre at a dose rate of 4 $\frac{\text{Gy}}{\text{min}}$ [225]. Depending on the treatment group assigned to the mouse, doses of 0, 5 or 15 Gy were delivered in single fractions. Following irradiation, mice were removed from isoflurane inhalation and allowed to recover in normal conditions with thermal support.

4.2.3 Tumour harvesting

For all cohorts, mice remained in microisolator cages and were allowed access to food and water *ad libitum* immediately following treatment until the time of tumour harvesting. The exact time of harvest post-irradiation was dependent on the mouse and therefore harvesting and dose groups for each cohort are summarized in Table 4.2. Euthanasia was achieved through isoflurane overdose (5% in oxygen) and cervical dislocation. Tumours were immediately excised, embedded in mounting medium (Tissue Tek O.C.T, Sakura Finetek Europe B.V., NL), snap frozen in liquid nitrogen and stored at -80°C.

4.3 Raman microscopy

4.3.1 Instrumentation

Raman spectra were collected using a Renishaw inVia Raman Microscope (Renishaw Inc., Illinois, IL, USA). For all tissue studies (chapters 6-8), a 100x dry objective (NA=0.9, Leica Microsystems, Wetzlar, Ge) was used, however for the microfluidics work of chapter 5 other objectives were also used. For all studies, a 785 nm continuous wave diode laser with laser power measured at the sample to be 55 ± 5 mW (yielding a power density of 0.53 ± 0.2 $\frac{\text{mW}}{\mu\text{m}^3}$). The laser sampling volume was measured to be 1.2 ± 0.3 μm (along the x-axis), 5.8 ± 0.3 μm (along y-axis) and 14.8 ± 0.5 μm (along z-axis). The laser volume used in this set-up allows for analysis at the single cell level. All spectrometer components and spectral acquisition parameters were controlled by WiRE version 3.0 software package (Renishaw).

The Raman spectrometer and associated components together with the incident laser

	Dose and Harvest Time	Number of Mice	Number of Spectra
Cohort A	0 Gy, 3 days	4	2032
	5 Gy, 3 days	4	2279
	15 Gy, 3 days	4	1969
Total spectra pre-processing		6648	
Total spectra post-processing		6280	
Cohort B	0 Gy, 1 day	3	1514
	15 Gy, 1 day	3	1540
	0 Gy, 3 days	4	2196
	5 Gy, 3 days	4	2007
	15 Gy, 3 days	5	1998
Total spectra pre-processing		9612	
Total spectra post-processing		9255	
Cohort C	0 Gy, 2 hrs	4	2049
	15 Gy, 2 hrs	4	1908
	0 Gy, 1 day	3	1380
	15 Gy, 1 days	3	1374
	0 Gy, 3 days	3	1499
	15 Gy, 3 days	3	1462
	0 Gy, 10 days	4	1923
	15 Gy, 10 days	4	2019
Total spectra pre-processing		14192	
Total spectra post-processing		13614	

Table 4.2: Dose and harvesting groups for the mouse cohorts.

and scattered Raman light paths are shown in Figure 4.1. The Raman excitation laser exits the laser source with dimensions of 5×2 mm^2 and passes through a beam expander, causing the laser spot to assume a circular shape of 5 mm diameter. This light is reflected onto a 785 nm high pass optical filter (Renishaw) which reflects 785 nm light and transmits light of wavelengths greater than 785 nm. The 785 nm light is then reflected in high purity to an upright microscope (Leica) focusing the laser light on the back aperture of the objective and so matching this aperture as close to 5 mm is important. The objective focuses the light on the sample which is held in place on a motorized microscope stage (Prior Scientific Inc., Rockland, MA, USA). The spatial position of the sample is electronically controlled with resolution of 0.1 μm along the x, y and z directions. The laser light is isotropically scattered and a portion of this light is collected by the objective, transmitted back through the optical filter and focused onto a 600 $\frac{\text{line}}{\text{mm}}$ diffraction grating. The spatially dispersed

light is then focused along the dispersion axis of an Andor iDUS DU-401A-BR-DD (back illuminated, deep deletion, single quartz window with anti-reflective coating optimized to 900 nm light) CCD (Andor Technology, South Windsor, CT, USA). The CCD is cooled to $-80°C$ using a thermoelectric cooler in order to reduce thermal noise on the detector. The CCD has dimensions of 1024×127 pixels, with a pixel size of 26×26 μm^2. The detector collection area along the dispersion axis was selected to be 600 pixels wide and centred around 1070 cm^{-1}, although this did vary throughout collection slightly. Regardless of slight variations, the spectral acquisition window always encompassed a region from 460 cm^{-1} to 1800 cm^{-1}.

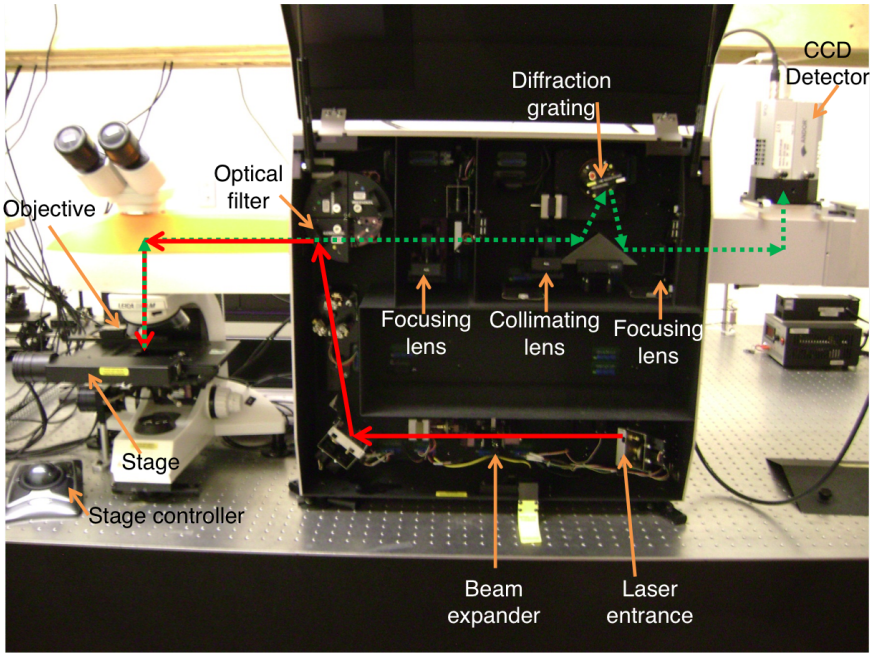


Figure 4.1: Raman spectrometer with incident (red) and scattered light paths (green).

4.3.2 Spectral acquisition

Procedures for Raman analysis are consistent throughout the three cohorts. Tumours were sectioned to 20 μm using a rotary microtome (HM 505, MICROM International GmbH, Walldorf, Ge) and placed on magnesium fluoride slides (Crystran Limited, Dorset, UK). Sections remained on ice until Raman analysis, and were allowed to air dry for 10 minutes prior to spectral acquisition using a commercial Raman spectrometer. In order to best consider tumour heterogeneity, 3 tissue sections were sliced per

tumour and Raman maps were acquired from several sub-regions within a section. Each tissue section was studied using two 100 μm $\times$100 μm maps or one 220 μm $\times$220 μm map. In total 5-8 maps were collected per tumour, using the 100$\times$ objective with a step size of 15 μm along the x and y dimensions. A detailed summary of the total number of spectra collected for each cohort and group can be found in table 4.2.

Since tissue is not always uniform, and can have tears as a result of the sectioning and plating, maps were collected in regions that are visibly intact and containing healthy and viable cells. Figure 4.2 shows regions of mapping for a tissue section, characterized by uniformity and healthy looking cells (cell wall intact) that are reasonably far away from uneven regions. The entire area to be mapped is investigated by eye prior to spectral mapping in order to ensure the area is uniform and free of debris. Visible light is used to adjust the z-position of the region of interest by ensuring it is in clear focus, and the laser spot is focused to a depth of 10 μm below the surface of the cell using the motorized sample stage.

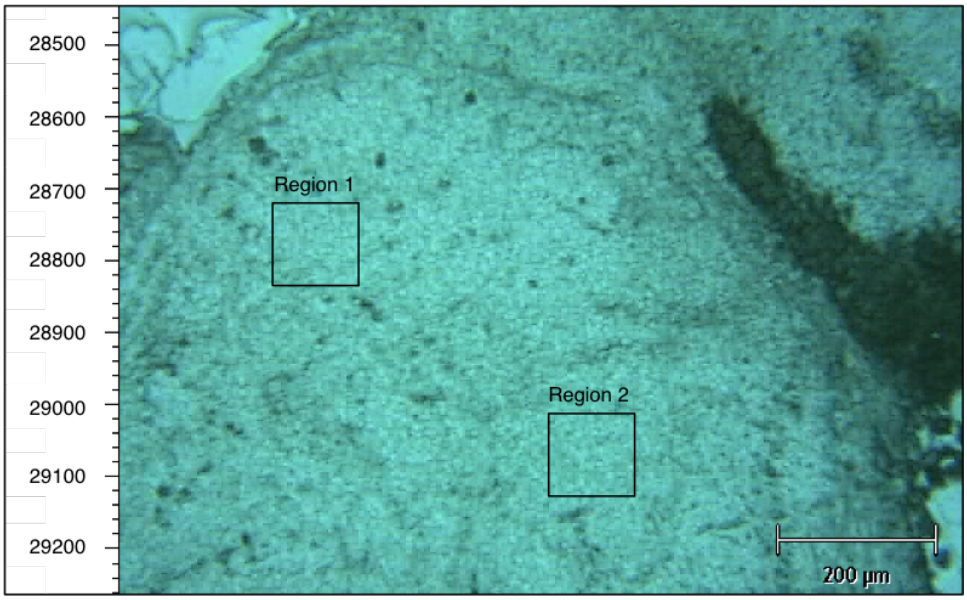


Figure 4.2: Mapping regions of a tissue section. Raman maps are automatically collected from intact and viable tissue regions with area 100μm $\times$ 100μm.

It is important to maintain consistent spectral acquisition parameters throughout Raman studies, in order to isolate spectral features that are a result of changes in tissue responses rather than inconsistencies in data acquisition [226]. Factors including the laser focusing, power, exposure time, sample handling and objective should be kept consistent in order to maintain reproducibility [226–228]. These spectral acquisition

parameters remained consistent between tumours, dose/time groups and cohorts for the tissue work presented in this dissertation. Some variations exist for the Raman studies with microfluidics in chapter 5, however these condition changes are discussed in detail in that chapter.

For tissue studies, spectra were collected using 100% laser power (55 ± 5 mW) for 20 seconds without the use of photobleaching. A silicon reference spectrum, centred at 520.00 ± 0.50 cm^{-1} was collected prior to data acquisition each day, and after every 6 hours. Any obvious problems in laser or system alignment which could affect laser intensity at the sample would be reflected in the intensity and location of this silicon reference peak. Any drifts in intensity or location prompted adjustment of system alignment as well as other system checks to restore it to baseline.

4.3.3 Data processing

Following spectral acquisition, the entire dataset containing spectra for all tumours within an experiment is batch processed. First, outlier spectra are manually identified and removed. Outliers may include spectra containing a cosmic ray, saturated spectra or spectra that are clearly not associated with live tissue. This is necessary because spectral mapping is carried out in an automated fashion, making it possible that spectra within the data set are affected by temporary changes to the data acquisition process (e.g. a bump to the instrument, flash of light in the room or exposure to a cosmic ray). The total number of spectra remaining in each cohort following outlier removal is listed in Table 4.2. This data set is then processed to remove background biological fluorescence, normalize spectra, shift spectra to account for system drifts during data acquisition and isolate correlated spectral features using PCA. All programs were developed using Matlab version 8.4.0.150421 R2014b (Mathworks Inc., Natick, MA, USA).

Background estimates and subtraction

Raman spectra of biological materials consist of the Raman bands associated with the biological material superimposed with a fluorescence spectrum arising from the organic molecules intrinsic to the sample volume and the MgF_2 slide if present in

the laser sampling volume. The intensity of background biological fluorescence is dependent on the amount of material present in the sample volume, and therefore varies throughout the tissue. Spectral background estimate and removal is therefore used to eliminate this source of variability between spectra.

Background fluorescence gives rise to a low frequency baseline structure of the Raman spectrum. In order to remove this component of the raw spectrum, a Savitsky-Golay filter is used to estimate the baseline (BL) of the spectrum [229]. A generalized moving average forms the basis of the Savitsky-Golay filter, where the coefficients of the filter are determined by linear least-squares regression to fit the spectrum BL within a window of interest to 1^{st} order. The size of the filter window is selected to be 7% of the total length of the spectral data set. This BL estimate gives an initial threshold intensity to differentiate between signal and BL at each point in the spectrum. The raw spectrum is then modified such that data points greater than the estimated BL are set to the value of the BL at that point and this modified data set is used to re-estimate the BL. In this way, the BL estimate conforms to the low frequency structure of the background and eliminates the high frequency Raman signals. This fitting process is reiterated 20 times, leading to convergence of a BL fit for the data. The estimated BL is then subtracted from the raw spectrum, leaving a spectrum with significantly less biological fluorescence contamination. Figure 4.3 shows an unprocessed Raman spectrum, together with a background estimate using the Savitsky-Golay filter and corresponding background subtracted spectrum.

Careful selection of the Savitsky-Golay filter window size is needed. First, the size of the filter window affects curvature of the BL estimate. A large filter window (e.g. 7% of the data range) leads to low curvature while a small filter window (e.g. 1% of the data range) leads to high curvature in the BL estimate. For this work, a filter size of 7% was selected based on visual optimization to the data set. With this selection, a balance in avoiding an overestimate of the BL while also avoiding an underestimate in the curvature of the BL is achieved.

Spectral shifting

A reference silicon spectrum is collected and used to account for system misalignments and to avoid major spectral shifts prior to each day of spectral acquisition. However,

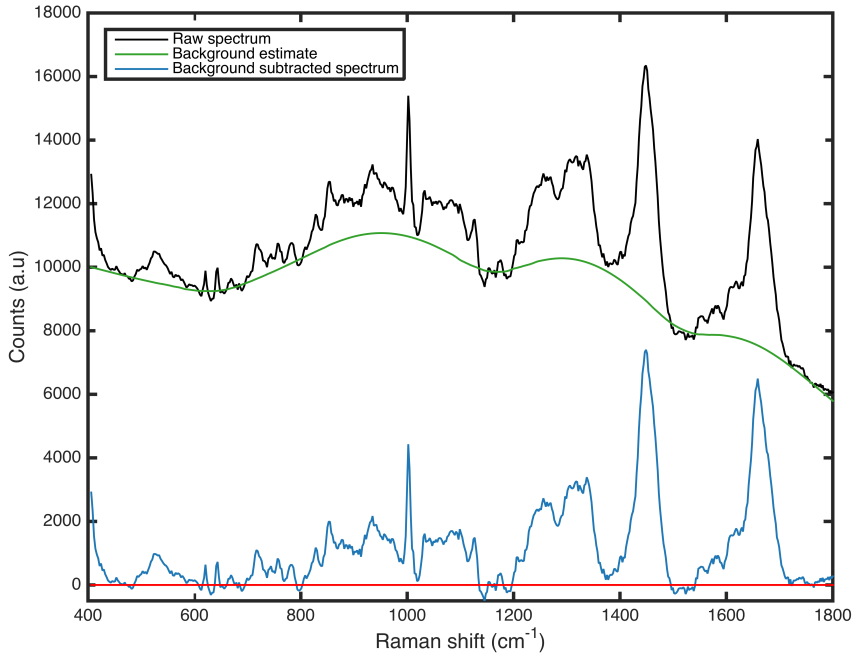


Figure 4.3: Raw and background subtracted Raman spectrum from tissue. An unprocessed Raman spectrum obtained from tissue (black) as well as the background estimate according to a Savitsky-Golay filter (green) and background subtracted spectrum (blue). The Savitsky-Golay filter window size was set to 7%.

slight drifts of the Raman system do still occur during data acquisition which lead to drifts in the Raman shift read out by the detector for a given peak. In order to account for these slight drifts, all spectra were aligned relative to the first spectrum in the data set. Alignment to the first spectrum is an arbitrary selection. Spectral shifts within a single day never exceeded 0.5 cm^{-1}, however within a data set shifts occurred up to 2 cm^{-1}.

Spectral shifting was carried out by first isolating and fitting the phenylalanine Raman band at 1004 cm^{-1} to a Gaussian distribution for both the reference spectrum (R) and spectrum to be shifted (S). The difference between the mean of the Gaussian distribution (μ) for each S spectrum and mean of the phenylalanine peak fit for R is calculated and defines the required shifting magnitude and direction. The intensity values for S are interpolated between subsequent pixels using a resolution of 0.01 over the entire range of the spectrum. Interpolation occurs between intensity values assigned to pixel $(i-1)$ and i (i denotes the pixel index in the array

containing all intensity values for S) if S is to be shifted to higher wavenumbers. Alternatively, interpolation occurs between pixels $(i+1)$ and i if S is to be shifted to lower wavenumbers. Interpolation results in a 100 data point model of the Raman spectrum between the two pixels, and the new shifted data set (S') at pixel i is filled with the interpolated value defined at the shifting distance between the two pixels. This interpolation and shift is repeated for all pixels in (S). Since the final pixel in S can not be filled by interpolated data, the pixel is instead filled with intensity data from the pixel adjacent to it. The fitting and shifting process is reiterated on S' relative to R to create S''. Overall, this process results in a set of intensity data (S'') which is shifted relative to the original data set (S) but maintains the same spectral shape and features and is aligned with R. Figure 4.4 illustrates the shifting process by comparing the mean phenylalanine peak position for a spectrum in the data set to the reference spectrum.

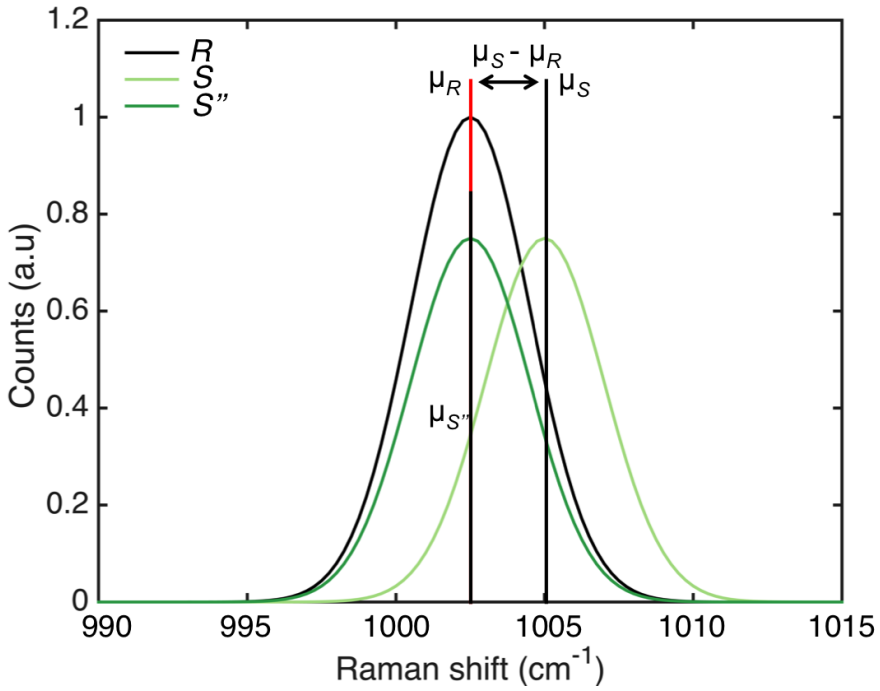


Figure 4.4: Raman spectral shifting using the phenylalanine peak. The reference spectrum (R) is used to determine the shifting distance ($\mu_S - \mu_R$) of a spectrum (S), resulting in a shifted spectrum (S'').

Spectral normalization

The absolute peak intensity in a Raman spectrum will be influenced by the amount of biological material in a the sample volume, Raman system alignment and minor fluctuations in laser output power. Spectra are therefore normalized to the total area under the baseline corrected and shifted spectrum, in order to account for these absolute intensity differences.

Principal component analysis

Principal component analysis is applied following spectral processing, in order to identify trends in the spectra as a function of dose and time post irradiation, as described in chapter 3, section 3.3. PCA isolates correlated Raman peaks within a spectrum (defined as the PCs) and scores the degree of expression of that PC for the entire data set (PC scores). Following from the technical description of PCA in section 3.3, the data input to Matlab consisted of an $n \times p$ array made of up n samples corresponding to the spectra in a given data set and p measurements corresponding to the number of data points in a single spectrum. Following PCA, a total of $(n-1)$ PCs and the corresponding component scores for each spectrum is output.

Statistical Methods

Component scores for a given spectrum do not follow a normal distribution within a tumour or dose group (tested using Anderson-Darling Test and Lilliefors Test as established in Matlab). Therefore, Tukey style box plots are used to represent the component scores for all spectra in a tumour or dose group. Median component score, along with 25^{th} and 75^{th} percentiles are used to represent PCA results. Whiskers on box plots represent the most extreme data points in the data set. The most extreme data points above and below the median [230] are defined as the PC scores that fall closest to,

$$1.5(75^{\text{th}}\text{percentile} - 25^{\text{th}}\text{percentile}). \tag{4.1}$$

Outliers are defined as all data points falling beyond this value, and are left off the

box plots for clarity. Notches on the box plots indicate the 95% confidence interval on the median, approximated assuming a normal distribution, although this assumption is also accurate for large samples of non-normal distributions [230]. Since data sets are considered to follow a non-normal distribution, statistically significant shifts in PC score between tumours or dose groups was tested using the chi-square statistic of the two-sided Wilcoxon rank sum test, to a 5% significance level.

Chapter 5

Raman Microfluidics

5.1 Introduction

Raman microfluidic systems capitalize on the exceptional spatial control of the Raman excitation laser [207] achieved with Raman microscopy and controlled manipulation of small fluid volumes using microfluidics. Together this is an ideal combination for studying micron sized particles such as single cells, in an environment that is amenable to cell viability. Raman microfluidic systems have shown particular value in biological analysis. They have been used to measure concentrations of bio-analytes in blood or other fluids [231, 232] and as a detection technique for circulating tumour cells [233]. Raman microfluidic systems have been used to distinguish non-cancer and cancerous cells [233, 234], differentiate between different leukemia cell lines [235] and distinguish blood-derived leukocytes from breast cancer and leukemia cells [236]. The ability of Raman microfluidic systems to distinguish between different types of cells in a label-free way shows promise for developing a Raman activated cell-sorting (RACS) system, which would operate similar to fluorescence activated cell sorting (FACS) however the detection technique is Raman analysis and therefore requires no prior sample manipulation and staining with fluorescent markers [235]. Raman microfluidic systems have not yet been applied to study radiobiological responses in cells, and have the ability to overcome many of the problems with traditional data acquisition techniques. This chapter presents four microfluidic system designs and investigates the spectral characteristics that each system design can yield.

5.1.1 Limitations for clinical implementation of single cell Raman spectroscopy

Several techniques for data acquisition of single cell Raman spectra exist. Cells can be fixed onto a disk of appropriately selected material and a dry objective can be used to identify individual cells from the pellet [132,135]. Alternatively, cells can be grown onto slides and analyzed with a dry objective [222] or kept in an aqueous solution and analyzed with an immersion objective [97]. These techniques pose several challenges for adaptation of single cell RS in the clinic.

The above mentioned single cell RS techniques involve long data acquisition times. This is due partly to the time it takes for the user to identify and isolate a cell to study and partly to the inherently weak Raman scattering cross section which leads to lengthy spectral acquisition times. As an example, the system reported in Harder et al. is optimized in terms of detector sensitivity, laser power density and system collection efficiency. Spectral acquisition takes 10 s per cell [132], while it takes approximately 30 s to identify and focus the laser for data acquisition. This is because the surface of the cell pellet is uneven and requires focal adjustments in order to identify the cells. Lengthy acquisition times limit the number of cells that can be studied in a reasonable amount of time.

In addition to long data acquisition times, traditional single cell Raman techniques are difficult to automate. This limits the number of cells from which data can be collected in a reasonable amount of time, and means the techniques are expensive in terms of human resources. These techniques require significant involvement from a specially trained researcher to collect data, limiting who can perform single cell Raman studies and adds to the cost of the technique. Several traditional acquisition techniques remove the cell from its natural environment and require fixation or freezing. This can stress the cells, potentially affecting its biochemical profile. Lastly, these techniques do not make efficient use of the sample, requiring large sample volumes. Patient samples are often limited in size, making efficient use of samples imperative.

Raman microfluidic systems are a promising alternative technique for collecting single cell Raman spectra because they facilitate an automated data collection process while keeping the cells in an amenable environment for proliferation. These systems facilitate analysis of larger proportions of cells, or highly controlled analysis of small

sample volumes, facilitating complete analysis of the radiation related changes occurring in a sample.

5.1.2 Instrumentation considerations

A basic schematic of a Raman microscope coupled with a microfluidic system is shown in Figure 5.1. An excitation laser is coupled to an upright microscope which holds the sample on a motorized stage. Excitation light passes through the microscope objective and is focused onto a small region of the microchannel. The Raman scattered light is collected by the microscope objective and is passed through the spectrometer and detector, producing the Raman spectrum.

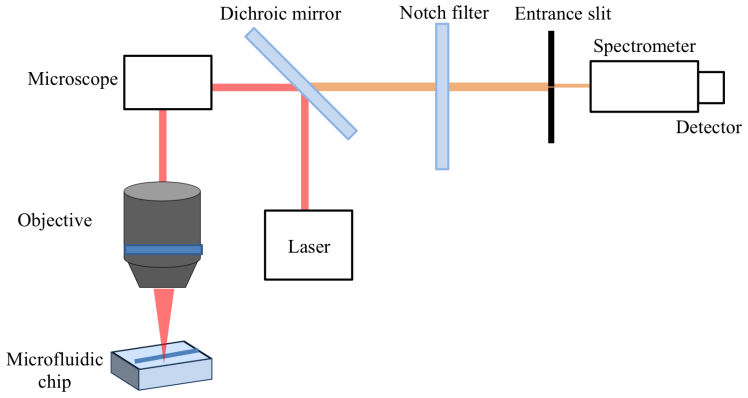


Figure 5.1: Raman microscope coupled with a microfluidic chip. Incident laser (red) and scattered light (orange) paths are shown.

Both Raman microscopy systems and microfluidics systems are fairly versatile, however some special considerations must be made in terms of chip design and microscope components for successful integration. Choice of chip material is important to ensure background signal is minimized to reduce interruption of the potentially subtle spectral changes associated with radiobiology work [132]. Due to the relatively extended (10 seconds) acquisition time associated with single cell RS it is important to immobilize the cells during spectral acquisition. The choice of immobilization technique must be selected to minimize any trapping-related damage induced in the cell, while

maintaining stable cell trapping and efficient automation capabilities for the system. A Raman microfluidic system which takes these factors into consideration is needed for further advancements in radiobiological RS studies.

Raman system considerations

The main considerations for the Raman system involve selection of the objective. Raman microfluidic applications require the use of a laser spot that is small enough to minimize its interaction with the microchannel walls. Therefore, consideration of objective NA as outlined in chapter 3, section 3.2.1 is important.

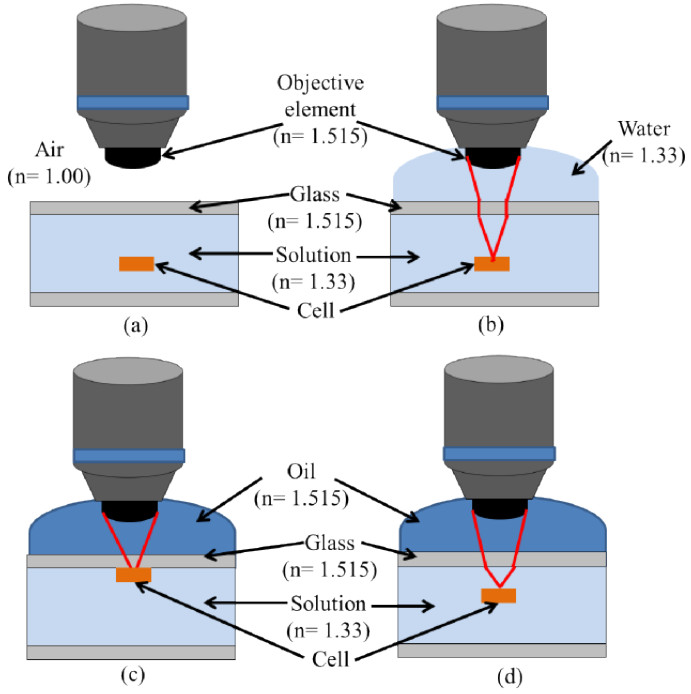


Figure 5.2: Objectives for observing particles under a coverslip. A particle (orange) suspended in solution under a coverslip. A dry objective (a), water immersion objective (b) and oil immersion (c & d) are shown.

In microfluidic systems the cells are suspended in isotonic solution beneath a window, as shown in Figure 5.2. In a dry objective situation, as shown in Figure 5.2a, light exiting the objective must pass through air, window, isotonic solution and finally the target. Each interface between different indices of refraction (n) result in scattering and refraction of the light. Large light refraction results in image aberrations [237], therefore a coverslip corrected water immersion objective is used to eliminate this.

In this case the only index of refraction change is through the coverslip, as shown in Figure 5.2b. Coverslip correction is therefore needed to account for refraction and is based on a 170 μm thick window with index of refraction 1.515 [212]. The system is very sensitive to the thickness and index of refraction of the coverslip therefore typically a correction collar is also present to account for slight variations.

Typically an oil immersion objective is favourable for samples located below a coverslip. However, such objectives are only valuable if the sample is directly under the coverslip, as shown in Figure 5.2c, because light no longer has to pass through the isotonic solution which has a much lower index of refraction. If light has to pass through the isotonic solution (Figure 5.2d), image aberrations quickly begin to be apparent (within less than 10 μm of distance through the isotonic solution) [237].

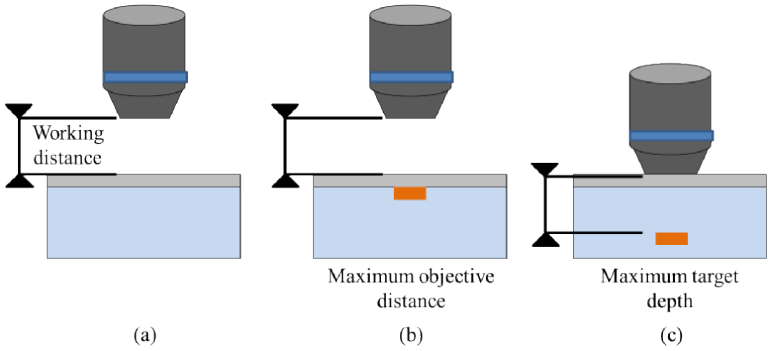


Figure 5.3: Objective working distance. The working distance of an objective is defined in (a). Based on the working distance defined for an objective, the maximum distance the objective can be placed from the top of the microchip is fixed (b). The maximum depth a particle can be placed below the coverslip is also predefined by the working distance of the objective (c).

The working distance of the objective is the distance from the front of the lens element of the objective to the closest surface of the coverslip when the target object is in sharp focus, as shown in Figure 5.3a [212]. The working distance is predefined for an objective based on its NA and magnification, decreasing as these two values increase. The working distance of the objective will dictate the maximum distance the objective can be placed from the top surface of the chip (as shown in Figure 5.3b), which would focus sharply on an object directly below the coverslip. Also the working distance dictates the maximum depth below the coverslip (objective right up against coverslip) for which the objective can focus on a target object (as shown in Figure 5.3c).

5.1.3 Microfluidic chip considerations

The basic components of a microfluidic chip include a chip substrate in which a microchannel, or series of microchannels, is made. The microchip should also contain an injection and extraction port that connects to tubing and syringe systems in order to pass the sample through the microchip.

Basic chip design

Depending on the substrate material used to make the chip, a Raman inert window may need to be incorporated in the chip to avoid interfering background signals from the chip substrate (discussed in more detail in the next section). If the chip is made of several components (e.g. base and window) these must all be tightly sealed together in order to avoid leakage and in order to successfully flow fluid through the microchannel.

When coupling the microfluidic chip and Raman system together the physical dimensions of the chip must also be considered. The objective used in the Raman microscope must be placed close to the surface of the microchip, usually a minimum of 250 μm. Therefore the chip must be designed such that the objective can be placed this close without meeting any obstructions. Also, the thickness of material between the objective and target object is constrained. Suitable objectives for Raman microfluidic applications will be corrected for a coverslip (nominally 170 μm thick) therefore the material between target object and objective must be limited to this thickness, as discussed in section 5.1.2.

It is also necessary to fabricate the chip to have a smooth surface (within the channel) to reduce scattering of the excitation laser. Scattered laser light creates a uniform background signal in the Raman spectrum which, if sufficiently strong, can severely degrade spectral quality or wash out the target object's Raman signal completely.

Chip material

Factors to consider in chip material selection include: the type of material, ease and time for fabrication using that material and bio-compatibility. Material should be

selected to reduce interference of Raman signals from unwanted materials (the microfluidic chip) and optimize Raman signals from the target material. Common materials used to make microfluidic chips include polydimethylsiloxane (PDMS), silicon, glass, and quartz.

Background considerations

Cells have a Raman fingerprint in the 400-1800 cm^{-1} and 2400-3600 cm^{-1} regions, therefore selecting a material that will minimize the presence of Raman peaks from the chip in these regions is important. Furthermore, selecting a material of high optical quality to reduce background fluorescence arising from the chip material will also minimize substrate spectral contamination.

Bulk samples of pure metals do not exhibit a Raman signal because free electrons present in the material block incident photons from reaching and interacting with the lattice bonds of the metal [238]. However, thin films of pure metals do exhibit Raman signals because the conductivity of nanometre thickness films is low and therefore allows photons to reach the lattice bonds of the metal [239]. Thin metal films or roughened metal surfaces can in fact be used to enhance Raman signals in techniques such as surface enhance Raman spectroscopy (SERS). Non-metals (both inorganics and organics) are typically Raman active. Many organics have characteristic Raman peaks in regions of interest for cell studies because the types of bonds present are similar to those found in biomolecules.

The Raman spectrum of some common microfluidic fabrication materials, collected using a 785 nm laser for 10 s, are shown in Figure 5.4. PDMS exhibits Raman peaks throughout the spectral region of interest for cells. Silicon (spectrum not shown in Figure 5.4) is used for calibration of the Raman system and is useful because of its strong peak at 520 cm^{-1}. Glass exhibits a broad and strong Raman signal around 1000 cm^{-1}. Quartz has a relatively flat Raman spectrum in the cell region, with a broad peak around 350 cm^{-1} [240], as well as at 400 cm^{-1}, 600 cm^{-1} and 800 cm^{-1}. Other than these peaks, quartz has a relatively flat Raman spectrum in the region of interest for cells. The spectrum of MgF_2 is also shown, and exhibits a sharp peak around 410 cm^{-1} however in general the spectrum of this material is very flat in the cell spectral range.

Chip materials with strong Raman signals will have greater negative impact on the spectral background if it is used to make the channels. Therefore, fabrication using MgF_2 is ideal. Fabrication using other materials with high background may also be possible with appropriate selection of channel dimension and through the addition of a Raman transparent window in the device.

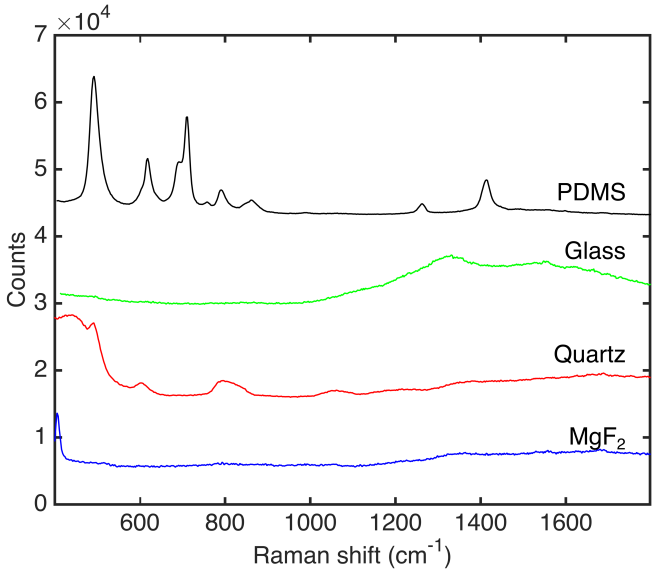


Figure 5.4: Materials suitable for microfluidic chip fabrication. Raman spectra acquired using a 785 nm laser, for 10 seconds focused on the surface of PDMS, glass, quartz and MgF_2.

Fabrication techniques

PDMS microchip fabrication is well established using soft lithography [241], and is a relatively quick and simple process with the advantage of rapid prototyping [242]. PDMS chips are also relatively inexpensive to make and therefore can be treated as disposable systems if desired. Fabrication of glass, silicon and quartz chips are more time consuming, possibly requiring the use of harsh chemical etching and high cost facilities [236, 240]. Microchips made from these materials are therefore typically intended to be reusable. Microchip fabrication using MgF_2 as the chip substrate has not been attempted in the literature.

Memory effect

The memory effect refers to particles or analytes sticking to the microchannel walls, permanently altering the Raman background of the chip [236,240]. Challenges associated with the memory effect can be alleviated by selecting a chip which is disposable after each use. Alternatively, if a reusable chip is necessary, the channel could be coated to protect the walls from contamination during analysis [243]. Washing the channels after each use would also be essential practice for reusable chips.

Microchannel system design

Physical dimensions of the microchannel should be selected so that the channel walls are not in the sampling volume of the laser spot, so as to minimize background signal from the chip substrate. However, if the walls are too large (greater than 1 mm) the fluid dynamics behave closer to those in macroscopic flows [244]. Employing certain trapping mechanisms may also place constraints on the allowed separations of channel walls. Such factors should be considered when designing the microchannels.

Aqueous medium and flow

Aqueous media are the basis of microfluidics. For Raman microfluidic applications involving cells, the aqueous medium should be selected such that it is compatible with cells and has negligible or minor Raman peaks in the spectral range of interest for cells. Pure water has weak Raman bands at 1640 cm^{-1} and 3300 cm^{-1} [240] and can be used effectively to suspend particles. However, PBS is preferred for suspending cells as it is an isotonic solution. The chemical composition of PBS is mainly water with some salts present (sodium phosphate, sodium chloride), therefore, the Raman spectrum is highly similar to that of pure water.

Regulation of the flow rate is required to ensure successful trapping (depends on the trapping mechanism being used), and appropriate time to acquire Raman spectra. Flow can be precisely controlled and driven by using pressure or vacuum via external pumps [245].

Trapping techniques

It takes a finite amount of time to collect a Raman spectrum of single cells (on the order of 10 seconds [132]), therefore, a cell suspended in fluid in the microchannel must be held in the sampling volume of the laser for that length of time in order to ensure optimal spectral quality is obtained. Furthermore, incorporation of trapping techniques for controlling cells in the microchannel allows the cell to be moved away from microchannel walls in order to avoid interrupting background signals and facilitates cell sorting and systemic analysis of a large collection of cells.

Several single-cell trapping mechanisms are available, including, mechanical, hydrodynamic, dielectrophoretic, acoustic and optical trapping. For Raman microfluidic applications it is important to select a trap which can stably hold single cells for the entire duration of the spectral acquisition period, does not damage the cell over that period, does not disrupt or interact with the incident or scattered light, rapidly traps the target object, is easily incorporated into a Raman microfluidic system, requires minimal pre-focusing of the sample into the trap and is relatively inexpensive.

5.1.4 Current designs for single cell Raman microfluidics

Perhaps the most extensively published Raman microfluidic system has been designed in PDMS. The popularity of PDMS designs can be attributed to the relatively low cost and time required for fabrication in this material. Lau et al. designed a PDMS microchip with a channel depth of 50 μm and width of 100 μm, bonded to glass coverslips [235]. This chip was coupled with a 660 nm laser for single beam optical trapping and Raman spectral acquisition. Acquisition times were 2 minutes per spectrum, which is relatively long compared to other single cell Raman studies [132]. Lau et al. suggest using a 785 nm laser to reduce acquisition times, as well as employing signal enhancing techniques such as SERS [235]. In this set-up the spectral range is limited to 700 cm^{-1}-1700 cm^{-1}, possibly due to the strong PDMS signals apparent at wavenumbers below 700 cm^{-1}. Tightly focused laser light also helps to minimize signal from the glass and PDMS, since a 100x oil immersion objective is used. Several valuable radiation-related Raman peaks are found at wavenumbers below 700 cm^{-1}, therefore it is desirable to include lower wavenumbers in the spectrum.

Perozziello et al. designed a microchip made of a hybrid of materials, selected to both enhance the Raman signal from cells while minimizing background from the chip materials [246]. Topaz was covered with 100 nm gold, and SU-8-50 was coated on this gold surface which formed the channels and a CaF_2 window sealed the chip. The gold acted to isolate the Raman active Topaz from producing a Raman signal, and also enhancing the signal-to-noise ratio in the Raman spectra. Cells were mechanically trapped in cavities made inside the channel, and nanodevices were formed near each trap to enhance the Raman signal. A 830 nm laser coupled with a 50x objective was used to focus and collect the laser light. They successfully observed H_2O_2 induced cell membrane damage using this device, by studying the 800-1800 cm^{-1} range. No spectra are presented in the paper, however, and also spectral acquisition times are not given [246].

More recent Raman microfluidic designs involve glass and mineral based chips. Dochow et al. demonstrated successful trapping and Raman spectral analysis of human tumour cells in a quartz capillary based system [247]. A quartz capillary made up the microchannel, with inner channel dimensions of 50x50 μm^2. Two parallel opposed single mode fibres were used to guide 1070 nm laser light for dual beam optical trapping, and a 785 nm laser was coupled to a 100x dry objective for Raman interrogation lasting 10 s per spectrum. The usable spectral range was from 950-1771 cm^{-1} due to disruptive peaks from quartz at 600 cm^{-1}, 800 cm^{-1} and 1060 cm^{-1} and of water at 1640 cm^{-1}.

Dochow et al. subsequently presented a microfluidic system wet-etched into borofloat-33 glass, consisting of a trapping chamber with a height of 60 μm and diameter of 190 μm [247]. Dual beam fibre trapping was carried out using a 1070 nm laser, and spectral acquisition was carried out using a 514 nm laser coupled with a 60x water immersion objective for a duration of 10 s per spectrum. The 514 nm laser was selected to reduce background signal from the glass substrate. The spectral quality obtained is superior to that presented in other PDMS studies, however the usable spectral range for this chip is from 550-1750 cm^{-1} and there exists a measurement artifact from 1000-1150 cm^{-1} which is less than ideal for radiobiological Raman studies. Further, Raman spectral acquisition using a 785 nm laser is preferred in order to reduce laser-induced damage to the cell and improve acquisition times [217, 235].

A microfluidic system wet-etched into quartz [236] was also investigated, allowing

Raman spectral acquisition using a 785 nm laser, due to lower Raman background in quartz compared to glass when probed using this wavelength [247]. Dual beam fibre trapping using a 1070 nm laser, and a 60x water immersion objective was used to focus and collect Raman scattered light. Raman spectral acquisition took 10 s per spectrum. Below 810 cm^{-1} as well as from 1497-1594 cm^{-1}, spectra were found to have residual spectral contributions from the quartz substrate and trapping laser [248]. This is not ideal for radiobiological Raman experiments which rely on spectral changes within these regions [132]. Further challenges identified by the authors include agglomeration of the tumour cells following trypsinization, and sedimentation of the cells at the bottom of the microchannel making trapping and isolation of single cells challenging [236].

The main challenge with current single cell Raman microfluidic techniques for applications in radiobiology is the limited usable spectral range due to interrupting background signals from the chip material. A Raman microfluidic chip with minimal spectral contributions from the chip itself is needed.

5.1.5 Objective

This chapter presents four microfluidic substrate designs, with the intention of assessing suitability for single-cell radiobiological Raman studies. Basic PDMS, gold coated PDMS, magnesium fluoride and parafilm-magnesium fluoride hybrid systems were fabricated. Next, single cell spectra were collected and analyzed for suitability in radiobiological studies. This chapter presents new fabrication techniques for Raman microfluidic studies showing that magnesium fluoride based systems are ideal for radiobiological applications.

5.2 Materials & Methods

5.2.1 PDMS system

Fabrication took place using standard soft lithography techniques as described in detail elsewhere [241]. Briefly, a silicon mask was used as a template to form 155

μm wide by 50 μm deep channels. Sylgard 184 (Krayden Inc., CO, USA) Silicone Elastomer Kit was used with a 10:1 elastomer to curing agent ratio to make the PDMS structure. This was de-gassed for 2 hours then baked at 80°C for approximately 5 hours. The PDMS chip was not sealed with a glass slide since a strong Raman signal arises from this material. Instead, the chip was sealed with a 170 μm thick MgF_2 coverslip (25 mm diameter, Global Optics UK Ltd, Poole, UK). The seal between the coverslip and PDMS chip was achieved purely through contact forces between the two surfaces.

5.2.2 Au-PDMS system

A PDMS chip as described in section 5.2.1 was used as the base for this prototype, therefore the Au-PDMS system has channel dimensions of 155 μm wide and 50 μm deep. The PDMS chip was then coated with gold following protocols described by Lee et al. [249]. This consisted of treating the PDMS with Oxygen Plasma using a Harrick Plasma cleaner/sterilizer, coating with 2 nm Ti (Alfa Aesar, MA, USA) at a 1 $\frac{\mathring{A}}{s}$ deposition rate, and then coating with Au (Alfa Aesar) to a thickness of either 150 nm or 250 nm at a rate of 1 $\frac{\mathring{A}}{s}$ using a Glovebox Evaporator (Angstrom Engineering Inc, ON, Ca). A 170 μm thick MgF_2 coverslip (Global Optics) was used as the top window for the system.

5.2.3 MgF_2 system

First, I attempted to wet etch an optical grade MgF_2 wafer (Global Optics) using 5 M HNO_3 over a period of 24 hours, which was unsuccessful. Next a 170 μm MgF_2 slide was etched using a Ti:Sapphire laser (Spectra-Physics, Spitfire Ti-Sapphire laser, CA, USA) with pulse width 120 fs, at 800 nm wavelength, with a repetition rate of 1 kHz. The average power of the etching laser was 0.025 mW, using a 50x, 0.55 NA objective. Two different channel dimensions were machined, the first consisted of a 15 mm long channel which was 100 μm wide and 37 μm deep. The second channel was 15 mm long, 207 μm wide and 75μm deep. Chips were covered using a second 170 μm MgF_2 coverslip.

5.2.4 Parafilm-MgF_2 system

This system consists of an optical grade MgF_2 base (170 μm thick, Global Optics) with Parafilm sealed onto it. A channel was formed in Parafilm by using an Exacto knife, and then sealed with a second MgF_2 surface (170 μm thick) using heat. The channel dimensions were limited by the width of the knife blade and thickness of the Parafilm, yielding a channel that was 79 μm wide and 200 μm deep.

5.2.5 Raman system

All experiments were carried out using the Renishaw inVia Raman Microscope as described in chapter 4. Spectra were collected using either a 100x dry objective (Leica Microsystems, Wetzlar, Ge, NA=0.9) or 60x water immersion objective (Olympus, ON, Ca, NA=1.2, coverslip corrected). Spectra were acquired using the 785 nm laser at 100% laser power for 10 s acquisition time.

The 60xw objective has a spot size of 1.8x10x29 μm^3, and power density of 0.1 $\frac{mW}{\mu m^3}$. This was measured by looking at the full-width-at-half-maximum of an intensity map of the 520 cm^{-1} silicon peak, along a gold-silicon interface. In comparison, the power density of the 100x dry objective is 2x5x10 μm^3 with a 0.5 $\frac{mW}{\mu m^3}$ laser power density at the sample volume.

5.2.6 Cell samples

The human NSCLC cell line H460 (as described in chapter 4, section 4.1.1) was used for cell studies. Cells were suspended in PBS for manipulation in the microchannels.

5.3 Results

5.3.1 PDMS system

The PDMS chip is shown in Figure 5.5a and channel characteristics as observed using 20x magnification can be found in Figure 5.5b. The microchannel base was found to

occasionally be inconsistent, likely due to air bubbles in the polymer during curing.



(a) **(b)**

Figure 5.5: PDMS system. PDMS system (a) and 20x microscope image of a microchannel (b).

Characteristic Raman spectra of the background of the PDMS channel taken using the 100x dry objective at the base, middle and top depths of the channel can be found in Figure 5.6a. Spectra collected at the base of the channel have higher background contamination from PDMS compared to spectra from the top of the channel. Several characteristic PDMS peaks can be observed in this spectrum, specifically at 500, 620, 710, 795, 865, 1260 and 1410 cm^{-1}. These peaks decrease in intensity at further distances from the channel base and wall. The background spectra are highly reproducible. Background spectra of the PDMS channel collected with the 60xw objective are shown in Figure 5.6b. The main difference between collection with the 100x and 60xw objective is that the baseline fluorescence is higher using the 60xw objective, and the baseline has more structure to it.

A cell spectrum collected in the PDMS microchannel is shown in Figure 5.7. The difference spectrum shows characteristic cell peaks, specifically around 1004, 1251, 1337, 1450, 1656 cm^{-1}. However, PDMS peaks are still present in the cell spectrum.

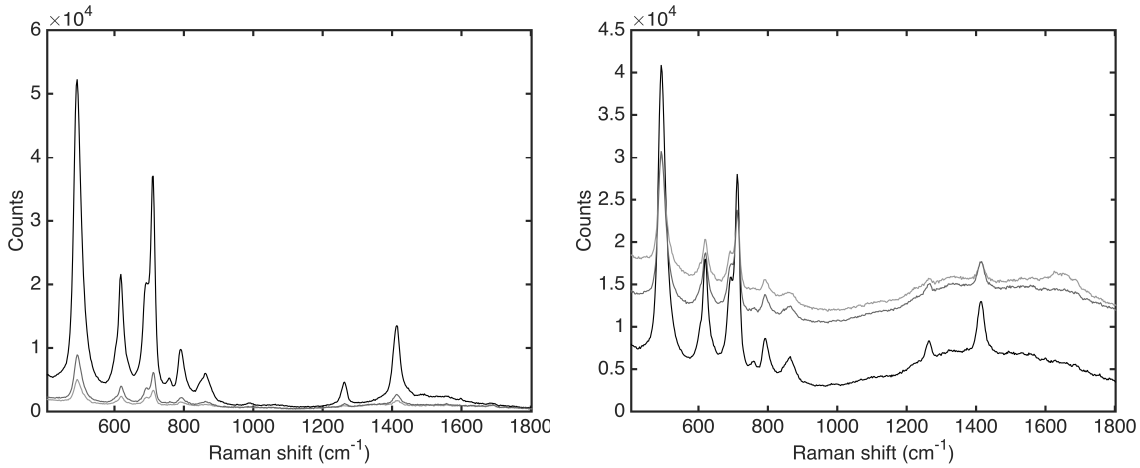


Figure 5.6: PDMS background spectra. Background spectra collected from the top (light grey), middle, and bottom (black) of a microchannel in the PDMS system using a 100x dry objective (a) and 60x water immersion objective (b).

5.3.2 Au-PDMS system

The Au-PDMS chip and corresponding microchannel is shown in Figure 5.8. Due to the flexible nature of the PDMS chip, the gold coating exhibited some cracking and rippling which could be minimized by reduced movement, distortion and handling of the chip once coated with gold. If the PDMS chip contains an inconsistent base due to manufacturing, the base will remain this way after gold deposition.

Background spectra collected with the 100x objective can be found in Figure 5.9a for a 250 nm Au coating. There is little difference between the 150 and 250 nm Au coatings, in terms of spectral quality. Background spectra contain higher fluorescence than in the PDMS chip, and some of the very strong PDMS peaks are still present (500, 620 cm^{-1}), especially from spectra collected at the base of the chip. This may be due to non-uniform chip coverage in some places. The background spectrum at the top of the Au-PDMS channel is fairly flat. Background spectra collected with the 60xw objective can be found in Figure 5.9b. The background fluorescence is much higher in these spectra, which is consistent with what was observed in the PDMS case and makes sense when changing from the 100x to 60xw objective. Due to the high background fluorescence, spectra at the bottom and middle of the channel are

saturated.

A cell spectrum collected in the Au-PDMS microchannel is shown in Figure 5.10. It is clear that there are very few characteristic cell peaks in the cell spectrum, likely because the high fluorescence background is washing them out in this system.

5.3.3 MgF_2 system

The first laser machined chip consisted of a 100 μm wide and 37 μm deep channel. The channel had some visible roughness and minor cracks at the edges. High background fluorescence was observed, likely due to the roughness of the channel. Therefore, a second laser machined chip was developed to reduce the background by increasing the

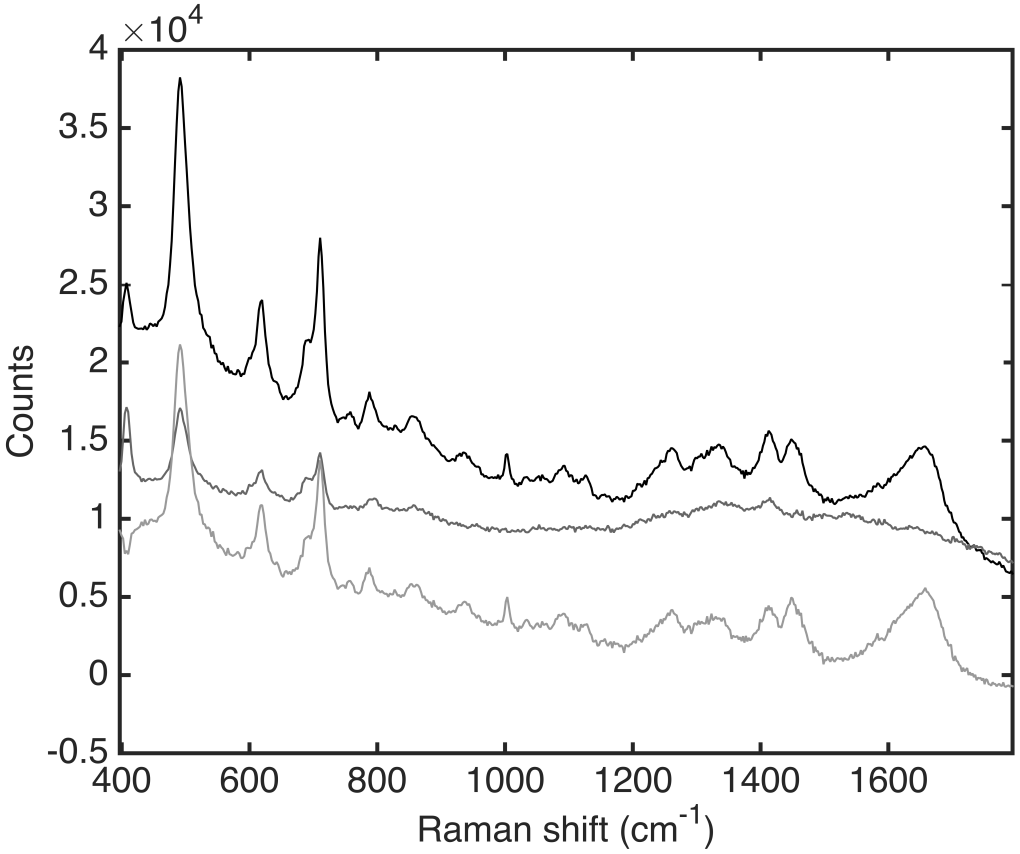
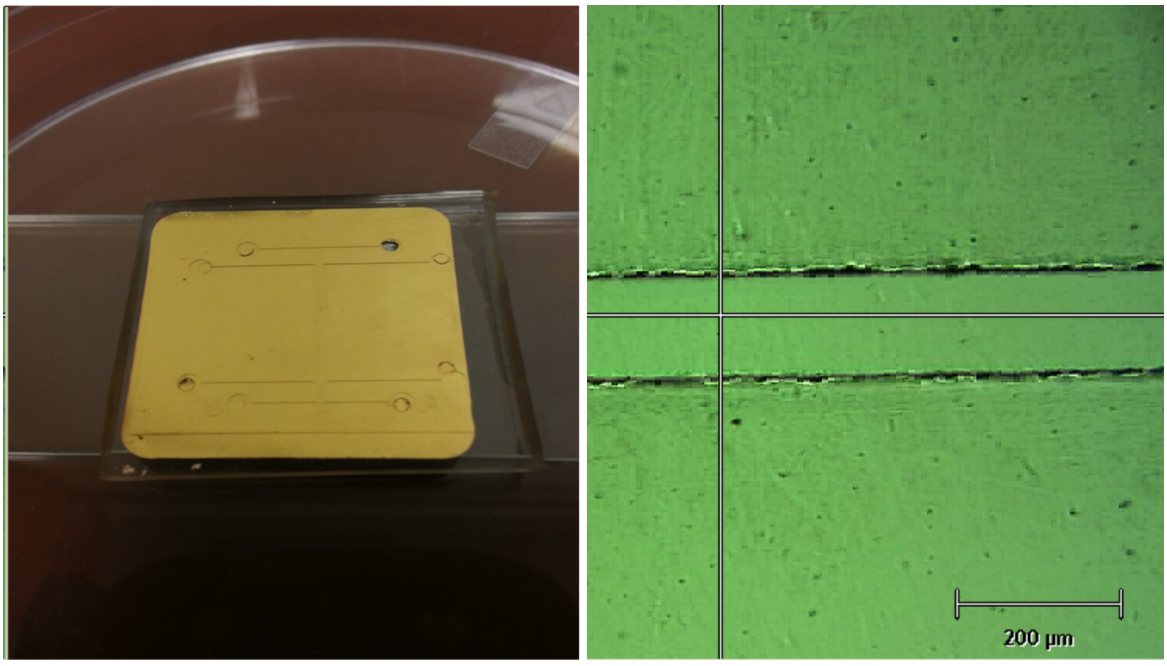
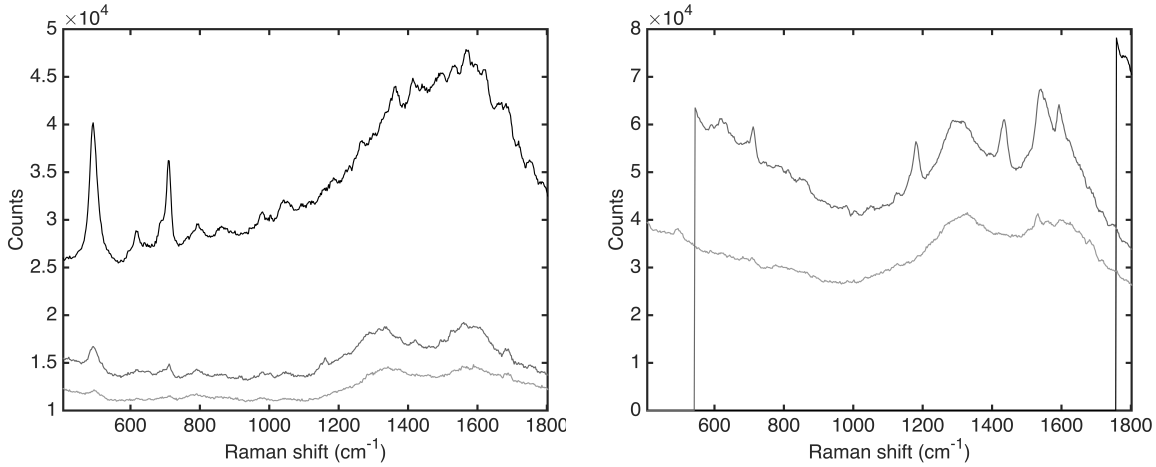


Figure 5.7: PDMS cell spectrum. Raman spectrum of a cell within a PDMS microchannel (black) with corresponding background spectrum and difference spectrum (light grey). Collected using the 60xw objective.



(a) **(b)**

Figure 5.8: Au-PDMS system. Au-PDMS system (a) and 20x microscope image of a microchannel (b).



(a) **(b)**

Figure 5.9: Au-PDMS background spectrum. Background spectra collected from the top (light grey), middle and bottom (black) of the Au-PDMS system using a 100x dry objective (a) and 60x water immersion objective (b).

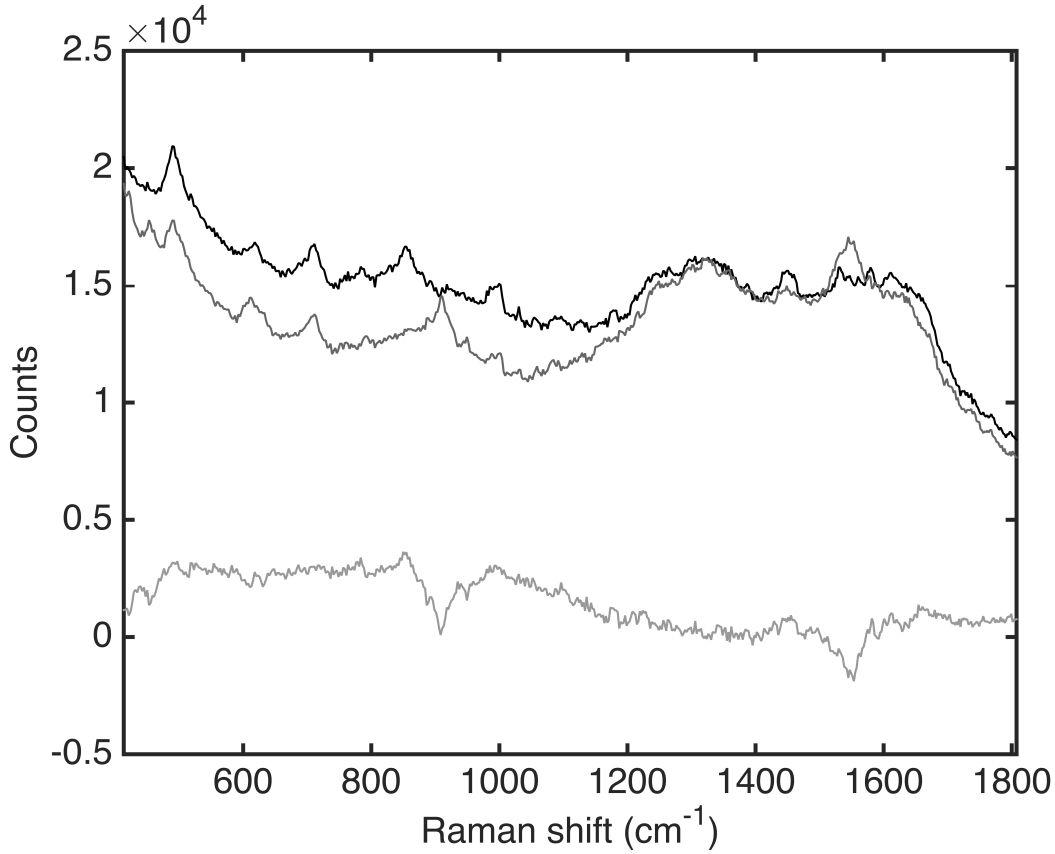
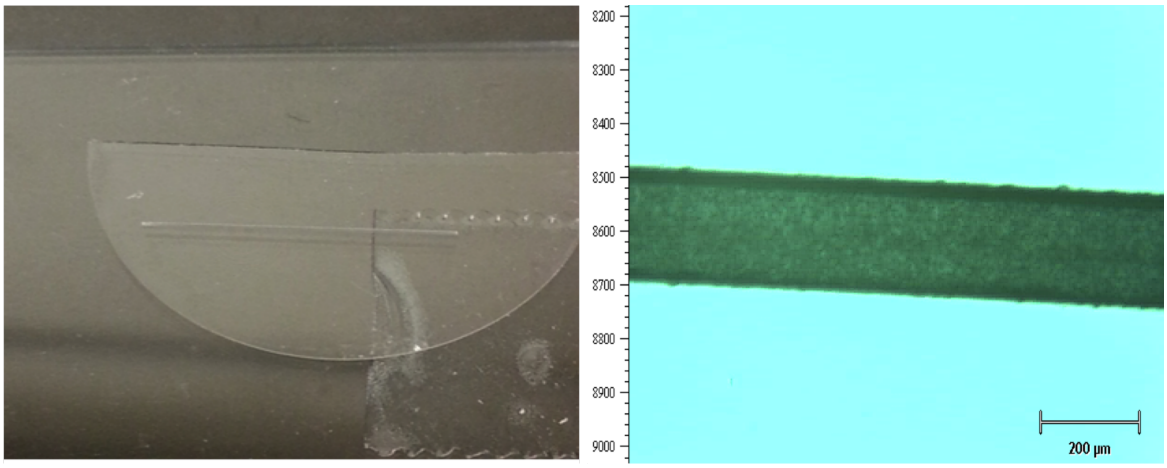


Figure 5.10: Au-PDMS cell spectra. Raman spectrum of a cell within a Au-PDMS microchannel (black), corresponding background spectrum and difference spectrum (light grey). Collected using the 60xw objective.

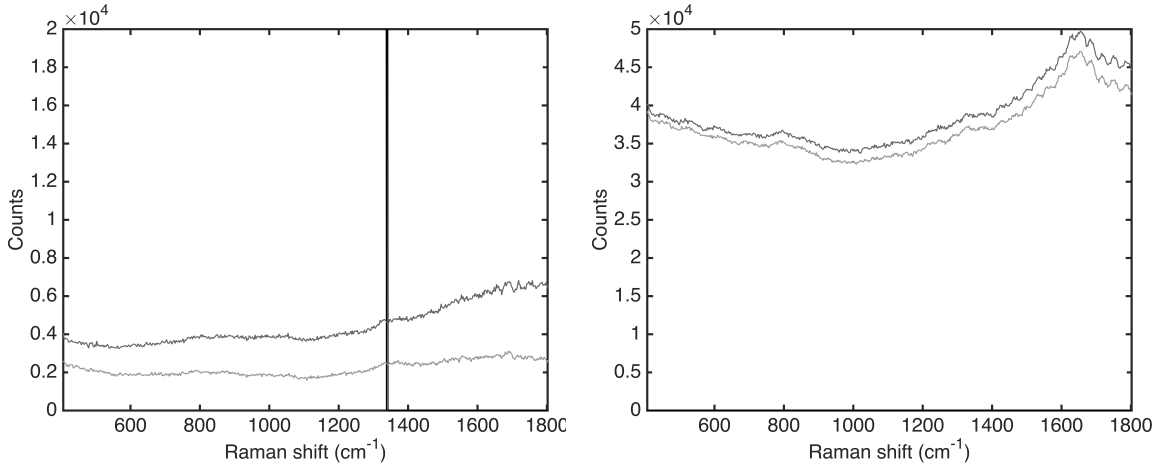
channel dimensions to 207 μm wide and 75 μm deep. This chip is shown in Figure 5.11. Again, roughness and minor cracks are visible at the channel edges, as shown in Figure 5.11b.

The background Raman spectrum collected with the 100x objective is shown in Figure 5.12a. The background spectra have no obvious peaks from the chip substrate only contain background fluorescence. The fluorescence is relatively high and is likely due to rough channel wall and base surfaces as a result of the machining process. High fluorescence means that background spectra collected near the channel base are saturated. Fluorescence reduces as the laser spot is moved away from the channel base, suggesting a deep channel with cell spectra collected at mid-depth or even a bit higher is ideal for spectral acquisition. Spectra collected with the 60xw objective (Figure 5.12b) contain higher background fluorescence compared to spectra collected



(a) **(b)**

Figure 5.11: MgF_2 system. MgF_2 system (a) and 20x microscope image of a microchannel (b).



(a) **(b)**

Figure 5.12: MgF_2 background spectra. Background spectra collected from the top (light grey), middle and bottom (black) of the MgF_2 system using a 100x dry objective (a) and 60x water immersion objective (b).

with the 100x objective, as expected. Again, the spectrum collected at the base of the channel was saturated at 100% laser power for 10x acquisition. A cell spectrum collected in the MgF_2 channel is shown in Figure 5.13. Several characteristic cell peaks are present in the difference spectrum, especially at wavenumbers below 1000

cm^{-1}.

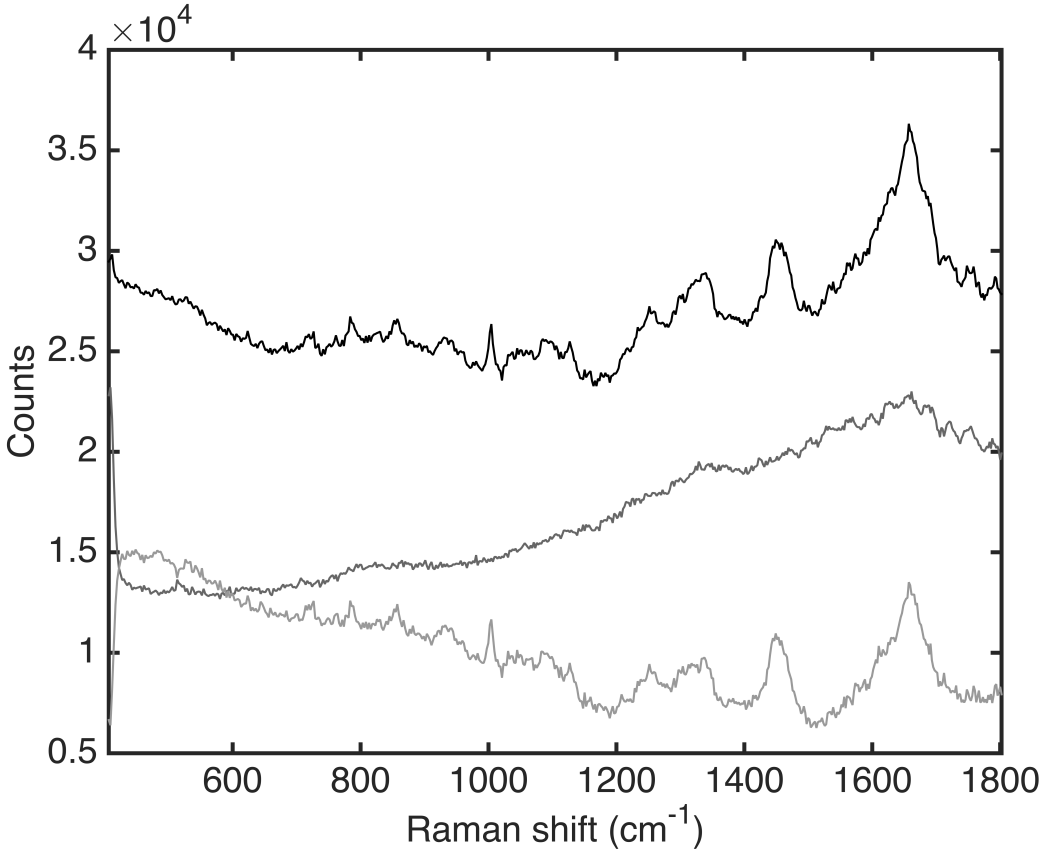
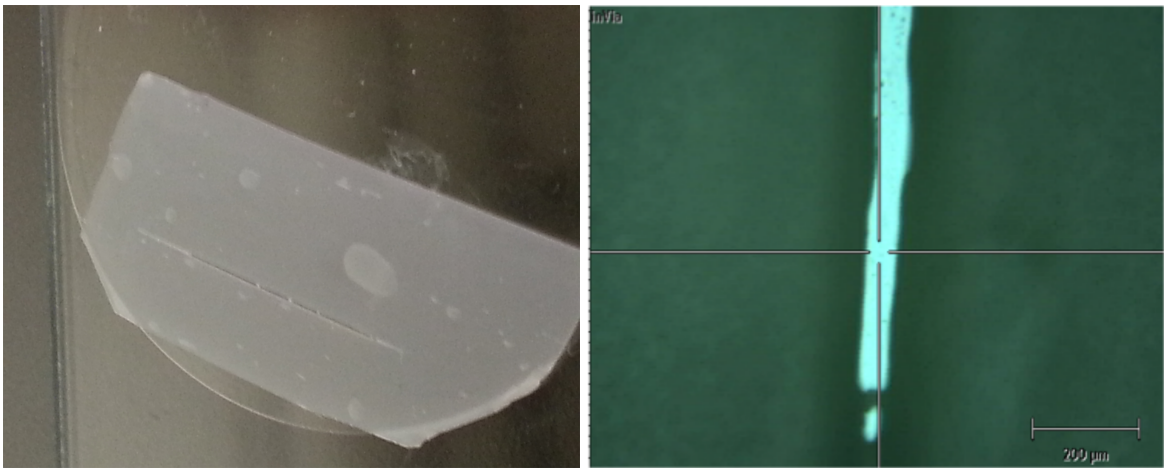


Figure 5.13: MgF_2 cell spectra. Raman spectrum of a cell within a MgF_2 microchannel (black), corresponding background spectrum and difference spectrum (light grey). Collected using the 60xw objective.

5.3.4 Parafilm-MgF_2 system

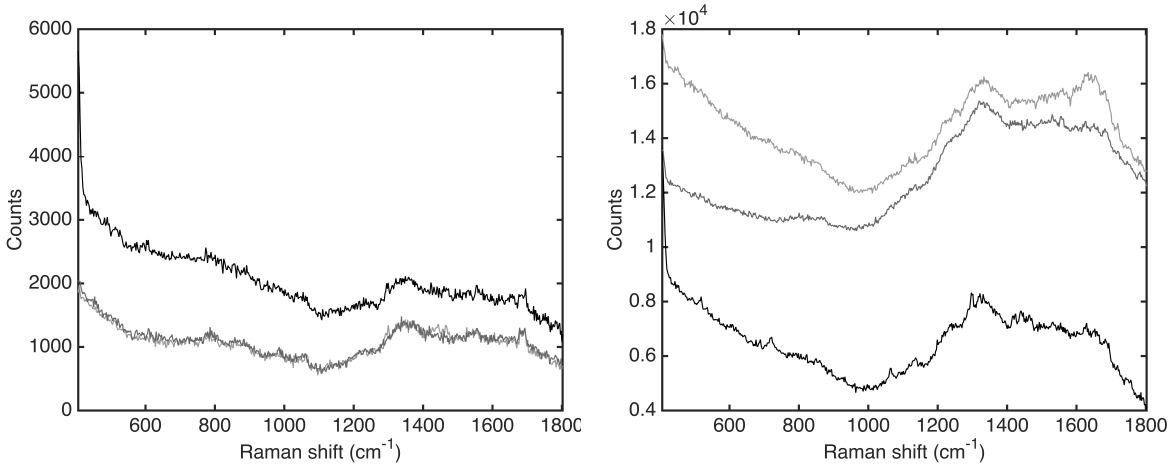
The Parafilm-MgF_2 chip and magnified view of the channel is shown in Figure 5.14. The background from this chip in both the 100x (5.15a) and 60xw cases (Figure 5.15b) is highly reproducible and contains mostly fluorescence from the objective its self. A characteristic MgF_2 peak is present at 410 cm^{-1} which reduces in intensity as distance from the channel base (which is made of MgF_2) increases. The presence of this peak is not of concern for radiobiological Raman studies because the lowest wavenumber of interest in previous work is around 450 cm^{-1} [132].

A typical cell spectrum collected from the Parafilm chip is shown in Figure 5.16. The



(a) **(b)**

Figure 5.14: Parafilm-MgF_2 system. Parafilm-MgF_2 system (a) and 20x microscope image of a microchannel (b).



(a) **(b)**

Figure 5.15: Parafilm-MgF_2 background spectra. Background spectra collected from the top (light grey), middle and bottom (black) of the Parafilm-MgF_2 system using a 100x dry objective (a) and 60x water immersion objective (b).

difference spectrum shows several characteristic cell spectral features. In addition to those observed in the PDMS cell spectrum, characteristic peaks at wavenumbers below 100 cm^{-1} (720, 857, 937 cm^{-1}) are also visible, due to the favourable background spectrum of the chip in this region compared to that of PDMS.

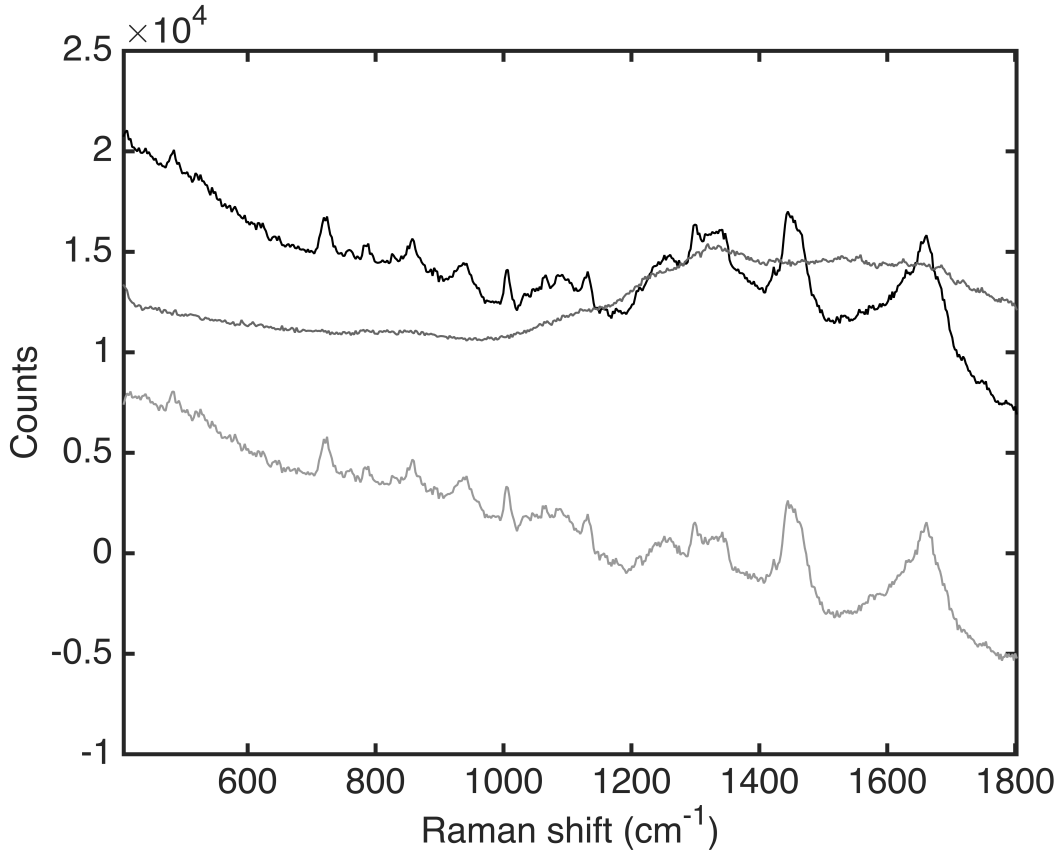


Figure 5.16: Parafilm-MgF_2 cell spectra. Raman spectrum of a cell within a Parafilm-MgF_2 microchannel (black) and corresponding background spectrum. Collected using the 60xw objective. The difference spectrum between the two is also shown (light grey).

5.4 Discussion

Four unique microfluidic systems were designed and evaluated for spectral characteristics of single cells within a microchannel. Manufacturing considerations varied from one system to the next and could be achieved with varying degrees of complexity.

The PDMS system was very easy to manufacture, with the entire process taking only 24 hours to complete. A reasonable degree of sealing can be obtained between the MgF_2 coverslip and PDMS upper surface purely by contact forces, but whether or not this could be maintained under high pressures involved with microfluidics is unclear. Unfortunately, the PDMS system produced spectra that were highly contaminated in key regions of interest for single cell studies and particularly for radiobiological work.

While this system could be cleaned and reused, the poor spectral quality makes this system a poor choice for radiobiological applications in its current state.

The process of coating gold on PDMS microsystems is not a difficult task, but does require access to specialized equipment. Beyond this, the natural contact sealing between the MgF_2 coverslip and surface of the Au-PDMS chip is poor. Therefore techniques for sealing this device would need to be investigated if this were to be used as a microfluidic system. The Au-PDMS chip is not reusable because it is difficult to fully remove all cells from the channels when soaking with suitable cell-cleaning materials such as ethanol or trypsin. More vigorous cleaning approaches such as sonication could prove to be valuable for cleaning the Au-PDMS system, however such vigorous techniques do not work well with the delicate gold coating.

In terms of spectral considerations, the background spectra collected in the Au-PDMS system have poor reproducibility. This means that throughout the channel and from one acquisition to the next, the background spectra will have different peaks present at varying intensities. This may be due to enhancing effects with the gold layer, and inconsistencies in what signal is enhanced each time. Also, inconsistent PDMS coverage with the gold may be contributing to the lack of reproducibility. Fixing the position within the channel in which cell spectra are collected could help to improve these inconsistencies. When 10 s of photobleaching as well as 100% laser power is used to collect spectra for 10 s, air bubbles form in the channel during acquisition. This is likely due to light reflections which pass through the constituents filling the channel many times, leading to heating, evaporation and formation of an air bubble. Evaporation effects can be avoided by reducing the laser power and not photobleaching. Due to a lack of reproducibility, persistent presence of PDMS peaks and increased background this design is a poor choice for radiobiological cell studies.

The main source of spectral contamination in the case of MgF_2 system was the roughness of the channel from machining which lead to high spectral background. However, cell spectra obtained from this system contain all of the key spectral features for cell studies with no impeding substrate-based contamination. While the MgF_2 system produced favourable spectral results, there are key issues with the manufacturing of this system. In particular, the time required to etch the 15mm long channel with dimensions 207 μm wide and 75 μm deep is about 10 hours. This time expense is less than ideal. Furthermore, sealing procedures were not implemented in this design

and would need to be developed. There is currently no known way to directly fuse two pieces of MgF_2 together. Some possible suggestions include bonding the pieces together using a suitable epoxy (e.g. Norland Optical Adhesive UV cured epoxy) and clearing the channel with a solvent or direct bonding and annealing. Therefore, despite the appealing spectral features of the MgF_2 system, the cost and manufacturing hurdles make this system less than ideal.

In contrast, the Parafilm-MgF_2 chip is relatively easy to fabricate. A second prototype intended to specifically test sealing this device was made using 1 mm thick glass slides as the base and top layers of the chip. Holes were formed in the Parafilm to catch fluid injected into the chip, and holes were drilled into the glass coverslip using a diamond drill (1.7 mm drill diameter). Injection tubing of 1/16" outer diameter was attached to a syringe using a female luer system for fluid injection and withdrawl. Sealing the injection tubes to the chip was initially carried out by using hot glue on the glass slide. Future sealing techniques could involve Oxygen Plasma sealing PDMS cubes with 1/16" holes punched into it, onto the glass surface above the holes in the glass and directly fitting the tubing into those PDMS holes. This system showed successful sealing between the glass slides and Parafilm, which was obtained purely through heat moulding of the Parafilm to the glass. This could be replicated with MgF_2 slides as well. Furthermore, Parafilm could possibly be replaced by another polymer or plastic that could be used to form the walls, while the window and base of the system are made out of MgF_2. It appears this window/base requirement is sufficient for controlling spectral quality. Therefore, this design has sufficient ease of manufacturing and promise for continued investigation. In terms of spectral quality, the Parafilm-MgF_2 system did not suffer from high levels of contamination and key cell spectral features were present.

5.5 Concluding statement

A Parafilm-MgF_2 microfluidic system was found to yield excellent cell Raman spectra while still offering relative ease of manufacturing compared to pure MgF_2 and PDMS based systems. While further manufacturing considerations will be important to move this design forward, specifically in making tube connections, there is a significant amount of potential for this device.

Chapter 6

Raman Spectroscopic Study of Irradiated Tumours: Non-Small Cell Lung Cancer

6.1 Preface

Content in this chapter is reproduced with permission from Nature Publishing Group, and has been published with the following citation:

> S.J. Harder (nee Van Nest), M. Isabelle, L. DeVorkin, J. Smazynski, W. Beckham, A.G. Brolo, J.J. Lum, A. Jirasek. Raman spectroscopy identifies radiation response in human non-small cell lung cancer xenografts. *Scientific Reports*, 6:21006, 2016.

This work was carried out using mouse Cohort A. The candidates role in the work presented in this publication includes assisting with experimental conception, design and set up, assisting treating mice on LINAC, assisting harvesting tumours. Collecting all Raman spectra, analyzing and reporting figures on all Raman results. Writing the initial manuscript draft for co-authors to review.

Experimental conception: AGB, AJ, JJL, MI, SJVN
Experimental design: AGB, AJ, JJLM LD, MI, SJVN, WB
Performed experiments: JS, LD, MI, SJVN, WB

Analyzed data: AGB, AJ, JJL, MI, SJVN
Made figures: MI, SJVN
Writing of manuscript: MI, SJVN

6.2 Introduction

Lung cancer is the second most common cancer in both men and women, accounting for 13% of all new cancers and 27% of all cancer deaths in Canada [250]. Surgical resection may be an option for early stage NSCLC and, in some cases, post-operative RT may be indicated. However, lung cancers in more advanced stages may not be candidates for surgery because of limiting factors such as tumour size, location, lymphatic involvement and the patients overall health status. In these cases, definitive RT may be used as an alternative treatment option. Radiation therapy uses high energy ionizing radiation to destroy diseased tissues while minimizing damage to healthy tissues. For NSCLC, typical definitive RT total doses are on the order of 60 Gy, delivered in 2 Gy fractions [251]. Patients with locally advanced NSCLC undergoing definitive RT showed 1 year survival rates of 18% in a randomized control trial evaluating the role of RT compared to chemotherapy or observation [252, 253]. Those patients who do not respond successfully to definitive RT may benefit from pre-screening techniques to assess radiation resistance or sensitivity, allowing further guidance in selecting an appropriate treatment regimen for the individual.

Paramount to successful RT treatment is the degree of radiosensitivity or radioresistance associated with a specific patients disease. Several factors can influence the extent of tumour response to radiation and, hence, successful outcome of RT including intrinsic radiation response of the tumour cells and the surrounding tumour microenvironment [163, 254]. As a consequence, there is currently no accepted technique to predict patient radiosensitivity or radioresistance. The ability to determine tissue radioresponse for a given patient would be a major step towards improving treatment outcome in radiotherapy. Predictors of cellular radiation response including DNA break repair [54], chromosome aberrations [55], apoptosis [56], hypoxia [255–257], cancer stem cell content [258] and genetic biomarkers of radioresistance [259, 260] have been previously investigated. These techniques can elucidate some of the im-

portant factors involved in resistance to radiotherapy in tumours. However, none of these techniques have been adopted in the clinic; presumably because many of them suffer from considerable limitations for clinical implementation, including tumour type specificity, invasiveness (requiring biopsy of tumour tissue) as well as cost in time and labour.

RS is a minimally invasive optical technique with the potential for pre-treatment characterization and early monitoring of biomolecular changes related to radiation response within tumour cells and tissues [105, 132, 135, 139, 141, 261, 262], providing opportunities for personalizing RT treatments. Raman spectra of biological materials in the 400-1800 cm^{-1} range yield a fingerprint of the sample's biomolecular content. Raman spectroscopy can therefore be applied to detect cellular changes resulting from metabolic processes and offers the potential to identify radiation-induced responses of tissue in a label-free and non-destructive manner [96, 217]. Raman spectroscopy has been used previously to study the effect of proton irradiation on mouse, swine, human tumour model xenograft and human basal cell carcinoma [142], and irradiated and unirradiated mouse brain tissue [143]. Vidyasagar et al., demonstrated that RS and unsupervised PCA on first derivative spectra could discriminate between responding and non-responding cervical cancer tissues collected post RT [140]. More recently, Yasser et al., used RS to show spectral differences in radioresistant oral cancer sublines [139]. These studies demonstrate the potential of RS to predict radioresistance and possible application of RS as a prognostic tool in cancer care and treatment.

Raman spectroscopy has been used to elucidate a radiation response in human epithelial tumour cell lines *in vitro* (NSCLC, breast, prostate), following exposure to single fractions (15, 30 or 50 Gy) of 6 MV photons [105, 135]. These studies also showed that RS was able to separate radiation-induced spectral changes from other simultaneously occurring sources of spectral variability, such as cell cycle. In a more recent study [132], human epithelial tumour cell lines irradiated with clinical doses of ionizing radiation (2-10 Gy) were analyzed *in vitro* (NSCLC, breast, prostate) using RS. This study further elucidated significant Raman biomarkers that could potentially be used to predict radioresistance in human tumour cells, including a dramatic increase in glycogen-related Raman spectral features following exposure to a dose of 2 Gy *in vitro* for the H460 NSCLC cell line. This response was validated using biochemical assays to show the accumulation of glycogen post-radiation, suggesting that glycogen may serve as a potential biomarker for radioresistance in human tumour cells studied

in vitro [263].

Unlike *in vitro* models, the tumour tissue microenvironment is a complex population of cell types (including lymphocytes, erythrocytes, stromal cells, fibroblasts and signalling molecules) as well as supporting tissue framework such as blood vasculature and extra-cellular matrix (ECM). This cellular heterogeneity has major consequences on tumour cell growth and progression as well as tumour response to cancer therapy, such as RT. Moreover, the metabolic constraints of low oxygen tension (hypoxia) [164, 264], has a classical role in radioresistance. Recently there has also been evidence to suggest the tumour-immune microenvironment has an effect on response to radiotherapy [265], leading to immune response modification in order to enhance the efficacy of RT in cancer therapy. In the current study, we demonstrate the value of RS for identifying radiation responses even in the presence of the complex tumour microenvironment and its associated effects on radiation response. This was achieved by studying NSCLC tumour xenografts exposed to ionizing radiation, using RS in combination with PCA. This study represents the novel application of RS to identify biochemical signatures of radiation response to clinical doses of ionizing radiation in human NSCLC tumour xenografts irradiated *in vivo*, warranting further investigation of primary tissue specimens from patients receiving RT and providing new opportunities for personalizing treatment.

6.3 Materials & methods

6.3.1 Cell lines and tumour xenografts

All animal procedures were approved by the University of Victoria Animal Care Committee and were performed in accordance with the Canadian Council on Animal Care. 6-8 week-old NOD.CB17-Prkdc^{scid}/J female mice were obtained from BCCRC Animal Resource Center (Vancouver, BC, Ca). Animals were housed in microisolator cages, and allowed access to food and water *ad libitum*. Animals were acclimatized for 1 week prior to study initiation.

The animals were anesthetized by isoflurane inhalation (1-3% for maintenance; up to 5% for induction) in oxygen from a precision vaporizer. The fur from the flank

of animals was shaved before tumour cell implantations. The human NSCLC cell line H460 (purchased from American Type Culture Collection, Manassas, VA, USA, ATCC # HTB-177, passage # 4, not listed as misidentified, tested pathogen-free with Charles River Laboratories, Montreal, QC, Ca) at a concentration of 5×10^6 cells in 0.1 ml PBS, were injected subcutaneously in the right flank of each animal.

6.3.2 Tumour irradiation and harvesting

Pre-determined exclusion criteria disqualified animals from receiving radiation treatment and continuing on in the study if the tumour was above 12 mm or below 10 mm. Tumours were measured three times per week with digital calipers and animals were randomized into treatment groups once their tumour size reached the pre-determined acceptable tumour size. To reduce any possible nosocomial infections during irradiation, a broad spectrum antibiotic (Enrofloxacin) was added to the drinking water 10 days prior to RT and the mice remained on this prophylaxis treatment until the end of the study. No blinding of the investigators to radiation dose received by a given mouse was done.

Once tumour sizes reached 10-12 mm diameter, the mice were prepared for tumour irradiation. Each mouse was anesthetized using a single IP injection of Ketamine/Dexdomitor mixture, dosed appropriately for body weight using 50 $\frac{\text{mg}}{\text{kg}}$ Ketamine and 0.5 $\frac{\text{mg}}{\text{kg}}$ Dexdomitor. After confirmation of anesthesia using a firm toe pinch, individual mice were placed into a custom-designed restraining acrylic chamber and a 10 mm non-toxic removable dental wax bolus was placed over the irradiation area. This chamber was placed near the isocentre of a Varian Truebeam STx LINAC (Varian Medical Systems Inc., Palo Alto, CA, USA). For radiation delivery, treatment dose plans utilizing parallel-opposed beam geometries were developed for tumour diameters of 10-15 mm using a phantom mouse and Eclipse (version 11) treatment planning software (Varian Medical Systems Inc.). The posterior base of the mouse tumour was aligned with the treatment isocentre using the OBI feature of the Varian Truebeam linear accelerator. Irradiations were carried out using a 6 MV photon beam with a nominal dose rate of 6 $\frac{\text{Gy}}{\text{min}}$ at isocentre. Depending on the treatment group, single fractions of 0, 5 and 15 Gy were delivered to the tumour tissue. Following irradiation, the mice were given 1 $\frac{\text{mg}}{\text{kg}}$ Atipamezole sedation reversal IP and mice were allowed to recover with thermal support.

Three days post-irradiation, mice were euthanized and tumours were removed. Tissue for Raman spectral analysis was embedded in mounting medium (Tissue-Tek O.C.T. Sakura Finetek Europe B.V., NL), snap frozen in liquid nitrogen, and stored at 80°C.

6.3.3 Raman microscopy measurements of tumour tissue

Tumours were prepared into 20 μm sections using a rotary microtome (HM 550; MICROM International GmbH, Walldorf, Ge) and placed on magnesium fluoride slides. Just prior to Raman measurements, these frozen sections were air-dried for 10 minutes. A Renishaw inVia Raman Microscope (Renishaw Inc., Illinois, IL, USA) coupled to a 785 nm diode laser (Renishaw) and dry objective (100×, NA=0.9) (Leica Microsystems, Wetzlar, Ge) was used to collect Raman map spectra. Spectra were registered using a thermoelectrically cooled CCD detector (Andor Technology, Connecticut, USA). The laser sampling dimensions were $2\times5\times10$ μm^3 and a laser power density at the sampling volume was 0.5 $\frac{mW}{\mu m^3}$. Spectra were acquired for 20 seconds per point, covering a spectral range of 460-1800 cm^{-1}.

A total of twelve mice were studied, with four mice in each dose group (0, 5 and 15 Gy). Animal sample size was selected to follow similar population sizes from previously published Raman studies involving animals and radiation exposure [143]. Five to eight unique mapping regions (map areas are between 100-220 μm^2, step size 15 μm) were analyzed over three tissue sections per mouse; resulting in a total of 6648 spectra prior to spectral processing. This experiment was repeated twice in the lab, however representative results from one of the studies is presented.

6.3.4 Spectral processing and statistical analysis

Spectra containing cosmic rays and obvious outliers (e.g. saturated spectra) were manually identified and removed from the data set. Following outlier removal, the data set contained a total of 6280 spectra. In-house algorithms were used to estimate and subtract spectral baseline arising from the substrate and biological fluorescence, shift spectra to account for calibration drifts during data acquisition, and normalize spectra to the total amount of biological material within the sampling volume, as previously outlined [266].

Baseline removal was carried out independently for each spectrum, using a modified signal removal method, tested and described in detail elsewhere [221]. Briefly, the baseline of a spectrum is initially estimated using a Savitzky-Golay zero-order filter. Spectral points with values above the estimated baseline are identified and subsequently reduced by a pre-specified amount to yield a residual spectrum. This residual spectrum is used to produce a new estimate of the baseline using the Savitzky-Golay filter and the process is reiterated over a pre-determined number of iterations. Following baseline removal, individual spectra were normalized to the total area under the baseline corrected spectrum.

Spectral shifting was carried out using the phenylalanine peak located at 1003 cm^{-1}, as described in detail elsewhere [133]. Briefly, the central wavenumber of the phenylalanine peak is identified for each spectrum using a Gaussian fit. The phenylalanine peak location in the spectrum to be shifted is compared to the peak location of the reference spectrum (difference was always less than 1 cm^{-1}) and a point-by-point interpolation of the spectrum is used to shift the spectrum by the required amount. This process is iterated twice, resulting in alignment of the phenylalanine peaks for the reference spectrum and shifted spectrum.

Principal component analysis, was used to separate out those components of the spectral dataset which contain variability due to radiation exposure and those contributed from other sources. Tukey style box plots, showing median PC score and 25^{th} and 75^{th} percentiles are used to represent PCA results for a given tumour and for a dose group (data set is comprised of all usable processed spectra from all tumours receiving the same dose). The most extreme data points, defined by the PC score closest to 1.5*(75^{th} percentile-25^{th} percentile) are represented by the whiskers in the box plots, and outliers (PC scores greater than the whiskers) are left off of the plots to improve clarity. Notches indicate the 95% confidence interval on the median, approximated assuming a normal distribution, but is accurate for large samples of other distributions as well [230]. The 0 Gy dose group has a sample size of n=2032 spectral points (n=436, 605, 557, 434 for each of the tumours), 5 Gy dose group n=2279 (n=755, 681, 437, 406 for each of the tumours) spectral points, 15 Gy dose group n=1969 (n=557, 552, 432, 428 for each of the tumours) spectral points.

Statistically significant shifts in PC score over a single tumour as well as over the entire dose group was tested using a two-sided Wilcoxon rank sum test to a 5% significance

level. The chi-square statistic of a Kruskal-Wallis test was used to estimate the relevance of the PCs in describing variability related to radiation dose (a non-parametric replacement for the f-statistic from a one-way ANOVA). The Kruskal-Wallis test is an extension of the Wilcoxon rank sum test beyond two groups. Both tests assume similar standard deviation among the test populations, a condition that is satisfied by the test populations examined. Comparison between *in vitro* and *in vivo* experiments was done using a Pearsons r value calculation.

6.3.5 Periodic acid-Schiff staining

periodic acid-Schiff (PAS) staining was performed using PAS reagent kit (Cat # 395-1; Sigma Aldrich, St. Louis, MO, USA). In this study, tumour tissue from a mouse irradiated with 15 Gy and unirradiated control tumour are presented. Mouse liver tissue was also studied using PAS staining, to act as a positive control for glycogen. Frozen tumour tissue was cut into 10 μm sections using a Rotary Microtome (HM 355 S; MICROM International GmbH, Walldorf, Ge) and adhered directly to a glass slide. Slides were fixed in 10% buffered formalin for 30 minutes at room temperature, washed three times in PBS, then rinsed in deionized (DI) water. Samples were then exposed to 1% periodic acid at room temperature for 5 minutes followed by three washes in DI water. Samples were stained with Schiff reagent for 15 minutes at room temperature, followed by a wash under running water for 10 minutes and a quick rinse in DI water. Samples were then dehydrated in 95% ethanol for 1 minute followed by three sequential submersions of the tissue in 100% ethanol. Eco-Mount mounting medium (Biocare Medical, Concord, CA, USA) was used for slides and imaged under bright field microscope at 20× magnification. Diastase (alpha-amylase) digestion (0.5%) was used to remove glycogen from samples providing a negative control.

6.3.6 Code availability

All computer code (to carry out spectral processing, data analysis, statistical testing) was derived from standard algorithms in Matlab (Mathworks, Natick, MA, USA), version R2014B, and can be accessed through this program.

6.4 Results

6.4.1 Principal components and score trends with radiation exposure.

Mice were implanted subcutaneously with 5×10^6 H460 cells, a human derived NSCLC model. When tumours reached 10-12 mm a 6 MV photon beam was used to irradiate the tumours *in vivo*, to doses of 0, 5 or 15 Gy. Tumours were harvested three days post-irradiation and Raman spectral maps were collected and analyzed using PCA. Principal component analysis is a widely-used multivariate analysis technique that can discriminate Raman spectra originating from biological systems [135, 140, 262, 267, 268]. All three dose groups were simultaneously analyzed using PCA, in order to reduce the spectral data set to a smaller number of variables (PCs) that describe the majority of the variance in the spectral data set. Therefore, PCs with high contribution to the variance in the data set indicate spectral features that significantly influence the separation of spectra among the different dose groups. In this study, 90% of the total variance in the data set can be described by considering the first five PCs.

Principal components that exhibit PC score trends related to radiation exposure were identified using the chi-square statistic of a Kruskal-Wallis test. This statistic uses the PC scores labelled with their associated dose group to characterize the ratio of inter-group variability to intra-group variability. The largest chi-square values among the first five PCs were attributed to PC1 (670) and PC2 (574), with the next largest chi-square value being over 70% smaller. The chi-square values of PC1 and 2 indicate considerable inter-group variability, suggesting the variability described by these PCs can be linked to radiation exposure. The PCs represent differences between spectra with varying PC score, as previously demonstrated [132]. Due to the overlapping nature of Raman bands originating from different biomolecular entities in the spectra of biological cells and tissue, particular care has been adopted in interpretation of single peaks within a PC. Single spectral bands in a PC are only assigned to a specific chemical entity when other bands associated with that entity are also present on the same side (positive or negative) of the PC.

The first principal component (PC1) isolated from the Raman data set (Figure 6.1a)

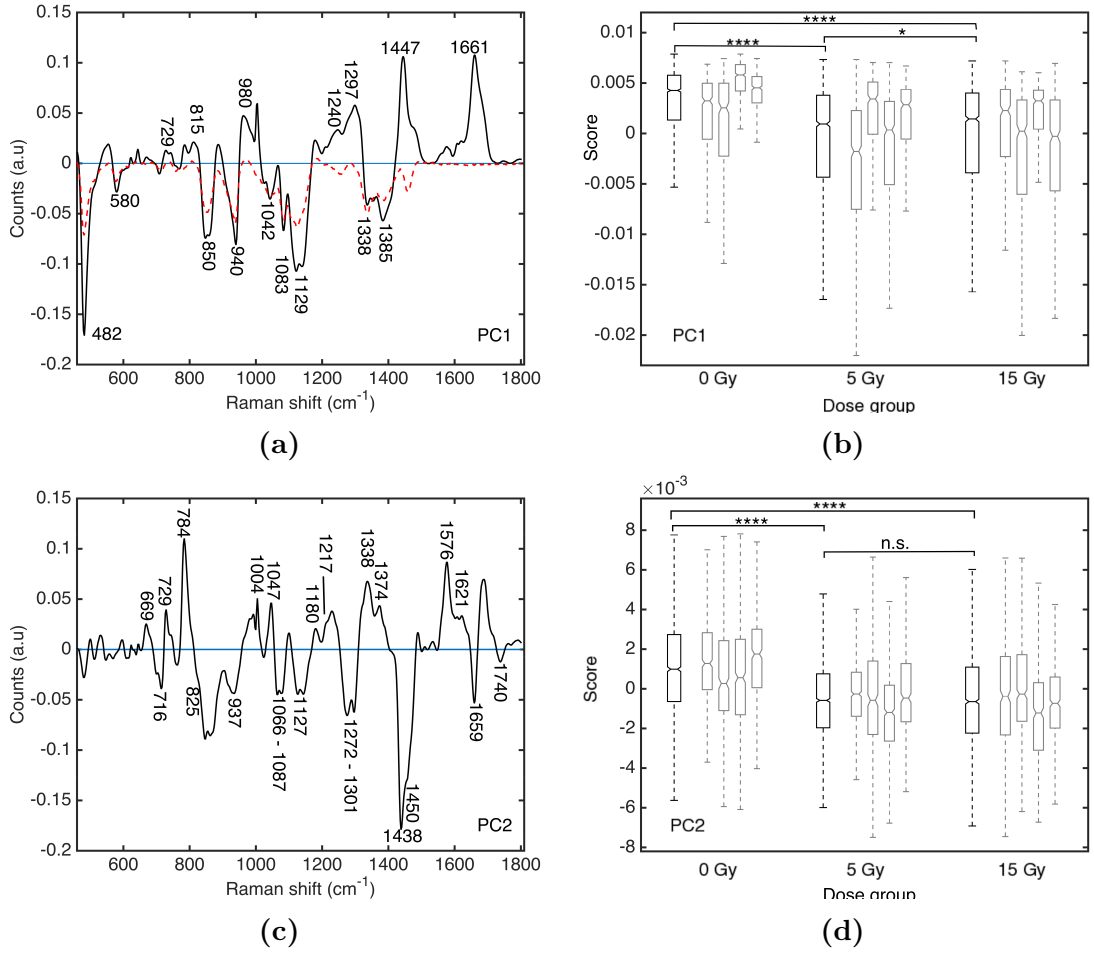


Figure 6.1: Radiation related Raman spectral changes identified using principal component analysis. Principal components (PC) 1 (a) and 2 (c) from H460 tumour tissue and corresponding PC score box plots (Tukey style box plot, outliers left out for clarity, notches indicate 95% confidence interval for the median) for PC1 (b) and PC2 (d). A statistically significant shift to more negative median PC1 and PC2 score was found for irradiated tumours compared to unirradiated tumours. Dashed red line in (a) corresponds to the Raman spectrum of pure glycogen (inverted, sample obtained from Life Technologies Inc., Burlington, ON, Canada). Black boxes represent PC score for all spectra collected over four tumours in a single dose group (15 Gy; n=1969, 5 Gy; n=2279, 0 Gy; n=2032). Grey boxes represent PC score for all spectra collected for an individual tumour. Statistical significance was tested using a two-sided Wilcoxon rank sum test to 5% significance level, ****p-value $\leq$ 0.0001, *p-value $\leq$ 0.05, n.s. not significant.

contributes to 69.9% of the total variance in the data set. Detailed Raman band assignment for PC1 can be found in Appendix A Table A.1, indicating positive features

arising from proteins and lipids and negative features from glycogen. In particular, strong positive features at 1661 cm^{-1}, 1447 cm^{-1} and from 1240-1297 cm^{-1} can be linked to Amide III (random coil, β-sheet and α-helix) and Amide I α-helix contributions in proteins, overlapping carbon-hydrogen (CH) vibrations in protein and lipids and carbon-carbon (CC) vibrational modes in lipids. Negative features in PC1 at 482 cm^{-1}, 850 cm^{-1}, 940 cm^{-1}, 1042 cm^{-1}, 1083 cm^{-1}, 1129 cm^{-1} and 1385 cm^{-1} can be attributed to glycogen.

Median PC score for a dose group was determined by evaluating the median PC score of spectra collected from all tumours exposed to a specific dose. Median PC1 scores from the 5 and 15 Gy dose groups (Figure 6.1b) show a statistically significant shift to more negative value relative to median PC1 score for unirradiated control tumours (p-value from Wilcoxon rank sum test of 9×10^{-122} for 0 Gy vs. 5 Gy dose group and 1×10^{-100} for 0 Gy vs. 15 Gy dose group). Median PC1 scores were found to be only slightly different between the 5 and 15 Gy dose groups (p-value of 0.045). This translates to an increase in the representation of negative features in PC1 for irradiated tumours compared to unirradiated controls. The proportion of spectra with negative PC1 scores is greater for irradiated (44% for 5 Gy, 41% for 15 Gy) tumours compared to the unirradiated controls (20% for 0 Gy). Furthermore, the PC1 score corresponding to the 25^{th} percentile is -4×10^{-3} for the 5 and 15 Gy dose groups and 1×10^{-3} for the 0 Gy dose group. Therefore, 25% of the spectra comprising the 0 Gy dose group have PC1 scores more negative than 1×10^{-3}, while in the 5 and 15 Gy dose groups 25% of the spectra have PC1 scores more negative than -4×10^{-3}. Taken together, these data indicate that there are more spectra with strong representation of the negative features outlined in PC1, in the irradiated tumour groups compared to the unirradiated controls. This tendency towards more negative PC scores corresponds to an increase in glycogen (negative features of PC1) relative to Amide III and I protein contributions and CH and CC vibrational modes in lipids (positive features) for irradiated compared to unirradiated tumours.

The second PC (PC2) isolated from the Raman data is shown in Figure 6.1c and contributes to 9.8% of the total variance in the data set. Detailed Raman band assignment for PC2 can be found in Appendix A Table A.2, indicating positive features associated with nucleic acids, tryptophan and phenylalanine and negative features associated with overlapping lipid and protein bands. In particular, strong positive bands are observed at 729 cm^{-1}, 1210 cm^{-1}, 1338 cm^{-1}, 1374 cm^{-1}, 1576 cm^{-1},

1621 cm^{-1} (tryptophan), 1004 cm^{-1}, 1047 cm^{-1}, 1180 cm^{-1}, 1210 cm^{-1} (phenylalanine), 669 cm^{-1}, 1328 cm^{-1}, 1342 cm^{-1}, 1374 cm^{-1}, 1576 cm^{-1} (guanine), 729 cm^{-1}, 1342 cm^{-1}, 1374 cm^{-1}, 1576 cm^{-1} (adenine) and 669 cm^{-1}, 784 cm^{-1}, 1365 cm^{-1} (thymine). Negative bands at 1066 cm^{-1}, 1080 cm^{-1}, 1127 cm^{-1}, 1284 cm^{-1}, 1450 cm^{-1}, 1460 cm^{-1}, 1659 cm^{-1} indicate overlapping protein (carbon-nitrogen (CN), CH and Amide III/I α-helix) and lipid (CC and CH) vibrational modes, with additional negative features at 716 cm^{-1} and 825 cm^{-1} indicating choline, as well as lipid bands at 1087 cm^{-1}, 1272 cm^{-1}, 1301 cm^{-1} and 1740 cm^{-1}.

Median PC2 scores over all spectra collected within a dose group (Figure 6.1d) also show a statistically significant shift to increasingly negative PC scores for irradiated tumours compared to unirradiated controls (p-value from Wilcoxon rank sum test of 5×10^{-109} for 0 Gy vs. 5 Gy dose group and 7×10^{-83} for 0 Gy vs. 15 Gy dose group). Median PC scores were not found to be significantly different between the 5 and 15 Gy dose groups (p-value of 0.65). Furthermore, the proportion of spectra with negative PC2 scores is greater in irradiated dose groups (63% for 5 Gy and 60% for 15 Gy) compared to unirradiated controls (34% for the 0 Gy). The PC2 score corresponding to the 25^{th} percentile is -2×10^{-3} for the 5 and 15 Gy dose groups and -6×10^{-4} for the 0 Gy dose group. Taken together, the irradiated dose groups contain a larger proportion of spectra with negative PC2 scores, and stronger expression of the negative features making up PC2, compared to the unirradiated controls. This suggests an increase in negative features attributed to choline and lipid (CC, CH)/protein (CN, CH, α-helix) relative to positive features attributed to nucleotides, phenylalanine and tryptophan for irradiated tumours compared to unirradiated control tumours.

Principal components 3-5 showed no considerable trends in PC score with respect to radiation exposure. Several sources of variability, such as tissue thickness and composition could manifest as contributing factors for these PCs. In summary, PCA indicates a radiation induced increase in glycogen relative to protein and lipid bands in PC1. Analysis also indicates an increase in lipid (including choline, CH, CC) and protein (CN, CH, α-helix) vibrational modes relative to nucleotides, phenylalanine and tryptophan in PC2.

6.4.2 Radiation-induced Raman differences in tissues correlate with *in vitro* signatures

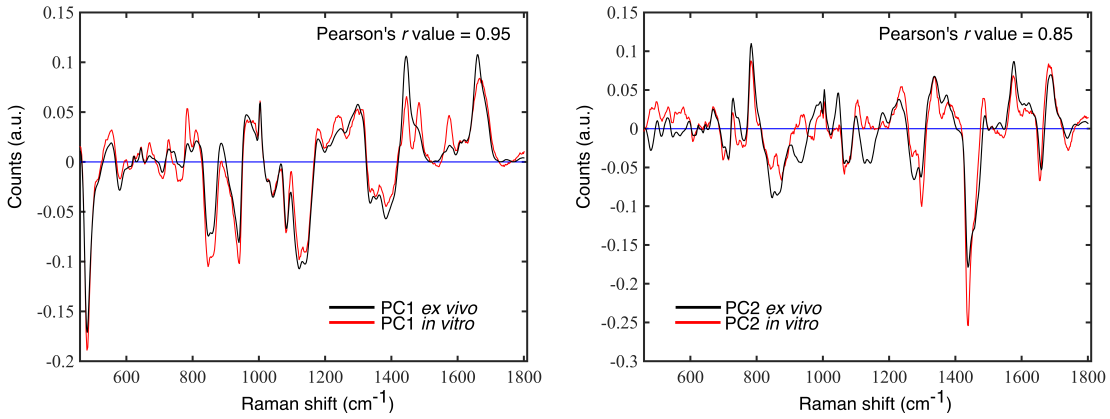
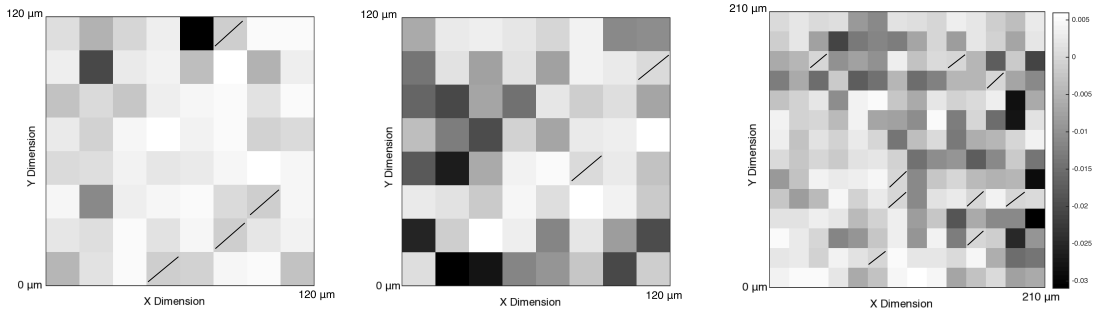


Figure 6.2: Comparison of principal components derived from Raman spectra of non-small cell lung cancer irradiated *in vitro* and *in vivo*. Principal component (PC) 1 (a) and PC2 (b) obtained for the current *ex vivo* study (black line) overlayed with the corresponding component obtained in a previous *in vitro* study on the H460 cell line. *In vitro* data was derived from principal component analysis on a Raman data set of H460 cells cultured an irradiated *in vitro* to doses of 0, 2, 4, 6, 8, 10, 30 and 50 Gy as presented and described previously [132]. Principal component 1 from this *ex vivo* study is highly correlated (Pearsons r value=0.95) to PC1 from the *in vitro* experiment, as is PC2 (Pearsons r value=0.85).

Figure 6.2 presents a comparison between the radiation related PCs identified in this *ex vivo* study and similar components identified in a previously published *in vitro* study on the H460 cell line (exposed to 2-50 Gy radiation doses). As shown in Figure 6.2a, there is a strong correlation between the first PC identified in the *in vitro* study [132] and the first PC identified in this *ex vivo* study (Pearsons r value=0.95). This suggests that the observed increase in glycogen content in irradiated tumours relative to unirradiated controls is consistent with *in vitro* studies using the H460 cell line. We also found a similar correlation between the second PC identified when compared to the *in vitro* study of H460 cells exposed to ionizing radiation [132] (Pearsons r value=0.85), as shown in Figure 6.2b.

6.4.3 Radiation-induced Raman signatures are expressed heterogeneously throughout tissue



(a) **(b)** **(c)**

Figure 6.3: Spatial maps of principal component (PC) 1 score at three unique regions within a single tumour irradiated to 15 Gy. The spatial variation of PC1 scores demonstrates tissue heterogeneity within an individual tumour. Map areas are 120 μm^2 for (a) and (b), 210 μm^2 for (c) and images are formed with 15×15 μm^2 pixels which correspond with the x and y step sizes during Raman map acquisition. Pixels with slashes indicate pixels for which no PC score information is available because the spectrum at that pixel was excluded from PCA (for reasons discussed in materials and methods section).

Principal component 1 score was plotted as a function of position for three unique regions of a tumour exposed to 15 Gy (Figure 6.3). Dark shaded regions indicate areas for which the Raman spectrum scored a relatively negative PC1 score, corresponding to a spectrum containing strong glycogen Raman bands. These maps demonstrate the diversity of PC1 score for the spectra collected within a tumour, and indicates heterogeneous spatial distribution of glycogen rich spectra within the tumour. The spread in PC score within a given tumour is a reflection of biochemical heterogeneity. During spectral acquisition, regions of visibly uneven tissue or necrotic areas within the section were avoided and maps were collected from select viable tumour regions. Therefore, despite visual consistency, large variations in biomolecular content appear to still be present. The observed intra-tumour heterogeneity in PC score is an indication that it is important to collect spectral maps from several locations within the tumour in order to avoid biasing the Raman spectral analysis of the sample.

6.4.4 Expression of radiation-induced Raman signatures varies among tumours

The median PC score for each tumour (each mouse) was calculated by determining the median PC score over all spectra collected from a single tumour, and is shown in Figures 6.1b and 6.1d. Among the four tumours studied in all three dose groups, median PC score was found to differ within the confidence interval on the median. For example, within the 0 Gy tumour group, median PC1 score for each of the four tumours (grey boxes, Figure 6.1b) was found to be $5.8 \pm 0.2 \times 10^{-3}$, $4.5 \pm 0.2 \times 10^{-3}$, $3.2 \pm 0.3 \times 10^{-3}$ and $2.5 \pm 0.5 \times 10^{-3}$. A two-sided Wilcoxon rank sum test (p-values$<$0.05) identified that PC1 score distributions associated with these four tumours segregate into three unique distributions. A similar analysis found that the four tumours belonging to the 15 Gy dose group segregate into three unique sub-groups, and in the 5 Gy dose group all four tumours had unique PC1 score distributions. This suggests there is a degree of variability in the expression of PC1 across different tumours. Two out of four tumours in each of the 5 and 15 Gy dose groups have median PC1 scores that overlap with median PC1 scores of a tumour in the 0 Gy dose group (within confidence interval on the median). Therefore, some tumours express the glycogen-related RS signature (PC1) more than others, highlighting the individual variability in terms of extent of expression of this signature.

Similar grouping of PC2 score distributions among tumours (grey boxes, Figure 6.1d) within a dose group was also observed. In this case, two unique tumour sub-groups formed per dose. Within confidence interval on the median, there was no overlap of the median PC scores between irradiated and unirradiated dose groups for PC2. This data further supports the observation that the extent of radiation-induced Raman spectral changes may be unique to an individual.

6.4.5 Glycogen accumulation confirmed using periodic acid-Schiff staining

To confirm the observed accumulation of glycogen in irradiated tumours, as indicated through PC1 score trends, we performed a PAS stain to visualize the total intracellular content of glycogen of tumour fragments that were harvested at three days

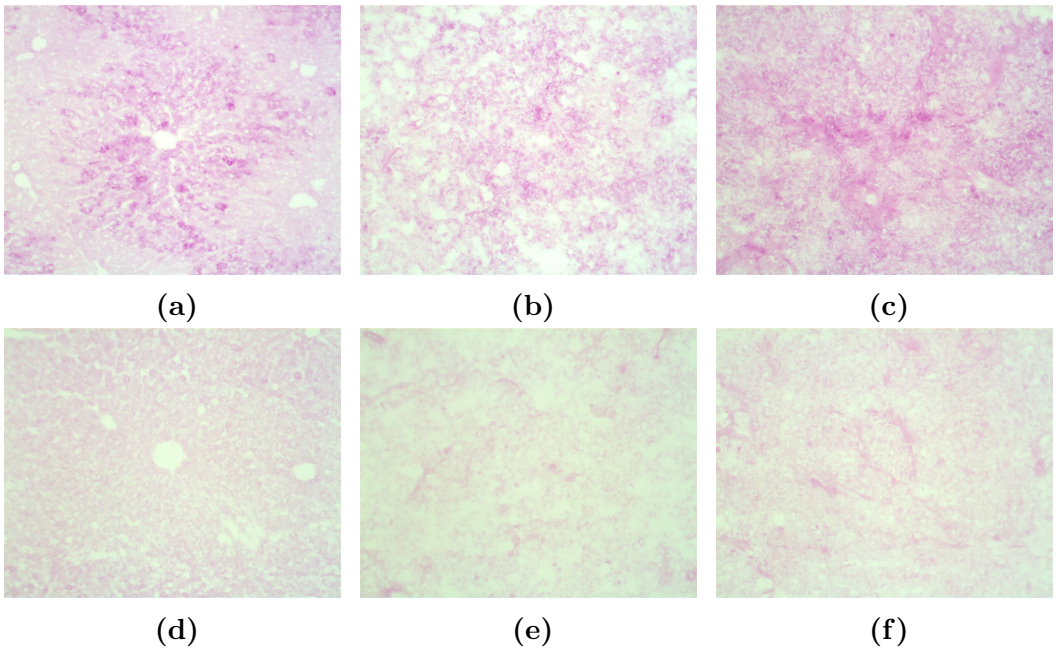


Figure 6.4: Periodic acidSchiff (PAS) staining images from irradiated and unirradiated tumour tissue and liver tissue control. A qualitative indication of increased glycogen content in irradiated (15 Gy) tissue compared to unirradiated (0 Gy) tissue was given by PAS staining. Images are collected at 20× magnification. PAS stained (a) Liver tissue (positive control) without diastase (alpha-amylase) and (d) with diastase. (b) Unirradiated control (0 Gy) H460 tumour tissue without diastase (alpha-amylase) and (e) with diastase. (c) Irradiated (15 Gy) H460 tumour tissue without diastase (alpha-amylase) and (f) with diastase.

post-irradiation. Normal liver tissue contains a large amount of glycogen and was used as a positive control. Intense PAS staining was observed in tissue sections of unirradiated control hepatocytes (Figure 6.4a). A weak but detectable PAS-staining of glycogen granules from tissue sections of an unirradiated tumour is shown in Figure 6.4b. In contrast to this, tissue sections from the 15 Gy irradiated tumour showed a strong PAS staining of glycogen granules (Figure 6.4c).

Diastase (alpha-amylase) was used to selectively digest glycogen prior to PAS staining (Figures 6.4d-6.4f). In all tissues examined, diastase reduced the intensity of PAS staining but did not fully eliminate it. This is due to background staining of other tissue constituents such as mucin, glycated proteins and basement membranes. Qualitatively, the difference in degree of PAS staining between digested unirradiated and irradiated tissue is less drastic than between undigested unirradiated and irradiated tissue, providing additional support for the observed accumulation of glycogen as a

metabolic response to irradiation, found using RS. Although there are disadvantages related to the specificity of the PAS stain, the distribution of PAS stained regions throughout the tissue further highlights the intra-tumoural spatial variability in PC1 score in Raman spectra measured throughout a given tumour.

6.5 Discussion

We have demonstrated the utility of RS in combination with PCA to detect radiation-induced biochemical changes in human NSCLC tumour (H460) xenografts. Analysis revealed unique radiation-related Raman signatures that can be linked to four major groups of biomolecules: nucleic acid, lipid, protein and carbohydrates.

The influence of radiation on nucleotide content was observed in PC2 through a radiation-induced reduction in Raman bands associated with guanine, adenine and thymine relative to protein and lipid spectral features. Principal component 1 did not contain peaks that could yield to an interpretable change in nucleic acid content.

Radiation-induced effects on lipid content were identified in PC1 as a reduction of CC and CH vibrational modes relative to glycogen. Furthermore, PC2 indicated a radiation-related increase in Raman bands associated with choline, CC, CH, and ester vibrational modes in lipids relative to nucleotide and protein bands associated with phenylalanine and tryptophan.

Analysis revealed radiation-induced effects on protein content in PC1 as a reduction in Amide III (random coil, α-helix and β-sheet) and Amide I α-helix bands relative to glycogen. Furthermore, PC2 identified a radiation-induced reduction in tryptophan and phenylalanine Raman bands. The second component also identified a radiation-induced increase in bands associated with CN and CH protein vibrational modes as well as bands associated with α-helix protein conformation, relative to features associated with nucleotides, tryptophan and phenylalanine.

Radiation-induced effects on carbohydrates were observed through PC1, which indicated an increase in glycogen spectral features in 5 and 15 Gy populations compared to unirradiated tumours. The second PC did not contain peaks that provided an interpretable change in carbohydrates within the tissue. The variety of radiation induced spectral changes observed over nucleic acid, lipid, protein and carbohydrate

content in this study indicate that multiple physiological or metabolic processes may be occurring within the tissue, in response to radiation.

Previous *in vitro* studies have linked the features in PC2 to variation in cellular nucleic acid, lipid and protein content as a result of variations in progression through the cell cycle [266]. However, unlike in this *ex vivo* experiment, segregation in PC score between irradiated and unirradiated populations was not observed *in vitro*. The segregation in PC2 score between irradiated and unirradiated populations may suggest a certain degree of cell cycle synchronization in the *ex vivo* case, however further studies are needed to assert this hypothesis.

The radiation-induced increase in glycogen containing spectra identified in irradiated tissue in this study, is consistent with *in vitro* studies carried out on the H460 cell line [132, 263] and was confirmed qualitatively using PAS stain. Furthermore, an earlier study reported a glycogen accumulation in brain tissue exposed to ionizing radiation [269], supporting our observations in this study. While the mechanisms for radiation-induced glycogen accumulation are not fully understood *in vitro*, a radiation-induced inactivation of GSK3β has been speculated to contribute to an increased capacity of glycogen synthase to produce cellular glycogen [263]. However, *in vivo* tumours comprise a significantly more complex system characterized by a heterogeneous microenvironment with an anisotropic distribution of hypoxic, glucose deprived and high lactate regions [163]. It is possible that the complex tumour physiology and biochemistry contributes to the mechanisms that yield the observed glycogen accumulation post RT. Specifically, hypoxic cells are more radioresistant than oxic cells [203, 270] causing oxic cells to be preferentially killed during RT. This leads to redistribution of blood within the tumour allowing for a degree of hypoxic recovery in irradiated compared to unirradiated tumours [264]. Glycogen accumulation has been shown to occur in brain tissue recovering from hypoxia [271], therefore this may be a possible explanation for increased expression of glycogen Raman spectral features in irradiated tumours.

The observed intra-tumour heterogeneities as well as the inter-individual variability in degree of expression of the glycogen Raman signature support the hypothesized link between increased glycogen post RT and hypoxia/hypoxic recovery. The tumour microenvironment is a complex mixture of different cell types and is characterized by drastic differences in pH, oxygen concentrations and nutrient distributions [164].

Intra-tumour heterogeneities in expression of the glycogen-related Raman signature may be a result of this inhomogeneity in microenvironment. Genetics and proteomics has unveiled crucial intra-tumour heterogeneities indicating evolutionary and protein function distributions which may affect prognostic evaluations of the disease [162,272]. Here, using Raman spectroscopic imaging, we uncover glycogen as a previously underappreciated factor to define a metabolic signature that may delineate intra-tumoural heterogeneity in NSCLC.

Tumour development (for example: vasculature development, cellular growth kinetics) plays an intrinsic role in determining the microenvironment of a tumour, including location and extent of regions of hypoxia throughout the tumour [163], and studies have shown that the degree of hypoxia can vary substantially among patients [270]. Since inbred mice are used as hosts and the tumour cells used in each mouse originate from the same source, inter-tumour variability may be linked to differences in microenvironment between tumours. Variations in the extent of hypoxia among individual mice and thus extent of hypoxic recovery following radiation exposure may therefore be an explanation for the variability in measured levels of glycogen for tumours exposed to the same dose of ionizing radiation. The observed inter-individual variability is further evidence of the unique radiation response associated with individuals based on their unique disease, and substantiates the notion of characterizing an individuals degree of radioresistance or sensitivity and personalizing RT because the metabolic response to radiation exposure is not the same for every individual.

6.6 Concluding statement

This study represents the novel application of RS to identify biochemical signatures of radiation response in human NSCLC tumour xenografts, irradiated *in vivo*. Multiple physiological or metabolic processes were measured within the tissue, in response to radiation, including a marked increase in glycogen spectral features in irradiated tumours. Spatial mapping revealed both intra- and inter-tumour heterogeneity in the distribution of glycogen and other RS spectral features. Collectively, these data demonstrate the utility of RS for detecting distinct radiobiological responses in human tumour xenografts, indicating the potential for future RS applications to monitor or predict radiation response in individuals.

Chapter 7

Radiation Effects on Tumour Metabolism in Non-small Cell Lung Cancer

7.1 Preface

The work in this chapter was carried out using mouse Cohorts A and C and is submitted for publication as of May 2018. The candidates role in the work presented in this chapter includes experimental conception, design and set up. Establishing tumours in the mice, monitoring mice tri-weekly, treating mice on the SARRP, harvesting tumours. Collecting all Raman spectra, analysis and reporting of results in figures, writing the initial manuscript draft for co-authors to review.

Experimental conception: AGB, AJ, JJL, LMN, SJVN
Experimental design: LMN, SJVN
Performed experiments: LMN, SJVN
Analyzed data: SJVN
Made figures: SJVN
Writing of manuscript: SJVN

7.2 Introduction

Radiation therapy plays a vital role in the management of NSCLC. Definitive RT is a standard treatment option for patients presenting with inoperable early-stage NSCLC [253,273–275] and a subset of patients with locally advanced stage III NSCLC [276–278]. Radiation therapy and chemotherapy is front line treatment for locally advanced NSCLC [277, 279], with one-year survival reported as low as 18% [253]. A meta-analysis of RT techniques for the treatment of medically inoperable early-stage NSCLC reported a 2-year overall survival estimate of 53% for conventional (60 Gy total, 2 Gy fractions) RT [280]. Improvements to radiation dose delivery and hypofractionation using SBRT have resulted in an improved 2-year survival of 70% [280]. Despite these advances local failure at 5 years following SBRT is reported as high as 20% [281]. This can be attributed in part to patient-specific heterogeneity both at the genomic and metabolic level of the tumour environment that leads to radioresistance and metastasis [273]. As such, better strategies for local control would mitigate these potential issues and improve clinical management in this setting. This includes consideration for biology-based treatment strategies [281] and individualized dose escalation [282] to address patient-specific heterogeneities.

Both intrinsic and extrinsic factors can influence tumour response and overall outcome of RT [254]. Hypoxia is a prominent feature in NSCLC and a well described characteristic of radioresistant tumours [205, 283, 284]. Biologically, hypoxia exerts pleiotropic effects on tumour cell biology with a key role of activating HIF-1, a transcriptional factor responsible for regulating cell survival, metabolism and invasiveness [205, 255, 270]. However, hypoxia is not a static event and cycles of hypoxia in different spatial regions of the tumour and throughout treatment can influence radiosensitivity, particularly when RT is given as fractionated doses [255, 264]. As a result of this regional distribution of oxygen, RT is cytotoxic to aerobically active cells. In contrast anaerobically active cells endure less radiation damage and can survive in order to resume growth and proliferation following reoxygenation [285].

Techniques to measure tumour hypoxia for prognostic value have been extensively investigated and include PET, tissue based assays relying on binding of 2-nitroimidazole drugs and polarographic needle electrode measurements [47,256,257]. However, additional factors affecting RT response beyond hypoxia may also warrant consideration. Nucleic acid break repair markers [54], circulating cell-free DNA [80] and genetic host

factors (e.g. single-nucleotide polymorphisms) [77, 79] have also been investigated as predictors of radiation response. Unfortunately, these techniques only assess a single indicator of the radiation response (e.g. hypoxia or DNA break repair). As such, they have not been implemented to monitor radiation resistance clinically, presumably due to limitations including insufficient clinical validation, invasiveness and cost.

Raman spectroscopy is a minimally-invasive, non-destructive and label-free optical spectroscopic technique that can track overall biomolecular changes in cells and tissue. These characteristics are favourable for biomedical applications and, in particular, allow for non-targeted monitoring of radiation resistance indicators in cells and tissue. Raman spectroscopy has shown promise as a way to monitor radiation response in a variety of systems including human lens epithelium [286], blood lymphocytes [141], oral [139], cervical [140], breast, prostate and lung cancers [132, 135, 287, 288]. In particular, applications of RS to NSCLC have revealed distinct radiation induced metabolic alterations in cells [132, 263] and tumour xenograft tissue [287]. These responses manifest as an accumulation of glycogen in irradiated samples when studied 72 hours post treatment. The observed glycogen accumulation was found to be associated with increased GSK3β and AMPKα signalling *in vitro*, however the dynamics within the tumour can be different and have not been investigated.

In this study, we investigate the nature of the radiation induced metabolic alterations observed in NSCLC tumour xenografts using RS. Modulations in glycogen levels within the tissue were observed, with lower levels of glycogen in irradiated samples after acute irradiation, and higher levels of glycogen in irradiated samples at later time points. These changes were stable and observed up to 10 days post treatment. Moreover, perturbations in the Raman glycogen signature are correlated to tumour regression and could be associated with radiation-induced reoxygenation. In irradiated tumours, low levels of glycogen co-register with hypoxia and subsequent increases in glycogen were found to track with reoxygenation following RT. Taken together, hypoxia and hypoxic recovery play a key role in radiation responses of NSCLC, making RS a valuable technique for measuring the radioresistance status of NSCLC.

7.3 Materials & methods

7.3.1 Cell lines and tumour implantation

All animal procedures were approved by the University of Victoria Animal Care Committee and performed in accordance with the guidelines set forth by the Canadian Council on Animal Care. NOD.CB17-Prkdc^{scid}/J female mice were obtained from BCCRC Animal Resource Center (Vancouver, BC, Ca). Animals were housed in HEPA filter microisolator cages within a bioexclusion containment room and allowed access to food and water *ad libitum*. Animals were acclimatized for 1 week prior to study initiation.

The human non-small cell lung cancer cell line H460 (purchased from ATCC, Manassas, VA, USA, ATCC # HTB-177, passage # 3, not listed as misidentified, tested pathogen-free with Charles River Laboratories, Montreal, QC, Ca) was used in this study. Cells were cultured according to previously established protocols [132] and subsequently injected subcutaneously in the right flank of each mouse at a concentration of 5×10^6 cells in 0.1 ml PBS.

7.3.2 Tumour irradiation and harvesting

Pre-determined exclusion criteria disqualified animals from receiving radiation treatment and continuing in the study if the tumour volume was below 80 mm^2 or above 130 mm^2. Tumours were measured three times per week with digital calipers and animals were randomized into treatment groups once their tumour size reached the pre-determined endpoint. Investigators were blinded to radiation dose delivered to a given mouse.

Mice were treated using a SARRP (Xstrahl, Gulmay Medical Inc., Suwanee, GA, USA), according to previously described techniques [288]. Briefly, mice were anesthetized using isoflurane inhalation (1-3%, in oxygen) and imaged using a single CBCT scan. Treatment plans were made using Muriplan (Gulmay Medical Inc.) and single fractions of 0 or 15 Gy were delivered to the tumour using two 220 kVp parallel opposed fields, collimated to 1×1 cm^2, at a dose rate of 4 $\frac{\text{Gy}}{\text{min}}$ [225]. For all studies involving evaluation of CAIX expression, tumours were irradiated with a clinical

linear accelerator using previously established protocols [287].

Tumours were measured and pimonidazole (PIMO) was injected IP at 100 $\frac{\text{mg}}{\text{kg}}$ one hour prior to euthanasia [289]. Tumours used for CAIX studies were not injected with PIMO prior to euthanasia. At 2 hours, 1 day, 3 days or 10 days post irradiation mice were euthanized, tumours extracted, embedded in mounting medium (Tissue-Tek O.C.T. Sakura Finetek Europe B.V., NL), flash frozen in liquid nitrogen and stored at $-80°$C.

7.3.3 *Ex vivo* Raman microscopy

Three consecutive tissue sections (each with a thickness of 20μm) were extracted from a given tumour, using a rotary microtome (HM 550; MICROM International GmbH, Walldorf, Ge) and placed on magnesium fluoride slides. A Renishaw inVia Raman Microscope (Renishaw Inc., Illinois, IL, USA) coupled to a 785 nm diode laser (Renishaw) and dry objective (100×, NA=0.9, Leica Microsystems, Wetzlar, Ge) was used to collect Raman map spectra. Spectra were collected using a thermoelectrically cooled CCD detector (Andor Technology, South Windsor, CT, USA). Spectra were acquired for 20 seconds per point, covering a spectral range of 420-1800 cm^{-1}. Raman maps were collected over an area of either 100×100 μm^2 or 200×200 μm^2 and were acquired using a step size of 15 μm in both dimensions. Two maps were collected from randomly selected regions within each tissue section, leading to a total of six maps collected per tumour (2 maps per section, 3 sections per tumour). This study included a total of 28 mice, 14 irradiated and 14 unirradiated (8 mice at 2 hours and 10 days post irradiation; 4 per dose group, 6 mice at 1 and 3 days post irradiation; 3 per dose group).

7.3.4 Spectral processing and analysis

The data set consisted of 14,192 spectra prior to outlier removal and reduced to 13,614 spectra after outliers (e.g. saturated spectra) and spectra contaminated with cosmic rays were visually identified and removed from the data set (2 hrs 0 Gy; n=2049, 2 hrs 15 Gy; n=1908, day 1 0 Gy; n=1380, day 1 15 Gy; n=1374, day 3 0 Gy; n=1499, day 3 15 Gy; n=1462, day 10 0 Gy; n=1923, day 10 15 Gy; n=2019).

In-house algorithms developed in Matlab (Mathworks, Natick, MA, USA, version R2014B) estimated and subtracted spectral background using a Savitsky-Golay zero-order filter [221], shifted spectra to account for instrument drift using the phenylalanine peak located at 1003 cm^{-1} and normalized spectra to the total amount of biological material in the sampling volume, as described previously [266]. Principal component analysis (standard function available in Matlab) was used to separate spectral features that contribute variability in the data set due to radiation exposure and those contributed from other sources. Due to the overlapping nature of major Raman bands arising from biomolecular components in tissue, only biomolecules with several contributing spectral bands arising on the same side (positive or negative) of the PC axis are definitively assigned and further considered in our analysis. Furthermore, biomolecular changes identified through RS are discussed in terms of relative changes as outlined in the positive and negative features of a given PC, rather than absolute changes in specific biomolecules.

7.3.5 Immunofluorescence imaging

Tissue was sectioned to 10 μm using a rotary microtome, placed on glass slides and fixed with PBS containing 2% paraformaldehyde (Alfa Aesar, MA, USA) for 1 minute. Fixed tissue sections were washed twice with PBS then blocked using PBS with triton-x (0.1%, Fisher Scientific) and bovine serum albumin (BSA) (2%, Roche Diagnostics, Mannheim, Ge). Cells were incubated at room temperature for one hour with anti-CAIX (1:50 dilution, antibody validated previously [290]) or anti-pimonidazole 1:10 dilution, hypoxyprobe 4.3.11.31 mouse MAb, HPI Inc, MA, USA) antibodies. Sections were then washed twice with PBS followed by a single wash of PBS with Triton-x (0.1%) and BSA (0.5%).

In the case of the singly stained CAIX sections, chicken anti-mouse Alexa Fluor 488 (1:100 dilution, Invitrogen Molecular Probes, OR, USA) was incubated for 30 minutes at room temperature, after which sections were washed twice with PBS, fixed using 2% paraformaldehyde for 1 minute then washed with PBS.

In the case of the doubly stained PIMO and γ-H2AX sections, chicken anti-mouse Alexa Fluor 488 secondary antibody (1:100 dilution, Life technologies, OR, USA) was incubated for 30 minutes, washed twice with PBS then incubated for one hour with

anti-γ-H2AX (1:50 dilution, rabbit MAb, Cell Signaling Technology, MA, USA). This was followed by two washes with PBS and a single wash of PBS with Triton-x (0.1%) and BSA (0.5%). Sections were incubated for 30 minutes with goat anti-rabbit Alexa Fluor 546 secondary antibody (1:100 dilution, Invitrogen, OR, USA), followed by two washes with PBS, a single wash with 2% paraformaldehyde for 1 minute and a final wash with PBS. For both the single and double stained sections nuclear localization was carried out using Vectashield Mounting Medium with DAPI (Vector Laboratories Inc., CA, USA).

Immunofluorescence (IF) images were collected at 20× magnification using an Olympus microscope coupled with a Nuance multi-spectral imaging system (Perkin Elmer, MA, USA) and multi-spectral laser (Excelitas Technologies). Percent coverage of IF images was assessed using FIJI (ImageJ). An intensity threshold was assigned to grey scale images of a given fluorophore to eliminate non-specific background staining. The percent area of the field of view containing intensities above this threshold was assessed and reiterated for each field of view.

7.3.6 Co-registration of Raman and immunofluorescence data

Raman mapping and CAIX IF imaging was carried out for the same region of a 20 μm thick tissue section for several tumours irradiated to 0 or 15 Gy. The Raman spectral map was collected using the Renishaw Raman system with a 20 μm step size in each dimension, over a 500 μm × 600 μm region using a 100× Leica dry objective. A white light image of the same region was also collected using the Renishaw system and a 10× Leica dry objective. The CAIX IF staining was achieved using the same protocol identified above, with images of DAPI and CAIX collected using 10× magnification.

Spectra contained within the Raman map were analyzed using PCA and the principal component score associated with glycogen (PC1) was plotted as a function of position. Image alignment and cropping was carried out in FIJI. The glycogen spectral map was aligned to the white light image using the associated coordinates with these two images. Next, the CAIX IF image was aligned manually using structural features of the tissue section. The CAIX IF image was then cropped in FIJI using the glycogen map as a mask. In house algorithms were developed in Matlab to segment the IF image and glycogen map into co-registered pixels. Mean IF intensity within a pixel

was then compared to glycogen score.

7.3.7 Statistical procedures

Statistical significance of PC score shifts were tested using a two-sided Wilcoxon rank sum test to a 5% significance level. This test assumes similar standard deviation among the test populations, a condition that is satisfied by the data sets examined. Statistical significance of shifts in mean IF staining was tested using a two-tailed Students t-test. Linear fitness of trends were assessed by determining the correlation coefficient between the dataset and a first-order polynomial fit to the dataset using standard Matlab algorithms. Data points outside the 75% prediction intervals for the data set were considered outliers in analysis of CAIX IF intensity against principal component score.

7.4 Results

7.4.1 Raman spectroscopy identifies radiation induced glycogen perturbations as early as 2 hours and up to 10 days post irradiation

Non-small cell lung cancer cells were injected subcutaneously in mice and tumours grew to approximately 10 mm in diameter. Tumours received conformal radiation therapy to a single dose of 15 Gy or were untreated, then harvested at 2 hours, 1, 3 or 10 days following irradiation. To better delineate the *in vivo* metabolic changes induced following radiation, a combination of RS and PCA was used. Correlated Raman spectral features within dose groups were identified at 2 hrs, 1, 3 and 10 days post irradiation. In this study, 75% of the total variance in the data set can be described by considering the first five principal components. However, all other components beyond PC1 and PC2 contribute to less than 8% of the total variance in the data set, per component. This is nearly half the variance described by PC2, therefore components three and higher are not described in detail in this report.

The first principal component (PC1) isolated in the Raman dataset contributes to

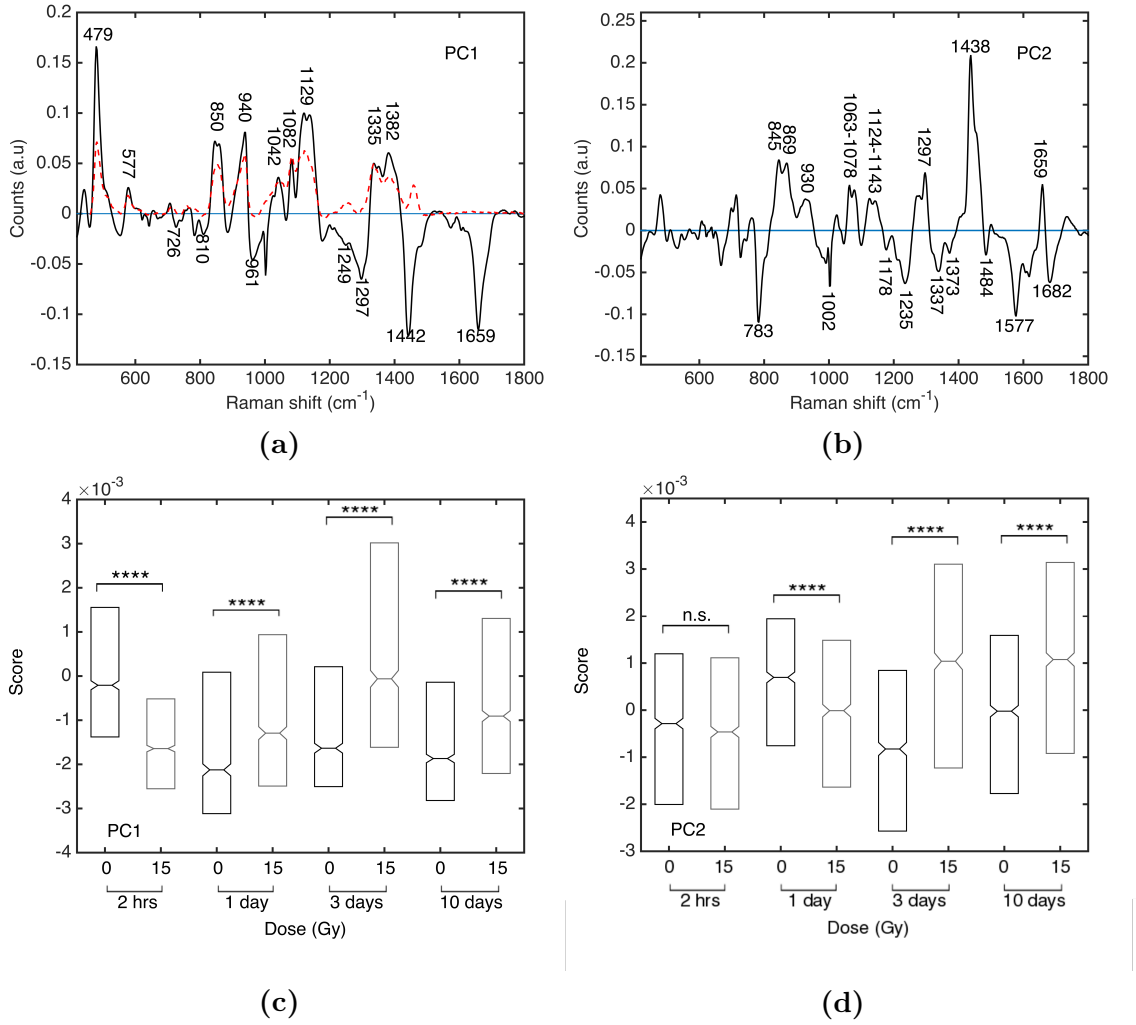


Figure 7.1: Raman spectral changes linked to glycogen (PC1) and cell cycle (PC2) in NSCLC xenograft tissue following irradiation. Principal component 1 (a) and PC2 (b) with corresponding box plots of PC1 score (c) and PC2 score (d) (Tukey style box plot, outliers left out for clarity, notches indicate 95% confidence interval on the median). Median PC scores are shown for all spectra collected over four tumours (2 hrs, 10 days) or three tumours (1 day, 3 days) in a single dose group and time point. Statistical significance: **** $p \leq 0.0001$, n.s.- not significant.

42% of the total variance in the dataset 7.1a. The spectral band assignment for PC1 indicated positive spectral features exclusively due to glycogen and negative bands arising from nucleic acids (adenine cytosine, thymine), protein (amide I and III, phenylalanine, carbon vibrational modes) and lipids (carbon vibrational modes; Appendix B, Table B.1)

Similarly, the second principal component (PC2) contributes 14% of the total variance in the dataset (Figure 7.1b). Several unique and positive features were due to protein (carbon-nitrogen bands, α-helix associated carbon-carbon vibrational modes, amide I/III bands) and lipid (carbon-nitrogen, carbon-hydrogen, carbon-carbon bands; Appendix B, Table B.2). In contrast, PC2 revealed a subset of negative features arising due to protein (phenylalanine, tyrosine, amide bands associated with random coil and β-sheet protein structure) and nucleic acids (guanine, adenine).

Next, the median PC1 score was determined for the spectra collected from all tumours at each dose and time point studied. The PC1 scores indicate that at 2 hours post irradiation there was an initial reduction in glycogen content of irradiated tumours compared to unirradiated tumours ($p<0.0001$; Figure 7.1c). However by 1 day post irradiation, the glycogen levels in irradiated tumours was greater than unirradiated tumours ($p<0.0001$) along with an overall increase in glycogen levels in irradiated tumours between day 1 and day 3 ($p<0.0001$). On day 10, tumours that received radiation continued to display twice as much glycogen compared to unirradiated controls ($p<0.0001$). Notably the total glycogen levels were lower than tumours examined on day 3 post irradiation.

To determine whether the spectral changes were unique to PC1, a similar analysis of PC2 scores was performed (Figure 7.1d). At 2 hours post irradiation, the median PC2 scores did not reveal any statistical difference between the irradiated and unirradiated groups ($p=0.14$). However, there was a positive shift in the PC2 scores 24 hours post irradiation, with the unirradiated group shifting more than the irradiated group ($p<0.0001$). At 3 and 10 days post irradiation, the 15 Gy group shifts to more positive median PC2 score while the unirradiated group shifts to a more negative score compared to day 1. Comparatively, the irradiated tumours displayed at least a 2-fold increase in PC2 score compared to the unirradiated controls at 3 and 10 days ($p<0.0001$).

7.4.2 Glycogen expression is correlated to tumour regression in NSCLC

Given the close relationship between radiation and metabolic changes, we examined whether the response to radiation, corresponding to the change in tumour area, was

associated with variances observed in PC1. As expected, with time, unirradiated tumours increased in area and ranged from 42 to 113 mm^2 (Figure 7.2). With the exception of two unirradiated tumours, median PC1 scores all fall below -1.71×10^{-3}, indicating minimal glycogen content relative to the remaining tumours in the data set. As such, large unirradiated tumours displayed low glycogen levels. In contrast, irradiated tumours which exhibited partial responses (area increases between 31-37 mm^2) or size reduction (on the order of 3 to 24 mm^2) at 3 and 10 days post treatment had correspondingly higher median PC1 scores, indicative of increased glycogen. A linear fit to this data set shows that glycogen content (PC1 score) is linearly correlated to change in tumour area (R^2=0.86).

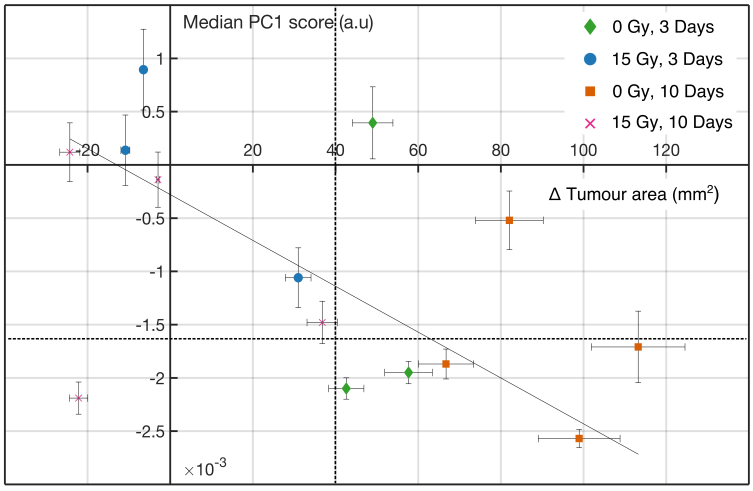


Figure 7.2: Raman spectroscopy identifies increased glycogen, which is correlated with radiation induced tumour regression. Median PC1 score as determined using RS is shown as a function of change in tumour area as measured from time of treatment to time of euthanasia. This is plotted for 0 Gy and 15 Gy irradiated tumours harvested at 3 and 10 days. Error bars represent 95% confidence interval on the median PC1 score, and an estimated measurement uncertainty of 10% on tumour area.

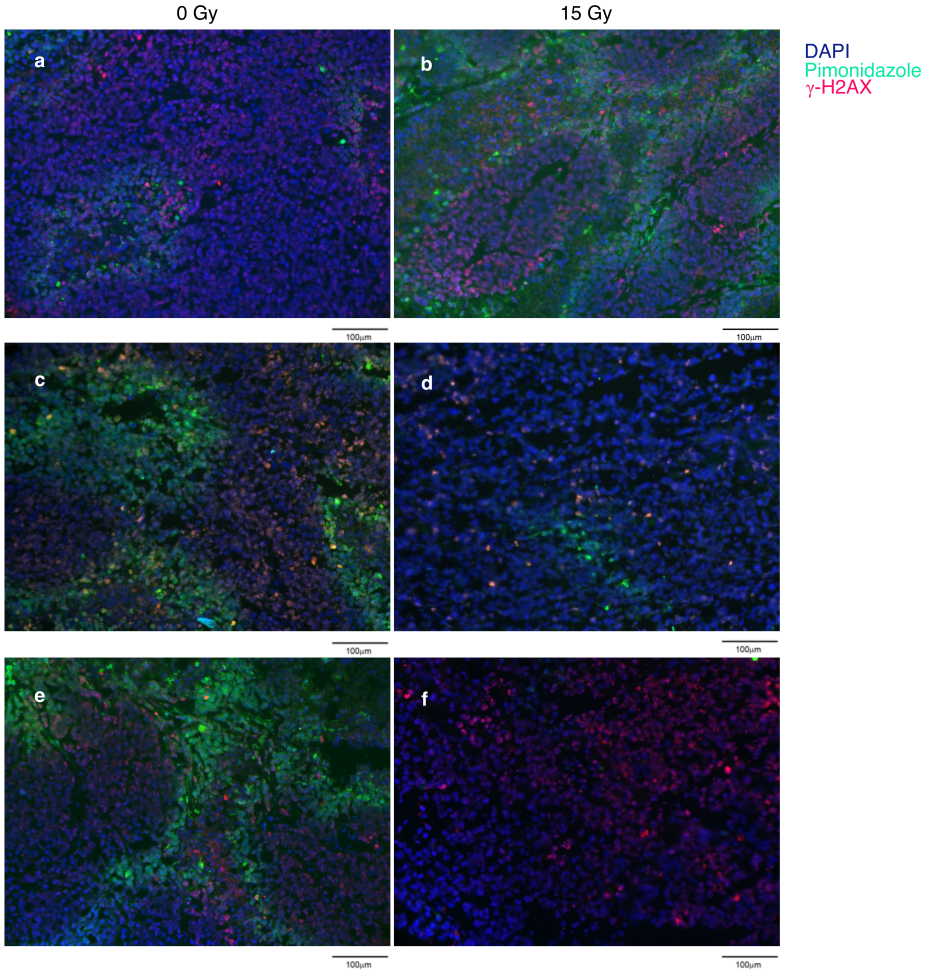
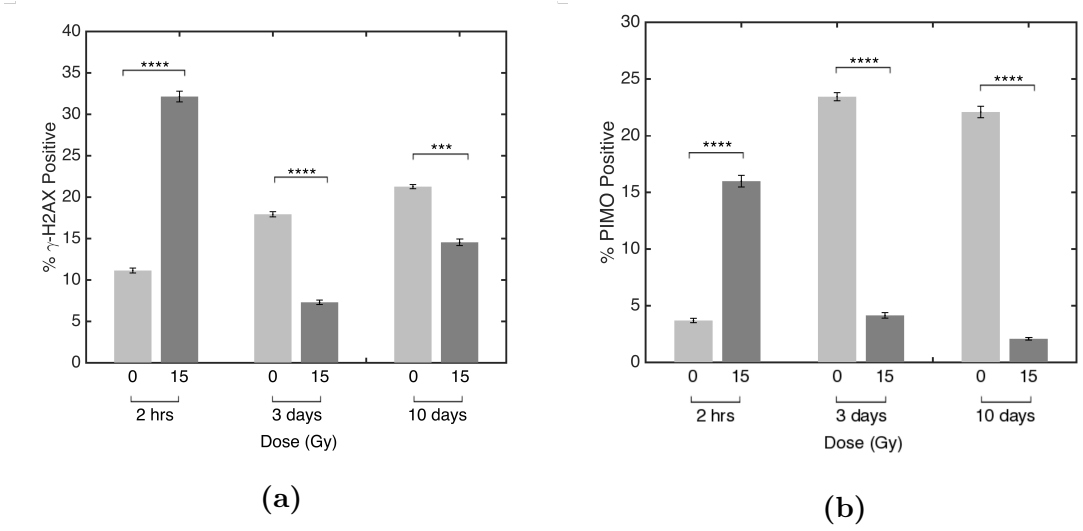


Figure 7.3: Concurrent immunofluorescence staining of γ-H2AX associated DNA damage, and hypoxia indicated through pimonidazole. Immunofluorescence images of 0 Gy (left panels) and 15 Gy (right panels) tumours harvested at 2 hours (a, b), 3 (c, d) and 10 (e, f) days post irradiation. Nuclear localization was made using DAPI (blue), while DNA damage was indicated through γ-H2AX (red) and hypoxia through pimonidazole (green).

7.4.3 DNA damage and hypoxia are associated with RT exposure

Given the extent of glycogen changes following RT, we examined whether this is a function of the extent of DNA damage and hypoxia. Pimonidazole stains cells which have been acutely exposed to low oxygen [291, 292] while CAIX, a transcriptional target of HIF-1, was used as a surrogate for cells which have been previously exposed

to hypoxia [293]. Furthermore, γ-H2AX staining enabled the localization of radiation-induced DNA double strand breaks [294]. Multi-parametric staining was performed to identify γ-H2AX (red), pimonidazole (green) and DAPI (blue) in irradiated and unirradiated tumours harvested at 2 hours, 3 and 10 days post-irradiation (Figure 7.3). The average percent area with positive staining was assessed for each dose and time point. As expected, DNA damage was found to be greater in irradiated tumours at 2 hours post-irradiation compared to the unirradiated controls ($p<0.0001$; Figure 7.4a). Similarly, irradiated tumours were found to have increased PIMO staining at 2 hours ($p<0.0001$; Figure 7.4b) indicating greater levels of hypoxia at this time.



(a) **(b)**

Figure 7.4: Quantification of immunofluorescence staining of γ-H2AX (a) and pimonidazole (b). Images were assessed for percent area stained positive for each marker. Mean percent coverage was determined for each dose group and time point (n=18 images per group), with error bars indicating standard error on the mean. **** $p \leq 0.0001$, *** $p \leq 0.001$.

At 3 and 10 days, unirradiated tumours were found to have increased levels of γ-H2AX compared to irradiated tumours ($p<0.0001$ day 3, $p=0.001$ day 10; Figure 7.4a). This is likely due to increased levels of hypoxia in unirradiated relative to irradiated tumours at 3 and 10 days as confirmed by PIMO staining ($p<0.0001$ for both 3 and 10 days; Figure 7.4b) and has also been reported in the literature [295].

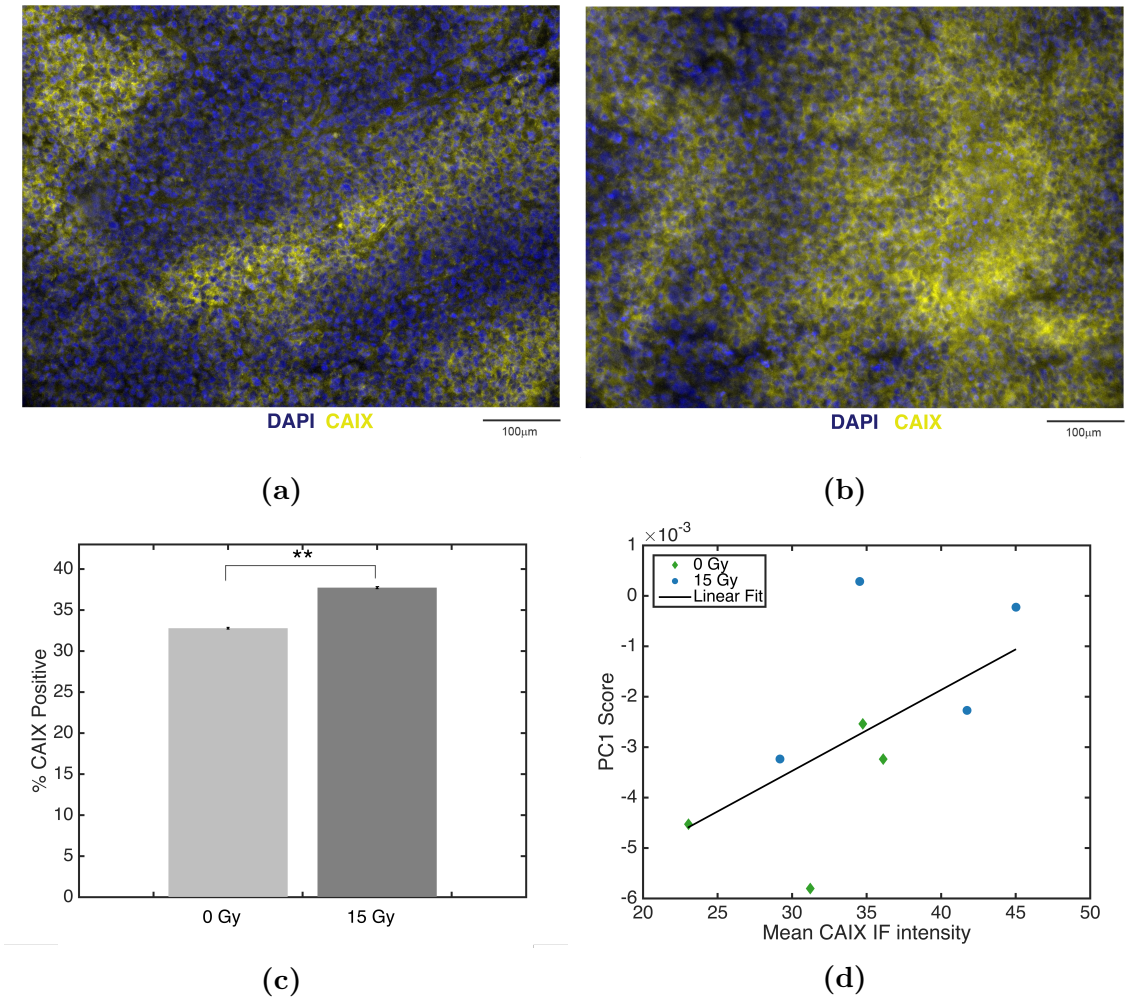


Figure 7.5: Trends in CAIX expression between irradiated and unirradiated tumours harvested at 3 days post-treatment. Immunofluorescence images showing nuclear localization through DAPI (blue) and surrogate marker for hypoxia through CAIX (yellow) for 0 Gy (a) and 15 Gy (b) tumours. The mean percent area positive for CAIX over several images per dose group (n=136 for 0 Gy, n=122 for 15 Gy) is shown in (c), indicating a statistically significant increase in CAIX staining for irradiated tumours (**$p \leq 0.01$). Error bars indicate standard error on the mean. (d) Median PC1 score indicating glycogen content is plotted against the mean percent CAIX positive for each 0 Gy and 15 Gy tumour studied at 3 days post-treatment. A linear correlation between glycogen content (PC1 score) and percent CAIX positive for a given tumour is shown (R^2=0.90, p=0.01).

7.4.4 Irradiated tumours exhibit higher CAIX expression

Given the direct relationship between tissue hypoxia and radiation sensitivity, the extent of CAIX positive tumour regions was quantified. This analysis revealed positive

association between CAIX expression levels (yellow) with tumours irradiated at 0 Gy (Figure 7.5a) and 15 Gy (Figure 7.5b) and harvested at 3 days post irradiation. In general, irradiated tumours show increased CAIX positive staining compared to unirradiated controls ($p<0.01$) at 3 days post-treatment. This trend is quantified in Figure 7.5c, through the average percent area positively stained for CAIX over all tumours in a dose group.

7.4.5 Intra-tumour glycogen expression is correlated to CAIX expression

Next, to elucidate the impact of radiation on CAIX expression, tissues collected on day 3 post-treatment were stained with CAIX. Overall, there was a linear relationship ($R^2=0.90$, $p=0.01$) between median PC1 score and mean CAIX IF coverage (Figure 7.5d). As expected, irradiated tumours fall along the upper right portion of the plot, suggesting increased glycogen levels and increased CAIX coverage while unirradiated tumours tend to lay in the lower left portion, indicating lower glycogen and CAIX levels.

In order to further correlate glycogen as measured through RS/PCA and CAIX IF, a pixel-by-pixel comparison between Raman maps and CAIX IF maps of the same tissue section was generated (Figure 7.6). A qualitative comparison of PC1 and CAIX IF maps for both the 0 Gy (Figures 7.6a,b) and 15 Gy (Figures 7.6c,d) sections shows similarities in the cellular co-expression of glycogen and CAIX. A quantitative pixel-based comparison of the two images shows a general correlation between increased CAIX intensity and increased PC1 score within a 100×100 μm^2 region. This result indicates that NSCLC tumour regions containing positive CAIX pixels spatially correlate to pixels with high PC1 scores and thus high glycogen content.

7.5 Discussion

This work uses RS to study key metabolic changes in irradiated NSCLC xenografts at various time points post RT. Changes in metabolic profile as indicated through PC1 as well as cell cycle changes indicated through PC2 were observed. Previous Raman

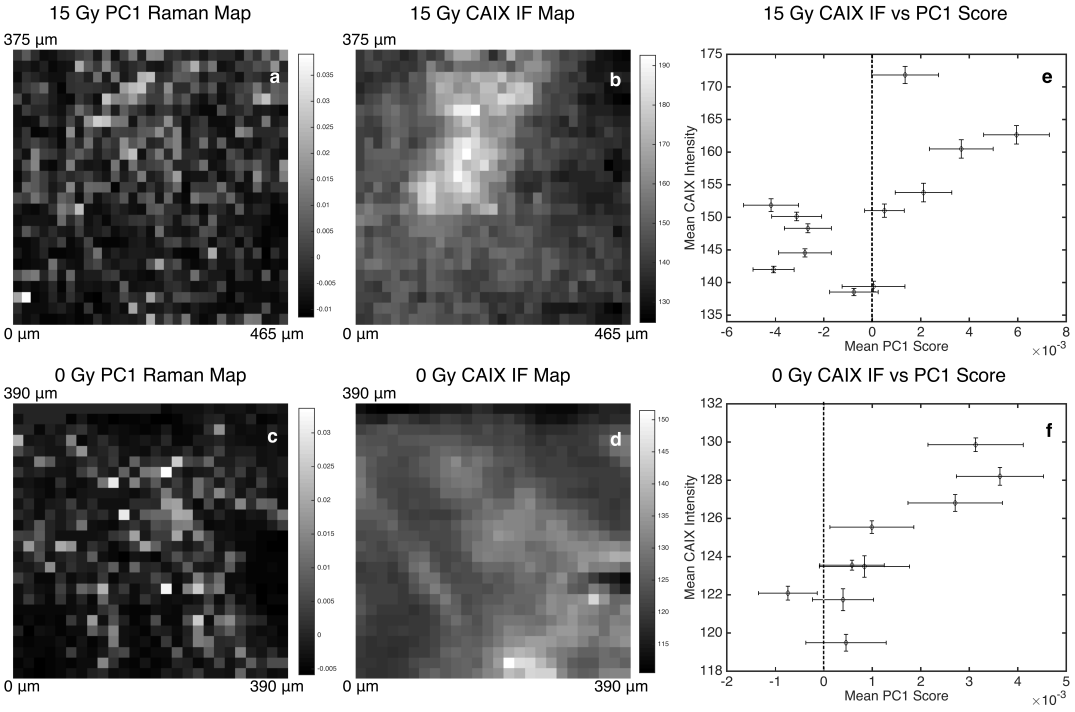


Figure 7.6: Local correlations between cellular glycogen using RS and CAIX immunofluorescence. Raman intensity maps of glycogen (PC1), indicating the spatial distribution (20×20 μm^2 pixel size) of glycogen in a 0 Gy (a) and 15 Gy (c) tissue section (harvested at 3 days). Coincident CAIX immunofluorescence intensity spatial maps (20×20 μm^2 pixel size) for the same region are also shown for 0 Gy (b) and 15 Gy (d). Bright regions indicate high CAIX stain intensity or high glycogen (PC1 score) at that pixel. The mean CAIX intensity for 100×100 μm^2 regions within each intensity map is plotted against the mean PC1 score in the same region (e-f), indicating a general correlation of high CAIX intensity linked to high PC1 scores. Error bars are the standard deviation.

and cell synchronization studies have linked PC2 spectral features to progression through cell cycle [266]. As observed in the current study, median PC2 score shifts at 1 day post treatment suggest a larger proportion of cells are in the S phase for irradiated tumours compared to unirradiated tumours. Cells in S phase are most radioresistant [296]; therefore, it is expected that following radiation exposure there is a larger proportion of cells in S phase. At 3 and 10 days post treatment, the median PC2 score for 15 Gy tumours has become more positive than the unirradiated controls. Similar to previous findings, this PC scoring is linked to cells in G1, with some cells in G2 and fewer cells in S phase [266]. Therefore, RS identified that the majority of irradiated cells are synchronized into S phase at 1 day post-irradiation and G1 phase

at 3 and 10 days post irradiation.

Previous studies have used RS to detect radiation induced metabolic alterations in human NSCLC tumour xenografts through changes in glycogen content at 3 days post treatment [287]. In this study we use RS to show that glycogen levels differ between irradiated and unirradiated tumours as early as 2 hours and as late as 10 days post treatment (Figure 7.1c). By tracking glycogen metabolism and tumour area, the radiation-induced glycogen signature was found to be linearly correlated to tumour regression (95% confidence interval). Untreated tumours continued to grow and contained less glycogen than the irradiated counterparts. The latter tumours had slower growth rates or regressed and contained relatively more glycogen. One possible explanation for this is that larger tumours have an increased metabolic burden and therefore consume more energy reserves by depleting glycogen stores. Alternatively, exposure to radiation and concomitant increase in cellular stress may switch cells to preserve energy stores in the form of glycogen.

At 2 hours post treatment we found reduced expression of the glycogen RS signature in irradiated tumours. We also show increased levels of γ-H2AX staining at 15 Gy, confirming radiation induced DNA damage has occurred in the tumours (Figure 7.3, Figure 7.4a). One possibility is that within 2 hours sufficient time has elapsed for the initial DNA damage response to have initiated and activated radiation-induced cell death [189, 198, 297]. Therefore an increase in PIMO positive staining in irradiated tumours could be an indication of selective cell kill towards oxygenated tumour regions at this time (Figure 7.3, Figure 7.4b). Taken together, reduced expression of the RS glycogen signature in irradiated tumours can be attributed to increased initial radiation induced damage response within the tumour or possibly hypoxic tumours.

Untreated tumours harvested at 3 and 10 days showed increases in size and increased levels of hypoxia, which is consistent with increased burden for tumour resources. Further, there was more γ-H2AX staining compared to unirradiated tumours, a result of the heightened hypoxic state of these tumours compared to irradiated tumours [295]. These tumours showed relatively lower glycogen RS scores, suggesting that cells may have adapted to high energy metabolic demand from radiation and hypoxic damage. Therefore, unirradiated tumours that possess low glycogen levels are more likely to be hypoxic, larger in size and have high levels of DNA damage.

Irradiated tumours harvested at 3 days post treatment contained higher glycogen

levels. These tumours were found to be smaller compared to the unirradiated controls, but also had less DNA damage and hypoxia. In order to understand how this observation may be linked to a radiation response in the tumour we must also consider trends in tumour size and CAIX staining. Irradiated tumours decreased in area at 3 days post treatment and consequently fewer cells are available to deplete tumour resources compared to before treatment, supporting tumour reoxygenation. Furthermore, hypoxic tissue is more radioresistant than normoxic tissue, therefore it is likely that a large portion of the tissue remaining in irradiated tumours at 3 days post-irradiation was hypoxic at time of treatment but became reoxygenated at 3 days post-irradiation. Evidence of reoxygenation is demonstrated by reduction in PIMO positive staining and greater CAIX staining in irradiated tumours compared to unirradiated tumours. CAIX is a relatively stable transmembrane protein and has been shown to remain present in cells even during recovery from hypoxic conditions, with significant positive staining shown up to 48 hours into reoxygenation for some cell lines [298]. Therefore the concurrent decrease in PIMO staining and relatively higher CAIX staining 3 days following irradiation supports the notion that irradiated tumours are recovering from hypoxia. The glycogen rich irradiated tumours appear to contain a higher concentration of cells that were hypoxic at the time of treatment and are reoxygenating at 3 days post treatment, compared to unirradiated controls.

Considering the PIMO and CAIX global staining trends at day 3, together with the correlation between CAIX positive regions and glycogen spectral regions, our results suggest that RS is able to not only identify glycogen signatures but track these changes over a defined period of 10 days. Importantly, the changes in glycogen were strongly associated with response of the tumour as a result of radiation induced DNA damage and tissue oxygenation. Specifically, we show that relatively lower levels of cellular glycogen are associated with larger tumours that have increased levels of hypoxia and DNA damage in the tumour. In contrast, higher glycogen levels are associated with relatively smaller tumours that have less hypoxia and minimal DNA damage, or treated tumours that have become reoxygenated.

7.6 Concluding statement

Raman spectroscopy offers a label-free and non-destructive way to monitor NSCLC response to radiation by measuring metabolic alterations within the tumour as a result of oxygenation state of the tissue. We show that RS can be used as early as 2 hours post irradiation to measure early metabolic signs of the NSCLC radiation response which is associated with elevated levels of hypoxia in the tumour. We also show that a radiation induced increase in glycogen can be detected as early as 1 day and up to 10 days post irradiation using RS, and is associated with changes in tissue reoxygenation. They key role that hypoxia and hypoxic recovery plays in radiation therapy of NSCLC means that RS is a valuable technique for measuring the radioresistance status of NSCLC.

Chapter 8

Raman Spectroscopic Study of Irradiated Tumours: Triple Negative Breast Cancer

8.1 Preface

Content in this chapter is reproduced with permission from Radiation Research Society, and has been published with the following citation:

> S.J. Van Nest, L.M. Nicholson, L. DeVorkin, A.G. Brolo, J.J. Lum, A. Jirasek. Raman Spectroscopic Signatures Reveal Distinct Biochemical and Temporal Changes in Irradiated Human Breast Adenocarcinoma Xenografts. *Radiation Research*, 2018.

This work was carried out using mouse Cohort B. The candidates role in the work presented in this publication include experimental conception, design and set up. Establishing tumours in the mice, monitoring the mice tri-weekly, treating mice on small animal radiation research platform, harvesting tumours. Collecting all Raman spectra, analyzing and reporting figures on all results. Writing the initial manuscript draft for co-authors to review.

Experimental conception: AGB, AJ, JJL, SJVN
Experimental design: AGB, AJ, JJL, LD, LMN, SJVN

Performed experiments: LD, LMN, SJVN
Analyzed data: SJVN
Made figures: SJVN
Writing of manuscript: SJVN

8.2 Introduction

Early-stage breast cancer is typically treated using a combination of surgery, radiation and chemotherapy [299]. Despite this, local control is not achieved for some patients. A previously published meta-analysis reported that adjuvant radiotherapy after surgery leads to positive 10-year recurrence outcomes, highlighting the importance of radiotherapy in breast cancer control [300]. However, a significant portion of patients are either over or under treated with radiation [300]. Beyond this, clinically significant heterogeneities in gene and protein expression [e.g. estrogen receptor (ER), progesterone receptor (PR) and human epidermal growth factor 2 (HER2)] have been identified in breast cancers [301–303]. The effect of these patient-specific heterogeneities on the radiation response of breast cancer is not yet understood and, for the most part, is not accounted for when determining radiation treatments. Therefore, a technique that stratifies patients based on radiation resistance or sensitivity would be valuable for guiding decisions on radiation therapy dose escalation or reduction for this disease.

To date, several approaches to identify radiation specific signatures that could be used to guide treatment decisions in radiotherapy have been studied. These techniques include: genetic signatures of radiation resistance or sensitivity [70, 259, 304], hypoxia localization [255, 257, 305–307], break repair markers [54], circulating cell-free tumour DNA [80] and single-nucleotide polymorphisms associated with tumour responses to radiation [77, 79]. While some of these techniques show promise, none are currently clinically implemented, due to factors such as insufficient clinical validation, as well as limitations including difficulty of implementation and expense of some of these techniques.

Raman spectroscopy is a minimally invasive, non-destructive and label-free optical spectroscopic technique that can measure the biomolecular content of cells and tissue [96, 217]. The characteristics of RS are favourable for biomedical applications and in

particular, offer an opportune technique for personalizing radiation therapy. Previous studies have explored the use of RS for studying radiation induced effects on *in vitro* and *ex vivo* irradiated systems. Specifically, RS in combination with PCA has been used to stratify radioresistant and radiosensitive oral [139] and cervical [140] cancer subtypes. Its utility has been demonstrated in the identification of biochemical signatures of radiation response in human lymphocytes [141], as well as cultured breast, lung and prostate cancer cell lines [132, 135]. Radiation induced changes in Raman spectra have been demonstrated using clinically relevant doses (250 Gy) [132], low radiation doses (<0.5 Gy) [137, 141] and bystander radiation effects [137]. Furthermore, RS can identify radiation induced spectral changes in skin (mouse, swine, human) and human pancreatic adenocarcinoma xenografts exposed to proton radiation *ex vivo* [142].

While *ex vivo* irradiation studies are valuable, tumour heterogeneity causes a complex biological response to radiation, exemplifying the need for *in vivo* irradiation investigations. As such, Lakshmi et al. showed that distinct Raman spectral features could be identified in mouse brain irradiated *in vivo* [143]. More recently, human NSCLC xenografts irradiated *in vivo* to clinically relevant doses (5 and 15 Gy) were found to demonstrate a dose dependent increase in Raman spectral bands associated with glycogen [287].

In the current study, we investigated radiation induced Raman spectral changes and their temporal evolution, in triple negative (ER-, PR- and HER2-) human breast adenocarcinoma xenografts irradiated *in vivo*. Using RS in combination with PCA, we found that radiation caused spectral changes linked to cell cycle alterations within the tumour as well as other protein-driven molecular changes. Importantly, spectral changes indicated that effects of radiation on the tumour could be monitored using RS at days 1 and 3. This study shows that RS can be used in tumour xenograft applications beyond NSCLC to identify radiation response signatures that are unique to cancer type, emphasizing the significance of RS for assessing radiation responses throughout treatment.

8.3 Materials & methods

8.3.1 Cell line and tumour xenografts

All animal procedures were approved by the University of Victoria Animal Care Committee (Victoria, BC, Ca) and performed in accordance with the guidelines set forth by the Canadian Council on Animal Care. NOD.CB17-Prkdc^{scid}/J female mice were obtained from BCCRC Animal Resource Center (Vancouver, BC, Ca). Animals were housed in HEPA filter microisolator cages within a bioexclusion containment room and allowed access to food and water *ad libitum*. Animals were acclimatized for one week prior to study initiation.

The human breast adenocarcinoma cell line MDA-MB-231 used in this study was purchased from American Type Culture Collection (Manassas, VA, USA, ATCC cat. no. HTB-26, passage no. 3, not listed as misidentified, tested pathogen-free with Charles River Laboratories, Montreal, QC, Ca). Cells were cultured and subsequently injected subcutaneously into the right flank of each mouse at a concentration of 5×10^6 cells in 0.1 ml PBS.

8.3.2 Tumour irradiation and harvesting

Predetermined exclusion criteria disqualified animals from irradiation and continuation in the study if the tumour volume was below 80 mm^2 or above 130 mm^2. Tumours were measured three times per week with digital calipers and animals were randomized into treatment groups once their tumour size reached the predetermined end point. Investigators were blinded to radiation dose received by a given mouse.

Mice were anesthetized using isoflurane inhalation (1-3%, in oxygen) and placed on the treatment bed of a small animal radiation research platform (Gulmay Medical Inc., Suwanee, GA, USA). Body temperature was maintained using BioVet stand-alone heating unit (M2Me Imaging, Cleveland, OH, USA). Mice were imaged using a single cone beam computed tomography scan and treatment plans were made using Muriplan (Gulmay Medical Inc.) treatment planning software. Two 220 kVp parallel opposed fields, collimated to 1×1 cm^2, were delivered to the tumour isocentre at a dose rate of 4 $\frac{\text{Gy}}{\text{min}}$ [225]. Depending on the treatment group, single fractions of

0, 5 or 15 Gy were delivered to the tumour. After irradiation, mice recovered from anesthesia by returning to a normal atmosphere and were provided thermal support. At day 1 or 3 mice were euthanized using isoflurane overdose (5%, in oxygen) and cervical dislocation. Tumours were immediately extracted, embedded in mounting media (Tissue-Tek O.C.T. Sakura Finetek Europe B.V., Alphen aan den Rijn, NL), flash frozen in liquid nitrogen and stored at -80°C.

8.3.3 *Ex vivo* Raman microscopy

To best account for tissue heterogeneity, Raman spectral maps were collected over many different regions of a tumour. For a given tumour, three consecutive tissue sections (each with a thickness of 20 μm) were obtained using a rotary microtome (cat. no. HM 550; MICROM International GmbH, Walldorf, Ge) and placed on magnesium fluoride slides. Prior to Raman measurements, frozen sections were air dried for 10 min. A Renishaw inVia Raman microscope (Renishaw Inc., West Dundee, IL, USA) coupled to a 785 nm diode laser (Renishaw) and dry objective (100×, NA=0.9, Leica Microsystems, Wetzlar, Ge) was used to collect Raman map spectra. Spectra were collected using a thermoelectrically cooled CCD detector (Andor Technology, South Windsor, CT, USA). The laser sampling dimensions were $2 \times 5 \times 10$ μm^3 and the laser power density at the sampling volume was ~ 0.5 $\frac{\text{mW}}{\mu\text{m}^3}$. Spectra were acquired for 20 s per point, covering a spectral range of 420-1800 cm^{-1}. Raman maps were collected over an area of either 100×100 μm^2 or 200×200 μm^2 and were acquired using a step size of 15 μm in both dimensions. Two maps were collected from randomly selected regions within each tissue section, leading to a total of six maps collected per tumour (2 maps per section, 3 sections per tumour). A total of 13 mice were analyzed at day 3 (4 mice each in the 0 and 5 Gy dose groups, and 5 mice in the 15 Gy dose group), and 6 mice were analyzed at day 1 (3 mice each in the 0 and 15 Gy dose groups).

8.3.4 Spectral processing and analysis

Outlier spectra (e.g. saturated) and spectra contaminated with cosmic rays were visually identified and removed from the data set. Prior to outlier removal the day 1 and day 3 data sets consisted of 3224 and 6388 spectra, respectively. After outlier removal the day 1 and day 3 data sets consisted of 3054 and 6201 spectra, respectively.

In-house algorithms developed using Matlab version R2014B (MathWorks Inc., Natick, MA, USA) were subsequently used to estimate and subtract spectral background, shift spectra and normalize spectra to the total amount of biological material in the sampling volume, as described elsewhere [266]. Briefly, for background subtraction a zero-order Savitsky-Golay filter was used to initially estimate the baseline of a spectrum [221]. A residual spectrum was produced by comparing the estimated baseline to the spectrum, and then this was used to produce a new estimate of the baseline together with the Savitzky-Golay filter. This process was reiterated twice, after which the estimated baseline was subtracted from the spectrum.

Spectral shifting due to instrument drift was corrected using the phenylalanine peak located at 1003 cm^{-1}, as described elsewhere [133]. In short, a Gaussian fit was used to identify the central wavenumber of the phenylalanine peak. Point-by-point interpolation was used to shift the spectrum relative to a reference spectrum in the data set. This process was iterated twice, resulting in alignment of the phenylalanine peaks for the spectra in the data set.

Principal component analysis (standard function available in Matlab) was used to separate out spectral features that contribute variability in the data set due to radiation exposure and those contributed from other sources. Tukey style box plots, showing median PC score as well as 25^{th} and 75^{th} percentiles were used to represent PCA results for a given dose group (processed spectra from all tumours receiving the same radiation dose). The 0 Gy dose group had a sample size (after processing) of 2196 (day 3) and 1514 (day 1), the 5 Gy dose group had a sample size of 2007 (day 3 only) and the 15 Gy dose group had a sample size of 1998 (day 3) and 1540 (day 1). Notches indicate the 95% confidence interval on the median, approximated assuming a normal distribution (accurate assumption for large samples of other distributions [230]).

8.3.5 Statistical analysis

Statistically significant shifts in PC score among dose groups were tested using a two-sided Wilcoxon rank sum test to a 5% significance level. This test assumes similar standard deviation among the test populations, a condition that is satisfied by the data sets examined. Comparison between *in vitro* and *ex vivo* Raman experiments was performed using the Pearsons r-value statistic.

8.4 Results

8.4.1 Principal component analysis identifies common spectral features between days 1 and 3

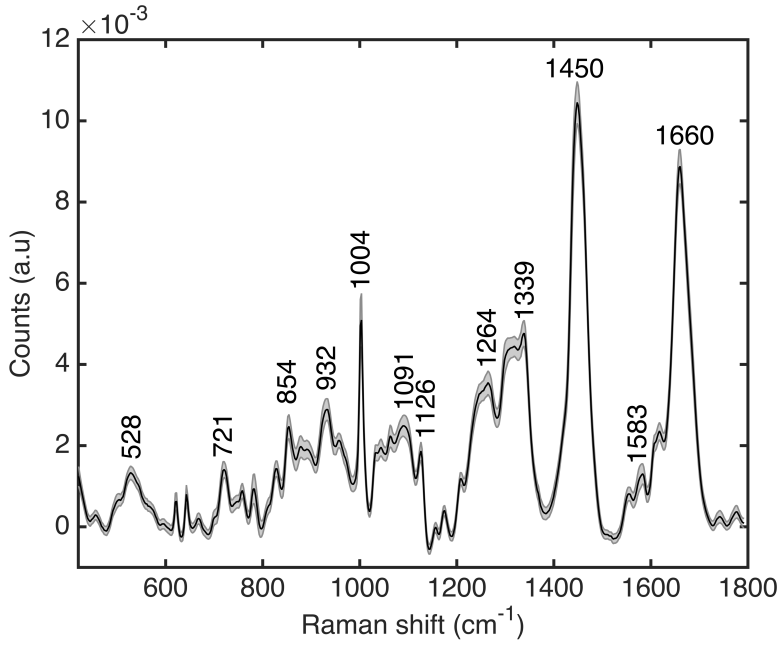


Figure 8.1: Mean Raman spectrum of MDA-MB-231 xenograft tissue. Mean Raman spectrum (black trace) calculated over spectra acquired from MDA-MB-231 xenograft tissue exposed to 0 Gy, 5 Gy and 15 Gy doses of ionizing radiation at 3 days post-irradiation. The standard deviation at each wavenumber (grey shading) is also shown.

Murine tumour xenografts were formed by implanting MDA-MB-231 cells subcutaneously in immune-compromised NOD.CB17-Prkdc^{scid}/J mice and exposed to either 0, 5 or 15 Gy. Tumours were harvested at days 1 and 3 and analyzed using RS. The mean Raman spectrum (with standard deviation) acquired for all tumours harvested at day 3 is shown in Figure 8.1. There are very minor differences between the mean spectrum at days 1 and 3, therefore only day 3 is presented. Raman spectra were then analyzed using PCA to identify correlated spectral changes with radiation exposure.

The resulting first five principal components extracted from the data set make up 61.74% (day 1) and 58.34% (day 3) of the total variance in the data set. However, all other components beyond PC1 and PC2 contribute less than 6% to the total

variance in the data set, per component. This is less than one-half of the variance described by PC2, and therefore components 3 and higher are not described in detail in this article. Due to the overlapping nature of major Raman bands arising from biomolecular components in tissue, spectral band interpretation within a PC was performed with caution. Only biomolecules with several contributing spectral bands arising on the same side (positive or negative) of the PC are definitively assigned and further considered in our analysis. Furthermore, biomolecular changes in the tissue are only discussed in terms of relative changes as outlined in the positive and negative features of a given PC, rather than absolute changes in specific biomolecules.

The spectral features contained in PC1 are highly correlated between the day 1 and day 3 data sets, with a Pearsons r-value correlation coefficient of 0.99. Similarly, PC2 is highly correlated between day 1 and 3 with a correlation coefficient of 0.96. For this reason, only the day 3 component is presented and assigned in this report, since the spectral assignments for day 1 and 3 are identical. However, trends in PC score vary among days harvested and dose groups; both trends are therefore presented for all cases studied.

The first principal component contributes to 30.47% and 29.13% of the total variance in the day 1 and day 3 data sets, respectively (Figure 8.2a). A detailed Raman band assignment for PC1 can be found in Table C.1 of Appendix C, which outlines positive bands attributed to nucleic acids, phenylalanine and tryptophan, as well as negative bands due to overlapping lipid and protein modes. In brief, positive bands were identified from phenylalanine (1001 cm^{-1}, 1047 cm^{-1}, 1180 cm^{-1}, 1212 cm^{-1}, 1577 cm^{-1}), tryptophan (728 cm^{-1}, 1212 cm^{-1}, 1337 cm^{-1}, 1577 cm^{-1}, 1618 cm^{-1}), adenine (728 cm^{-1}, 1337 cm^{-1}, 1377 cm^{-1}, 1577 cm^{-1}), guanine (668 cm^{-1}, 1337 cm^{-1}, 1377 cm^{-1}, 1577 cm^{-1}) and thymine (668 cm^{-1}, 783 cm^{-1}, 1235 cm^{-1}, 1377 cm^{-1}). Negative bands indicating overlapping protein [carbon-nitrogen (C-N), carbon-carbon (C-C), carbon-hydrogen (C-H), amide III/I α-helix] and lipid (C-C, C-H) vibrational modes were identified (1063 cm^{-1}, 1079 cm^{-1}, 1128 cm^{-1}, 1269 cm^{-1}, 1455 cm^{-1}, 1658 cm^{-1}). Additional negative features indicating various vibrational modes of lipids (C-H: 1296 cm^{-1}, 1439 cm^{-1} and C-O: 1743 cm^{-1}) were also present.

As shown in Figure 8.3a, the second PC contributes 15.96% and 13.66% of the total variance in the day 1 and day 3 data sets, respectively. Table C.2 (found in Appendix C) provides a detailed band assignment for this component. Positive features were

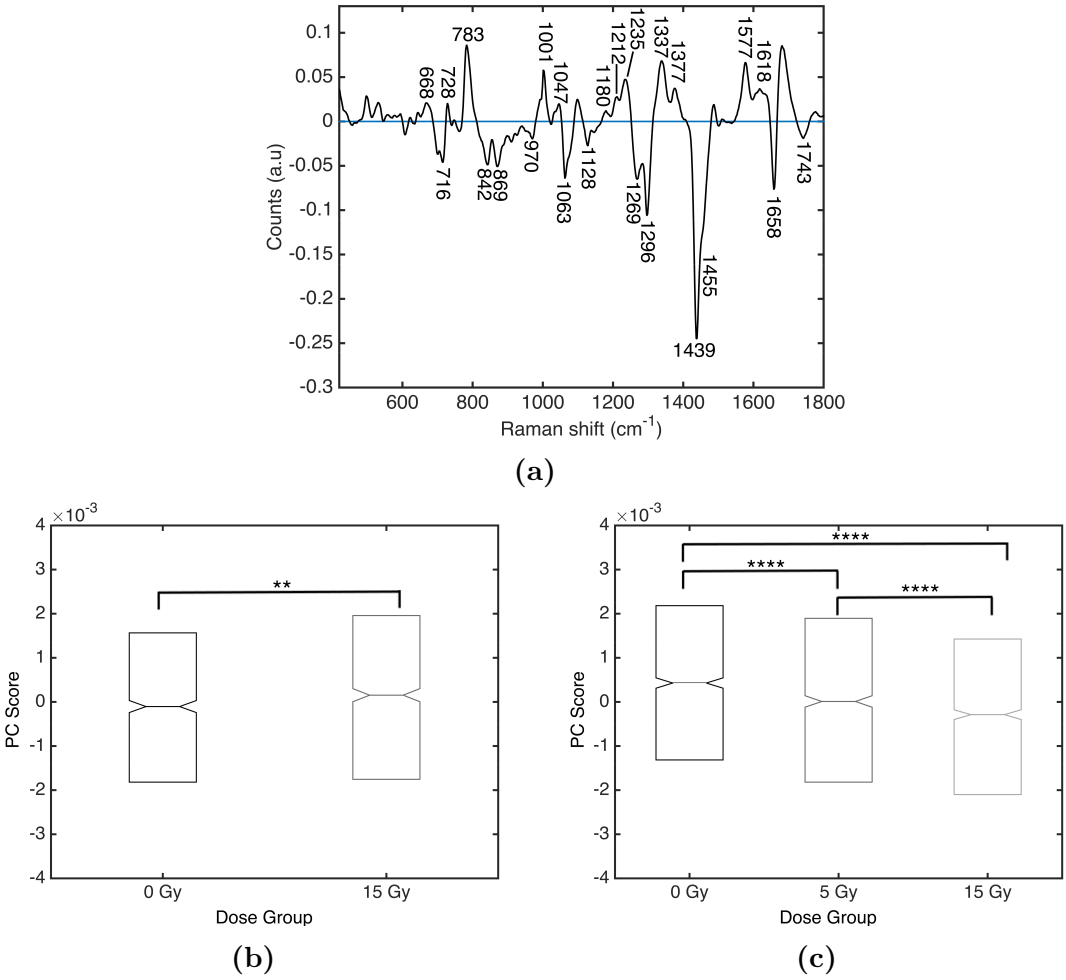


Figure 8.2: Raman spectral changes linked to cell cycle (PC1) in MDA-MB-231 xenograft tissue following radiation. Principal component 1 (a) and corresponding PC score box plot for day 1 (b) and day 3 (c) experiments (Tukey style box plot, outliers left out for clarity, notches indicate 95% confidence interval for the median). Median PC scores are shown for all spectra collected over three tumours (day 1) or four tumours (day 3, 5 tumours in the 15 Gy day 3 group) in a single dose group and time point (day 1 0 Gy; n=1529, day 1 15 Gy; n=1540, day 3 0 Gy; n=2194, day 3 5 Gy; n=2007, day 3 15 Gy; n=2505). Trends in median PC1 score indicate a statistically significant increase in phenylalanine, tryptophan, adenine, guanine, thymine and β-sheet linked amide bands relative to various protein and lipid C-C, C-H, C-N/O bands at 1 day post irradiation for both the 5 and 15 Gy dose groups, with the opposite occurring at 3 days post irradiation. ****p-value ≤ 0.0001, **p-value ≤ 0.01.

found to originate from nucleic acids, α-helix protein contributions and lipid vibrational modes. In particular, PC2 has positive features that confirm the presence of

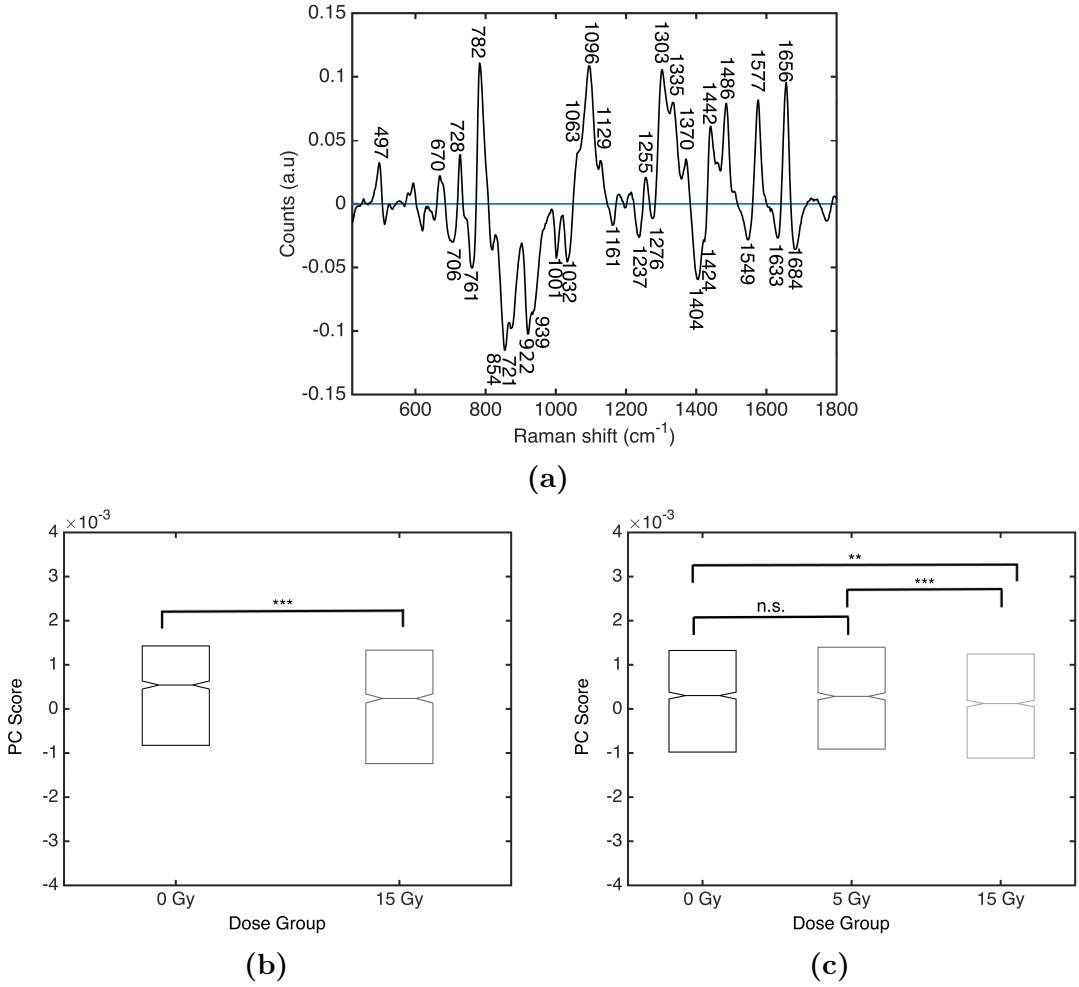


Figure 8.3: Biochemical response (PC2) in MDA-MB-231 xenograft tissue following radiation. Principal component 2 (a) and corresponding PC score box plot for day 1 (b) and day 3 (c) experiments (Tukey style box plot, outliers left out for clarity, notches indicate 95% confidence interval for the median). Median PC scores are shown for all spectra collected over three tumours (day 1) or four tumours (day 3, 5 tumours in the 15 Gy, day 3 group) in a single dose group and time point (day 1 0 Gy; n=1529, day 1 15 Gy; n=1540, day 3 0 Gy; n=2194, day 3 5 Gy; n=2007, day 3 15 Gy; n=2505). Trends in median PC2 score indicate a statistically significant increase in tryptophan, proline, phenylalanine and β-sheet amide bands relative to adenine, guanine, thymine, cytosine and DNA backbone, protein (α-helix amide bands, C-N bands) and lipids (C-C and C-H) in the 15 Gy dose group but not the 5 Gy dose group. ***p-value ≤ 0.001, **p-value ≤ 0.01, n.s. not significant.

adenine (728 cm^{-1}, 1255 cm^{-1}, 1335 cm^{-1}, 1486 cm^{-1}, 1577 cm^{-1}), guanine (497 cm^{-1}, 670 cm^{-1}, 1335 cm^{-1}, 1486 cm^{-1}, 1577 cm^{-1}), thymine (497 cm^{-1}, 670 cm^{-1}, 782 cm^{-1}),

cytosine (782 cm^{-1}, 1255 cm^{-1}), DNA/RNA backbone (1096 cm^{-1}, 1301 cm^{-1}, 1335 cm^{-1}, 1444 cm^{-1}), amide I/III α-helix (1255 cm^{-1}, 1656 cm^{-1}), C-N vibrations in protein (1063 cm^{-1}, 1126 cm^{-1}) as well as C-C vibrational modes (1063 cm^{-1}, 1656 cm^{-1}) and C-H vibrational modes (1301 cm^{-1}, 1335 cm^{-1}, 1370 cm^{-1}, 1444 cm^{-1}) in lipids. Negative features in PC2 originate from various protein contributions. Specifically, negative features of PC2 arise from tryptophan (706 cm^{-1}, 761 cm^{-1}, 1549 cm^{-1}), proline (854 cm^{-1}, 922 cm^{-1}, 939 cm^{-1}), phenylalanine (1004 cm^{-1}, 1034 cm^{-1}), C-O protein vibrational modes (1161 cm^{-1}, 1404 cm^{-1}) and amide I/III β-sheet (1237 cm^{-1}, 1679 cm^{-1}).

8.4.2 Principal component analysis identifies spectral composition changes in human breast adenocarcinoma xenografts that are radiation dose dependent

Median PC score was calculated for the data set containing spectra collected from each tumour exposed to a specific dose (0, 5 or 15 Gy) and harvested at either day 1 or 3. Score plots (Figure 8.2b) indicate that at day 1 , median PC1 score was significantly increased (p-value from Wilcoxon rank sum test of 0.01) from the 0 Gy to 15 Gy dose groups. Median PC1 score plot for day 3 (Figure 8.2c) conversely showed a significant shift towards negative PC score for the 5 Gy ($p<0.0001$) and 15 Gy dose groups ($p<0.0001$) compared to unirradiated control. In a similar manner, there was an observed significant shift towards a more negative median PC1 score between the 5 and 15 Gy dose groups at day 3. Taken together, these results indicate a strong degree of variation in protein, lipid and nucleic acid bands, as outlined in Table C.1 (Appendix C), with radiation exposure in MDA-MB-231 xenograft tissue. Specifically, PC1 indicates radiation induced increases in phenylalanine, tryptophan, adenine, guanine, thymine and β-sheet linked amide molecular bands relative to various protein and lipid C-C, C-H, C-N/O bands at day 1 compared to day 3.

Median PC2 score plots (Figure 8.3b) indicate that at day 1, median PC2 score was significantly reduced ($p<0.001$) from 0 Gy to 15 Gy. Similarly, at day 3, median PC2 scores were also found to be significantly reduced ($p<0.005$) from 0 Gy to 15 Gy, but not significantly reduced between 0 Gy and 5 Gy (p-value of 0.62). Taken together, these results indicate an increase in specific protein bands (tryptophan,

proline, phenylalanine, β-sheet amide bands) relative to nucleic acids (adenine, guanine, thymine, cytosine and deoxyribose phosphate DNA backbone), protein (α-helix amide bands, C-N bands) and lipids (C-C and C-H) in tissue exposed to 15 Gy but not the lower dose (5 Gy).

8.4.3 Raman spectroscopy identifies spectral changes at days 1 and 3 that are related to radiation exposure

Trends within a dose group can also be observed as tissue progresses from day 1 to 3. In the case of the unirradiated controls, the median PC1 score showed a statistically significant ($p<0.0001$) increase from an initially negative score on day 1 to a positive score on day 3 (Figures 8.2b and 8.2c). For 15 Gy irradiated tumours, median PC1 score was initially positive and showed a statistically significant shift ($p<0.0001$) to a negative value at day 3. Figures 8.3b and 8.3c show that the PC2 score of the 0 Gy dose group extracted at day 1 is significantly decreased ($p\leq0.05$) relative to the 0 Gy dose group extracted on day 3. Tumours exposed to 15 Gy had an increase in median PC2 score from day 1 to 3, however, this shift was not found to be statistically significant (p-value of 0.23).

8.4.4 Correlation of spectral features between *in vitro* and *ex vivo* Raman studies

Figure 8.4 shows PC1 and PC2 from the current study, compared to *in vitro* MDA-MB-231 cell line radiation spectral signatures (exposed to 250 Gy, and harvested at day 3) previously reported by our group [132]. There is a strong correlation between PC1 (Pearsons r-value of 0.96) and PC2 (Pearsons r-value of 0.70) derived from the *in vitro* and *ex vivo* Raman studies. In both experiments, RS in combination with PCA discriminated between irradiated MDA-MB-231 cells/tumours from unirradiated controls, through expression of the bands represented in PC2. In our previously published *in vitro* study we did not report a trend in PC1 with radiation dose, as was found in this *ex vivo* Raman study.

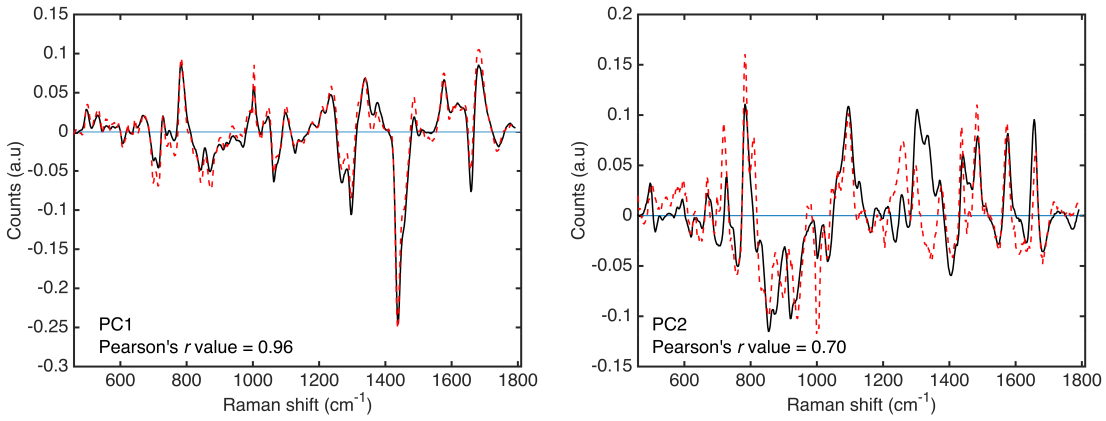


Figure 8.4: Comparison of principal components derived from Raman spectra of *in vivo* irradiated MDA-MB-231 tumour xenografts and cells irradiated *in vitro*. Principal component 1 (a) and 2 (b) isolated in the current *ex vivo* Raman study (black trace) is overlaid with the corresponding component obtained in the previously published *in vitro* study (red trace) using the MDA-MB-231 cell line. *In vitro* results were derived from PCA on a Raman data set of MDA-MB-231 cells cultured and irradiated *in vitro* to doses of 0, 2, 4, 6, 8, 10, 30 and 50 Gy as presented and described previously by our group [132]. *Ex vivo* Raman study used MDA-MB-231 tumours irradiated to 5, 10 and 15 Gy, *in vivo*. PC1 from this *ex vivo* Raman study is highly correlated (Pearsons r-value = 0.96) to PC1 from the *in vitro* experiment, as is PC2 (Pearsons r-value = 0.70).

8.5 Discussion

We have demonstrated the application of RS in combination with PCA to identify radiation induced biochemical changes in human breast adenocarcinoma (MDA-MB-231) xenografts. Dose dependent changes in spectra were tracked at days 1 and 3. At both time points, the principal components isolated from the data sets were highly correlated. Importantly, this suggests that cellular content fluctuations, chemical changes due to radiation exposure, background variation and tissue composition are shared characteristics among breast adenocarcinoma xenografts between day 1 and 3.

Radiobiological responses detected by both PC1 and PC2 in this study can be classified into three major classes of biomolecules: nucleic acid, lipid and protein. PC1 identified radiation induced increases in phenylalanine, tryptophan, adenine, guanine,

thymine and β-sheet linked amide bands relative to various protein and lipid C-C, C-H, C-N/O bands and α-helix linked amide protein bands at day 1, with the opposite occurring at day 3. Previously published results have linked PC1 to cellular content variation with progression through the cell cycle [266]. PC1 isolated in the current *ex vivo* Raman study significantly correlates to this previously identified component and therefore may give insight into cell cycle phases in the tumour. In particular, the statistically significant shift in median PC1 score in the 15 Gy population at day 1 suggests that a larger proportion of cells are in the S phase for irradiated tumours, according to previously published Raman and cell synchronization studies [266]. Cells in S phase are most radioresistant [264]; therefore, it is expected that after radiation exposure there could be a larger proportion of cells in S phase within the tumour. Since the cell doubling time for MDA-MB-231 has been reported to be between 27.78 and 29.92 hours [308], we could expect that at day 1 after treatment, irradiated tumours have maintained synchronization into S phase and have progressed one cycle of cell division back into S phase.

At day 3 the median PC1 score for both 5 and 15 Gy tumours has become more negative than for the unirradiated controls, suggesting increased expression of protein and lipid C-C, C-H, C-N/O bands and α-helix linked amide protein bands relative to phenylalanine, tryptophan, adenine, guanine, thymine and β-sheet linked amide bands. These findings have been observed in other studies where a negative PC score is correlated with features pertaining to cells in G1, with some cells in G2 and fewer cells in S phase [266]. Following from this, the majority of irradiated cells on day 3 are synchronized into G1 phase. Therefore, it is possible that PC1 presented in this study is tracking cell cycle synchronization with more cells in the radioresistant S phase at day 1 and in G1 phase at day 3 compared to unirradiated tumours. However, further studies to fully assert this observation are required, and are beyond the scope of the current work.

Comparison of PC1 score trends reported in this *ex vivo* Raman study to those previously published for the MDA-MB-231 cell line *in vitro* was also performed. PC1 did not show any appreciable trend with radiation dose *in vitro*, but did show such a trend in this *ex vivo* work (Figure 8.2). While the reason for this discrepancy is unclear, it is possible that the cell cycle related changes represented by the spectral features expressed in PC1 may be unique to tumour response kinetics when exposed to radiation *in vivo*, rather than *in vitro* cell cultures. This possibility is supported

by similar trends that we observed in a comparable PC score identified for NSCLC (H460) tumours irradiated *in vivo* [287].

PC2 identified a radiation induced increase in specific protein bands (tryptophan, proline, phenylalanine, β-sheet amide bands) relative to nucleic acid (adenine, guanine, thymine, cytosine and DNA backbone), protein (α-helix amide bands, C-N bands) and lipids (C-C and C-H) in tumours exposed to 15 Gy but not 5 Gy (Figure 8.3). PC2 was found to be highly correlated to a previously reported component from an *in vitro* study in which the spectral features were also found to arise from radiation doses of 6 Gy or higher [132]. These spectral features have not yet been linked to a specific biological process. Vilalta et al. have shown that MDA-MB-231 cells increase secretion of granulocyte-macrophage colony-stimulating factor (GMCSF) when exposed to doses above 4 or 5 Gy [309]. GMCSF is a glycoprotein that has been linked to tumour cell migration and self-seeding [309]. Further studies linking the protein features contained in PC2 to specific protein increases, such as GMCSF, would be valuable.

Both PC1 and PC2 contain spectral features linked to specific amino acids (tryptophan, phenylalanine, proline), as well as spectral features linked to general protein structure (e.g., β-sheet and α-helix amide bands). Tryptophan and phenylalanine have a propensity towards β-sheet secondary structure, and both PC1 and PC2 found that the spectral bands of these two amino acids were positively correlated with β-sheet spectral bands. While there is not enough information in this study to determine if there is a link between the amino acid bands and general protein structure bands isolated in the PCA results, it is possible that they are linked.

Importantly, since NOD/SCID mice lose both their T- and B-cell responses, an aspect of the overall response to radiation is lacking in this murine model. This lack of immune response may mean that the dominant Raman spectral signatures observed in the current murine model differ from what would be observed in the case of an intact immune system. While this is the case, the fact that RS can identify a biochemical response to radiation, as demonstrated in this study, is highly valuable.

Taken together, the results presented here demonstrate the applicability of RS to differentiate between irradiated and nonirradiated human breast adenocarcinoma xenografts. Previously published work addressing the use of RS to identify signatures of radioresponse in cancer tissue have been limited to NSCLC. To our knowledge, the

current work demonstrates for the first time that RS is not limited solely to NSCLC, and is in fact applicable to breast adenocarcinoma. Furthermore, we show that RS is not limited to the identification of carbohydrate-based biochemical changes, as was found for NSCLC [287]. Indeed, this report demonstrates both a common and unique component to the biochemical nature of the radiation response signature between breast and NSCLC xenografts. Specifically, the cell cycle-related set of spectral features identified in the current study appears to commonly trace radiation exposure in both NSCLC [287] and breast tumour xenografts. However, this study also identifies an additional unique radiation induced signature in breast adenocarcinoma (PC2) that involves protein, nucleic acid and lipid spectral bands.

8.6 Concluding statement

The importance of this study is underscored by the varied clinical responses to radiation therapy in breast cancer patients. These heterogeneous effects may be due to both spatial and temporal changes in the disease across dose and time. Here, we extend on previously reported findings to show that human breast adenocarcinoma xenografts that are irradiated show distinct biochemical and temporal evolution of Raman spectral features. Several physiological changes measured within the tissue were found to be linked to radiation exposure. These included molecular changes linked to cell cycle alterations as well as other protein, lipid and nucleic acid driven molecular changes that could be tracked at days 1 and 3. While the biological consequences of these Raman spectral transformations to radiation exposure require further investigation, this work emphasizes the utility of a Raman spectroscopy-based approach to identify potential new combinatorial strategies that may enhance the benefits of radiation treatment for breast cancer.

Chapter 9

Conclusion

This dissertation presents key steps towards implementation of Raman spectroscopy (RS) in radiation oncology. Distinct signatures of radiation response in human lung and breast tumour xenograft models were identified, investigated over various time points and linked to key radiation response factors for tumours. Taken together, this work asserts RS as a valuable technique for measuring radiation response in tumours. Further, clinical implementation of RS was explored through the investigation and development of Raman microfluidic systems.

Radiation induced accumulation of glycogen was found to occur in human non-small cell lung cancer (NSCLC) tumour xenografts exposed to doses of 5 and 15 Gy. This work presented the first application of RS to study radiation response signatures in tumours that were irradiated *in vivo*. Metabolic fluctuations as measured by changes in glycogen content using RS were found to vary, with an initial radiation induced reduction in glycogen at 2 hours post treatment. A subsequent and stable increase in glycogen was tracked with RS from 1 day up to 10 days post treatment. This work shows that RS is sensitive to radiation induced metabolic alterations in NSCLC and can track these changes for several days following treatment, facilitating applications to track radiation response in patient biopsies which may not be attainable immediately after irradiation.

Further, glycogen Raman signatures were found to be correlated to tumour regression and hypoxic status of the tumour. In particular, elevated levels of hypoxia as a result of an acute radiation exposure (2 hours post treatment) were found to be

associated with low glycogen levels. In contrast, increased glycogen levels were found to be associated with tumours that are regressing and reoxygenation within the tissue. Therefore, we show that RS offers a label-free and non-destructive (to tissue) technique for monitoring radiation induced metabolic alterations within the tumour as a result of oxygenation status of the tissue.

This technique was also applied to human breast adenocarcinoma tumour xenografts, and indicated a radiation induced Raman spectral signature linked to protein level alterations at 1 and 3 days following exposure to 15 Gy doses of radiation, but not 5 Gy. These results emphasize that RS is not limited solely to monitoring metabolism-based radiation responses, as found in NSCLC. Further, the nature of the radiation response Raman signature is dependent on the disease type, and gives macroscopic insight into the primary molecular mechanisms of radiation response for that disease.

Clinical implementation of single cell RS through development of a Raman microfluidic platform was also investigated. Candidate substrate materials were studied for their suitability in microfluidic applications with RS and engineering technicalities for developing the devices were investigated. Both a pure MgF_2 system and a Parafilm-MgF_2 system were found to produce reasonable spectral quality for applications of RS in radiobiology studies.

Taken together, RS is a valuable technique for measuring distinct radiobiological responses in human tumour xenografts that may be linked to relevant intra-tumoural factors for radiation resistance, including hypoxia (in the case of NSCLC). Several key directions of investigation should be pursued moving forward. Full assertion of RS for clinical implementation to measure radiation response in patients will rely on validation in human specimens. Therefore, clinical trials investigating the ability of RS to detect radiation response signatures either *in vivo* or based on patient biopsies should be pursued. Further, the immune response has the potential to influence Raman signatures and should be investigated. This work demonstrates the value of RS for radiobiological studies, offering a unique view into the molecular response of biological systems to radiation exposure. As such, there are several valuable avenues of applications of this technique for radiobiology investigations moving forward.

Raman spectroscopy can be used to monitor radiation responses in tumours, providing key insight into the driving factors of radiation response mechanisms in this complex environment. These signatures of radiation response provide valuable infor-

mation as a step towards monitoring and predicting radiation response in individuals during radiation therapy, ultimately leading towards a clinically amenable technique for personalization of radiation therapy.

Bibliography

[1] R. A. Weinberg, *The Biology of Cancer*. Garland Science, 2007. Chapter 2.

[2] K. D. Miller, R. L. Siegel, C. C. Lin, A. B. Mariotto, J. L. Kramer, J. H. Rowland, K. D. Stein, R. Alteri, and A. Jemal, "Cancer treatment and survivorship statistics, 2016," *CA: a cancer journal for clinicians*, vol. 66, no. 4, pp. 271–289, 2016.

[3] B. D. Smith, B. G. Haffty, L. D. Wilson, G. L. Smith, A. N. Patel, and T. A. Buchholz, "The future of radiation oncology in the united states from 2010 to 2020: Will supply keep pace with demand?," *Journal of clinical oncology*, vol. 28, no. 35, pp. 5160–5165, 2010.

[4] J. Bernier, E. J. Hall, and A. Giaccia, "Radiation oncology: a century of achievements," *Nature Reviews Cancer*, vol. 4, no. 9, p. 737, 2004.

[5] D. Verellen, M. De Ridder, N. Linthout, K. Tournel, G. Soete, and G. Storme, "Innovations in image-guided radiotherapy," *Nature Reviews Cancer*, vol. 7, no. 12, p. 949, 2007.

[6] H. Johns and J. Cunningham, "A precision Cobalt 60 unit for fixed field and rotation therapy," *Am. J. Roentgenol Radium Therapy Nuclear Med.*, vol. 81, pp. 4–12, 1959.

[7] J. V. Dyk, *The Modern Technology of Radiation Oncology, Volume 2: A compendium for Medical Physicists and Radiation Oncologists*. Madison, WI, USA: Medical Physics Publishing Corporation, 2005.

[8] T. Bortfeld, A. L. Boyer, W. Schlegel, D. Kahler, and T. Waldron, "Realization and verification of three-dimensional conformal radiotherapy with modulated

fields," *Int. J. Radiat. Oncol. Biol. Phys.*, vol. 30, no. 4, pp. 899–908, 1994.

[9] S. Webb, "The physical basis of IMRT and inverse planning," *Brit. J. Radiol.*, vol. 76, pp. 678–689, 2003.

[10] C. Nutting, D. Dearnaley, and S. Webb, "Intensity modulated radiation therapy: a clinical review," *Brit. J. Radiol.*, vol. 73, pp. 459–469, 2000.

[11] S. Marnitz, M. Stuschke, J. Bohsung, A. Moys, I. Reng, R. Wurm, and V. Budach, "Intraindividual comparison of conventional three-dimensional radiotherapy and intensity modulated radiotherapy in the therapy of locally advanced non-small cell lung cancer," *Strahlenther Onkol*, vol. 11, pp. 651–658, 2002.

[12] A. Eisbruch, L. Marsh, M. Martel, J. Ship, R. Haken, A. Pu, B. Fraass, and A. Lichter, "Comprehensive irradiation of head and neck cancer using conformal multisegmental fields: Assessment of target coverage and noninvolved tissue sparing.," *Int. J. Radiat. Oncol. Biol. Phys.*, vol. 41, no. 3, pp. 559–568, 1998.

[13] K. Vineberg, A. Eisbruch, M. Coselmon, D. McShan, M. Kessler, and B. Fraass, "Is uniform target dose possible in IMRT plans in the head and neck?," *Int. J. Radiat. Oncol. Biol. Phys.*, vol. 52, no. 5, pp. 1159–1172, 2002.

[14] M. Zelefsky, Z. Fuks, M. Hunt, Y. Yamada, C. Marion, C. Ling, H. Amols, E. Venkatraman, and S. Leibel, "High-dose intensity modulated radiation therapy for prostate cancer: Early toxicity and biochemical outcome in 772 patients," *Int. J. Radiat. Oncol. Biol. Phys.*, vol. 53, no. 5, pp. 1111–1116, 2002.

[15] C. Burman, C. Chui, G. Kutcher, S. Leibel, M. Zelefsky, T. LoSasso, S. Spirou, Q. Wu, J. Yang, J. Stein, R. Mohan, Z. Fuks, and C. Ling, "Planning, delivery and quality assurace of intensity-modulated radiotherapy using dynamic multileaf collimator: A strategy for large-scale implementation for the treatment of carcinoma of the prostate," *Int. J. Radiat. Oncol. Biol. Phys.*, vol. 39, no. 4, pp. 863–873, 1997.

[16] J. Bedford and A. Warrington, "Commissioning of volumetric modulated arc therapy (VMAT)," *Int. J. Radiat. Oncol. Biol. Phys.*, vol. 73, no. 2, pp. 537–545, 2009.

[17] M. Baumann, M. Krause, J. Overgaard, J. Debus, S. M. Bentzen, J. Daartz, C. Richter, D. Zips, and T. Bortfeld, "Radiation oncology in the era of precision medicine," *Nature Reviews Cancer*, vol. 16, no. 4, p. 234, 2016.

[18] H. Zhang and J.-J. Sonke, "Directional interpolation for motion weighted 4d cone-beam ct reconstruction," in *International Conference on Medical Image Computing and Computer-Assisted Intervention*, pp. 181–188, Springer, 2012.

[19] J. Olsen, O. Green, and R. Kashani, "World's first application of mr-guidance for radiotherapy.," *Missouri medicine*, vol. 112, no. 5, pp. 358–360, 2015.

[20] J. J. Lagendijk, B. W. Raaymakers, A. J. Raaijmakers, J. Overweg, K. J. Brown, E. M. Kerkhof, R. W. van der Put, B. Hårdemark, M. van Vulpen, and U. A. van der Heide, "Mri/linac integration," *Radiotherapy and Oncology*, vol. 86, no. 1, pp. 25–29, 2008.

[21] R. J. Ginsberg and L. V. Rubinstein, "Randomized trial of lobectomy versus limited resection for t1 n0 non-small cell lung cancer," *The Annals of Thoracic Surgery*, vol. 60, no. 3, pp. 615–623, 1995.

[22] H. Blomgren, I. Lax, I. Näslund, and R. Svanström, "Stereotactic high dose fraction radiation therapy of extracranial tumors using an accelerator: clinical experience of the first thirty-one patients," *Acta Oncologica*, vol. 34, no. 6, pp. 861–870, 1995.

[23] J. Wulf, U. Hädinger, U. Oppitz, W. Thiele, R. Ness-Dourdoumas, and M. Flentje, "Stereotactic radiotherapy of targets in the lung and liver," *Strahlentherapie und Onkologie*, vol. 177, no. 12, pp. 645–655, 2001.

[24] K. K. Herfarth, J. Debus, F. Lohr, M. L. Bahner, B. Rhein, P. Fritz, A. Hoss, W. Schlegel, and M. F. Wannenmacher, "Stereotactic single-dose radiation therapy of liver tumors: results of a phase i/ii trial," *Journal of Clinical Oncology*, vol. 19, no. 1, pp. 164–170, 2001.

[25] M. H. Bilsky, Y. Yamada, K. M. Yenice, M. Lovelock, M. Hunt, P. H. Gutin, and S. A. Leibel, "Intensity-modulated stereotactic radiotherapy of paraspinal tumors: a preliminary report," *Neurosurgery*, vol. 54, no. 4, pp. 823–831, 2004.

[26] E. L. Chang, A. S. Shiu, M.-F. Lii, L. D. Rhines, E. Mendel, A. Mahajan, J. S. Weinberg, L. A. Mathews, B. W. Brown, M. H. Maor, *et al.*, "Phase i clinical evaluation of near-simultaneous computed tomographic image-guided stereotactic body radiotherapy for spinal metastases," *International Journal of Radiation Oncology Biology Physics*, vol. 59, no. 5, pp. 1288–1294, 2004.

[27] P. C. Gerszten, S. A. Burton, C. P. Belani, S. Ramalingam, D. M. Friedland, C. Ozhasoglu, A. E. Quinn, K. J. McCue, and W. C. Welch, "Radiosurgery for the treatment of spinal lung metastases," *Cancer*, vol. 107, no. 11, pp. 2653–2661, 2006.

[28] S. Ryu, F. Fang Yin, J. Rock, J. Zhu, A. Chu, E. Kagan, L. Rogers, M. Ajlouni, M. Rosenblum, and J. H. Kim, "Image-guided and intensity-modulated radiosurgery for patients with spinal metastasis," *Cancer*, vol. 97, no. 8, pp. 2013–2018, 2003.

[29] R. L. Tanner, N. A. Baily, and J. W. Hilbert, "High-energy proton depth-dose patterns," *Radiation research*, vol. 32, no. 4, pp. 861–874, 1967.

[30] J. S. Loeffler and M. Durante, "Charged particle therapyoptimization, challenges and future directions," *Nature reviews Clinical oncology*, vol. 10, no. 7, p. 411, 2013.

[31] D. De Ruysscher, M. M. Lodge, B. Jones, M. Brada, A. Munro, T. Jefferson, and M. Pijls-Johannesma, "Charged particles in radiotherapy: a 5-year update of a systematic review," *Radiotherapy and Oncology*, vol. 103, no. 1, pp. 5–7, 2012.

[32] K. A. Kuhlthau, M. B. Pulsifer, B. Y. Yeap, D. R. Morales, J. Delahaye, K. S. Hill, D. Ebb, A. N. Abrams, S. M. MacDonald, N. J. Tarbell, *et al.*, "Prospective study of health-related quality of life for children with brain tumors treated with proton radiotherapy," *Journal of Clinical Oncology*, vol. 30, no. 17, p. 2079, 2012.

[33] R. Atun, D. A. Jaffray, M. B. Barton, F. Bray, M. Baumann, B. Vikram, T. P. Hanna, F. M. Knaul, Y. Lievens, T. Y. Lui, *et al.*, "Expanding global access to radiotherapy," *The lancet oncology*, vol. 16, no. 10, pp. 1153–1186, 2015.

[34] G. Minniti, D. Amelio, M. Amichetti, M. Salvati, R. Muni, A. Bozzao, G. Lanzetta, S. Scarpino, A. Arcella, and R. M. Enrici, "Patterns of failure and comparison of different target volume delineations in patients with glioblastoma treated with conformal radiotherapy plus concomitant and adjuvant temozolomide," *Radiotherapy and Oncology*, vol. 97, no. 3, pp. 377–381, 2010.

[35] A. Auperin, C. Le Pechoux, J. Pignon, C. Koning, B. Jeremic, G. Clamon, L. Einhorn, D. Ball, M. Trovo, H. Groen, *et al.*, "Concomitant radiochemotherapy based on platin compounds in patients with locally advanced non-small cell lung cancer (nsclc): a meta-analysis of individual data from 1764 patients," *Annals of oncology*, vol. 17, no. 3, pp. 473–483, 2006.

[36] M. Baumann, T. Herrmann, R. Koch, W. Matthiessen, S. Appold, B. Wahlers, L. Kepka, G. Marschke, D. Feltl, R. Fietkau, *et al.*, "Final results of the randomized phase iii chartwel-trial (aro 97-1) comparing hyperfractionated-accelerated versus conventionally fractionated radiotherapy in non-small cell lung cancer (nsclc)," *Radiotherapy and Oncology*, vol. 100, no. 1, pp. 76–85, 2011.

[37] J. A. Torok, Y. Wu, L. R. Prosnitz, G. J. Kim, A. W. Beaven, L. F. Diehl, and C. R. Kelsey, "Low-dose consolidation radiation therapy for early stage unfavorable hodgkin lymphoma," *International Journal of Radiation Oncology Biology Physics*, vol. 92, no. 1, pp. 54–59, 2015.

[38] E. Halperin, C. Perez, and L. Brady, *Principles and Practice of Radiation Oncology, 5^{th} edition*. Philadelphia, PA, USA: Lippincott Williams & Wilkins, 2008.

[39] A. Begg, "Predicting response to radiotherapy: Evolutions and revolutions," *Int. J. Radiat. Biol.*, vol. 85, no. 10, pp. 825–836, 2009.

[40] L. Peters, W. Brock, J. Chapman, and G. Wilson, "Predictive assays of tumor radiocurability," *Am. J. Clin. Oncol.*, vol. 11, no. 3, pp. 275–287, 1988.

[41] D. Azria, A. Lapierre, S. Gourgou, D. De Ruysscher, J. Colinge, P. Lambin, M. Brengues, T. Ward, S. M. Bentzen, H. Thierens, *et al.*, "Data-based radiation oncology: Design of clinical trials in the toxicity biomarkers era," *Frontiers in oncology*, vol. 7, p. 83, 2017.

[42] N. G. Burnet, J. Johansen, I. Turesson, J. Nyman, and J. H. Peacock, "Describing patients' normal tissue reactions: concerning the possibility of individualising radiotherapy dose prescriptions based on potential predictive assays of normal tissue radiosensitivity," *International journal of cancer*, vol. 79, no. 6, pp. 606–613, 1998.

[43] S. L. Tucker, F. B. Geara, L. J. Peters, and W. A. Brock, "How much could the radiotherapy dose be altered for individual patients based on a predictive assay of normal-tissue radiosensitivity?," *Radiotherapy and Oncology*, vol. 38, no. 2, pp. 103–113, 1996.

[44] L. Peters, "Radiation therapy tolerance limits: For one or for all? - Janeway Lecture," *Cancer*, vol. 77, no. 11, pp. 2379–2385, 1996.

[45] S. M. Bentzen and J. Overgaard, "Patient-to-patient variability in the expression of radiation-induced normal tissue injury," in *Seminars in radiation oncology*, vol. 4, pp. 68–80, Elsevier, 1994.

[46] C. N. Andreassen, J. Alsner, and J. Overgaard, "Does variability in normal tissue reactions after radiotherapy have a genetic basis–where and how to look for it?," *Radiotherapy and Oncology*, vol. 64, no. 2, pp. 131–140, 2002.

[47] R. P. Hill, R. G. Bristow, A. Fyles, M. Koritzinsky, M. Milosevic, and B. G. Wouters, "Hypoxia and predicting radiation response," in *Seminars in radiation oncology*, vol. 25, pp. 260–272, Elsevier, 2015.

[48] A. Marusyk, V. Almendro, and K. Polyak, "Intra-tumour heterogeneity: a looking glass for cancer?," *Nature Reviews Cancer*, vol. 12, no. 5, p. 323, 2012.

[49] F. Lohaus, A. Linge, I. Tinhofer, V. Budach, E. Gkika, M. Stuschke, P. Balermpas, C. Rödel, M. Avlar, A.-L. Grosu, *et al.*, "Hpv16 dna status is a strong prognosticator of loco-regional control after postoperative radiochemotherapy of locally advanced oropharyngeal carcinoma: results from a multicentre explorative study of the german cancer consortium radiation oncology group (dktk-rog)," *Radiotherapy and oncology*, vol. 113, no. 3, pp. 317–323, 2014.

[50] A. Linge, S. Löck, V. Gudziol, A. Nowak, F. Lohaus, C. von Neubeck, M. Jütz, A. Abdollahi, J. Debus, I. Tinhofer, *et al.*, "Low cancer stem cell marker ex-

pression and low hypoxia identify good prognosis subgroups in hpv (-) hnscc after postoperative radiochemotherapy: a multicenter study of the dktk-rog," *Clinical Cancer Research*, vol. 22, no. 11, pp. 2639–2649, 2016.

[51] T. Bjork-Eriksson, C. West, E. Karlsson, and C. Mercke, "Tumor radiosensitivity (SF_2) is a prognostic factor for local control in head and neck cancer," *Int. J. Radiat. Oncol. Biol. Phys.*, vol. 46, no. 1, pp. 13–19, 2000.

[52] C. West, S. Davidson, S. Roberts, and R. Hunter, "The independence of intrinsic radiosensitivity as a prognostic factor for patient response to radiotherapy of carcinoma of the cervix.," *Brit. J. Cancer*, vol. 76, no. 9, pp. 1184–1190, 1997.

[53] T. Bjork-Eriksson, C. West, E. Karlsson, N. Slevin, S. Davidson, R. James, and C. Mercke, "The in vitro radiosensitivity of human head and neck cancers," *Brit. J. Cancer.*, vol. 77, no. 12, pp. 2371–2375, 1998.

[54] E. C. Bourton, P. N. Plowman, D. Smith, C. F. Arlett, and C. N. Parris, "Prolonged expression of the gamma-H2AX DNA repair biomarker correlates with excess acute and chronic toxicity from radiotherapy treatment," *International Journal of Cancer*, vol. 129, no. 12, pp. 2928–2934, 2011.

[55] J. M. Coco Martin, E. Mooren, C. Ottenheim, W. Burrill, M. I. Nunez, D. Sprong, H. Bartelink, and A. C. Begg, "Potential of radiation-induced chromosome aberrations to predict radiosensitivity in human tumour cells.," *International journal of radiation biology*, vol. 75, no. 9, pp. 1161–1168, 1999.

[56] E. L. Levine, A. Renehan, R. Gossiel, S. E. Davidson, S. A. Roberts, C. Chadwick, D. P. Wilks, C. S. Potten, J. H. Hendry, and R. D. Hunter, "Apoptosis, intrinsic radiosensitivity and prediction of radiotherapy response in cervical carcinoma.," *Radiotherapy and oncology : journal of the European Society for Therapeutic Radiology and Oncology*, vol. 37, no. 1, pp. 1–9, 1995.

[57] M. Nordsmark and J. Overgaard, "A confirmatory prognostic study on oxygenation status and loco-regional control in advanced head and neck squamous cell carcinoma treated by radiation therapy," *Radiotherapy and Oncology*, vol. 57, no. 1, pp. 39–43, 2000.

[58] P. Vaupel, K. Schlenger, C. Knoop, and M. Höckel, "Oxygenation of human tumors: evaluation of tissue oxygen distribution in breast cancers by computer-

ized o2 tension measurements," *Cancer research*, vol. 51, no. 12, pp. 3316–3322, 1991.

[59] M. I. Koukourakis, A. Giatromanolaki, E. Sivridis, K. Simopoulos, J. Pastorek, C. C. Wykoff, K. C. Gatter, and A. L. Harris, "Hypoxia-regulated carbonic anhydrase-9 (ca9) relates to poor vascularization and resistance of squamous cell head and neck cancer to chemoradiotherapy," *Clinical Cancer Research*, vol. 7, no. 11, pp. 3399–3403, 2001.

[60] M. Luukkaa, T. Jokilehto, P. Kronqvist, T. Vahlberg, R. Grénman, P. Jaakkola, and H. Minn, "Expression of the cellular oxygen sensor phd2 (egln-1) predicts radiation sensitivity in squamous cell cancer of the head and neck," *International journal of radiation biology*, vol. 85, no. 10, pp. 900–908, 2009.

[61] A. C. Begg, K. Haustermans, A. A. Hart, S. Dische, M. Saunders, B. Zackrisson, H. Gustaffson, P. Coucke, N. Paschoud, M. Hoyer, *et al.*, "The value of pretreatment cell kinetic parameters as predictors for radiotherapy outcome in head and neck cancer: a multicenter analysis," *Radiotherapy and Oncology*, vol. 50, no. 1, pp. 13–23, 1999.

[62] A. Urruticoechea, I. E. Smith, and M. Dowsett, "Proliferation marker ki-67 in early breast cancer," *Journal of clinical oncology*, vol. 23, no. 28, pp. 7212–7220, 2005.

[63] N. Bouzubar, K. Walker, K. Griffiths, I. Ellis, C. Elston, J. Robertson, R. Blamey, and R. Nicholson, "Ki67 immunostaining in primary breast cancer: pathological and clinical associations," *British journal of cancer*, vol. 59, no. 6, p. 943, 1989.

[64] N. N. Khodarev, M. Beckett, E. Labay, T. Darga, B. Roizman, and R. R. Weichselbaum, "Stat1 is overexpressed in tumors selected for radioresistance and confers protection from radiation in transduced sensitive cells," *Proceedings of the National Academy of Sciences of the United States of America*, vol. 101, no. 6, pp. 1714–1719, 2004.

[65] A. McIlwrath, P. Vasey, G. Ross, and R. Brown, "Cell cycle arrests and radiosensitivity of human tumor cell lines: Dependence on wild-type p53 for radiosensitivity," *Cancer Res.*, vol. 54, pp. 3718–3722, 1994.

[66] W. Slichenmyer, W. Nelson, R. Slebos, and M. Kastan, "Loss of p53-associated G1 checkpoint does not decrease cell survival following DNA damage," *Cancer Res.*, vol. 53, pp. 4164–4168, 1993.

[67] S. Scott, J. Earle, and P. Gumerlock, "Functional p53 increases prostate cancer cell survival after exposure to fractionated doses of ionizing radiation," *Cancer Res.*, vol. 63, pp. 7190–7196, 2003.

[68] J. Williams, Y. Zhang, J. Russell, C. Koch, and J. Little, "Human tumor cells segregate into radiosensitivity groups that associate with ATM and TP53 status," *Acta Oncologica*, vol. 46, pp. 628–638, 2007.

[69] J. Williams, Y. Zhang, H. Zhou, D. Gridley, C. Koch, J. Russel, J. Slater, and J. Little, "A quantitative overview of radiosensitivity of human tumor cells across histological type and TP53 status," *Int. J. Radiat. Biol.*, vol. 84, no. 4, pp. 253–264, 2008.

[70] C. Speers, S. Zhao, M. Liu, H. Bartelink, L. J. Pierce, and F. Y. Feng, "Development and Validation of a Novel Radiosensitivity Signature in Human Breast Cancer," *Clinical Cancer Research*, vol. 21, no. 16, pp. 3667–3678, 2015.

[71] S. Eschrich, J. Pramana, H. Zhang, H. Zhao, D. Boulware, J. Lee, G. Bloom, C. Rocha-Lima, S. Kelley, D. Calvin, T. Yeatman, A. Begg, and J. Torres-Roca, "A gene expression model of intrinsic tumor radiosensitivity: Prediction of response and prognosis after chemoradiation," *Int. J. Radiat. Oncol. Biol. Phys.*, vol. 75, no. 2, pp. 489–496, 2009.

[72] J. Torres-Roca, S.Eschrich, H. Zhao, G. Bloom, J. Sung, S. McCarthy, A. Cantor, A. Scuto, C. Li, S. Zhang, R. Jove, and T. Yeatman, "Prediction of radiation sensitivity using a gene expression classifier," *Cancer Res.*, vol. 65, no. 16, pp. 7169–7176, 2005.

[73] K. A. Ahmed, J. J. Caudell, G. El-Haddad, A. E. Berglund, E. A. Welsh, B. Yue, S. E. Hoffe, A. O. Naghavi, Y. A. Abuodeh, J. M. Frakes, *et al.*, "Radiosensitivity differences between liver metastases based on primary histology suggest implications for clinical outcomes after stereotactic body radiation therapy," *International Journal of Radiation Oncology Biology Physics*, vol. 95, no. 5, pp. 1399–1404, 2016.

[74] K. A. Ahmed, P. Chinnaiyan, W. J. Fulp, S. Eschrich, J. F. Torres-Roca, and J. J. Caudell, "The radiosensitivity index predicts for overall survival in glioblastoma," *Oncotarget*, vol. 6, no. 33, p. 34414, 2015.

[75] S. Eschrich, W. Fulp, Y. Pawitan, J. F. nd M. Smid, J. Martens, M. Echevarria, W. Kamath, J. Lee, E. Harris, J. Bergh, and J. Torres-Roca, "Validation of a radiosensitivity molecular signature in breast cancer," *Clin. Cancer Res.*, vol. 18, no. 18, pp. 5134–5143, 2012.

[76] J. G. Scott, A. Berglund, M. J. Schell, I. Mihaylov, W. J. Fulp, B. Yue, E. Welsh, J. J. Caudell, K. Ahmed, T. S. Strom, *et al.*, "A genome-based model for adjusting radiotherapy dose (gard): a retrospective, cohort-based study," *The Lancet Oncology*, vol. 18, no. 2, pp. 202–211, 2017.

[77] J. C. Kim, Y. J. Ha, S. A. Roh, D. H. Cho, E. Y. Choi, T. W. Kim, J. H. Kim, T. W. Kang, S. Y. Kim, and Y. S. Kim, "Novel single-nucleotide polymorphism markers predictive of pathologic response to preoperative chemoradiation therapy in rectal cancer patients," *International Journal of Radiation Oncology Biology Physics*, vol. 86, no. 2, pp. 350–357, 2013.

[78] E. D. Maring, P. S. Tawadros, C. J. Steer, and J. T. Lee, "Systematic review of candidate single-nucleotide polymorphisms as biomarkers for responsiveness to neoadjuvant chemoradiation for rectal cancer," *Anticancer research*, vol. 35, no. 7, pp. 3761–3766, 2015.

[79] N. Niu, Y. Qin, B. L. Fridley, J. Hou, K. R. Kalari, M. Zhu, T.-Y. Wu, G. D. Jenkins, A. Batzler, and L. Wang, "Radiation pharmacogenomics: a genome-wide association approach to identify radiation response biomarkers using human lymphoblastoid cell lines," *Genome research*, vol. 20, no. 11, pp. 1482–1492, 2010.

[80] A. A. Chaudhuri, M. S. Binkley, E. C. Osmundson, A. A. Alizadeh, and M. Diehn, "Predicting Radiotherapy Responses and Treatment Outcomes Through Analysis of Circulating Tumor DNA," *Seminars in Radiation Oncology*, vol. 25, no. 4, pp. 305–312, 2015.

[81] S. A. Mattonen, D. A. Palma, C. Johnson, A. V. Louie, M. Landis, G. Rodrigues, I. Chan, R. Etemad-Rezai, T. P. Yeung, S. Senan, *et al.*, "Detection of

local cancer recurrence after stereotactic ablative radiation therapy for lung cancer: physician performance versus radiomic assessment," *International Journal of Radiation Oncology Biology Physics*, vol. 94, no. 5, pp. 1121–1128, 2016.

[82] A. Marusyk and K. Polyak, "Tumor heterogeneity: causes and consequences," *BBBA-Rev. Cancer*, vol. 1805, no. 1, pp. 105–117, 2010.

[83] J. Rajendran, D. Schwartz, J. O'Sullivan, L. Peterson, P. Ng, J. Scharnhorst, J. Grierson, and K. Krohn, "Tumor hypoxia imaging with [F-18] fluoromisonidazole positron emission tomography in head and neck cancer," *Clin. Cancer Res.*, vol. 12, no. 18, pp. 5435–5441, 2006.

[84] N. Mayr, W. Yuh, J. Arnholt, J. Ehrhardt, J. Sorosky, V. Magnotta, K. Berbaum, W. Zhen, A. Paulino, L. Oberley, A. Sood, and J. Buatti, "Pixel analysis of MR perfusion imaging in predicting radiation therapy outcome in cervical cancer," *J. Magn. Reson. Imaging*, vol. 12, no. 6, pp. 1027–1033, 2000.

[85] M. Fuss, F. Wenz, M. Essig, M. Muenter, J. Debus, T. Herman, and M. Wannenmacher, "Tumor angiogenesis of low-grade astrocytomas measured by dynamic susceptibility contrast-enhanced MRI (DSC-MRI) is predictive of local tumor control after radiation therapy," *Int. J. Radiat. Oncol. Biol. Phys.*, vol. 51, no. 2, pp. 478–482, 2001.

[86] A. Salskov, V. Tammisetti, J. Grierson, and H. Vesselle, "FLT: Measuring Tumor Cell Proliferation In Vivo With Positron Emission Tomography and 3-Deoxy-3-[F^{18}] Fluorothymidine," in *Semin. Nucl. Med.*, vol. 37, pp. 429–439, Elsevier, 2007.

[87] H. Keen, B. Dekker, L. Disley, D. Hastings, S. Lyons, A. Reader, P. Ottewell, A. Watson, and J. Zweit, "Imaging apoptosis in vivo using I^{124}-annexin V and PET," *Nucl. Med. Biol.*, vol. 32, no. 4, pp. 395–402, 2005.

[88] S. Nimmagadda, E. Ford, J. Wong, and M. Pomper, "Targeted molecular imaging in oncology: focus on radiation therapy," in *Semin. Radiat. Oncol.*, vol. 18, pp. 136–148, Elsevier, 2008.

[89] C. Van de Wiele, C. Lahorte, W. Oyen, O. Boerman, I. Goethals, G. Slegers, and R. Dierckx, "Nuclear medicine imaging to predict response to radiotherapy: a review," *Int. J. Radiat. Oncol. Biol. Phys.*, vol. 55, no. 1, pp. 5–15, 2003.

[90] C. Capirci, L. Rampin, P. Erba, F. Galeotti, G. Crepaldi, E. Banti, M. Gava, S. Fanti, G. Mariani, P. Muzzio, and D. Rubello, "Sequential FDG-PET/CT reliably predicts response of locally advanced rectal cancer to neo-adjuvant chemo-radiation therapy," *Eur. J. Nucl. Med. Mol. Imaging*, vol. 34, no. 10, pp. 1583–1593, 2007.

[91] H. Fabian and P. Anzenbacher, "New developments in Raman spectroscopy of biological systems," *Vib. Spectrosc.*, vol. 4, no. 2, pp. 125–148, 1993.

[92] A. Alix, G. Pedanou, and M. Berjot, "Fast determination of the quantitative secondary structure of proteins by using some parameters of the Raman amide I band," *J. Mol. Struct.*, vol. 174, pp. 159–164, 1988.

[93] D. Goodwin and J. Brahms, "Form of DNA and the nature of interactions with proteins in chromatin," *Nucleic Acids Res.*, vol. 5, no. 3, pp. 836–850, 1978.

[94] G. Thomas Jr, "Raman spectroscopy of protein and nucleic acid assemblies," *Annu. Rev. Biophys. Biomol. Struct.*, vol. 28, no. 1, pp. 1–27, 1999.

[95] G. Puppels, F. de Mul, C. Otto, J. Greve, M. Robert-Nicoud, D. Arndt-Jovin, and T. Jovin, "Studying single living cells and chromosomes by confocal Raman microspectroscopy," *Nature*, vol. 347, pp. 301–302, 1990.

[96] G. J. Puppels, H. S. Garritsen, G. M. Segers-Nolten, F. F. de Mul, and J. Greve, "Raman microspectroscopic approach to the study of human granulocytes.," *Biophysical journal*, vol. 60, no. 5, pp. 1046–1056, 1991.

[97] I. Notingher, S. Verrier, S. Haque, J. M. Polak, and L. L. Hench, "Spectroscopic study of human lung epithelial cells (A549) in culture: Living cells versus dead cells," *Biopolymers - Biospectroscopy Section*, vol. 72, no. 4, pp. 230–240, 2003.

[98] K. Short, S. Carpenter, J. Freyer, and J. Mourant, "Raman spectroscopy detects biochemical changes due to proliferation in mammalian cell cultures," *Biophys. J.*, vol. 88, pp. 4274–4288, 2005.

[99] S. Verrier, I. Notingher, J. Polak, and L. Hench, "In situ monitoring of cell death using Raman microspectroscopy," *Biopolymers*, vol. 74, pp. 157–162, 2004.

[100] C. Krafft, L. Neudert, T. Simat, and R. Salzer, "Near infrared Raman spectra of human brain lipids," *Spectrochim. Acta A*, vol. 61, pp. 1529–1535, 2005.

[101] C. Sudworth and N. Krasner, "Raman spectroscopy of Alzheimer's diseased tissue," in *Biomedical Optics 2004*, pp. 93–101, International Society for Optics and Photonics, 2004.

[102] C. Sudworth, J. Archer, and D. Mann, "The potential use of Raman spectroscopy for the diagnosis of Alzheimer's disease," in *Photonics North 2005*, pp. 59691G–59691G, International Society for Optics and Photonics, 2005.

[103] J. Caillé, M. Pigeon-Gosselin, and M. Pézolet, "Laser Raman study of internally perfused muscle fibers effect of Mg^{2+}, ATP and Ca^{2+}," *BBA-Gen. Subjects*, vol. 758, no. 2, pp. 121–127, 1983.

[104] R. Manoharan, Y. Wang, and M. Feld, "Histochemical analysis of biological tissues using Raman spectroscopy," *Spectrochim. Acta A*, vol. 52, pp. 215–249, 1996.

[105] Q. Matthews, A. G. Brolo, J. Lum, X. Duan, and A. Jirasek, "Raman spectroscopy of single human tumour cells exposed to ionizing radiation in vitro.," *Physics in medicine and biology*, vol. 56, no. 1, pp. 19–38, 2011.

[106] S. Hawi, W. Campbell, A. Kajdacsy-Balla, R. Murphy, F. Adar, and K. Nithipatikom, "Characterization of normal and malignant human hepatocytes by Raman microspectroscopy," *Cancer Lett.*, vol. 110, pp. 35–40, 1996.

[107] A. Mizuno, H. Kitajima, K. Kawauchi, S. Muraishi, and Y. Ozaki, "Near-infrared Fourier transform Raman spectroscopic study of human brain tissues and tumours," *J. Raman Spectrosc.*, vol. 25, no. 1, pp. 25–29, 1994.

[108] C. Frank and R. McCreery, "Raman specroscopy of normal and diseased human breast tissues," *Anal. Chem.*, vol. 67, pp. 777–783, 1995.

[109] A. Haka, K. Shafer-Peltier, M. Fitzmaurice, J. Crowe, R. Dasari, and M. Feld, "Diagnosing breast cancer by using Raman spectroscopy," *PNAS*, vol. 102, no. 35, pp. 12371–12376, 2005.

[110] C. Liu, B. Das, W. S. Glassman, G. Tang, K. Yoo, H. Zhu, D. Akins, S. Lubicz, J. Cleary, R. Prudente, E. Celmer, A. Caron, and R. Alfano, "Raman, fluorescence, and time-resolved light scattering as optical diagnostic techniques

to separate diseased and normal biomedical media," *J. Photochem. Photobiol. B: Biol.*, vol. 16, pp. 187–209, 1992.

[111] C. Krishna, N. Prathima, R. Malini, B. Vadhiraja, R. Bhatt, D. Fernandes, P. Kushtagi, M. Vidyasagar, and V. Kartha, "Raman specroscopy studies for diagnosis of cancers in human uterine cervix," *Vib. Spectrosc.*, vol. 41, pp. 136–141, 2006.

[112] K. Chen, Y. Qin, F. Zheng, M. Sun, and D. Shi, "Diagnosis of colorectal cancer using Raman spectroscopy of laser-trapped single living epithelial cells," *Opt. Lett.*, vol. 31, no. 13, pp. 2015–2017, 2006.

[113] M. Feld, R. Manoharan, J. Salenius, J. Orenstein-Carndona, T. Roemer, J. F. Brennan III, R. Dasari, and Y. Wang, "Detection and characterization of human tissue lesions with near-infrared Raman spectroscopy," *SPIE*, vol. 2388, pp. 99–104, 1995.

[114] A. Molckovsky, L. W. K. Song, M. Shim, N. Marcon, and B. Wilson, "Diagnostic potential of near-infrared Raman spectroscopy in the colon: differentiating adenomatous fom hyperplastic polyps," *Gastrointest. Endosc.*, vol. 57, no. 3, pp. 396–402, 2003.

[115] N. Stone, C. Kendall, N. Shepherd, P. Crow, and H. Barr, "Near-infrared Raman spectroscopy for the classification of epithelial pre-cancers and cancers," *Journal of Raman Spectroscopy*, vol. 33, no. 7, pp. 564–573, 2002.

[116] D. Lau, Z. Huang, H. Lui, C. Man, K. Berean, M. Morrison, and H. Zeng, "Raman spectroscopy for optical diagnosis in normal and cancerous tissue of the nasopharynx- preliminary findings," *Laser. Surg. Med.*, vol. 32, pp. 210–214, 2003.

[117] C. Lieber, S. Majumder, D. Ellis, D. Billheimer, and A. Mahadevan-Jansen, "In vivo nonmelanoma skin cancer diagnosis using Raman microspectroscopy," *Laser. Surg. Med.*, vol. 40, pp. 461–467, 2008.

[118] A. Mahadevan-Jansen, M. Mitchell, N. Ramanujam, U. Utzinger, and R. Richards-Kortum, "Development of a fiber optic probe to measure NIR Raman spectra of cervical tissue in vivo," *Photochem. Photobiol.*, vol. 68, no. 3, pp. 427–431, 1998.

[119] A. Nijssen, T. B. Schut, F. Heule, P. Caspers, D. Hayes, M. Neumann, and G. Puppels, "Discriminating basal cell carcinoma from its surrounding tissue by Raman spectroscopy," *J. Invest. Dermatol.*, vol. 119, no. 1, pp. 64–69, 2002.

[120] J. Desroches, M. Jermyn, K. Mok, C. Lemieux-Leduc, J. Mercier, K. St-Arnaud, K. Urmey, M.-C. Guiot, E. Marple, K. Petrecca, *et al.*, "Characterization of a raman spectroscopy probe system for intraoperative brain tissue classification," *Biomedical optics express*, vol. 6, no. 7, pp. 2380–2397, 2015.

[121] C. Frank and R. McCreery, "The use of Raman spectroscopy to differentiate between different prostatic adenocarcinoma cell lines," *Brit. J. Cancer*, vol. 92, pp. 2166–2170, 2005.

[122] C. P. Shaw and A. Jirasek, "The use of ultraviolet resonance raman spectroscopy in the analysis of ionizing-radiation-induced damage in dna," *Applied Spectroscopy*, vol. 63, no. 4, pp. 412–422, 2009.

[123] K. Sailer, "Radiation-induced structural modifications in dsDNA analysed by FT-Raman spectroscopy," *Int. J. Radiat. Biol.*, vol. 69, no. 5, pp. 601–613, 1996.

[124] A. Synytsya, P. Alexa, J. de Boer, M. Loewe, M. Moosburger, M. Wurkner, and K. Volka, "Raman spectroscopic study of calf thymus DNA: an effect of proton- and γ-irradiation," *J. Raman Spectrosc.*, vol. 38, pp. 1406–1415, 2007.

[125] A. Synytsya, P. Alexa, J. de Boer, M. Loewe, M. Moosburger, M. Wurkner, and K. Volka, "Raman spectroscopic study of serum albumins: an effect of proton and γ-irradiation," *J. Raman Spectrosc.*, vol. 38, pp. 1646–1655, 2007.

[126] A. Torreggiani, M. Tamba, I. Manco, M. Faraone-Mennella, C. Ferreri, and C. Chatgilialoglu, "Radiation damage of lysozyme in a biomimetic model: some insights by Raman spectroscopy," *J. Mol. Struct.*, vol. 744, pp. 767–773, 2005.

[127] K. Sailer, S. Viaggi, and M. Nusse, "Kinetics of radiation- and cytochrome c- induced modifications in liposomes analysed by FT- Raman spectroscopy," *BBA*, vol. 1329, pp. 259–268, 1997.

[128] S. Verma, "Low levels of irradiation modify lipid domains in model membranes: A laser Raman study," *Radiat. Res.*, vol. 107, pp. 183–193, 1986.

[129] S. Verma and A. Rastogi, "Role of proteins in protection against radiation-induced damage in membranes," *Radiat. Res.*, vol. 122, pp. 130–136, 1990.

[130] S. Verma and N. Sonwalkar, "Structural changes in plasma membranes prepared from irradiated Chinese hamster V79 cells as revealed by Raman spectroscopy," *Radiat. Res.*, vol. 126, pp. 27–35, 1991.

[131] A. Synytsya, A. Synytsya, P. Alexa, R. Wagner, M. Davidkova, and K. Volka, "Raman spectroscopic study on sodium hyaluronate: an effect of proton and γ irradiation," *J. Raman Spectrosc.*, vol. 42, pp. 544–550, 2011.

[132] S. J. Harder, Q. Matthews, M. Isabelle, A. Brolo, J. Lum, and A. Jirasek, "A Raman spectroscopic study of cell response to clinical doses of ionizing radiation," *Applied Spectroscopy*, vol. 69, no. 2, 2015.

[133] S. J. Harder, "Raman Spectroscopy of Tumour Cells Exposed to Clinically Relevant Doses of Ionizing Radiation," Master's thesis, University of Victoria, 2013.

[134] N. Jafarzadeh, A. Mani-Varnosfaderani, K. Gilany, S. Eynali, H. Ghaznavi, and A. Shakeri-Zadeh, "The molecular cues for the biological effects of ionizing radiation dose and post-irradiation time on human breast cancer skbr3 cell line: A raman spectroscopy study," *Journal of Photochemistry and Photobiology B: Biology*, vol. 180, pp. 1–8, 2018.

[135] Q. Matthews, A. Jirasek, J. Lum, and A. Brolo, "Biochemical signatures of in vitro radiation response in human lung, breast and prostate tumour cells observed with Raman spectroscopy," *Phys. Med. Biol*, vol. 56, pp. 6839–6855, 2011.

[136] P. Meksiarun, P. H. Aoki, S. J. Van Nest, R. G. Sobral-Filho, J. J. Lum, A. G. Brolo, and A. Jirasek, "Breast cancer subtype specific biochemical responses to radiation," *Analyst*, 2018.

[137] A. D. Meade, O. Howe, V. Unterreiner, G. D. Sockalingum, H. J. Byrne, and F. M. Lyng, "Vibrational spectroscopy in sensing radiobiological effects: analyses of targeted and non-targeted effects in human keratinocytes.," *Faraday discussions*, vol. 187, pp. 213–234, 2016.

[138] D. Rizzo, *Fundamentals of Anatomy and Physiology 3ed.* Clifton Park, N.Y.: Delmar Cengage Learning, 2010.

[139] M. Yasser, R. Shaikh, M. K. Chilakapati, and T. Teni, "Raman spectroscopic study of radioresistant oral cancer sublines established by fractionated ionizing radiation," *PLoS ONE*, vol. 9, no. 5, 2014.

[140] M. S. Vidyasagar, K. Maheedhar, B. M. Vadhiraja, D. J. Fernendes, V. B. Kartha, and C. M. Krishna, "Prediction of radiotherapy response in cervix cancer by Raman spectroscopy: A pilot study," *Biopolymers*, vol. 89, no. 6, pp. 530–537, 2008.

[141] A. Maguire, I. Vegacarrascal, L. White, B. McClean, O. Howe, F. M. Lyng, and A. D. Meade, "Analyses of ionizing radiation effects in vitro in peripheral blood lymphocytes with Raman spectroscopy," *Radiation Research*, vol. 183, 2015.

[142] A. Synytsya, P. Alexa, J. Besserer, J. De Boer, S. Froschauer, R. Gerlach, M. Loewe, M. Moosburger, I. Obstová, P. Quicken, B. Sosna, K. Volka, and M. Würkner, "Raman spectroscopy of tissue samples irradiated by protons.," *International journal of radiation biology*, vol. 80, no. 8, pp. 581–591, 2004.

[143] R. Jyothi Lakshmi, V. B. Kartha, C. Murali Krishna, J. G. R Solomon, G. Ullas, and P. Uma Devi, "Tissue Raman spectroscopy for the study of radiation damage: brain irradiation of mice.," *Radiation research*, vol. 157, no. 2, pp. 175–182, 2002.

[144] J. Orten and O. Neuhaus, *Human Biochemistry 9ed.* Saint Louis, MO, USA: The C.V. Mosby Company, 1975.

[145] E. Travis, *Primer of Medical Radiobiology 2ed.* St. Louis, MO, USA: Mosby-Year Book, INC., 1989.

[146] S. Bolsover, E. Shephard, H. White, and J. Hyams, *Cell Biology: A Short Course.* Hoboken, NJ, USA: John Wiley & Sons, Inc., 2011.

[147] Z. Darzynkiewicz, T. Sharpless, L. Staiano-Coico, and M. Melamed, "Subcompartments of the G1 phase of cell cycle detected by flow cytometry," *Proc. Natl. Acad. Sci. USA*, vol. 77, no. 11, pp. 6696–6699, 1980.

[148] H. Crissman, Z. Darzynkiewicz, R. Tobey, and J. Steinkamp, "Correlated measurements of DNA, RNA, and protein in individual cells by flow cytometry," *Science*, vol. 228, no. 4705, pp. 1321–1324, 1985.

[149] Z. Darzynkiewicz, F. Traganos, and M. Melamed, "New cell cycle compartments identified by multiparameter flow cytometry," *Cytometry*, vol. 1, no. 2, pp. 98–108, 1980.

[150] H. Lodish, A. Berk, S. L. Zipursky, P. Matsudaira, D. Baltimore, and J. Darnell, *Molecular Cell Biology 4ed.* New York, NY, USA: W.H. Freeman, 2000.

[151] B. Alberts, D. Bray, K. Hopkin, A. Johnson, J. Lewis, M. Raff, K. Roberts, and P. Walter, *Essential cell biology.* Garland Science, 2014.

[152] C. E. Zois, E. Favaro, and A. L. Harris, "Glycogen metabolism in cancer," *Biochemical pharmacology*, vol. 92, no. 1, pp. 3–11, 2014.

[153] P. J. Roach, A. A. Depaoli-Roach, T. D. Hurley, and V. S. Tagliabracci, "Glycogen and its metabolism: some new developments and old themes," *Biochemical Journal*, vol. 441, no. 3, pp. 763–787, 2012.

[154] R. Singh and A. M. Cuervo, "Autophagy in the cellular energetic balance," *Cell metabolism*, vol. 13, no. 5, pp. 495–504, 2011.

[155] O. H. Warburg and F. Dickens, *The metabolism of tumours: investigations from the Kaiser Wilhelm Institute for Biology, Berlin-Dahlem.* Constable & Company Limited, 1930.

[156] O. Warburg, "On the origin of cancer cells," *Science*, vol. 123, no. 3191, pp. 309–314, 1956.

[157] O. Warburg, "On respiratory impairment in cancer cell," *Science*, vol. 124, no. 3215, pp. 269–270, 1956.

[158] D. Hanahan and R. A. Weinberg, "Hallmarks of cancer: the next generation," *cell*, vol. 144, no. 5, pp. 646–674, 2011.

[159] R. G. Jones and C. B. Thompson, "Tumor suppressors and cell metabolism: a recipe for cancer growth," *Genes & development*, vol. 23, no. 5, pp. 537–548, 2009.

[160] R. J. DeBerardinis, J. J. Lum, G. Hatzivassiliou, and C. B. Thompson, "The biology of cancer: metabolic reprogramming fuels cell growth and proliferation," *Cell metabolism*, vol. 7, no. 1, pp. 11–20, 2008.

[161] P. P. Hsu and D. M. Sabatini, "Cancer cell metabolism: Warburg and beyond," *Cell*, vol. 134, no. 5, pp. 703–707, 2008.

[162] M. Gerlinger, A. J. Rowan, S. Horswell, J. Larkin, D. Endesfelder, E. Gronroos, P. Martinez, N. Matthews, A. Stewart, P. Tarpey, I. Varela, B. Phillimore, S. Begum, N. Q. Mcdonald, A. Butler, D. Jones, K. Raine, C. Latimer, C. R. Santos, M. Nohadani, A. C. Eklund, B. Spencer-dene, G. Clark, L. Pickering, G. Stamp, M. Gore, Z. Szallasi, J. Downward, P. A. Futreal, and C. Swanton, "Intratumor heterogeneity and branched evolution revealed by multiregion sequencing," *New England Journal of Medicine*, vol. 366, no. 10, pp. 883–892, 2012.

[163] P. Vaupel, "Tumor microenvironmental physiology and its implications for radiation oncology," *Seminars in Radiation Oncology*, vol. 14, no. 3, pp. 198–206, 2004.

[164] M. Yoshimura, S. Itasaka, H. Harada, and M. Hiraoka, "Microenvironment and radiation therapy," *BioMed Research International*, vol. 2013, 2012.

[165] S. J. Lunt, N. Chaudary, and R. P. Hill, "The tumor microenvironment and metastatic disease," *Clinical & experimental metastasis*, vol. 26, no. 1, pp. 19–34, 2009.

[166] M. Dewhirst, H. Kimura, S. Rehmus, R. Braun, D. Papahadjopoulos, K. Hong, and T. Secomb, "Microvascular studies on the origins of perfusion-limited hypoxia.," *The British journal of cancer. Supplement*, vol. 27, p. S247, 1996.

[167] A. L. Harris, "Hypoxia a key regulatory factor in tumour growth," *Nature Reviews Cancer*, vol. 2, no. 1, p. 38, 2002.

[168] M. W. Dewhirst, "Relationships between cycling hypoxia, hif-1, angiogenesis and oxidative stress," *Radiation research*, vol. 172, no. 6, pp. 653–665, 2009.

[169] R. A. Cairns, T. Kalliomaki, and R. P. Hill, "Acute (cyclic) hypoxia enhances spontaneous metastasis of kht murine tumors," *Cancer research*, vol. 61, no. 24,

pp. 8903–8908, 2001.

[170] H. Kimura, R. D. Braun, E. T. Ong, R. Hsu, T. W. Secomb, D. Papahadjopoulos, K. Hong, and M. W. Dewhirst, "Fluctuations in red cell flux in tumor microvessels can lead to transient hypoxia and reoxygenation in tumor parenchyma," *Cancer research*, vol. 56, no. 23, pp. 5522–5528, 1996.

[171] L. C. Fru, E. B. Adamson, D. D. Campos, S. B. Fain, S. L. Jacques, A. J. Van Der Kogel, K. P. Nickel, C. Song, R. J. Kimple, and M. W. Kissick, "Potential role of the glycolytic oscillator in acute hypoxia in tumors," *Physics in Medicine & Biology*, vol. 60, no. 24, p. 9215, 2015.

[172] P. Vaupel, S. Briest, and M. Höckel, "Hypoxia in breast cancer: pathogenesis, characterization and biological/therapeutic implications," *Wiener Medizinische Wochenschrift*, vol. 152, no. 13-14, pp. 334–342, 2002.

[173] M. Höckel and P. Vaupel, "Biological consequences of tumor hypoxia," in *Seminars in oncology*, vol. 28, pp. 36–41, Elsevier, 2001.

[174] P. Vaupel and L. Harrison, "Tumor hypoxia: causative factors, compensatory mechanisms, and cellular response," *The oncologist*, vol. 9, no. Supplement 5, pp. 4–9, 2004.

[175] P. Maxwell, G. Dachs, J. Gleadle, L. Nicholls, A. Harris, I. Stratford, O. Hankinson, C. Pugh, , and P. Ratcliffe, "Hypoxia-inducible factor-1 modulates gene expression in solid tumors and influences both angiogenesis and tumor growth," *Proceedings of the National Academy of Sciences*, vol. 94, no. 15, pp. 8104–8109, 1997.

[176] C. Chen, N. Pore, A. Behrooz, F. Ismail-Beigi, and A. Maity, "Regulation of glut1 mrna by hypoxia-inducible factor-1 interaction between h-ras and hypoxia," *Journal of Biological Chemistry*, vol. 276, no. 12, pp. 9519–9525, 2001.

[177] N. C. Denko, "Hypoxia, hif1 and glucose metabolism in the solid tumour," *Nature Reviews Cancer*, vol. 8, no. 9, p. 705, 2008.

[178] M. S. Patel and L. G. Korotchkina, "Regulation of mammalian pyruvate dehydrogenase complex by phosphorylation: complexity of multiple phosphorylation

sites and kinases," *Experimental & molecular medicine*, vol. 33, no. 4, p. 191, 2001.

[179] M. C. Brahimi-Horn, G. Bellot, and J. Pouyssegur, "Hypoxia and energetic tumour metabolism," *Current opinion in genetics & development*, vol. 21, no. 1, pp. 67–72, 2011.

[180] N. Pescador, D. Villar, D. Cifuentes, M. Garcia-Rocha, A. Ortiz-Barahona, S. Vazquez, A. Ordoñez, Y. Cuevas, D. Saez-Morales, M. L. Garcia-Bermejo, *et al.*, "Hypoxia promotes glycogen accumulation through hypoxia inducible factor (hif)-mediated induction of glycogen synthase 1," *PloS one*, vol. 5, no. 3, p. e9644, 2010.

[181] S. Fogarty and D. Hardie, "Development of protein kinase activators: Ampk as a target in metabolic disorders and cancer," *Biochimica et Biophysica Acta (BBA)-Proteins and Proteomics*, vol. 1804, no. 3, pp. 581–591, 2010.

[182] A. McBride and D. Hardie, "Amp-activated protein kinase–a sensor of glycogen as well as amp and atp?," *Acta physiologica*, vol. 196, no. 1, pp. 99–113, 2009.

[183] N. Goda, H. E. Ryan, B. Khadivi, W. McNulty, R. C. Rickert, and R. S. Johnson, "Hypoxia-inducible factor 1α is essential for cell cycle arrest during hypoxia," *Molecular and cellular biology*, vol. 23, no. 1, pp. 359–369, 2003.

[184] M. S. Soengas, R. Alarcon, H. Yoshida, R. Hakem, T. Mak, S. Lowe, *et al.*, "Apaf-1 and caspase-9 in p53-dependent apoptosis and tumor inhibition," *Science*, vol. 284, no. 5411, pp. 156–159, 1999.

[185] F. K. . ed., *The Physics of Radiation Therapy.* Philadelphia, PA, USA: Lippincott Williams and Wilkins, 2003.

[186] H. Johns and J. Cunningham, *The Physics of Radiology 4ed.* Springfield, IL, USA: Charles C Thomas Publisher, 1983.

[187] E. Podgorsak, *Radiation Physics for Medical Physicists 2ed.* Springer-Verlag Berlin Heidelberg, 2010.

[188] F. Attix, *Introduction to Radiological Physics and Radiation Dosimetry.* Weinheim, Germany: Wiley-VCH Verlag GmbH & Co. KGaA, 2004.

[189] M. C. Joiner, A. van der Kogel, and G. G. Steel, *Basic Clinical Radiobiology*. London, U.K.: Edward Arnold, 2009.

[190] B. G. Wouters and A. C. Begg, *Basic Clinical Radiobiology*. London, U.K.: Edward Arnold, 2009.

[191] R. Warters, K. Hofer, C. Harris, and J. Smith, "Radionuclide toxicity in cultured mammalian cells: elucidation of the primary site of radiation damage," *Curr. Top. Radiat. Res. Q.*, vol. 12, no. 1-4, pp. 389–407, 1978.

[192] R. Warters and K. Hofer, "Radionuclide toxicity in cultured mammalian cells," *Radiat. Res.*, vol. 69, pp. 348–358, 1977.

[193] S. Matsuoka, B. Ballif, A. Smogorzewska, E. McDonald III, K. Hurov, J. Luo, C. Bakalarski, Z. Zhao, N. Solimini, Y. Lerenthal, Y. Shiloh, S. Gygi, and S. Elledge, "ATM and ATR substrate analysis reveals extensive protein networks responsive to DNA damage," *Sci. Signal.*, vol. 316, no. 5828, pp. 1160–1166, 2007.

[194] J. Lukas, C. Lukas, and J. Bartek, "Mammalian cell cycle checkpoints: signalling pathways and their organization in space and time," *DNA Repair*, vol. 3, no. 8, pp. 997–1007, 2004.

[195] M. Kastan and J. Bartek, "Cell-cycle checkpoints and cancer," *Nature*, vol. 432, no. 7015, pp. 316–323, 2004.

[196] M. Fernet, F. Mégnin-Chanet, J. Hall, and V. Favaudon, "Control of the G2/M checkpoints after exposure to low doses of ionising radiation: implications for hyper-radiosensitivity.," *DNA Repair*, vol. 9, no. 1, pp. 48–57, 2010.

[197] B. Xu, S. Kim, D. Lim, and M. Kastan, "Two molecularly distinct G2/M checkpoints are induced by ionizing irradiation," *Mol. Cell. Biol.*, vol. 22, no. 4, pp. 1049–1059, 2002.

[198] B. Endlich, I. Radford, H. Forrester, and W. Dewey, "Computerized video time-lapse microscopy studies of ionizing radiation-induced rapid-interphase and mitosis-related apoptosis in lymphoid cells," *Radiat. Res.*, vol. 153, no. 1, pp. 36–48, 2000.

[199] B. G. Wouters, *Basic Clinical Radiobiology.* London, U.K.: Edward Arnold, 2009.

[200] H. Forrester, C. Vidair, N. Albright, C. Ling, and W. Dewey, "Using computerized video time lapse for quantifying cell death of X-irradiated rat embryo cells transfected with c-myc or c-Ha-ras," *Cancer Res.*, vol. 59, no. 4, pp. 931–939, 1999.

[201] L. Hayflick, "The limited in vitro lifetime of human diploid cell strains," *Exp. Cell Res.*, vol. 37, no. 3, pp. 614–636, 1965.

[202] W. Sinclair, "Cyclic X-Ray Responses in Mammalian Cells in Vitro 1," *Radiat. Res.*, vol. 178, no. 2, pp. AV112–AV124, 2012.

[203] L. H. Gray, A. D. Conger, M. Ebert, S. Hornsey, and O. C. A. Scott, "The concentration of oxygen dissolved in tissues at the time of irradiation as a factor in radiotherapy," *British Journal of Radiology*, vol. 26, no. 312, pp. 638–648, 1953.

[204] M. R. Horsman, B. G. Wouters, M. C. Joiner, and J. Overgaard, *Basic Clinical Radiobiology.* London, U.K.: Edward Arnold, 2009.

[205] A. Salem, M.-C. Asselin, B. Reymen, A. Jackson, P. Lambin, C. M. West, J. P. OConnor, and C. Faivre-Finn, "Targeting hypoxia to improve non–small cell lung cancer outcome," *Journal Of The National Cancer Institute*, vol. 110, no. 1, pp. 14–30, 2018.

[206] C. Raman and K. Krishnan, "The production of new radiations by light scattering. Part I," *P. Roy. Soc. Lond. A*, vol. 122, no. 789, pp. 23–35, 1928.

[207] E. Smith and G. Dent, *Modern Raman Spectroscopy A Practical Approach.* West Sussex, England: John Wiley & Sons, Ltd., 2005.

[208] D. Long, *The Raman effect a unified treatment of the theory of Raman scattering by molecules.* West Sussex, England: John Wiley & Sons, Ltd., 2002.

[209] R. Clark and T. Dines, "Resonance Raman spectroscopy, and its application to inorganic chemistry," *Angew. Chem. Int. Ed. Engl.*, vol. 25, pp. 131–158, 1986.

[210] J. Ferraro and K. Nakamoto, *Introductory Raman Spectroscopy*. San Diego, CA, USA: Academic Press INC., 1994.

[211] D. Piston, "Choosing objective lenses: the importance of numerical aperture and magnification in digital optical microscopy," *Biol. Bull.*, vol. 195, pp. 1–4, 1998.

[212] M. Abramowitz, K. Spring, H. Keller, and M. Davidson, "Basic principles of microscope objectives," *BioTechniques*, vol. 33, no. 4, pp. 772–781, 2002.

[213] J. Lerner and A. Thevenon, *The Optics of Spectroscopy: A Tutorial*. Edison, NJ, USA: HORIBA Jobin Yvon, 2013.

[214] J. Pemberton, R. Sobocinski, and G. Sims, "The effect of charge traps on Raman spectroscopy using a Thomson-CSF charge coupled device detector," *Appl. Spec.*, vol. 44, no. 2, pp. 328–330, 1990.

[215] I. Jolliffe, *Principal Component Analysis*. New York, N.Y.: Springer-Verlag New York, Inc., 2002.

[216] G. J. Puppels, J. H. F. Olminkhof, G. M. J. Segers-Nolten, C. Otto, F. F. M. De Mul, and J. Greve, "Laser irradiation and Raman spectroscopy of single living cells and chromosomes: Sample degradation occurs with 514.5 nm but not with 660 nm laser light," *Experimental Cell Research*, vol. 195, no. 2, pp. 361–367, 1991.

[217] I. Notingher, S. Verrier, H. Romanska, A. E. Bishop, J. M. Polak, and L. L. Hench, "In situ characterisation of living cells by Raman spectroscopy," *Spectroscopy*, vol. 16, no. 2, pp. 43–51, 2002.

[218] K. Schuster, I. Reese, E. Urlaub, J. Gapes, and B. Lendi, "Multidimensional information on the chemical composition of single bacterial cells by confocal Raman microspectroscopy," *Anal. Chem.*, vol. 72, pp. 5529–5534, 2000.

[219] D. Pappas, B. Smith, and J. Winefordner, "Raman spectroscopy in bioanalysis," *Talanta*, vol. 51, pp. 131–144, 2000.

[220] I. Notingher and L. Hench, "Raman microspectroscopy: a noninvasive tool for studies of individual living cells in vitro," *Expert Rev. Med. Devices*, vol. 3, no. 2, pp. 215–234, 2006.

[221] G. Schulze, A. Jirasek, M. M. L. Yu, A. Lim, R. F. B. Turner, and M. W. Blades, "Investigation of selected baseline removal techniques as candidates for automated implementation," *Applied Spectroscopy*, vol. 59, no. 5, pp. 545–574, 2005.

[222] C. Krafft, T. Knetschke, A. Siegner, R. H. Funk, and R. Salzer, "Mapping of single cells by near infrared Raman microspectroscopy," *Vibrational Spectroscopy*, vol. 32, no. 1, pp. 75–83, 2003.

[223] J. Mourant, K. Short, S. Carpenter, N. Kunapareddy, L. Coburn, T. Powers, and J. Freyer, "Biochemical differences in tumorigenic and nontumorigenic cells measured by Raman and infrared spectroscopy," *J. Biomed. Optics*, vol. 10, no. 3, pp. 031106–1 – 031106–15, 2005.

[224] N. Uzunbajakava, a. Lenferink, Y. Kraan, B. Willekens, G. Vrensen, J. Greve, and C. Otto, "Nonresonant Raman imaging of protein distribution in single human cells," *Biopolymers - Biospectroscopy Section*, vol. 72, no. 1, pp. 1–9, 2003.

[225] F. Verhaegen, P. Granton, and E. Tryggestad, "Small animal radiotherapy research platforms.," *Physics in medicine and biology*, vol. 56, no. 12, pp. R55–R83, 2011.

[226] P. Schroeder, N. Melear, and R. Pruett, "Quantitative analysis of anatase in Georgia kaolins using Raman spectroscopy," *Appl. Clay Sci.*, vol. 23, pp. 299–308, 2003.

[227] H. Behrens, J. Roux, D. Neuville, and M. Siemann, "Quantification of dissolved H_2O in silicate glasses using confocal microRaman spectroscopy," *Chem. Geol.*, vol. 229, pp. 96–112, 2006.

[228] A. Sadezky, H. Muckenhuber, H. Grothe, R. Niessner, and U. Poschl, "Raman microspectroscopy of soot and related carbonaceous materials: Spectral analysis and structural information," *Carbon*, vol. 43, pp. 1731–1742, 2005.

[229] A. Savitzky and M. Golay, "Smoothing and differentiation of data by simplified least squares procedures," *Anal. Chem.*, vol. 36, no. 8, pp. 1627–1639, 1964.

[230] M. Krzywinski and N. Altman, "Points of Significance: Visualizing samples with box plots," *Nature Methods*, vol. 11, no. 2, pp. 119–120, 2014.

[231] A. M. Enejder, T.-W. Koo, J. Oh, M. Hunter, S. Sasic, M. S. Feld, and G. L. Horowitz, "Blood analysis by raman spectroscopy," *Optics letters*, vol. 27, no. 22, pp. 2004–2006, 2002.

[232] P. Ashok, G. Singh, K. Tan, and K. Dholakia, "Fiber probe based microfluidic raman spectroscopy," *Optics express*, vol. 18, no. 8, pp. 7642–7649, 2010.

[233] U. Neugebauer, S. Dochow, C. Krafft, T. Bocklitz, J. Clement, and J. Popp, "Diagnostics of tumor cells by combination of raman spectroscopy and microfluidics," in *European Conferences on Biomedical Optics*, pp. 80870J–80870J, International Society for Optics and Photonics, 2011.

[234] A. Pallaoro, M. R. Hoonejani, G. B. Braun, C. Meinhart, and M. Moskovits, "Combined sers biotags (sbts) and microfluidic platform for the quantitative ratiometric discrimination between noncancerous and cancerous cells in flow," in *SPIE NanoScience+ Engineering*, pp. 84600T–84600T, International Society for Optics and Photonics, 2012.

[235] A. Y. Lau, L. P. Lee, and J. W. Chan, "An integrated optofluidic platform for raman-activated cell sorting.," *Lab on a chip*, vol. 8, pp. 1116–20, Jul 2008.

[236] S. Dochow, C. Beleites, T. Henkel, G. Mayer, J. Albert, J. Clement, C. Krafft, and J. Popp, "Quartz microfluidic chip for tumour cell identification by raman spectroscopy in combination with optical traps.," *Analytical and bioanalytical chemistry*, vol. 405, pp. 2743–6, Mar 2013.

[237] M. Brenner, S. Schwartz, T. Fellers, and M. Davidson, "Nikon Microscopy U: Water immersion objectives," *http://www.microscopyu.com/articles/optics/waterimmersionobjectives.html*, cited December 2014.

[238] I. R. Lewis and H. Edwards, *Handbook of Raman spectroscopy: from the research laboratory to the process line*. CRC Press, 2001.

[239] R. Nemanich, C. Tsai, and G. Connell, "Interference-enhanced raman scattering of very thin titanium and titanium oxide films," *Physical Review Letters*, vol. 44,

no. 4, p. 273, 1980.

[240] A. F. Chrimes, K. Khoshmanesh, P. R. Stoddart, A. Mitchell, and K. Kalantar-Zadeh, "Microfluidics and raman microscopy: current applications and future challenges.," *Chemical Society reviews*, vol. 42, pp. 5880–906, Jul 2013.

[241] Y. Xia and G. M. Whitesides, "Soft lithography," *Annual review of materials science*, vol. 28, no. 1, pp. 153–184, 1998.

[242] S. K. Sia and G. M. Whitesides, "Microfluidic devices fabricated in poly (dimethylsiloxane) for biological studies," *Electrophoresis*, vol. 24, no. 21, pp. 3563–3576, 2003.

[243] K. R. Ackermann, T. Henkel, and J. Popp, "Quantitative online detection of low-concentrated drugs via a sers microfluidic system," *ChemPhysChem*, vol. 8, no. 18, pp. 2665–2670, 2007.

[244] K. V. Sharp, R. J. Adrian, J. G. Santiago, and J. I. Molho, *Liquid flows in microchannels*, ch. 6. Boca Raton, Florida, USA: CRC Press LLC, 2002.

[245] D. Laser and J. Santiago, "A review of micropumps," *Journal of micromechanics and microengineering*, vol. 14, no. 6, p. R35, 2004.

[246] G. Perozziello, R. Catalano, M. Francardi, E. Rondanina, F. Pardeo, F. D. Angelis, N. Malara, P. Candeloro, G. Morrone, and E. D. Fabrizio, "A microfluidic device integrating plasmonic nanodevices for raman spectroscopy analysis on trapped single living cells," *Microelectronic Engineering*, vol. 111, pp. 314–319, 2013.

[247] S. Dochow, C. Krafft, U. Neugebauer, T. Bocklitz, T. Henkel, G. Mayer, J. Albert, and J. Popp, "Tumour cell identification by means of raman spectroscopy in combination with optical traps and microfluidic environments.," *Lab on a chip*, vol. 11, pp. 1484–90, Apr 2011.

[248] C. Krafft, S. Dochow, C. Beleites, and J. Popp, "Cell identification using raman spectroscopy in combination with optical trapping and microfluidics," in *SPIE BiOS*, pp. 893906–893906, International Society for Optics and Photonics, 2014.

[249] T.-W. Lee, S. Jeon, J. Maria, J. Zaumseil, J. W. Hsu, and J. A. Rogers, "Soft-contact optical lithography using transparent elastomeric stamps and appli-

cation to nanopatterned organic light-emitting devices," *Advanced functional materials*, vol. 15, no. 9, pp. 1435–1439, 2005.

[250] G. Bromfield, D. Dale, P. De, K. Newman, R. Rahal, A. Shaw, H. Weir, R. Woods, L. Xie, A. Demers, L. Ellison, R. Semenciw, and J.-M. Daigle, "Canadian Cancer Statistics 2015," tech. rep., Canadian Cancer Society, Toronto, ON, Canada, 2015.

[251] J. Y. Chang, J. D. Bradley, R. Govindan, and R. Komaki, *Principles and Practice of Radiation Oncology*. Philidelphia, PA, USA: Lippincott Williams & Wilkins, 5 ed., 2008.

[252] B. Roswit, M. E. Patno, R. Rapp, A. Veinbergs, B. Feder, J. Stuhlbarg, and C. B. Reid, "Thr survival of patients with inoperable lung cancer: A large-scale randomized study of radiation therapy versus placebo," *Radiology*, vol. 90, no. 4, 1968.

[253] G. Rodrigues, H. Choy, J. Bradley, K. E. Rosenzweig, J. Bogart, W. J. Curran, E. Gore, C. Langer, A. V. Louie, S. Lutz, M. Machtay, V. Puri, M. Werner-Wasik, and G. M. Videtic, "Definitive radiation therapy in locally advanced non-small cell lung cancer: Executive summary of an American Society for Radiation Oncology (ASTRO) evidence-based clinical practice guideline," *Practical Radiation Oncology*, vol. 5, no. 3, pp. 141–148, 2015.

[254] J. Karar and A. Maity, "Modulating the tumor microenvironment to increase radiation responsiveness," *Cancer Biology and Therapy*, vol. 8, no. 21, pp. 1994–2001, 2009.

[255] H. Harada, "How can we overcome tumor hypoxia in radiation therapy?," *Journal of Radiation Research*, vol. 52, no. 5, pp. 545–556, 2011.

[256] M. Langenbacher, R. J. Abdel-Jalil, W. Voelter, M. Weinmann, and S. M. Huber, "In vitro hypoxic cytotoxicity and hypoxic radiosensitization. Efficacy of the novel 2-nitroimidazole N,N,N-tris[2-(2-nitro-1H-imidazol-1-yl)ethylamine.," *Strahlentherapie und Onkologie : Organ der Deutschen Röntgengesellschaft ... [et al]*, vol. 189, no. 3, pp. 246–254, 2013.

[257] J. D. Chapman, E. L. Engelhardt, C. C. Stobbe, R. F. Schneider, and G. E. Hanks, "Measuring hypoxia and predicting tumor radioresistance with nuclear

medicine assays," *Radiotherapy and Oncology*, vol. 46, no. 3, pp. 229–237, 1998.

[258] M. Baumann, M. Krause, and R. Hill, "Exploring the role of cancer stem cells in radioresistance.," *Nature reviews. Cancer*, vol. 8, no. 7, pp. 545–554, 2008.

[259] J. Akervall, S. Nandalur, J. Zhang, C. N. Qian, N. Goldstein, P. Gyllerup, Y. Gardinger, J. Alm, K. Lorenc, K. Nilsson, J. Resau, G. Wilson, and B. Teh, "A novel panel of biomarkers predicts radioresistance in patients with squamous cell carcinoma of the head and neck," *European Journal of Cancer*, vol. 50, no. 3, pp. 570–581, 2014.

[260] J. F. Torres-roca, "A molecular assay of tumor radiosensitivity: a roadmap towards biology-based personalized radiation therapy," *Personal medicine*, vol. 9, no. 5, pp. 547–557, 2013.

[261] S. Devpura, K. N. Barton, S. L. Brown, O. Palyvoda, S. Kalkanis, V. M. Naik, F. Siddiqui, R. Naik, and I. J. Chetty, "Vision 20/20: The role of Raman spectroscopy in early stage cancer detection and feasibility for application in radiation therapy response assessment," *Medical Physics*, vol. 41, no. 5, p. 50901, 2014.

[262] I. Delfino, G. Perna, M. Lasalvia, V. Capozzi, L. Manti, C. Camerlingo, and M. Lepore, "Visible micro-Raman spectroscopy of single human mammary epithelial cells exposed to x-ray radiation," *Journal of Biomedical Optics*, vol. 20, no. 3, p. 035003, 2015.

[263] Q. Matthews, M. Isabelle, S. J. Harder, J. Smazynski, W. Beckham, A. G. Brolo, A. Jirasek, and J. J. Lum, "Radiation-induced glycogen accumulation detected by single cell Raman spectroscopy is associated with radioresistance that can be reversed by metformin," *PLoS ONE*, vol. 10, no. 8, p. e0135356, 2015.

[264] M. R. Horsman, B. G. Wouters, M. C. Joiner, and J. Overgaard, *Basic Clinical Radiobiology*. London, UK: Edward Arnold, 4 ed., 2009.

[265] S. L. Shiao and L. M. Coussens, "The tumor-immune microenvironment and response to radiation therapy," *Journal of Mammary Gland Biology and Neoplasia*, vol. 15, no. 4, pp. 411–421, 2010.

[266] Q. Matthews, A. Jirasek, J. Lum, X. Duan, and A. G. Brolo, "Variability in Raman spectra of single human tumor cells cultured in vitro: correlation with cell cycle and culture confluency," *Applied Spectroscopy*, vol. 64, no. 8, pp. 871–887, 2010.

[267] Y. H. Ong, M. Lim, and Q. Liu, "Comparison of principal component analysis and biochemical component analysis in Raman spectroscopy for the discrimination of apoptosis and necrosis in K562 leukemia cells: errata," *Optics Express*, vol. 20, no. 22, p. 25041, 2012.

[268] A. D. Meade, C. Clarke, F. Draux, G. D. Sockalingum, M. Manfait, F. M. Lyng, and H. J. Byrne, "Studies of chemical fixation effects in human cell lines using Raman microspectroscopy," *Analytical and Bioanalytical Chemistry*, vol. 396, no. 5, pp. 1781–1791, 2010.

[269] J. Miquel, P. R. Lundgren, and J. O. Jenkins, "Effects of Roentgen radiation on glycogen metabolism of the rat brain," *Acta radiologica: therapy, physics, biology*, vol. 5, no. 1, pp. 123–132, 1966.

[270] P. Vaupel, O. Thews, and M. Hoeckel, "Treatment resistance of solid tumors: role of hypoxia and anemia.," *Medical oncology (Northwood, London, England)*, vol. 18, no. 4, pp. 243–259, 2001.

[271] M. Z. Ibrahim, E. Pascoe, S. Alam, and J. Miquel, "Glycogen and phosphorylase activity in rat brain during recovery from several forms of hypoxia.," *The American journal of pathology*, vol. 60, no. 3, pp. 403–420, 1970.

[272] S. Ramon y Cajal, L. De Mattos-Arruda, N. Sonenberg, J. Cortes, and V. Peg, "The intra-tumor heterogeneity of cell signaling factors in breast cancer: p4E-BP1 and peIF4E are diffusely expressed and are real potential targets," *Clinical and Translational Oncology*, vol. 16, pp. 937–941, 2014.

[273] D. E. Dosoretz, M. J. Katin, P. H. Blitzer, J. H. Rubenstein, D. H. Galmarini, G. R. Garton, and S. A. Salenius, "Medically inoperable lung carcinoma: the role of radiation therapy," in *Seminars in radiation oncology*, vol. 6, pp. 98–104, Elsevier, 1996.

[274] C. Falkson, E. Vella, E. Yu, M. El-Mallah, R. Mackenzie, P. Ellis, and Y. Ung, "Guideline for radiotherapy with curative intent in patients with early-stage

medically inoperable non-small-cell lung cancer," *Current Oncology*, vol. 24, no. 1, p. e44, 2017.

[275] M. K. Buyyounouski, P. Balter, B. Lewis, D. J. D'Ambrosio, T. J. Dilling, R. C. Miller, T. Schefter, W. Tomé, E. E. Harris, R. A. Price, *et al.*, "Stereotactic body radiotherapy for early-stage non-small-cell lung cancer: report of the astro emerging technology committee," *International Journal of Radiation Oncology Biology Physics*, vol. 78, no. 1, pp. 3–10, 2010.

[276] L. E. Gaspar, "Optimizing chemoradiation therapy approaches to unresectable stage iii non–small cell lung cancer," *Current opinion in oncology*, vol. 13, no. 2, pp. 110–115, 2001.

[277] N. Ramnath, T. J. Dilling, L. J. Harris, A. W. Kim, G. C. Michaud, A. A. Balekian, R. Diekemper, F. C. Detterbeck, and D. A. Arenberg, "Treatment of stage iii non-small cell lung cancer: Diagnosis and management of lung cancer: American college of chest physicians evidence-based clinical practice guidelines," *Chest*, vol. 143, no. 5, pp. e314S–e340S, 2013.

[278] K. Sigel, L. Lurslurchachai, M. Bonomi, G. Mhango, C. Bergamo, M. Kale, E. Halm, and J. Wisnivesky, "Effectiveness of radiation therapy alone for elderly patients with unresected stage III non-small cell lung cancer.," *Lung cancer (Amsterdam, Netherlands)*, vol. 82, no. 2, pp. 266–70, 2013.

[279] C. P. Belani, H. Choy, P. Bonomi, C. Scott, P. Travis, J. Haluschak, and W. J. Curran Jr, "Combined chemoradiotherapy regimens of paclitaxel and carboplatin for locally advanced non–small-cell lung cancer: A randomized phase ii locally advanced multi-modality protocol," *Journal of clinical oncology*, vol. 23, no. 25, pp. 5883–5891, 2005.

[280] J. P. Grutters, A. G. Kessels, M. Pijls-Johannesma, D. De Ruysscher, M. A. Joore, and P. Lambin, "Comparison of the effectiveness of radiotherapy with photons, protons and carbon-ions for non-small cell lung cancer: a meta-analysis," *Radiotherapy and Oncology*, vol. 95, no. 1, pp. 32–40, 2010.

[281] S. Baker, M. Dahele, F. J. Lagerwaard, and S. Senan, "A critical review of recent developments in radiotherapy for non-small cell lung cancer," *Radiation oncology*, vol. 11, no. 1, p. 115, 2016.

[282] P. McCloskey, B. Balduyck, P. E. Van Schil, C. Faivre-Finn, and M. OBrien, "Radical treatment of non-small cell lung cancer during the last 5 years," *European Journal of Cancer*, vol. 49, no. 7, pp. 1555–1564, 2013.

[283] L. Li, M. Hu, H. Zhu, W. Zhao, G. Yang, and J. Yu, "Comparison of 18f-fluoroerythronitroimidazole and 18f-fluorodeoxyglucose positron emission tomography and prognostic value in locally advanced non–small-cell lung cancer," *Clinical lung cancer*, vol. 11, no. 5, pp. 335–340, 2010.

[284] Q.-T. Le, E. Chen, A. Salim, H. Cao, C. S. Kong, R. Whyte, J. Donington, W. Cannon, H. Wakelee, R. Tibshirani, *et al.*, "An evaluation of tumor oxygenation and gene expression in patients with early stage non–small cell lung cancers," *Clinical Cancer Research*, vol. 12, no. 5, pp. 1507–1514, 2006.

[285] R. Murata, Y. Shibamoto, K. Sasai, N. Oya, T. Shibata, T. Takagi, and M. Abe, "Reoxygenation after single irradiation in rodent tumors of different types and sizes," *International Journal of Radiation Oncology Biology Physics*, vol. 34, no. 4, pp. 859–865, 1996.

[286] C. H. Allen, A. Kumar, S. Qutob, B. Nyiri, V. Chauhan, and S. Murugkar, "Raman micro-spectroscopy analysis of human lens epithelial cells exposed to a low-dose-range of ionizing radiation," *Physics in Medicine & Biology*, vol. 63, no. 2, p. 025002, 2018.

[287] S. J. Harder, M. Isabelle, L. DeVorkin, J. Smazynski, A. G. Brolo, J. J. Lum, and A. Jirasek, "Raman spectroscopy identifies radiation response in human non-small cell lung cancer xenografts," *Scientific Reports*, p. 6:21006, 2016.

[288] S. J. Van Nest, L. M. Nicholson, L. DeVorkin, A. G. Brolo, J. J. Lum, and A. Jirasek, "Raman spectroscopic signatures reveal distinct biochemical and temporal changes in irradiated human breast adenocarcinoma xenografts," *Radiation research*, vol. 189, no. 5, pp. 497–504, 2018.

[289] K. Schlie, A. Westerback, L. DeVorkin, L. R. Hughson, J. M. Brandon, S. MacPherson, I. Gadawski, K. N. Townsend, V. I. Poon, M. A. Elrick, *et al.*, "Survival of effector cd8+ t cells during influenza infection is dependent on autophagy," *The Journal of Immunology*, vol. 194, no. 9, pp. 4277–4286, 2015.

[290] J. E. Spowart, K. N. Townsend, H. Huwait, S. Eshragh, N. R. West, J. N. Ries, S. Kalloger, M. Anglesio, S. M. Gorski, P. H. Watson, *et al.*, "The autophagy protein lc3a correlates with hypoxia and is a prognostic marker of patient survival in clear cell ovarian cancer," *The Journal of pathology*, vol. 228, no. 4, pp. 437–447, 2012.

[291] J. Raleigh, S. Chou, G. Arteel, and M. Horsman, "Comparisons among pimonidazole binding, oxygen electrode measurements, and radiation response in c3h mouse tumors," *Radiation research*, vol. 151, no. 5, pp. 580–589, 1999.

[292] A. J. Varghese, S. Gulyas, and J. K. Mohindra, "Hypoxia-dependent reduction of 1-(2-nitro-1-imidazolyl)-3-methoxy-2-propanol by chinese hamster ovary cells and kht tumor cells in vitro and in vivo," *Cancer research*, vol. 36, no. 10, pp. 3761–3765, 1976.

[293] S. Kaluz, M. Kaluzová, S.-Y. Liao, M. Lerman, and E. J. Stanbridge, "Transcriptional control of the tumor-and hypoxia-marker carbonic anhydrase 9: A one transcription factor (hif-1) show?," *Biochimica et Biophysica Acta (BBA)-Reviews on Cancer*, vol. 1795, no. 2, pp. 162–172, 2009.

[294] S. Burma, B. P. Chen, M. Murphy, A. Kurimasa, and D. J. Chen, "Atm phosphorylates histone h2ax in response to dna double-strand breaks," *Journal of Biological Chemistry*, vol. 276, no. 45, pp. 42462–42467, 2001.

[295] E. E. Graves, M. Vilalta, I. K. Cecic, J. T. Erler, P. T. Tran, D. Felsher, L. Sayles, A. Sweet-Cordero, Q.-T. Le, and A. J. Giaccia, "Hypoxia in models of lung cancer: implications for targeted therapeutics," *Clinical Cancer Research*, vol. 16, no. 19, pp. 4843–4852, 2010.

[296] D. Zips, *Basic Clinical Radiobiology*. London, UK: Edward Arnold, 4 ed., 2009.

[297] M. Garcia-Barros, F. Paris, C. Cordon-Cardo, D. Lyden, S. Rafii, A. Haimovitz-Friedman, Z. Fuks, and R. Kolesnick, "Tumor response to radiotherapy regulated by endothelial cell apoptosis," *Science*, vol. 300, no. 5622, pp. 1155–1159, 2003.

[298] M. Ilie, V. Hofman, J. Zangari, J. Chiche, J. Mouroux, N. M. Mazure, J. Pouysségur, P. Brest, and P. Hofman, "Response of caix and caxii to in

vitro re-oxygenation and clinical significance of the combined expression in nsclc patients," *Lung cancer*, vol. 82, no. 1, pp. 16–23, 2013.

[299] G. Curigliano, H. J. Burstein, E. P. Winer, M. Gnant, P. Dubsky, S. Loibl, M. Colleoni, and F. Andre, "De-escalating and escalating treatments for early-stage breast cancer : the St. Gallen International Expert Consensus Conference on the Primary Therapy of Early Breast Cancer 2017," *Annals of Oncology*, vol. 28, no. June, pp. 1700–1712, 2017.

[300] E. B. C. T. C. Group, "Effect of radiotherapy after breast-conserving surgery on 10-year recurrence and 15-year breast cancer death : meta-analysis of individual patient data for 10 801 women in 17 randomised trials," *The Lancet*, vol. 378, pp. 1707–1716, 2011.

[301] T. Sørlie, R. Tibshirani, J. Parker, T. Hastie, J. S. Marron, A. Nobel, S. Deng, H. Johnsen, R. Pesich, S. Geisler, J. Demeter, C. M. Perou, P. E. Lønning, P. O. Brown, and D. Botstein, "Repeated observation of breast tumor subtypes in independent gene expression data sets," *PNAS*, vol. 100, no. 14, pp. 8418–8423, 2003.

[302] T. C. G. A. Network, "Comprehensive molecular portraits of human breast tumours," *Nature*, vol. 490, pp. 61–70, 2012.

[303] M. Kyndi, F. B. Sørensen, H. Knudsen, M. Overgaard, and H. M. Nielsen, "Estrogen Receptor , Progesterone Receptor , HER-2 , and Response to Postmastectomy Radiotherapy in High-Risk Breast Cancer : The Danish Breast Cancer Cooperative Group," *Journal of Clinical Oncology*, vol. 26, no. 9, pp. 1419–1426, 2008.

[304] J. F. Torres-Roca, W. J. Fulp, J. J. Caudell, N. Servant, M. A. Bollet, M. van de Vijver, A. O. Naghavi, E. E. Harris, and S. A. Eschrich, "Integration of a Radiosensitivity Molecular Signature Into the Assessment of Local Recurrence Risk in Breast Cancer," *International Journal of Radiation Oncology*Biology*Physics*, vol. 93, no. 3, pp. 631–638, 2015.

[305] N. Lee, H. Schoder, B. Beattie, R. Lanning, N. Riaz, S. Mcbride, N. Katabi, D. Li, B. Yarusi, S. Chan, L. Mitrani, Z. Zhang, D. G. Pfister, E. Sherman, S. Baxi, J. Boyle, L. G. T. Morris, I. Ganly, R. Wong, and J. Humm, "Strategy

of Using Intratreatment Hypoxia Imaging to Selectively and Safely Guide Radiation Dose De-escalation Concurrent With Chemotherapy for Locoregionally Advanced Human Papillomavirus- Related Oropharyngeal Carcinoma," *International Journal of Radiation Oncology Biology Physics*, vol. 96, no. 1, pp. 9–17, 2016.

[306] K. R. Luoto, R. Kumareswaran, and R. G. Bristow, "Tumor hypoxia as a driving force in genetic instability," *Genome Integrity*, vol. 4, no. 5, 2013.

[307] M. Nordsmark, S. M. Bentzen, V. Rudat, D. Brizel, E. Lartigau, P. Stadler, A. Becker, M. Adam, M. Molls, J. Dunst, D. J. Terris, and J. Overgaard, "Prognostic value of tumor oxygenation in 397 head and neck tumors after primary radiation therapy . An international multi-center study," *Radiotherapy and Oncology*, vol. 77, pp. 18–24, 2005.

[308] R. Limame, A. Wouters, B. Pauwels, E. Fransen, M. Peeters, F. Lardon, O. De, and P. Pauwels, "Comparative Analysis of Dynamic Cell Viability , Migration and Invasion Assessments by Novel Real-Time Technology and Classic Endpoint Assays," *PLoS ONE*, vol. 7, no. 10, 2012.

[309] M. Vilalta, M. Rafat, A. J. Giaccia, and E. E. Graves, "Recruitment of Circulating Breast Cancer Cells Is Stimulated by Radiotherapy," *Cell Reports*, vol. 8, no. 2, pp. 402–409, 2014.

[310] C. Yu, E. Gestl, K. Eckert, D. Allara, and J. Irudayaraj, "Characterization of human breast epithelial cells by confocal Raman microspectroscopy," *Cancer Detection and Prevention*, vol. 30, no. 6, pp. 515–522, 2006.

[311] D. Naumann, "FT-infrared and Raman spectroscopy in biomedical research," *Applied Spectroscopy Reviews*, vol. 36, no. 2&3, pp. 239–298, 2001.

[312] S. A. Overman, K. L. Aubrey, K. E. Reilly, O. Osman, S. J. Hayes, P. Serwer, and G. J. Thomas, "Conformation and interactions of the packaged double-stranded DNA genome of bacteriophage T7.," *Biospectroscopy*, vol. 4, no. 5 Suppl, pp. S47–S56, 1998.

[313] K. M. Omberg, J. C. Osborn, S. L. Zhang, J. P. Freyer, J. R. Mourant, and J. R. Schoonover, "Raman spectroscopy and factor analysis of tumorigenic and non-tumorigenic cells," *Applied Spectroscopy*, vol. 56, no. 7, pp. 813–819, 2002.

[314] H. Nawaz, A. Garcia, A. D. Meade, F. M. Lyng, and H. J. Byrne, "Raman micro spectroscopy study of the interaction of vincristine with A549 cells supported by expression analysis of bcl-2 protein.," *The Analyst*, vol. 138, no. 20, pp. 6177–84, 2013.

Appendices

Appendix A

Principal Component Band Assignments in Non-Small Cell Lung Cancer Study

	Assignment		
Raman shift (cm^{-1})	**Protein**	**Lipid**	**Carb.**
482			Glyc.
580			Glyc.
729		C-N hg. [97]	
815		O-P-O [97]	
850			Glyc.
940			Glyc.
980		C-C hg. [97]	
1042			Glyc.
1083			Glyc.
1129			Glyc.
1240	Am. III rc. [97]		
1245	Am. III β [97]		
1274	Am. III β [97]	=CH def. [97]	
1284	Am. III α [97]	=CH def. [97]	
1297		CH_2 tw. [97]	
1338			Glyc.
1385			Glyc.
1447	CH def. [97]	CH def. [97]	
1465	CH def. [97]	CH def. [97]	
1661	Am. I α [97]	C=C str. [97]	

Table A.1: Raman peak assignment for radiation induced component (PC1) in H460 tumour xenografts of Cohort A. Only main contributors of a band are listed. Abbreviations: Glycogen (glyc), head groups (hg), Amide (Am), random coil (rc), beta sheet (β), deformation (def), alpha helix (α), twist (tw), stretch (str).

	Assignment		
Raman shift (cm^{-1})	**Nucleic Acid**	**Protein**	**Lipid**
668	G,T [262]		
716			Cho. [262]
729	A [97]	Tryp. [97]	
784	T [97]		
825			Cho. [141]
937		C-C bk. str. α [97]	
1004		Phe. [97]	
1047		Phe. [262]	
1066		C-N str. [97]	C-C str. [97]
1080		C-N str. [97]	C-C str. [97]
1087			C-C str. [97]
1127		C-N str. [97]	C-C str. [97]
1180		Phe. [262]	
1210		Phe., Tryp. [97]	
1272			=CH def. [262]
1284		Am. III α [97]	=CH def. [97]
1031			CH_2 tw. [97]
1328	G [97]		
1338		Tryp. [142]	
1342	A, G [97]		
1365	T [262]		sym. str. CH_3 [97]
1374	A,G [310]	Tryp. [142]	
1450		CH def. [97]	CH def. [97]
1460		CH def. [97]	CH def. [97]
1576	A,G [310]	Tryp. [142]	
1607		Phe. [97]	
1621		Tryp. [97]	
1659		Am. I α [97]	C=C str. [97]
1740			C=O ester [97]

Continued ...

Table A.2: Raman peak assignment for cell cycle component (PC2) in H460 tumour xenografts of Cohort A. Only main contributors of a band are listed.

Table A.2 continued ...

	Assignment		
Raman shift (cm^{-1})	**Nucleic Acid**	**Protein**	**Lipid**

Table A.2: Raman peak assignment for cell cycle component (PC2) in H460 tumour xenografts of Cohort A. Only main contributors of a band are listed. Abbreviations: Guanine (G), Thymine (T), Choline (Cho), Adenine (A), Tryptophan (Tryp), backbone (bk), stretch (str), alpha helix (α), Phenylalanine (Phe), Amide (Am), deformation (def), twist (tw), symmetric (sym).

Appendix B

Principal Component Band Assignments in Non-Small Cell Lung Cancer Metabolism Study

	Assignment			
Raman shift (cm^{-1})	**Nucleic Acid**	**Protein**	**Lipid**	**Carb.**
479				Glyc.
580				Glyc.
726	A [222]			
784	C,U ring str. [311]			
810			O-P-O [97]	
850				Glyc.
940				Glyc.
955-994	d. [312]	C-C str. [312]	C-C [97]	
1002		Phe. sym. rb. [97]		
1042				Glyc.
1082				Glyc.
1129				Glyc.
1178		Phe. ring str. [313] Tyr. [224]		
1249	T [312]	Am. III β [97]		
1297	A [96]	CH def. [96]	CH_2 tw. [97]	
1335				Glyc.
1382				Glyc.
1442		CH def. [97]	CH def. [97]	
1659	T,C,G [312]	Am. I [312]		

Table B.1: Raman peak assignment for radiation induced component (PC1) in H460 tumour xenografts of Cohort C. Only main contributors of a band are listed. Abbreviations: Glycogen (Glyc), Adenine (A), Cytosine (C), Uracil (U), stretch (str), deoxyribose (d), Phenylalanine (Phe), symmetric (sym), ring breathing (rb), Tyrosine (Tyr), Thymine (T), Amide (Am), beta sheet (β), deformation (def), twist (tw), Cytosine (C), Guanine (G).

	Assignment			
Raman shift (cm^{-1})	**Nucleic Acid**	**Protein**	**Lipid**	**Carb.**
666	G,T [222], [312]			
714			Cho. [222]	
714			C-N str. [115]	

Continued ...

Table B.2: Raman peak assignment for cell cycle component (PC2) of H460 tumour xenografts in Cohort C. Only main contributors of a band are listed.

Table B.2 continued ...

	Assignment			
Raman shift (cm^{-1})	**Nucleic Acid**	**Protein**	**Lipid**	**Carb.**
726	A [222]			
784	U,C [115]			
855	O-P-O str. [97]	tyr. r.b. [222]		
927		C-C bk. α [142]		
1004		Phe. sym. rb. [222]		
1071		C-N str. [97]	C-C str. [222]	
1134		C-N str. [97]	C-C str. [97, 222]	
1178	DNA/RNA	Phe. ring str. [313]		
	ring vib. [313]	C-H bd. Tyr. [97, 313]		
1235		Am. III rc. [97]		
1272		Am III α [97, 142]		
1297		Am. III α [97]	CH def. [97]	
1338	CH_3CH_2 wg. [115]			
1373	T [222]			
	A,G [312]			
1438			CH_2 def. [222]	
1577	A,G [222]			
1618		Tyr. [311]		
		Tryp. [115]		
1659		Am. I α [115]	C=C str. [115]	
1682		Am. I β [142]		

Table B.2: Raman peak assignment for cell cycle component (PC2) in H460 tumour xenografts of Cohort C. Only main contributors of a band are listed. Abbreviations: Guanine (G), Thymine (T), Choline (Cho), stretch (str), Adenine (A), Uracil (U), Cytosine (C), backbone (bk), Phenylalanine (Phe), symmetric (sym), ring breathing (rb), Deoxyribonuclease (DNA), ribonuclease (RNA), vibration (vib), bending (bd), Tyrosine (Tyr), Amide (Am), random coil (rc), alpha helix (α), wagging (wg), deformation (def), Tryptophan (Tryp), beta sheet (β).

Appendix C

Principal Component Band Assignments in Breast Cancer Study

	Assignment			
Raman shift (cm^{-1})	**Nucleic Acid**	**Protein**	**Lipid**	**Carb.**
668	G,T [222, 312]			
716			Cho. [222]	
728	A [97]	Trp. [97]		
783	U,C,T rb. [97]			
	O-P-O sym. str. [224]			
817-900	O-P-O str. [97]	Tyr. [222, 311]		
1001		Phe. rb. [97, 313]		
1047		Phe. [262]		C-O str. [97]
1053-1090		C-N str. [97]	C-C [222]	C-O str. [97]
1128		C-N str. [224]		
		C-C str. [222]		
1180		Phe., Tyr. [224]		
1212		Phe., Tyr. [222],		

Continued ...

Table C.1: Raman peak assignment for MDA-MB-231 tumour xenograft (Cohort B) cell cycle component (PC1). Only main contributors of a band are listed.

Table C.1 continued ...

	Assignment			
Raman shift (cm^{-1})	**Nucleic Acid**	**Protein**	**Lipid**	**Carb.**
		Am III [224], Tryp. [97]		
1235	T [312]	Am III β [312]		
1269		Am. III α [142]	CH def. [97]	
1296			CH_2 def. [311]	
			CH_2 tw. [142, 222]	
1337	A,G [97]	CH def. [97], Tryp. [142]		
1377	A, G, T [222]			
1439			CH_2 def. [222]	
1455		CH_2 def. [142]	CH_2 def. [142]	
1577	G,A [222]	Tryp., Phe. [142]		
1618		Tyr., Tryp. [97]		
1658		Am. I α [142]	C=C [142]	
1682		Am. I β [142]		
1743			C=O [142]	

Table C.1: Raman peak assignment for MDA-MB-231 tumour xenograft cell cycle component (PC1) of Cohort B. Only main contributors of a band are listed. Abbreviations: Guanine (G), Thymine (T), Choline (Cho), Adenine (A), Tryptophan (Tryp), Uracil (U), Cytosine (C), ring breathing (rb), symmetric (sym), stretch (str), Tyrosine (Tyr), Phenylalanine (Phe), Amide (Am), alpha helix (α), beta sheet (β), deformation (def), twist (tw).

	Assignment			
Raman shift (cm^{-1})	**Nucleic Acid**	**Protein**	**Lipid**	**Carb.**
497	G,T [222]			
670	G,T [222]			
706		Tryp. [314]		
728	A rb. [222]			
761		Tryp. [222]		
782	C rb.,T [96], U str. [311]			
854		Tyr. rb. [96, 115] Prol. [115]		
922		C-C str. Prol. [115]	Lact. acid [115]	Gluc. [115]
939		C-C str. Prol. C-C str. Val. C-C str. α bk. [115]		Glyc. [115]
1004		Phe. sym. rb. [222]		
1034		Phe. C-H bd. [115]		
1063		C-N str. [97]	C-C str. [222]	
1096	PO_2 bk. [222]			
1126		C-C str. [222] C-N str. [313]		
1161		C-O vib., COH def. [142]		C-O vib., COH def. [142]
1237	T [96]	Am. III β [96, 142]		
1255	C,A [312]	Am III α [142, 222]		
1301	DNA/RNA rv. [313]		CH_2 tw. [313]	
1335	A,G [97] CH_2, CH_3 wag. [142]		CH_2, CH_3 wag. [142]	
1370		Tryp. [142]	CH_3 sym. str. [97]	
1404		COO^- sym.		
1404		str. [142]		
1424	A,G [96] CH_2 bk. [222]		CH_3 asym. def., =CH def. [142]	

Continued ...

Table C.2: Raman peak assignment for radiation induced component (PC2) in MDA-MB-231 tumour xenografts of Cohort B. Only main contributors of a band are listed.

Table C.2 continued ...

	Assignment			
Raman shift (cm^{-1})	**Nucleic Acid**	**Protein**	**Lipid**	**Carb.**
1444	DNA rp. [96]	CH_2 bd. [115]	CH_2 bd. [115]	
1486	G,A [224]			
1549		Tryp. [115]		
1577	G,A [222]			
1656		Amide I α [142]	C=C str. [142]	
1679		Amide I β [142]		

Table C.2: Raman peak assignment for MDA-MB-231 tumour xenograft radiation induced component (PC2) of Cohort B. Only main contributors of a band are listed. Abbreviations: Guanine (G), Thymine (T), Tryptophan (Tryp), Adenine (A), ring breathing (rb), Cytosine (C), Urasil (U), stretch (str), Tyrosine (Tyr), Proline (Prol), Lactic Acid (Lac. acid), Glucose (Gluc), Glycogen (Glyc), Valine (Val), alpha helix (α), backbone (bk), Phenylalanine (Phe), symmetric (sym), bending (bd), vibration (vb), deformation (def), Amide (Am), beta sheet (β), ring vibration (rv), twist (tw), wagging (wag), asymmetric (asym), ring pucker (rp).